Development of the Control Assembly Pattern and Dynamic Analysis of the Generation IV Large Gas-cooled Fast Reactor (GFR)

THÈSE N^{O} 4437 (2009)

PRÉSENTÉE LE 9 JUILLET 2009
À LA FACULTÉ SCIENCES DE BASE
LABORATOIRE DE PHYSIQUE DES RÉACTEURS ET DE COMPORTEMENT DES SYSTÈMES
PROGRAMME DOCTORAL EN ENERGIE

ÉCOLE POLYTECHNIQUE FÉDÉRALE DE LAUSANNE

POUR L'OBTENTION DU GRADE DE DOCTEUR ÈS SCIENCES

PAR

Gaëtan GIRARDIN

acceptée sur proposition du jury:

Prof. L. Rivkin, président du jury
Prof. R. Chawla, directeur de thèse
Dr K. Mikityuk, rapporteur
Prof. G. Rimpault, rapporteur
Prof. J. Wallenius, rapporteur

ÉCOLE POLYTECHNIQUE
FÉDÉRALE DE LAUSANNE

Suisse
2009

Abstract

During the past ten years, different independent factors, such as the rapidly increasing worldwide demand in energy, societal concerns about greenhouse gas emissions, and the high and volatile prices for fossil fuels, have contributed to the renewed interest in nuclear technology. It is in this context that the Generation IV international forum (GIF) launched the initiative, in 2000, to collaborate on the research and development (R&D) efforts needed for the next generation, i.e. Generation IV, of nuclear reactors. These advanced systems will be ideally deployed beyond the year 2030, following the Generation III or III+ nuclear power plants, which are mainly based on light water technology and are currently entering deployment. A particular goal set for Generation IV systems is closure of the nuclear fuel cycle. Thus, apart from improvements in safety, they are expected to offer a better utilization of natural resources, as also a minimization of long-lived radioactive wastes.

Among the systems selected by the GIF, the Gas-cooled Fast Reactor (GFR) is a highly innovative system with advanced fuel geometry and materials (fuel pellets of mixed uranium-plutonium carbide within a plate-type, honeycomb structure made of SiC). It is in the context of the large, 2400 MWth reference GFR design that the present doctoral research has been conducted, the principal aim having been to develop and qualify the control assembly (CA) pattern and corresponding CA implementation scheme for this system. The work has been carried out in three successive and complementary phases: (1) validation of the neutronics tools, (2) the CA pattern development and related static analysis, and (3) dynamic core behavior studies for hypothetical CA driven transients.

The deterministic code system ERANOS and its associated nuclear data libraries for fast reactors were developed and validated for the previous generation of sodium-cooled reactors. The validation of ERANOS for GFR applications was, therefore, the first task to be realized in the present research. This has entailed a systematic reanalysis of the GFR-relevant, integral data generated at PSI during the GCFR-PROTEUS experimental program of the 1970's.

Thus, during the first phase of the thesis, the reference PROTEUS test lattice from these experiments has been analyzed with ERANOS-2.0 and its associated, adjusted nuclear data library ERALIB1, in order to derive a reference computational scheme to be used later for the GFR analysis. Additionally, benchmark calculations were performed with the Monte Carlo code MCNPX, allowing one to both check the deterministic results and to analyze the sensitivity to different modern data libraries. It has been found that, for the main reaction rate ratios, the new analysis of the GCFR-PROTEUS reference lattice generally yields good agreement – within 1σ measurement uncertainty – with experimental values and with the Monte Carlo simulations. As shown by the analysis, the predictions were in somewhat better agreement in the case of the adjusted ERALIB1 library. The applicability of ERANOS-2.0/ERALIB1 as the reference neutronics tool for the GFR analysis could thus be demonstrated. Furthermore, neutronics aspects related to the novel features of the GFR, for which new experimental investigations are needed, were highlighted.

In the second phase of the research, the CA pattern was developed for the GFR, based on iterative neutronics and thermal-hydraulics calculations, 2D and 3D neutronics models for the reactor core having first been set up using the reference ERANOS-2.0/ERALIB1 computational scheme. For the thermal-hydraulics analysis, the CEA code COPERNIC was used. This design work was followed by the study of an appropriate CA implementation scheme (number of CAs and corresponding positions within the core). Detailed neutronics studies revealed the existence of large CA interaction effects, so-called shadowing/anti-shadowing effects leading to an

amplification/reduction of the CA worth. The interactions between the absorber pins within a CA, and between the CAs themselves, were investigated in detail, with the goal to optimize the CA efficiency, in terms of the absorber fraction and minimization of the associated heterogeneity effects.

The proposed CA pattern consists of 54 absorber pins placed in a triangular lattice. Each absorber pin is a stainless-steel tube filled with highly enriched ^{10}B boron carbide pellets. As a result of the detailed investigations, the absorber pin diameter could be chosen such as to minimize the pin-to-pin influence within the assembly. In particular, a central part of the CA was designed without any absorber pins (zone filled with stagnant helium). A final reduction of the heterogeneity effect (difference between homogeneous and heterogeneous treatments) to 13% was achieved through this feature. Of special importance, the neutronics investigations performed for the reference GFR core ("2004-Core"), especially those related to the CA interactions, have directly contributed to a new core design ("2007-Core"), with the height-to-diameter ratio having been increased to 0.6, compared to 0.3 for the reference core.

During the third phase, detailed coupled, 3D neutron-kinetics (NK) and 1D thermal-hydraulics (TH) models were developed for the GFR core, the aim being to arrive at an in-depth understanding of the 3D core behavior during CA driven transients, especially from the viewpoint of spatial effects. The coupled models were developed using the PARCS code for the 3D NK and the TRACE code for the 1D TH modeling. Particular attention was paid to have each individual fuel sub-assembly and CA represented, in order to allow the analysis of local deformations of the 3D distributions of power and safety related parameters, such as the coolant, cladding and fuel temperatures. The validation of the coupled full-core models was performed against reference ERANOS-VARIANT calculations. In particular, the CA worth and reactivity feedbacks were benchmarked, the discrepancies being shown to be relatively low (< 10%).

The principal goal of the 3D transient analysis has been to verify the adequacy of the developed CA pattern and implementation scheme on the basis of the dynamic analysis of a wide range of operational and accidental CA withdrawals. Accordingly, CA driven transients were simulated systematically, without scram actuation, for two constant speeds, viz. (1) an operational speed of 2 mm/s and (2) an ejection speed of ~20 cm/s. From the various cases simulated, a variety of insights have been obtained, e.g. it has been shown that the withdrawal at operational speed of a single CA does not significantly impact the core safety in terms of the assumed temperature limits. It has also been highlighted that the "2007-Core" design presents better safety features, compared to the reference core, with lower predicted values for the TH results (coolant, cladding and fuel temperatures). Another interesting finding (from the spatial effects analysis) has been that a symmetrical withdrawal of CAs, from a given CA bank, leads to strongly reduced power shape deformations, as compared to an asymmetrical withdrawal. The quantification of such effects is clearly important from the viewpoint of defining appropriate operational procedures for the CAs.

Special care was taken to assess the sensitivity of the 3D core behavior to various parameters, such as the CA implementation scheme, the CA withdrawal speed, the number of CAs being withdrawn/ejected, the core power level and fuel burnup. It has been shown, from the various cases analyzed, that the sensitivity to a reduction of the number of CAs in the core is relatively modest. On the other hand, the dynamic analysis associated with burnt fuel, viz. the simulation of the core behavior at beginning of equilibrium cycle, has revealed significantly larger peaking factors and correspondingly, higher temperatures, compared to the situations with fresh fuel. The differences can largely be explained by the reduced values of safety related parameters, in particular the delayed neutron fraction and the Doppler constant.

In brief, the present research has resulted in the development of the control assembly pattern and implementation scheme for the 2400 MWth Generation IV GFR. The adequacy of the

developed concept for the CAs has been verified by carrying out 3D dynamic analysis of a wide range of CA driven transients.

Keywords: nuclear power plants, Generation IV, gas-cooled fast reactor (GFR), GCFR-PROTEUS, ERANOS-2.0, MCNPX, control assembly (CA) pattern, CA implementation scheme, FAST code system, TRACE, PARCS, transient analysis, 3D spatial kinetics, thermal-hydraulics, fuel cycle analysis.

Version abrégée

Durant les dix dernières années, différents facteurs indépendants, tels que l'augmentation rapide et mondiale de la demande énergétique, des inquiétudes sociétales à propos des gaz à effet de serre, ainsi que les prix des combustibles fossiles hauts et volatiles ont contribué au renouveau de l'intérêt pour la technologie nucléaire. Dans ce contexte, un forum international Génération IV (« GIF ») a été lancé en 2000 pour assister les efforts de recherche et développement (R&D) nécessaires aux réacteurs nucléaires de la quatrième Génération (« Gen-IV »). Ces systèmes avancés vont être idéalement déployés au delà des années 2030, après le déploiement des réacteurs de troisième Génération (« Gen-III » ou « Gen-III+ »). Ces derniers sont principalement basés sur la technologie des réacteurs à eau légère. En particulier, un des but pour les systèmes de quatrième Génération consiste dans la fermeture du cycle du combustible. En complément de l'amélioration des caractéristiques de sûreté, il est attendu de ces systèmes non seulement une meilleure utilisation des ressources naturelles, mais également une minimisation des déchets hautement radioactifs.

Parmi les systèmes choisis par le GIF, le Réacteur à Neutrons Rapides refroidi au Gaz (RNR-G) est un système particulièrement innovant, avec une géométrie et un combustible innovants (pastilles de combustible composées de carbure d'uranium et de plutonium, positionnées à l'intérieur de plaques en nid d'abeille de SiC). Le travail de recherche a été mené dans le contexte du RNR-G de référence à 2400 MWth. Le but principal a été de développer et de qualifier le design de l'assemblage de contrôle et le schéma d'implantation correspondant à ce système. Le travail a été réalisé en trois phases successives et complémentaires : (1) la validation des outils neutroniques, (2) le développement du design de l'assemblage de contrôle et les études statiques correspondantes, (3) les études du comportement dynamique du cœur durant des transitoires hypothétiques liés aux assemblages de contrôle.

Le code de système déterministe ERANOS ainsi que ses bibliothèques de données nucléaires relatives aux réacteurs rapides furent développés et validés pour la génération précédente de réacteurs au sodium. La première tâche réalisée dans la présente recherche, fût la validation d'ERANOS pour application au RNR-G. Cela a impliqué une analyse systématique des données intégrales obtenues au PSI dans les années 1970, pendant le programme expérimental GCFR-PROTEUS.

Pendant la première phase de la thèse, le réseau-test de référence de PROTEUS utilisé dans ces expériences, a été réinterprété avec ERANOS et la bibliothèque nucléaire ajustée ERALIB1, afin de dériver un schéma de calcul de référence, pour être utilisé, plus tard, pour l'analyse du RNR-G. De manière complémentaire, des calculs de références ont été réalisés avec le code de Monte Carlo MCNPX, visant à vérifier les résultats déterministes, et à analyser la sensibilité des résultats aux différentes modernes librairies. Pour les taux de réactions principaux, la nouvelle analyse du réseau de référence GCFR-PROTEUS donne généralement des résultats en bon accord – dans l'incertitude expérimentale 1σ – avec les résultats expérimentaux, ainsi qu'avec les simulations de Monte Carlo. Comme démontré par l'analyse, les prédictions étaient somme toute, en meilleur accord avec l'utilisation de la librairie ajustée ERALIB1. L'utilisation d'ERANOS-2.0/ERALIB1 comme outil neutronique de référence a ainsi pu être démontrée pour l'analyse du RNR-G. En outre, certains aspects neutroniques liés aux nouvelles caractéristiques du RNR-G, pour lesquelles de nouvelles investigations expérimentales sont nécessaires ont été mis en évidence.

Dans une seconde phase de cette recherche, le design de l'assemblage de contrôle (AC) du GFR a été développé, basé sur des calculs à caractère itératif, neutroniques et thermo-hydrauliques. En premier, des modèles neutroniques 2D et 3D du cœur du réacteur ont été créés, basés sur le schéma de calculs de référence ERANOS-2.0/ERALIB1. Pour l'analyse thermo-hydraulique, le code COPERNIC du CEA a été utilisé. Le travail de design a été poursuivi par l'étude d'un schéma de l'implantation des assemblages de contrôle (nombre et position dans le cœur). Des études détaillées de neutronique ont révélés l'existence de grands effets d'interaction entre les AC, appelés effets d'ombre/d'anti-ombre, conduisant à une amplification/réduction de l'anti-réactivité des AC. Les interactions entre les barreaux absorbants à l'intérieur d'un AC, ainsi qu'entre les AC eux-mêmes, ont été investiguées dans le détail, dans le but d'optimiser l'efficacité des AC (en terme de la fraction d'absorbant et la minimisation des effets d'hétérogénéité associés).

Le design d'un AC proposé consiste en 54 barreaux absorbants, situés dans un réseau triangulaire. Chaque barreau absorbant comporte un tube en acier inoxydable rempli de pastilles de carbure de bore ^{10}B hautement enrichi. Résultant d'investigations détaillées, le diamètre des pastilles absorbantes a été choisi de manière à minimiser l'influence « barreau-à-barreau » à l'intérieur de l'assemblage. En particulier, une partie centrale de l'assemblage a été conçue sans aucun barreau absorbant (zone remplie d'hélium statique). Par ce biais, une réduction, à 13%, des effets d'hétérogénéité, a été obtenue. Les investigations neutroniques effectuées pour le cœur RNR-G de référence (« 2004-Cœur »), spécialement, celles liées à l'étude des interactions entre les AC, ont directement contribué au nouveau design du cœur (« 2007-Cœur »). Le rapport hauteur sur diamètre a été augmenté à 0.6, comparé à la valeur de 0.3 pour le cœur de référence.

Pendant la troisième phase, des modèles couplés et détaillés, cinétiques 3D et thermo-hydrauliques 1D, ont été développés pour le cœur RNR-G ; le but était d'arriver à une compréhension, en profondeur, du comportement 3D du cœur pendant des transitoires induits par le mouvement d'AC. Plus particulièrement, les transitoires ont été étudiés du point de vue des effets spatiaux. Les modèles couplés ont été développés en utilisant le code PARCS pour la cinétique 3D et le code TRACE pour la modélisation thermo-hydraulique. Un intérêt particulier a été de représenter, de manière individuelle, chaque assemblage de combustible et chaque AC, pour permettre, l'analyse des déformations locales des distributions 3D de paramètres liées à la sûreté, telles que les températures du caloporteur, de la gaine et du combustible. La validation des modèles complets et couplés du cœur a été réalisée par rapport à des résultats de référence ERANOS-VARIANT et CATHARE. En particulier, l'anti-réactivité des AC et les effets de contre-réactivité ont été comparés ; les différences trouvées étant relativement petites (< 10%).

Le but principal de l'analyse 3D des transitoires a été de vérifier l'applicabilité du design d'assemblage de contrôle et du schéma d'implémentation, basée sur l'analyse dynamique du réacteur dans un large panel de situations, tant opérationnelles qu'accidentelles. En conséquence, des transitoires induits par le mouvement des AC, ont été systématiquement simulés, sans l'activation du scram, et ce, pour deux vitesses constantes, i.e. (1) une vitesse opérationnelle de 2 mm/s et (2) une vitesse d'éjection de l'ordre de 20 cm/s. Dans les cas simulés, une compréhension étendue a été obtenue ; par exemple, il a été montré que le retrait, à vitesse opérationnelle d'un AC, n'affecte pas de manière significative la sûreté du cœur en terme de températures limites. Il a aussi été mis en évidence que le cœur « 2007-Cœur » présente de meilleures caractéristiques de sûreté, comparé au cœur de référence, avec des valeurs thermo-hydrauliques plus basses. Une autre découverte intéressante, par l'analyse des effets spatiaux : un retrait des AC de manière symétrique, d'un rideau particulier, conduit à une forte réduction des déformations de la nappe de puissance, et ce, comparé à un retrait asymétrique. La quantification de tels effets est clairement importante du point de vue de la définition des procédures opérationnelles adéquates pour les AC.

Une attention particulière a été portée à l’étude de la sensibilité du comportement 3D du cœur à divers paramètres, comme le schéma d’implémentation des AC, la vitesse de retrait des AC, le nombre d’AC étant retiré/éjecté, le niveau de puissance et l’irradiation du combustible. Il a été montré, pour les différents cas analysés, que la sensibilité à une réduction du nombre d’AC dans le cœur est relativement modeste. D’un autre point de vue, l’analyse dynamique associée au combustible irradié, i.e. la simulation du comportement du cœur au commencement du cycle d’équilibre, a révélé des facteurs de forme plus importants, et de manière consécutive, des températures plus élevées, comparées aux situations avec le combustible frais. Les différences peuvent être largement expliquées par la réduction des valeurs des paramètres associés à la sûreté, en particulier, la fraction de neutrons retardés et la constante Doppler.

En bref, la recherche actuelle a conduit au développement du design de l’assemblage de contrôle et du schéma d’implémentation pour le RNG de quatrième Génération à 2400 MWth. L’applicabilité du concept développé d’assemblage de contrôle a ensuite été vérifiée en effectuant une analyse 3D de la dynamique du réacteur pour une large étendue de transitoires induits par le mouvement des assemblages de contrôle.

Mots clés: centrales nucléaires, Génération IV, réacteur à neutrons rapides refroidi au gaz (RNR-G), GCFR-PROTEUS, MCNPX, design de l’assemblage de contrôle, schéma d’implantation, système de code FAST, TRACE, PARCS, analyse des transitoires, cinétique spatiale 3D, analyse du cycle du combustible.

Contents

List of Abbreviations

ADS	Accelerator-Driven Systems
AGR	Advanced Gas-cooled Reactor
AV	Arbeitsgemeinschaft Versuchsreaktor
BOC	Beginning-Of-Cycle
BOEC	Beginning-Of-Equilibrium-Cycle
BOL	Beginning-Of-Life
BWR	Boiling Water Reactor
CA	Control Assembly
CAIS	Control Assembly Implementation Scheme
CAP	Control Assembly Pattern
CEA	Commissariat à l'Energie Atomique
CEFR	China Experimental Fast Reactor
CERCER	ceramic-ceramic
CMFD	Coarse Mesh Finite Difference
CPFR	China Prototype Fast Reactor
CSD	Control System Device
CZP	Cold Zero Power
DHR	Decay Heat Removal
DSD	Diverse Safety Device
EDF	Electricité de France
EFPD	Effective Full Power Days
EFR	European Fast Reactor
EFRUG	European Fast Reactor Utilities Group
EGPT	Extended Generalized Perturbation Theory
EIR	Eidgenössiches Institut für Reaktorforschung
ENIGMA	Experimental Neutron Investigation of Gas-cooled reactor at MAsurca
EOC	End-Of-Cycle
EOL	End-Of-Life
EPR	European Pressurized Reactor
ETDR	Experimental Technology Demonstration Reactor
ETGCFR	Existing Technology Gas-Cooled Fast Reactor
FAST	Fast-spectrum Advanced Systems for power production and resource managemenT
FIMA	Fission per Initial Metal Atom
FBTR	Fast Breeder Test Reactor
GA	General Atomics
GCFR	Gas-Cooled Fast Reactor
GFR	Gas-cooled Fast Reactor
GIF	Generation IV International Forum
GNEP	Global Energy Partnership
GS	Gagging Scheme
GT-MHTR	Gas Turbine - Modular High Temperature Reactor
H/D	Height-to-Diameter ratio
HFP	Hot Full Power
HG	Heat Generation

HTC	Heat Transfer Correlation
HTGCFR	High Temperature Gas-Cooled Fast Reactor
HTR	High Temperature Reactor
IAEA	International Atomic Energy Agency
IE	Initiating Event
IL	Infinite-Lattice
INPRO	International Project on Innovative Nuclear Reactors and Fuel Cycles
JNC	Japan Nuclear Cycle Development Institute
JNFL	Japan Nuclear Fuel Limited
KAERI	Korea Atomic Energy Research Institute
KALIMER	Korea Advanced LIquid MEtal Reactor
LFR	Lead-cooled Fast Reactor
LOCA	Loss Of Coolant Accident
LOF	Loss Of Flow
LWR	Light Water Reactor
MA	Minor Actinide
MCNPX	Monte Carlo N-Particle eXtended
MFP	Mean Free Path
MOX	Mixed OXide
MSR	Molten Salt Reactor
NK	Neutron-Kinetics
NPP	Nuclear Power Plant
NRC	Nuclear Regulatory Commission
PARCS	Purdue Advanced Reactor Core Simulator
PBMR	Pebble Bed Modular Reactor
PCRV	Pre-stressed Concrete Reactor Vessel
PFBR	Prototype Fast Breeder Reactor
PMD	Power Map Deformation
PSI	Paul Scherrer Institut
PWR	Pressurized Water Reactors
R&D	Research and Development
RCS	Reference Computational Scheme
RIA	Reactivity Insertion Accident
SA	Sub-Assembly
SCWR	Super-Critical Water Reactor
SFR	Sodium-cooled Fast Reactor
SNR	Schneller Naturiumgekühlter Reaktor
SVP	Eigenvalue Separation
TH	Thermal-Hydraulics
TRACE	Transient Reactor Analysis CodE
TRU	TRansUranic nuclides
TVO	Teosulliden Voiny Oy
VBA	Visual Basic for Applications
VHTR	Very High Temperature Reactor
XS	cross-sections

Chapter 1

1 Introduction

This chapter aims at providing a general introduction in terms of (1) the current worldwide context of nuclear energy (see Section 1.1), (2) a short description of existing nuclear technologies (see Sections 1.2 and 1.3), (3) on-going international programs on advanced nuclear systems (see Section 1.4), and (4) the scope and structure of this doctoral thesis (see Sections 1.5 and 1.6).

1.1 Global panorama of nuclear energy in the world

The worldwide demand in energy is continuously increasing and will continue to increase in the short and longer term. This observation is quite independent of the political and social will to stabilise, if not decrease, the energy consumption per capita in the developed countries. There are two essential reasons for the growing demand for energy and, in particular, for electricity: the global population growth and the industrial development mainly on two major continents, i.e. Asia and South-America. These two factors are predicted to lead to a doubling of energy consumption before 2050 [1].

Meanwhile, two other reasons, independent of the demand in energy, have to be taken into account when considering the need for new nuclear power plants. Firstly, the relative contribution of electricity to global energy consumption (about 16% at the current time [2]) is expected to increase markedly, partly due to new needs for electricity (e.g. desalination plants, heat pumps and, in the longer term, hydrogen production for transport purposes). Secondly, there is the urgent need to replace old existing nuclear power plants, particularly in the USA and Europe.

Today a widely recognised, new driver to justify the use of nuclear technology is global warming. Recent climate change findings have led decision makers, media and the public to realise that the use of fossil fuel must be reduced and replaced by low-emission sources of energy such as nuclear and hydro-power. These two, in fact, currently represent the only available large-scale alternatives to fossil energy for the continuous and reliable supply of electricity. Additionally, as carbon emission will soon be taxed in the European Union, the economic benefits and competitiveness of nuclear power will increase further. In the European Union, as well as in Switzerland, people are also starting to realise how vulnerable they would be, if their governments were to think it sufficient to simply buy oil, gas and electricity abroad. In this sense, nuclear power represents a more independent source of energy in the short term, due to the high energy content of the fuel loaded in a reactor core.

The worldwide nuclear energy situation is described below [3; 4; 5], in general terms in Subsection 1.1.1, in the context of new fast reactor constructions in Subsection 1.1.2, with a particular view on European perspectives in Subsection 1.1.3, and in terms of the situation on uranium resources in Subsection 1.1.4.

1.1.1 General situation

As of 1st January 2008, according to the International Atomic Energy Agency [2; 3], there were a total of 444 nuclear power reactors operating in the world (in 31 countries), with a total net capacity of 375.5 GWe. Although no nuclear power plants were shutdown for the long-term during 2007, there were five NPP retirements (corresponding to eight units) in 2006. Again, with January 2008 as reference, 34 units or 23 GWe were under construction, which represents 8% of the total number of plants. The units under construction are presented in Figure 1.1. The world's fleet of nuclear power reactors maintained a high average availability factor of 83% (data for the year 2006). The availability factor has been almost constant since 2000, indicating the high degree of reliability of the existing reactors.

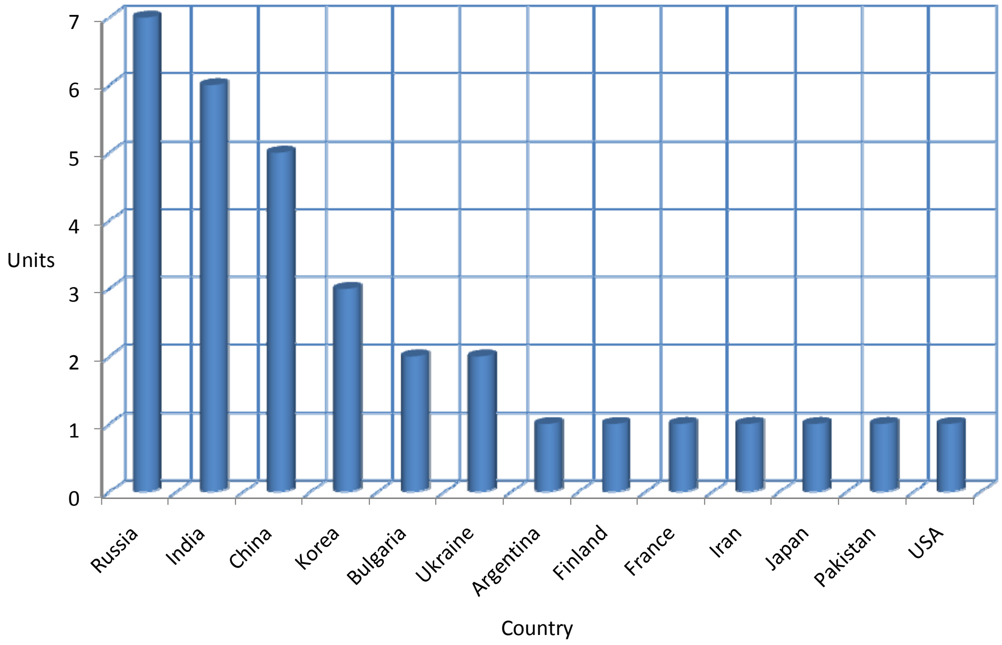

Figure 1.1 The nuclear reactors under construction worldwide

Three new reactor units were connected to the grid in 2007 [3; 6]: one in India (Kaiga-3 of 202 MWe), one in China (Tianwan-2 of 1000 MWe) and the last one in Rumania (Cernavoda-2 of 655 MWe). Additionally, one reactor unit returned to the grid in USA (Brown Ferry-1 of 1065 MWe), after a long shutdown. Principally in Asia and in Russia, 2007 was an important year for the initiation of new nuclear power units. China officially started the construction of two plants:

Qinshan II-4 (PWR of 610 MWe) and Hongyanhe-1 (PWR of 1000 MWe). Also in Asia, South Korea started the construction of Shin Wolsong-1 (PWR of 960 MWe). In the eastern part of the country, Russia began the construction of two low power units. These are first-of-their-kind floating nuclear power plants (see Figure 1.2), called Severodvinsk-Akademik Lomonosov-1 and 2 (PWR-KLT-40, 2 times 30 MWe). To complete this global panorama, France started the construction of Flamanville-3, a PWR of 1600 MWe.

Figure 1.2 Artistic view of the floating nuclear power plant PWR-KLT 40 [7]

Clearly, Asia is the most active region in the world in terms of new nuclear deployment and capacity expansion, with 28 of the worldwide 39 new reactors to be connected to the grid located there.

In addition to the construction of new reactor units to increase the net capacity, the other possibility is to upgrade, or to extend the lifetime of existing nuclear plants. In 2006, the US Nuclear Regulatory Commission (NRC) approved eight more licence renewals of 20 years (for a total licensed life of 60 years for each reactor, instead of 40 years as based on the original design calculations and safety evaluations). Similarly, in the Netherlands, the government granted a 20-year extension to the Borssele nuclear power plant for a total licensed lifetime of 60 years.

1.1.2 Construction of fast reactors

Compared to LWRs, the construction of fast reactors is much more modest. However, several prototype reactors are under construction or development. The following systems are being constructed or modified at the moment:

- The 65 MWth / 25 MWe China Experimental Fast Reactor (CEFR) is under commissioning. This is the first step in the Chinese fast reactor technology development program. As a second step, a 600 MWe China Prototype Fast Reactor (CPFR) is presently under consideration.
- The 280 MWe prototype reactor MONJU in Japan was stopped temporarily due to a leak in the non-radioactive secondary heat transport system that occurred in December 1995 during the 40%-power pre-operational testing phase. In the Japanese program, it was clarified that MONJU is at the core of the country’s fast reactor research activities, and

steps were taken to resume its operation as soon as possible. The local governor of Fukui gave the consent for plant modification of MONJU in 2005, and the Japan Nuclear Cycle Development Institute (JNC) started the necessary work soon thereafter. The MONJU restart is foreseen for 2009.

- The 500 MWe Prototype Fast Breeder Reactor (PFBR) is under construction in India. PFBR is a pool type sodium-cooled fast reactor with two primary pumps, four intermediate heat exchangers and two secondary loops. There are eight integrated steam generator units (four per secondary loop) in which steam at 763 K and 17.2 MPa is produced. Four separate safety-grade decay heat exchangers are provided to remove the decay heat directly from the hot pool. The hot and cold pool sodium temperatures are 820 and 670 K, respectively. The manufacture of both safety and main vessels is progressing well. First criticality is planned for September 2010.

1.1.3 Nuclear perspectives in Europe

The situation within the European Union is certainly going to change in the near term, compared to the stagnation observed in recent years. A first signal was the project of the Finnish utility, TVO (Teosulliden Voiny Oy) [8] to build a new reactor in Finland, as a result of the growth in the demand for electricity of around 25% predicted to take place in Finland by the year 2015. This view was based on a number of studies, including one of the economics of different power-generating technologies, which showed that a nuclear power plant was the most cost-effective option. The other important aspect was the wish of the government to reduce the market’s dependence on power purchases; the country presently imports more than 70% of its electricity. Finally, the use of nuclear energy – a carbon-dioxide-free energy source – would make it easier for Finland to meet its commitments under the Kyoto Protocol. Consequently, in 2000, TVO applied to the Finnish Ministry of Trade and Industry for a decision according to the Finnish Nuclear Energy Act. The government granted the construction license in 2005. A Framatome ANP/Siemens consortium was chosen to built an advanced European Pressurised water Reactor, EPR, of 1600 MWe at the west end of the island Olkiluoto, next to plant units Olkiluoto 1 and 2 [9].

After the Finnish decision, EDF announced the intention to build a new nuclear power plant in France to respond to the growth in the demand for electricity and also in view of the plants that are planned to be decommissioned in the near future. In 2004, EDF decided to implement an EPR (Flamanville-3, 1600 MWe), as a first model of a new French series, on the existing site of Flamanville. After scoping studies and impact assessment, Electricité de France obtained the authorisation in 2007 [10].

This progress is followed by the United Kingdom that recently adopted a new energy law, which will give the country the juridical bases to allow pursuing the investments in nuclear power plants. For the British Government, nuclear power plants are part of the strategy to be adopted in the context of the national energy mix. A recent survey [11] has shown that, in the coming 20-year period, the country will need to replace about one third of its electrical capacity (i.e. 12 GW of fossil-burning plants) for environmental reason. In the same period, 10 GW of existing NPP capacity will have reached its end-of-life. To guarantee electricity supply, the utilities will have to connect to the grid as much as 30 GW of new capacity during the next 20 years. A lot of effort will be put to renew the nuclear power in the United Kingdom, which should lead to the start of the construction of the first new nuclear power plant at the beginning of 2013 so as to complete it by 2018.

In Bulgaria, the site of Belene was approved for the construction of a new nuclear plant. The three Baltic countries and Poland have agreed to build by 2015 a new nuclear plant in Lithuania. Finally, in Turkey, a new law has been voted to allow the construction of a NPP.

To complete this overview in Europe, it is worth mentioning that, in 2008, three major Swiss utilities, viz. ATEL, the AXPO Group and BKW-FMB [5] have launched official procedures to obtain the general authorisation from the “Swiss Federal Nuclear Safety Inspectorate (ENSI)” to build new reactors in view of an extension of the production, and the replacement, of four old reactors: Beznau I and II, Mühleberg and Gösgen. However, the complexity of the legal procedure, which requires three formal phases, viz. the general authorisation, the construction authorisation and the authorisation to exploit the plant, will render the schedule much longer than that envisaged in the United Kingdom. At the moment, in the most optimistic scenario, as much as 12 years are needed to go through all the three authorisations [4, 5].

1.1.4 Economics of uranium and consideration of resources

Higher worldwide market prices for fossil fuels have put nuclear power on the agenda of many countries currently without nuclear power and have revived interest, as seen with the panorama presented above, in countries with stagnating nuclear power programs. Higher market prices for fossil fuels clearly increase the competitiveness of nuclear power. A doubling of international prices for fossil fuels translates into a generation cost increase of about 35-45% for coal-fired electricity and 70-80% for natural gas. In contrast, a doubling price of uranium prices increases nuclear generating cost by only about 5%. Recently, uranium prices have been increasing, as shown in Figure 1.3, but these have not significantly affected the electricity price. The main reason for the increase is that demand has been high, with fuel production remaining below fuel consumption. Additionally, the market is under pressure with the generally high demand for any kind of raw material.

The identified conventional resources for uranium are currently estimated at 5.5 millions of tons. This is a significant increase compared to 2005. At the same time, undiscovered conventional resources are estimated at 7.3 million tonnes at a price lower than 130$/kgU. Unconventional uranium resources, e.g. from seawater, phosphate deposits and thorium, will further expand the resource availability [12].

Regarding uranium enrichment facilities, the NRC recently gave authorisation to build a new centrifugation enrichment plant. Japan Nuclear Fuel Limited (JNFL) has proceeded to begin test production at the new Japanese enrichment plant in Rokkasho. Finally, Russia and Kazakhstan have together created the International Uranium Enrichment Center in East Siberia. The construction of new, less energy consuming enrichment plants is effectively leading to a general modernisation of uranium enrichment technology worldwide.

On the basis of the figures given earlier, and assuming nuclear electricity production at the current level with the once-through fuel cycle, the potential of the world's identified uranium resources is estimated to be in the range of 70 years [13], which is clearly low regarding the sustainability of the resources. This represents one of the main motivations to develop advanced nuclear systems operating with closed fuel cycles (Generation IV systems). These would feature better efficiency not only from the thermodynamic viewpoint, but also with respect to fuel economy. Advanced fast reactors operating with a closed fuel cycle would, for example, allow simply using depleted uranium as the feed and thus be much more compatible with the conditions for sustainable development. In such a situation, the known conventional uranium resources would be sufficient for several millennia.

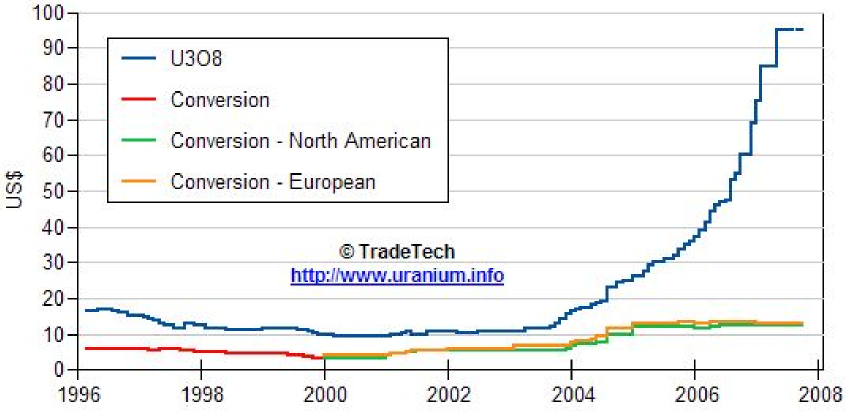

Figure 1.3 Evolution of the U_3O_8 price per pound from 1996 to 2008 [14]

1.2 Existing technology: thermal-spectrum reactors

This section provides general information about existing thermal-spectrum nuclear power plant technology. In addition to the most widely used light water reactors (LWRs), which are described in Subsections 1.2.1 and 1.2.2, thermal-spectrum gas-cooled reactors are introduced in Subsection 1.2.3. The purpose thereby is to provide a basis for understanding the similarities and differences between existing nuclear power plants and the advanced reactor concept considered in the present research, viz. the gas-cooled fast reactor, which will be addressed separately in Chapter 2.

1.2.1 Pressurized water reactors

Pressurized water reactors (PWRs, as well as VVERs of Russian design) are Generation II nuclear power reactors that use ordinary water under high pressure as coolant and neutron moderator (see Figure 1.4). The primary coolant loop is kept under sufficiently high pressure to prevent the water from boiling. PWRs are the most common type of power producing reactor and are widely used all over the world. The first prototype was originally designed at the Oak Ridge National Laboratory in the USA for use as a nuclear submarine power plant.

The primary coolant water in a PWR flows through the reactor at a temperature of ~315°C. As indicated, the water remains liquid despite the high temperature due to the high pressure in the primary coolant loop, i.e. ~15 MPa. The primary coolant loop heats water in a secondary circuit that becomes saturated steam (in most designs at about 6.2 MPa and 275°C) for use in a steam turbine.

The uranium used in PWR fuel is usually enriched up to several percent in ^{235}U, in the range of 4-5%. There is also the possibility to burn mixed oxide (MOX), i.e. $(U,Pu)O_2$. The fuel is in the form of cylindrical pellets, which are put into tubes of a corrosion-resistant zirconium metal alloy (Zircaloy). The finished fuel rods are grouped in fuel assemblies, which are then used to build the core of the reactor. A typical PWR has fuel assemblies of 200 to 300 rods each, and a large reactor would have about 150-250 such assemblies with 80-100 tonnes of uranium in total. A PWR's power is usually in the range from 900 to 1500 MWe.

In most commercial PWRs, reactivity adjustment to maintain the nominal reactor power as the fuel is burned up is normally achieved by varying the concentration of boric acid dissolved in the primary reactor coolant and changing the position of control rods in the core. The boron readily absorbs neutrons, and increasing or decreasing its concentration in the reactor coolant will therefore affect the neutron balance correspondingly.

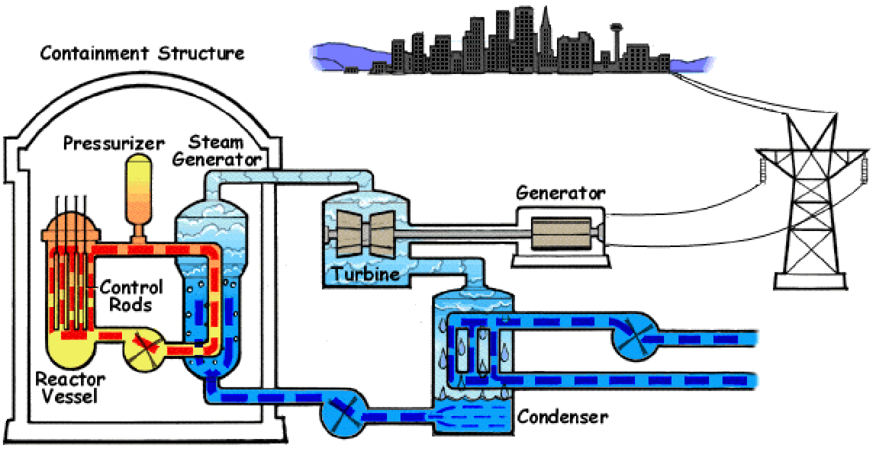

Figure 1.4 General concept and schematic of a pressurised water reactor (PWR) unit

1.2.2 Boiling water reactors

A Boiling Water Reactor (BWR) is a type of LWR developed by the General Electric Company in the mid 1950s. A schematic of a BWR plant is shown in Figure 1.5. The reactor is characterised by two-phase fluid flow (water and steam) in the upper part of the core. The main motivation for the BWR is the possibility to reduce costs through the absence of heat exchangers and the use of lower-pressure components. The design of pressure vessel internals, however, is more complex.

In contrast to pressurised water reactors that utilise both a primary and a secondary loop, in BWRs the steam going to the turbine that powers the electrical generator is produced in the reactor core rather than in steam generators. There is just a single circuit in which the water is at a lower pressure of about 7.5 MPa, so that it boils in the core at about 285°C. The reactor is designed to operate with steam comprising 12–15% of the mass of the two-phase coolant flow in the top part of the core, resulting in less moderation, lower neutron efficiency and lower power density than in the bottom part of the core.

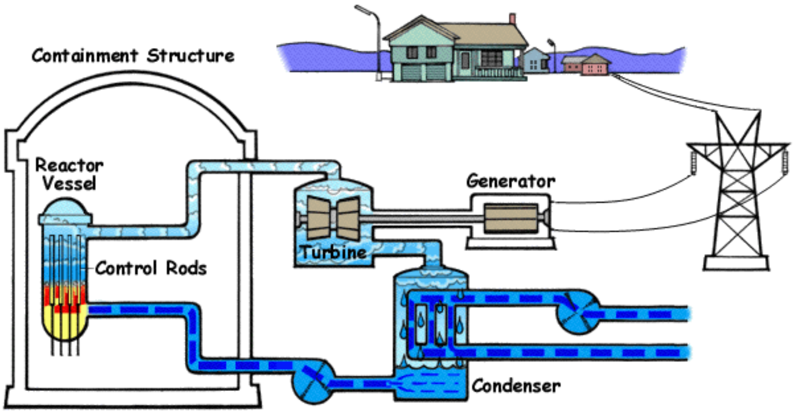

Figure 1.5 General concept and schematic of a boiling water reactor (BWR) unit

1.2.3 Gas-cooled reactors

Another possibility to sustain a reaction chain in order to produce heat within a nuclear reactor is to cool the core with a gas and to moderate the neutrons with solid material, such as graphite. A gas (CO_2 or helium) coolant features certain favourable physical properties, e.g. low (for CO_2) or almost no (for helium) neutron absorption and optical transparency allowing visual safety inspection within the vessel. Moreover, a gas coolant has no phase change in the core, reducing the risk of a possible reactivity accident at the moment of transition (liquid to gas, for instance). The hot outlet gas can be run directly through a gas turbine to produce electricity in a Brayton cycle (direct cycle operation), for instance. The use of a direct cycle, combined with a high outlet temperature, provides potential advantages such as a thermal efficiency as high as 50%.

One of the drawbacks of using CO_2 as the coolant and graphite as the moderator is the corrosion of solid graphite by CO_2 at high temperature ($C + CO_2 \rightarrow 2\,CO$). Graphite itself, on the other hand, has the advantage of providing a large thermal inertia to the reactor core, an important safety aspect. The corrosion problem with graphite was, in fact, an important motivation for developing helium-cooled reactors, since helium does not react chemically with other core materials.

Most of the early development of gas-cooled reactors was centred on thermal-spectrum systems using graphite moderator, metal-clad metallic fuel and carbon dioxide coolant. The commercial deployment of such systems started in the mid-1950s, primarily in the United

Kingdom and France, with natural-uranium fuelled Magnox systems and, later, with Advanced Gas-cooled Reactors (AGRs). To improve economic performance (compared to Magnox), the AGR operates at a higher gas temperature and uses enriched uranium fuel (instead of natural uranium) so as to require less frequent refuelling. There are still a number of operating reactors of this type in the United Kingdom, while the older units have either been shutdown or will be decommissioned in the near future mainly for economical reasons.

Later, helium was envisaged as the coolant for gas-cooled systems, and so-called high temperature reactors (HTRs) such as, most recently, HTTR [15] and HTR-10, have been built [16]. In such systems, the fuel is commonly in the form of tiny coated particles embedded in graphite [17; 18].

Further relevant information about the history and development of thermal-spectrum gas-cooled reactors can be found in Appendix A.

1.3 Existing technology: fast-spectrum reactors

Basic physics aspects of fast reactors are briefly presented in Section 1.3.1, while a historical review is given in Section 1.3.2. In the context of the CAP development carried out currently for the Generation IV GFR (see Section 1.5), the corresponding design options for the sodium-cooled fast reactors Superphénix and EFR [19] (European Fast Reactor) have been considered as a first step. These two systems are briefly described in Sections 1.3.3 and 1.3.4, respectively.

1.3.1 Fast breeder reactors: basic physics aspects

Due to their higher neutron economy, fast-spectrum reactors provide the possibility to breed more fissile material (in the core and/or in blankets surrounding the core) than is consumed. After the initial fuel loading, such a reactor can in effect, be refuelled by simply adding natural or depleted uranium, and hence the term Fast Breeder Reactor (FBR). To convert a fertile nucleus into a fissile one, while at the same time sustaining the nuclear chain reaction, at least one additional neutron is required per neutron absorbed in the reactor, implying that the ratio $\eta = \nu \frac{\sigma_f}{\sigma_a}$ needs to be greater than 2, with ν being the number of neutrons released per fission, σ_f the fission cross section of the fissile nuclide and σ_a its absorption cross-section. Typically, η increases with energy, and ^{239}Pu is the most favourable fissile nuclide.

Almost parallel to the development of thermal-spectrum reactors in the 1950's, research and development was also focused on fast-spectrum reactors, cooled by either a liquid metal (for instance, Na, NaK or PbBi) or a gas (CO_2 or helium) [20]. The design choice for a rapid breeding of fissile material imposed the requirement of a high power density for a high neutron economy, as also a minimisation of the coolant volume fraction in order to reduce moderation. The resulting stringent requirements on heat removal capability of the coolant led to a concentration of effort on liquid metals, and hence the classical name: Liquid Metal Fast Breeder Reactor (LMFBR). Early systems used mercury cooling and plutonium metal fuel. Molten lead-bismuth cooling has been used in Russian naval propulsion units as well as some other reactor prototypes. At the present time, most operating fast reactors are cooled by liquid sodium.

As regards gaseous coolants for fast reactors, most candidates are light nuclei. However, these do not induce excessive moderation due to their low density (~1000 times less dense that any solid material). Additionally, gas helps to reduce considerably the void effect which is one of the major problems for sodium fast-spectrum reactors. Other advantages of a gaseous coolant for a fast reactor are a reduction of parasitic absorption by the coolant, as also a harder spectrum leading to a better neutron economy and, in turn, to a higher breeding gain. Moreover, gases are less corrosive than liquid metals.

Different physical phenomena occur in a fast-spectrum reactor that impact its safety. For example, if the fission power is increased due to a reactivity insertion ρ, the fuel temperature increases first, providing a negative reactivity feedback due to increase of U^{238} absorptions (Doppler effect). Then, the coolant density will decrease resulting in: (1) a spectrum hardening caused by the reduction of moderation by the coolant (positive contribution to reactivity), (2) a reduction of the coolant absorption (positive contribution), (3) a reduction of the scattering reactions in the coolant and thus the increase of neutron leakage (negative contribution). Usually, in a fast reactor, the core is designed such that the leakage term provides the largest single effect. However, the net coolant-void effect in a sodium-cooled system is usually slightly positive. In the GFR, on the other hand, coolant voiding is not a significant issue from the reactivity viewpoint because the coolant is relatively transparent to neutrons.

A specific safety problem for a fast reactor (compared to a thermal-spectrum reactor) is possible core compaction. In the case of a severe mechanical core deformation, the fuel can potentially be rearranged in a more compact geometry, which may increase the reactivity (mainly due to a decrease in the leakage term).

An important safety-related advantage for a liquid metal coolant in a fast reactor is the high heat removal capability in the context of establishing natural convection for passive Decay Heat Removal (DHR). For a GFR, the main safety issue is DHR under accidental conditions, viz. in a rapid loss of coolant accident (LOCA), as also in a loss of flow (LOF) event.

In recent years, and principally in the context of the Generation IV initiative, fast-spectrum reactors have once again gained popularity. This is mainly related to their ability to promote the sustainability of nuclear energy via drastically improved fuel utilisation on the one hand, and the complete closure of the nuclear fuel cycle on the other. In the latter context, the possibility of recycling the so-called minor actinides (MAs), i.e. Np, Am and Cm, represents a big step forward towards a major reduction of long-lived radioactive wastes. Compared to the situation with current-day reactors operated in the once-through mode, mainly fission products will have to be placed in the final repository, reducing the radio-toxicity hazard by up to 2 orders of magnitude and hence, also the time that the wastes need to be kept separated from the biosphere [21].

1.3.2 Fast reactor development

The first fast reactor was built at Los Alamos, New Mexico, in 1946 and called "Clementine". The power was low, viz. only 25 kWth, the main purpose being for its research use as a fast neutron source. It used plutonium metal fuel and mercury as coolant.

Almost at the same time, at Argonne National Laboratory, the development of the Experimental Breeder Reactor (EBR) was started, in order to support the construction of a prototype power reactor [22]. Demonstration reactors, such as the EBR-II in the USA, BOR-60 in the former USSR, RAPSODIE in France and DFR in the UK, were constructed in the 1950s and 1960s. These led to prototype power reactors such as Phénix in France, PFR in the United Kingdom and BN-350 in Kazakhstan. The combined experience obtained from the prototype and demonstration reactors was later used to build full-scale power plants like Superphénix in France and BN-600 in Russia. Additionally in Germany, the KNK-II reactor [23] was developed a few years after Phénix and offered a low electrical power of 20 MW. This reactor was followed by the 300 MWe Schneller Naturiumgekülter Reaktor (SNR300) [23] in Kalkar, Germany. For political reason, however, this reactor was never operated.

More recently, in India, the small-size Fast Breeder Test Reactor (FBTR), is being used for various test irradiations, fuel therein having attained peak burn-ups of over 100 GWd/t [24]. In Japan, as indicated in Subsection 1.1.2, the 280 MWe prototype fast reactor MONJU is expected to restart in 2009. In the Republic of Korea, the Korea Atomic Energy Research Institute (KAERI) has been developing the KALIMER (Korea Advanced LIquid MEtal Reactor), a pool-type sodium-cooled reactor, under a long-term national R&D program. KAERI completed the conceptual design of the 150 MWe KALIMER in 2002. Recently, a development project for a 600 MWe unit has been initiated [24]. In Russia, consecutive to the commercial and technical success of the BN-600, the development has started of advanced and innovative FR designs with enhanced safety, e.g. a large sodium-cooled FR with mixed oxide fuel, as well as BREST-300, a lead-cooled demonstration FR with nitride fuel, and SVBR-75/100, a small modular lead-bismuth cooled reactor [24].

As seen above, almost all fast reactors being operated and developed are sodium-cooled reactors. A summary of the existing and planned Sodium-cooled Fast Reactors (SFRs) is presented in Table 1.1, along with their main design characteristics. Not included in the list is the BN-800 reactor, construction of which should start in Russia in 2012 [25].

SFRs, with 18 reactors, have achieved a cumulated operation of more than 300 reactor-years, which is clearly of importance [25]. This operational experience has significantly improved the knowledge in this technology, as also in the related fabrication processes. Problems specific to SFRs (e.g. sodium/water reactions, the handling of fuel assemblies in a non-transparent environment, corrosion, sodium leaks, impurities in the circuit, etc.) have been encountered on many occasions, and considerable improvements have been made in their context. In more general terms, SFRs have several intrinsic characteristics which are conducive to safety. For example, the thermal inertia of the coolant is large, thanks to the large primary sodium volume, and the piping is at low pressure.

Of interest in the context of the present work is the core sensitivity to reactivity variations, which were observed for instance in Superphénix and FBTR. Such neutronic instabilities can, at the beginning of operation, necessitate modifications of the fuel and control assembly loadings of the core, before full nominal power is reached [26].

Table 1.1 Sodium-cooled fast reactors in the world [25]

Reactor	Country	Power (thermal/electric), MW	First criticality	Shutdown date	Operating years
EBR-I	USA	1.4 / 0.2	1951	1963	12
BR-5/BR-10	Russia	8 /-	1958	2002	44
DFR	UK	60 / 15	1959	1977	18
EBR-II	USA	62 / 20	1961	1991	30
EFBR	USA	200 / 61	1963	1972	9
Rapsodie	France	40 / -	1967	1983	16
BOR-60	Russia	55 / 12	1968	in operation	39
SEFOR	USA	20 / -	1969	1972	3
BN-350	Kazakhstan	1000 / 350	1972	1999	27
Phenix	France	563 / 250	1973	2009	34
PFR	UK	650 / 250	1974	1994	20
Joyo	Japan	50-75/ -	1977	in operation	30
KNK-II	Germany	58 / 20	1977	1991	14
FFTF	USA	400 / -	1980	1993	13
BN-600	Russia	1470 / 600	1980	in operation	24
Superphénix	France	3000 / 1240	1985	1997	12
FBTR	India	40 / 13	1985	1997	12
Monju	Japan	714 / 280	1994	to restart	13

1.3.3 Superphénix

The 1200 MWe, commercial large-size LMFBR, Superphénix, built and operated by an international consortium consisting of France, Germany and Italy, reached full power operation in 1986 after 9 years of construction and commissioning tests [27; 28; 29] (see Figure 1.6).

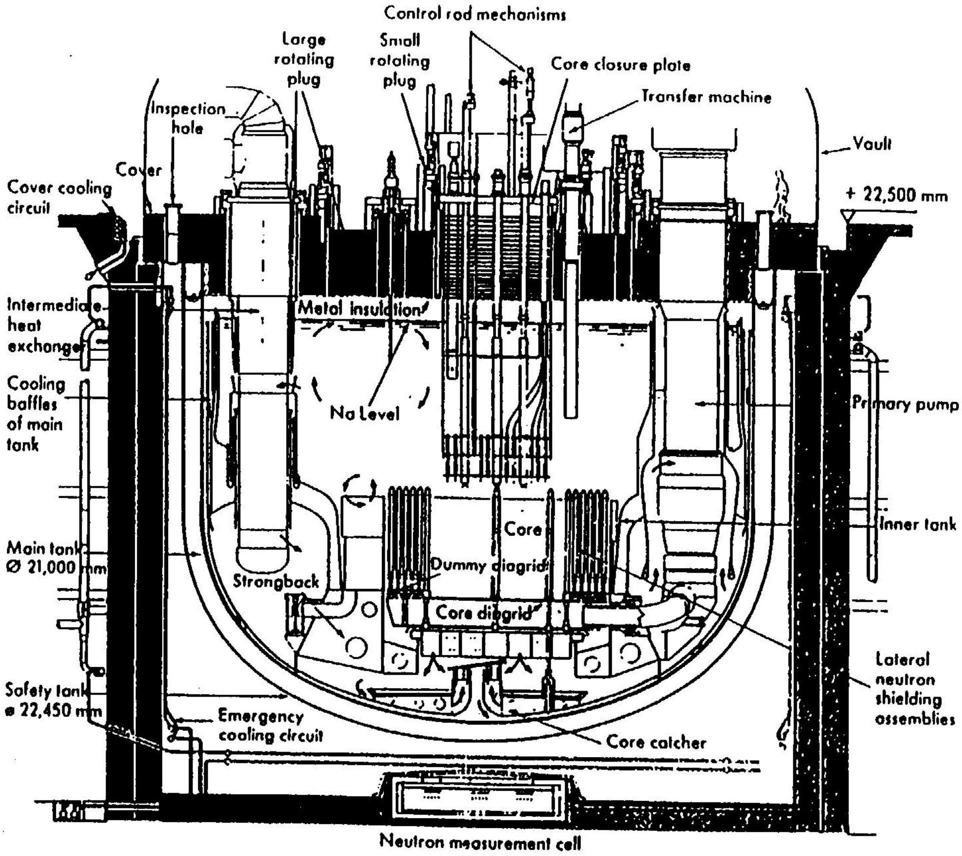

Figure 1.6 Schematic view of Superphénix

Superphénix was a pool-type, sodium-cooled fast-spectrum reactor, and the core contained 4 main zones: (1) the fuel region, divided in 2 zones with 2 different Pu-contents (~15% in the inner zone and ~18% in the outer), (2) a radial breeder region surrounding the fuel subassemblies (SAs), (3) a steel reflector region to improve the neutron economy and (4) a radial shielding zone. Regarding the control rods, three independent banks were installed, 2 for the power control and reactivity adjustments, and an additional one to scram the reactor. The control assembly design of the main control bank is discussed in greater detail in Chapter 4. The fuel SA contained a total of 271 pins with wire spacing, placed in a hexagonal wrapper tube. The pins were loaded with MOX fuel pellets over the active core height, and with depleted UO_2 pellets in the lower and upper axial blankets [30; 31; 32].

In more general terms, Superphénix represents the follow-up of the Phénix reactor (the French, small-scale demonstration FBR), constructed in 1973. Phénix is still under operation today while, on the contrary, Superphénix, was decommissioned for economical and political reasons in 1997. It is also useful to recall that Phénix was developed with the experience gained in the experimental loop-type sodium-cooled fast reactor, RAPSODIE, at CEA-Cadarache. The system was shut down after the discovery of a leak in the double-walled reactor vessel.

1.3.4 European Fast Reactor

In 1988, as a follow up of Superphénix, certain European utilities decided, in the framework of the European Fast Reactor Utilities Group (EFRUG), to finance the preliminary design of a large sodium-cooled power plant, called European Fast Reactor (EFR) [22; 33]. The EFR core is depicted schematically in Figure 1.7. At that time, the main objective was to carry out the timely design for a series of NPPs to be started around 2010. The principal targeted improvements (relative to Superphénix) were construction and operation cost reductions, and safety improvements especially for DHR.

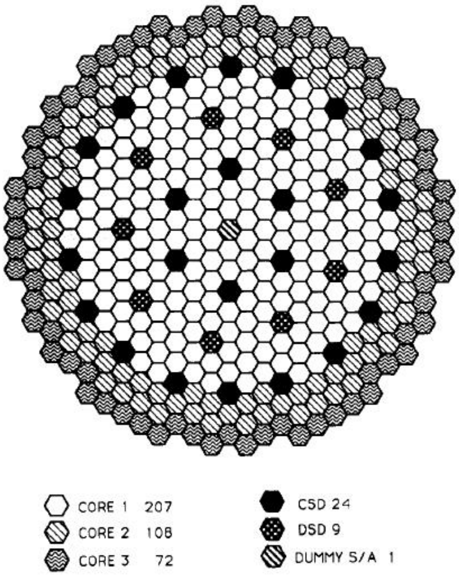

Figure 1.7 EFR core layout

Compared to Superphénix, the plant power in EFR was increased, based on economic considerations, to 1500 MWe. Additionally, the main reactor vessel was reduced in diameter from 21 m to 17 m, largely as a result of optimisation of the heat exchangers. Other changes and optimisations were made with the objective to make the reactor simpler, easier and cheaper than Superphénix. The EFR core has been designed to have a high burnup (20%) and a long residence time, in order to minimise fuel cycle costs. The core has three zones, each with a different Pu-content, and is surrounded by a row of breeder subassemblies, as also axial blankets located above and below the core. One specific feature is a certain flexibility with regard to the breeding characteristics, the size of the radial and axial blanket regions being adjustable for this purpose [33].

The reactivity change during normal operation in EFR is compensated for by using two independent banks of Control System Devices (CSDs), the first one being placed in the inner fuel region while the second bank is located at the interface between the inner and intermediate core regions. Each CSD rod design is composed of 37 high-enriched (90%-^{10}B) boron carbide (B_4C)

absorber pins surrounded by a hexagonal stainless steel wrapper. Additionally, Diverse System Device (DSD) rods are placed between the two banks of CSD rods.

1.4 International collaboration programs on advanced systems

1.4.1 The Generation IV Initiative

Beginning in 2000, a new and large international forum has begun to discuss the needs, principally, in terms of research and development for next-generation reactors, viz. Generation IV systems [34]. To better clarify the term "generation" in the nuclear energy development context, one may recall that nuclear power plants of the first generation are the first that ever existed, i.e. prototypes. The second generation consists of the nuclear power plants currently in operation, and the third generation represents advanced plants based on evolutionary developments of the second generation. The latter are reactors characterised by improved features from both safety and economics viewpoints, as exemplified by the EPR under construction in Finland and France.

Logically, the next generation of innovative nuclear energy systems corresponds to Generation IV. The different generations are presented in a chart in Figure 1.8. Here, we use the term nuclear systems, rather than nuclear reactors, for the reason that, even though the nuclear reactor represents the central piece, the NPP system as a whole contains the energy conversion and other auxiliary equipment, and also implies the use of supplementary facilities related to the fuel cycle (fuel element fabrication, management of the irradiated fuel, wastes treatment and storage, etc.).

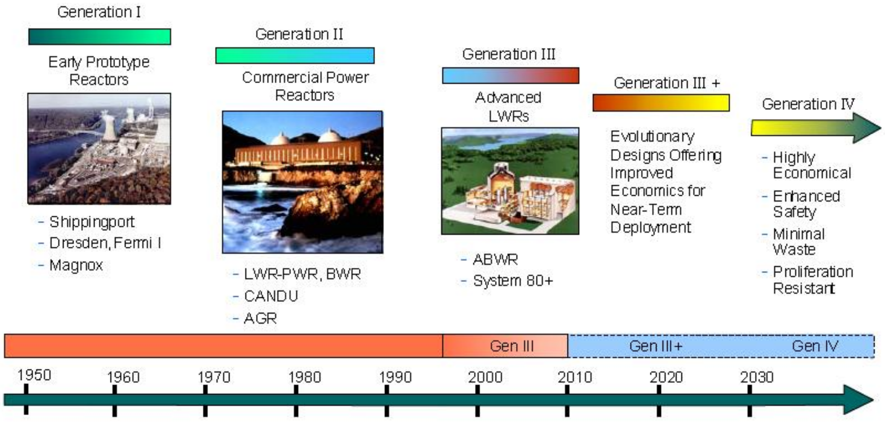

Figure 1.8 The evolution of nuclear power plant systems in terms of generations [34]

It is in this context that ten countries, viz. Argentina, Brazil, Canada, France, Japan, the Republic of Korea, the Republic of South Africa, Switzerland, the United Kingdom, and the United States, have agreed on a general framework for international cooperation in research for a future generation of nuclear energy systems. These countries form the so-called Generation IV International Forum (GIF), its operations being overseen by a Policy Group, supported by an

Experts Group [35]. The Policy Group acts as a decision-making body for high-level initiatives and issues, while the Experts Group oversees the various cross-cutting and system-specific R&D collaborations.

The main objectives of the Generation IV initiative is to have advanced nuclear systems available for commercial deployment about the year 2040, when a considerable number of current (Generation II) nuclear power plants will be close to the end of their operating licenses.

To help the GIF understand the opinions of countries not represented in the GIF and to identify opportunities to work with the relevant international organisations, the GIF charter provides for the participation of the International Atomic Energy Agency and the OECD Nuclear Energy Agency as permanent observers. In addition, membership status has recently been accorded to EURATOM, the international organisation representing the interests of the members of the European Union member states with nuclear power plants. Very recently, the GIF Policy Group voted unanimously to offer membership also to China and Russia [36].

Senior GIF representatives participate in committees that coordinate research activities required to develop the six next-generation nuclear energy systems that GIF selected in its December 2002 Generation IV Roadmap. The selected system concepts are the gas-cooled fast reactor (the system addressed in the present research, Figure 1.9), the lead-cooled fast reactor (Figure 1.10), the molten salt reactor (Figure 1.11), the sodium-cooled fast reactor (Figure 1.12), the supercritical water-cooled reactor (Figure 1.13), and the very-high-temperature reactor (Figure 1.14). To arrive at these six concepts, approximately 100 different NPP concepts were analyzed and evaluated for their potential to meet the goals set for Generation IV systems, viz. advanced nuclear safety, nuclear non-proliferation and physical protection, competitive economics, and waste minimisation as well as optimisation of natural resource utilisation.

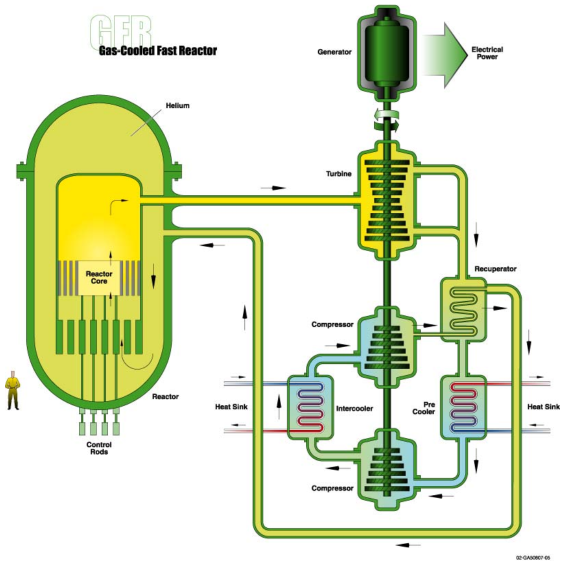

Figure 1.9 Gas-cooled Fast Reactor (GFR)

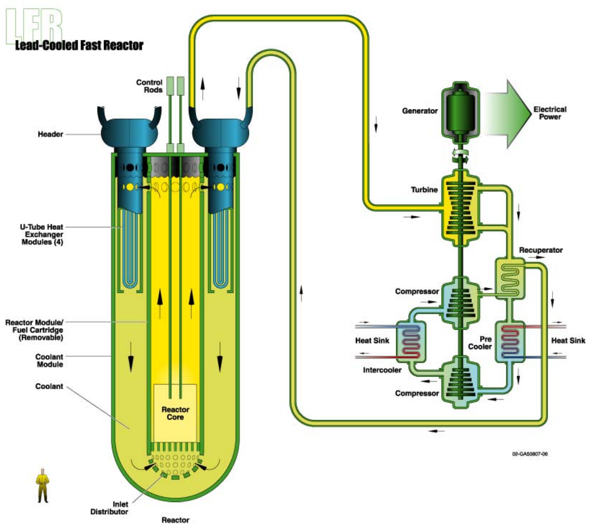

Figure 1.10 Lead-cooled Fast Reactor (LFR)

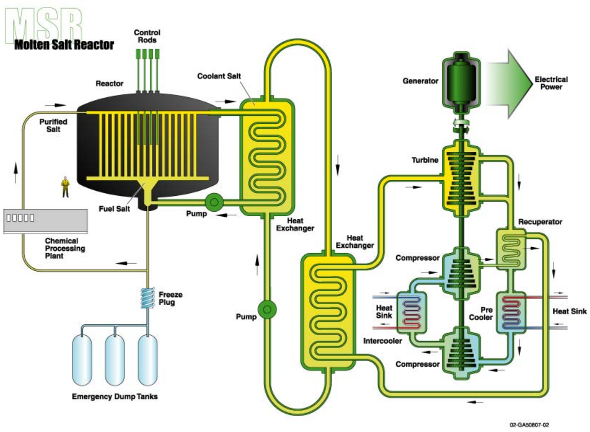

Figure 1.11 Molten Salt Reactor (MSR)

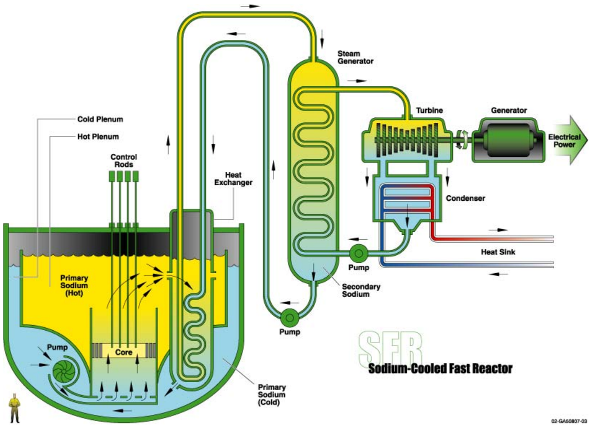

Figure 1.12 Sodium-cooled Fast Reactor (SFR)

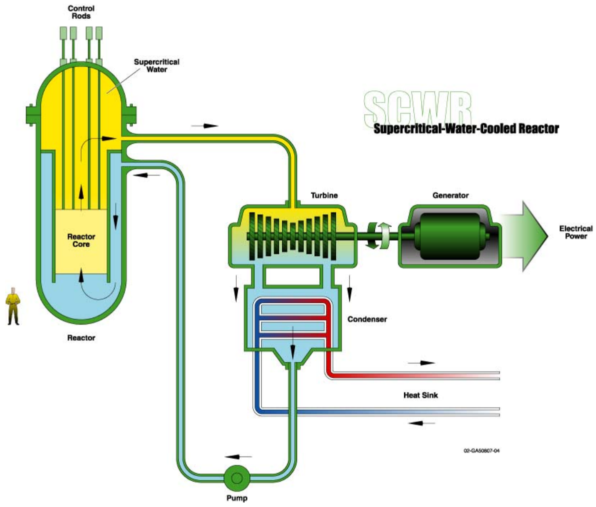

Figure 1.13 Super-Critical Water Reactor (SCWR)

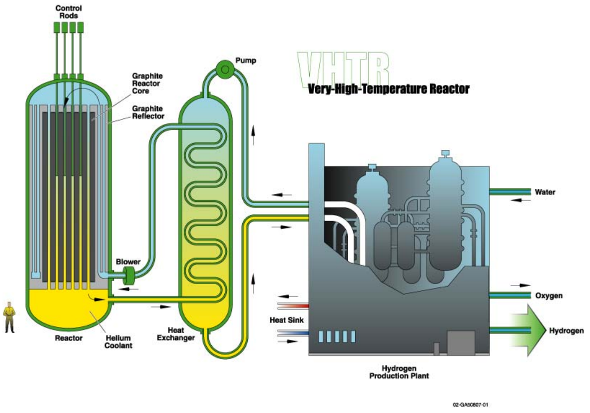

Figure 1.14 Very High Temperature Reactor (VHTR)

It should be mentioned that it is not only the Generation IV International Forum that promotes the renewed interest in nuclear energy. Brief descriptions of other international programs are given below, along with their relationship to GIF.

1.4.2 The international Project on Innovative Nuclear Reactors and Fuel Cycles (INPRO)

The international Project on Innovative Nuclear Reactors and Fuel Cycles (INPRO) is one of the parallel programs initiated by the IAEA in 2001 [37; 38]. In general terms, INPRO has 28 members contributing to the program, which consists of supporting a safe and sustainable, economic and proliferation-resistant use of nuclear technology to meet the global energy needs for the 21st century. INPRO is aiming at facilitating the synergy between the technology holders and the users so that they can jointly take the necessary actions required for achieving the desired innovations in nuclear reactors and fuel cycles. The missions of INPRO are broad and include the development of new methodologies, which complement those of GIF. To facilitate the exchanges, all country members of GIF are also members of INPRO.

1.4.3 Global Nuclear Energy Partnership (GNEP)

After the Generation IV initiative, the US Department of Energy launched in 2006 the Global Energy Partnership (GNEP) [39], motivated by the need to be even more global for future nuclear energy development and the concern about the fate of spent nuclear fuel. Up to now, 35 countries are participating in GNEP as direct partners or as observers. A list of objectives, called the GNEP Statement of Principles, is defining the partnership. The main goals are to expand the use of nuclear power to meet growing energy demand in a sustainable manner, to establish the necessary international link with other internal programs or partners in order to develop and demonstrate advanced fast reactors that consume transuranic elements from recycled spent fuel. Proliferation-resistance and waste management are also included in this program. Finally, cooperation between GNEP, GIF and INPRO is affirmed in the GNEP Statement of Principles.

1.5 Scope of the present thesis

The present doctoral work aims at contributing to the design development and analysis of the Generation IV advanced Gas-cooled Fast Reactor (GFR) with specific neutronics and thermal-hydraulics studies. The basic GFR design chosen for the present research, as will be highlighted later, is the large reference GFR design (“2004-Core”), with a thermal unit power of 2400 MWth [40; 41; 42; 43; 44; 45; 46; 47] and a core fuelled with ceramic-ceramic (CERCER) fuel plates. The large design was preferred to other concepts mainly because it represents the state-of-the-art for GFR development and currently serves as a reference design being studied in a broad international framework.

It needs to be stressed that, although a reference at present, the large Gen IV GFR design is by no means finalised, neither at the conceptual level nor at the engineering level. As such, it is a subject for a wide range of interdisciplinary R&D. Certain system features, complementary to the reactor (e.g. individual safety systems, the energy conversion system for the direct cycle option, etc.) have in fact not yet been designed and are being addressed at an early stage within an international framework, involving several different research institutions such as CEA and PSI. The underlying goal of the current collaborative R&D effort is clearly to have, by 2030, a well defined, detailed design for a GFR that meets the Generation IV requirements (see Section 1.4).

It is in the above context that the present doctoral research has been performed, the principal subject addressed being the control system design and related safety analysis for the GFR core. The three main aspects treated are:

1. *Neutronics tools validation*. The GFR is an advanced reactor system characterised by several unique features, apart from its fast neutron spectrum and the use of helium as

coolant. Thus, the fuel geometry (fuel pellets within a plate-type honeycomb structure) and material choice (CERCER) are highly innovative, and there are no specific computational tools available for the neutronics analysis. Existing computer codes and data libraries for fast reactors have been mainly developed and validated for the current (or past) generation of systems (Phénix, Superphénix, etc.), i.e. for sodium-cooled reactors. These tools have to be checked, verified and finally validated for gas-cooled designs. Thus, the physics impact of design differences (e.g. the innovative GFR fuel geometry and the use of novel materials such as SiC [48], (U,Pu)C in the core and Zr_3Si_2 in the reflectors) has to be carefully assessed. One specific difference for the GFR core is the absence of sodium and oxygen. This in itself impacts the neutron spectrum due to the absence of certain resonances, which are characteristic of sodium-cooled and oxide-fuelled cores. The specificities of the GFR core design have been the main motivation to perform, as the first phase of the present doctoral research, a verification of the existing neutronics tools and, in particular, of the deterministic code system ERANOS-2.0 in association with its adjusted nuclear data library ERALIB1 [49]. The latter was originally developed and optimised taking into account experimental data from a wide range of integral experiments for sodium-cooled reactors operating with MOX fuel. The verification has been performed in two main steps. First, ERANOS has been used for a reanalysis of the reference lattice of the GCFR-PROTEUS experimental program carried out at PSI in the 1970s [50]. In a second part, benchmark calculations have been performed with the Monte Carlo code MCNPX, in conjunction with a range of modern data libraries, in order to check the deterministic results and to observe the sensitivity to nuclear data.

2. *GFR control assembly design development and neutronics analysis*. Here, the research has been concentrated on the development of an adequate and specific control system device, viz. an appropriate CAP and its implementation scheme. As part of the design optimisation, specific neutronics aspects involving the physical interactions occurring between individual CAs, as well as between absorber pins within a single assembly, have been analyzed. The detailed analyses carried in this context have constituted a significant contribution to the development of a new core design in the framework of the international GFR collaboration.
3. *Core dynamic behavior studies*. The design development briefly described above has largely been based on static analysis. In the final phase of the current research, complementary dynamics studies have been carried out for the GFR core in order to obtain new, safety related insights in the context of the implemented CAP. Thereby, the principal emphasis has been on the detailed study of the dynamics of CA ejections and withdrawals at different speeds. This has allowed one to observe and understand the complex interactions occurring between different core regions and how these interactions can be propagated and/or amplified. Implications on the operational safety of the GFR have also formed part of these investigations. Finally, certain sensitivity analyses have been performed in order to identify possible ways to improve the overall GFR core design and performance.

1.6 Structure of the thesis

The present doctoral thesis is organized in a total of six chapters, including the present introductory chapter. In Chapter 2, the general background is presented, with a description and discussion of the main design features of the large reference Generation IV GFR. To start with, the past developments of gas-cooled fast-spectrum reactors are described. Then, a brief review is made of experimental neutronics programs, past and future, which have GFR development as the aim, viz. the GCFR-PROTEUS experimental campaign at PSI and the ENIGMA experimental program in MASURCA at CEA-Cadarache. In addition, a description of the first planned, fast-spectrum GFR prototype, the ETDR, is provided. This reactor is to be seen as the first operating system, which would combine gas coolant technology with a fast-spectrum core. Finally, the computational tools applied in the present research are described. These codes are ERANOS, PARCS and TRACE, which form part of the FAST code system at PSI, as well as CEA's thermal-hydraulics code COPERNIC.

The detailed description of the GCFR-PROTEUS experimental program and the new analysis of the reference test lattice, using both ERANOS and MCNPX, are presented in Chapter 3. Although the analysis carried out has provided a certain degree of validation for use of the adjusted ERALIB1 data library for a gas-cooled core, it has been shown that significant validation needs still remain for the Generation IV GFR.

Chapter 4 considers first the design of the large reference 2400 MWth GFR using plate-type fuel. The reactivity needs to operate the core, as well as the safety margins needed to scram the reactor in case of failure of the CA control commands, are assessed for defining the requirements for the CAP. The development of the CAP, on the basis of coupled neutronics and thermal-hydraulics calculations, is presented in detail. Particular attention has thereby been given to establishing the implementation scheme for the CAs in order to fulfill the reactivity requirements. Also described are the supplementary neutronics calculations, which have been undertaken to provide an in-depth understanding of the different complex phenomena occurring in a large fast-spectrum core. In terms of the design and safety requirements, the CA worth has been calculated with improved accuracy using perturbation theory to take into account the 3D geometry of the developed CAP. It is shown that, compared to previous results for commercial fast reactors, a significant reduction has been achieved, with the developed design, for the neutronics penalties which result essentially from heterogeneity effects

In Chapter 5, the dynamic behavior of the large reference GFR core is analyzed using advanced computational tools involving the coupling of 3D neutron kinetic (NK) and 1D thermal-hydraulic (TH) models. As a first step, the full core NK-TH models have been developed and benchmarked against reference static ERANOS calculations (for the neutronics part) and thermal-hydraulics design results obtained with the CATHARE code at CEA-Cadarache (for the thermal-hydraulics part). The coupling of the two models has been done using an external mapping scheme, specific tools having been developed in order to automate creation of the input decks. The coupled models have then been used to assess the core dynamics behavior for a wide range of CA driven transients. This allows one to understand, in depth, the GFR core behavior during hypothetical accident events such as the withdrawal at high speed of a CA and to assess, in a preliminary manner, the safety of the core in relation to this particular type of accident. The impact in terms of power map deformation has been studied in detail. Simplified models have also been developed and applied, in order to identify the discrepancies which can result from neglecting the explicit consideration of spatial effects. Finally, recommendations have been provided for reactor operation, in the context of CA movements.

Although the investigations reported in Chapter 5 mainly pertain to the large reference GFR core under BOL conditions, two complementary sets of investigations have currently been carried out in relation to: (1) the effects of fuel burnup for the reference core operating in closed-cycle mode and (2) GFR core design evolution as represented by the “2007-Core” design. These complementary studies are presented separately (as Appendix D and E). However, the related findings (sensitivity to fuel composition changes due to burnup, impact of design parameters such as the height-to-diameter (H/D) ratio, etc.) are reported in Chapter 5 itself.

Finally, Chapter 6 provides the main conclusions to be drawn from this research, as also the recommendations for future work.

Chapter 2

2 General background

This chapter gives the general background for the present doctoral research.

To start with, a brief description is given in Section 2.1 of past R&D programs related to Gas-cooled Fast Reactors (GFRs). Particular mention is made here of the program of integral neutronics experiments performed at PSI, i.e. GCFR-PROTEUS. The detailed analysis performed of some of the corresponding integral data, in the context of this thesis, is presented later in Chapter 3.

In order to provide integral neutronics data, which are more directly representative of the novel core materials envisaged for the Generation IV GFR (mixed carbide fuel, etc.), it is planned to soon launch a new experimental program, called ENIGMA, at CEA Cadarache. This is described in Section 2.2.

Section 2.3 describes the Experimental Technology Demonstration Reactor (ETDR), which is planned to be the first ever, gas-cooled fast-reactor, aimed at demonstrating the basic technological features of the Generation IV GFR. The “start-up” core of the ETDR, however, will largely employ conventional materials (MOX fuel, etc.).

The main design characteristics of the reference large 2400 MWth GFR – the main system considered in the current research – are presented in Section 2.4.

Finally, Section 2.5 presents the computational tools used in this thesis. In particular, a description is given of PSI’s FAST code system, which incorporates ERANOS, PARCS and TRACE (see below). The complete list of the individual computer codes used currently is the following:

(1) ERANOS-2.0 : the deterministic, fast-spectrum neutronics code developed at CEA,
(2) MCNPX-2.5: the Monte Carlo transport code from Los Alamos,
(3) COPERNIC: the thermal-hydraulics code developed at CEA,
(4) PARCS: the spatial neutron-kinetics code developed at Purdue University,
(5) TRACE: the thermal-hydraulics code developed by the U.S. Nuclear Regulatory Commission (US-NRC) for best-estimate analysis of LWR system behavior.

2.1 Gas-cooled Fast Reactors: past developments

This section reviews the past development of GFRs in Subsection 2.1.1, while the context of the use of the integral GCFR-PROTEUS data is presented in Subsection 2.1.2.

2.1.1 General

Several R&D projects on Gas-Cooled Fast Reactors (GCFRs, as they were termed earlier) have been conducted in the past.

In Germany, research on GCFRs was performed at the Karlsruhe and Jülich nuclear centres, in collaboration with industry. A so-called Gas Breeder Memorandum [51] was written to study the feasibility and economics of such systems. Three concepts were envisaged, based on three different working fluids: helium, steam and CO_2, the reference and preferred option being helium cooling. The main design characteristics given in the Gas Breeder Memorandum were a conventional core (1000 MWe) with oxide pin-type fuel technology, the cladding material being stainless steel of 316-type. The energy conversion system was an indirect one using a secondary steam cycle.

In parallel to the developments performed in Europe, General Atomics, in the U.S., developed a 300 MWe GCFR designed to demonstrate the practicality and performance benefits of the concept [52]. The main objective was to achieve low-cost power from a high-performance breeder reactor, with a high degree of inherent safety and reliability. The fuel design was mostly based on LMFBR fuel technology, the entire helium-cooled primary loop being contained in a Pre-stressed Concrete Reactor Vessel (PCRV) with cavities for the main components. In brief, GA’s 300 MWe GCFR was cooled with helium, with $(U,Pu)O_2$ in stainless steel cladding as the fuel material [52].

More recently, GCFR related R&D has been performed in the context of the European CAPRA-CADRA collaboration [53]. This research program, involving France, Germany and Belgium, was mainly related to the development of sodium-cooled FRs for plutonium and minor actinides burning. However, during the later stages of the collaboration, the emphasis was shifted to the analysis of gas-cooled FRs, as also of ADSs. In this context, the UK joined the collaboration and contributed to the design and performance assessment of an Existing Technology Gas Cooled Fast Reactor (ETGCFR). The ETGCFR, which had a large CO_2 cooled fast reactor core of 3600 MWth with conventional MOX fuel pins, is largely based on AGR technology and aims at the transmutation of MAs both homogeneously and in heterogeneous targets. A variant at high temperature based on particle fuel, i.e. the High Temperature Gas Cooled Fast Reactor (HTGCFR), was also studied in the framework of the CAPRA-CADRA program.

2.1.2 The GCFR-PROTEUS experiments

Switzerland also took part in the earlier GCFR related R&D, having had the intention of building gas-cooled reactors as one of the possible options for electricity production, mainly due to their apparent technical simplicity and the high level of inherent safety of the thermal-spectrum systems (see Appendix A).

It is in this context that the experimental program, GCFR-PROTEUS [50; 54], was carried out during the 1970's at the PROTEUS critical facility of the former "Eidgenössiches Institut für Reaktorforschung" (EIR), now the Paul Scherrer Institut (PSI). The principal aim of the integral experiments was to study the physics characteristics of gas-cooled fast reactors as envisaged at the time, so as to provide a validation base for the available neutronics tools, which had been developed mainly in relation to sodium-cooled fast reactors.

The GCFR-PROTEUS integral data have remained, to this day, among the most relevant for helping bridge the gap between the wide range of experimental results available for SFRs and the neutronics characteristics of the GFR. Accordingly, they have been re-analyzed in the context of the present research (see Chapter 3), comparisons being carried out between various measured neutron-balance components (mainly reaction rate ratios) and the corresponding results obtained using ERANOS-2.0.

The fuel used for the GCFR-PROTEUS reference test lattice consisted of pellets of $(U,Pu)O_2$ containing 15% Pu. The fuel rods were formed by filling stainless-steel tubes with capsules, each consisting of 8 pellets sealed in a thin aluminum can. Due to the absence of the sodium coolant, the reference GCFR-PROTEUS neutron spectrum analyzed is rather hard with several resonances (characteristic of SFRs) missing. In this sense, the validation domain of ERANOS and its associated data library ERALIB1 (adjusted largely on the basis of SFR-relevant experiments) has been extended in a GFR-relevant manner – an important step for the present work – in which ERANOS/ERALIB1 has served as the basic neutronics tool. It needs to be mentioned, however, that the neutron spectrum of the Generation IV GFR is considerably softer than that of the GCFR-PROTEUS reference lattice due to the presence of light elements like C and Si in the former case. The need for new integral experiments is thus certainly given (see the following section, for instance).

In carrying out the GCFR-PROTEUS analysis with ERANOS-2.0/ERALIB1, comparisons of the calculational results have been made, not only with experimental values, but also with Monte Carlo results obtained in conjunction with a range of different modern nuclear data libraries. Apart from providing a check on the deterministic methods used in ERANOS, this has also served to underline the significant sensitivity of the integral parameters to the basic differential data used.

The detailed GCFR-PROTEUS related investigations are presented in Chapter 3.

2.2 The ENIGMA experimental program

A new experimental program called ENIGMA ("Experimental Neutron Investigation of Gas-cooled reactor at MAsurca") is currently under planning in the Commissariat à l'Energie Atomique (CEA) at Cadarache, to provide novel experimental data for a better characterisation of the specific neutronics features of the Generation IV GFR. The experiments are to be performed at the MASURCA fast reactor critical facility.

MASURCA is a fast-spectrum, air-cooled reactor operating at a maximal thermal power of five kW (see Figure 2.1) [55]. The core has a volume of 6000 litres and is made of about 1000 hanging tubes, which can be loaded with pellets of steel, Na, different Pu and U fuel types (oxide, metallic, etc.) and/or other materials of specific interest. Each MASURCA square SA is made of 64 rods arranged in a 8x8 square pitch within a square steel tube [56]. By replacing the sodium-rodlets in recently investigated configurations by air and by introducing, at well-chosen places within the core, carbide-rodlets, a representative Generation IV GFR spectrum can be achieved using the available MASURCA fuel inventory [57].

The experimental results being sought, e.g. critical mass, spectral indices, control rod worths, etc., could be used for the validation of neutronics design tools for the GFR in a representative manner. At the current time, a major refurbishment of the MASURCA facility is in progress, and the upgraded reactor should be ready by 2012 for embarking on the new experimental program.

Taking into account operational constraints on the MASURCA reactor, the ENIGMA program will be divided into three phases [55]: (1) an initial phase with the same reference core configuration as in use just before the MASURCA refurbishment was initiated (essentially, a very first GFR-relevant configuration set up using existing MASURCA fuel), (2) a phase with new innovative materials in specific test zones, and (3) a final phase that could be a small mock-up of the 50 MWth ETDR experimental reactor (see next section).

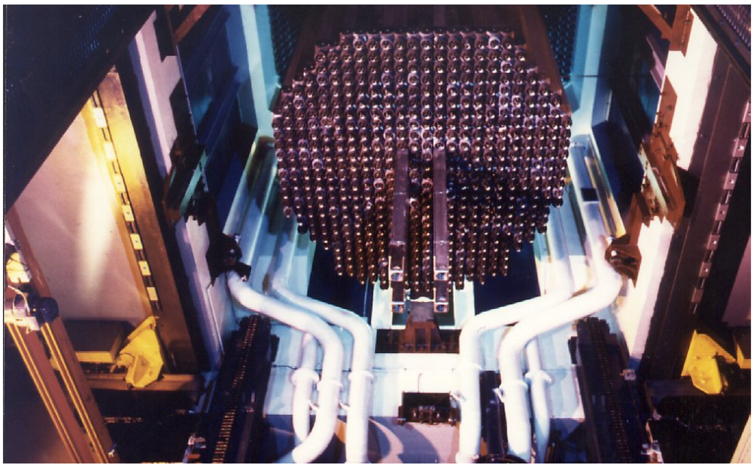

Figure 2.1 A view of the MASURCA reactor at CEA-Cadarache phases [55]

In more specific terms, the first experimental phase ("ENIGMA-1") will allow, following the MASURCA refurbishment, the new instrumentation and the safety systems to be tested on the basis of an earlier used reference configuration. One of the generic goals is to study independently and, in an analytical manner, different effects in specific types of central test zones.

The physics phenomena/parameters of interest are:

(1) the neutron spectrum,
(2) the streaming occurring between the fuel plates,

(3) the increased moderation and the impact of innovative materials,
(4) the impact of low-grade Pu, and finally,
(5) the control assembly heterogeneity.

The second phase ("ENIGMA-2") will be performed taking into account the experience gained from the first phase and will also take benefit of the advances made in GFR development work in general. This phase will additionally require the availability of new materials (e.g. Zr_3Si_2 reflectors), to be tested in the framework of specific reactor configurations

The reference ENIGMA fuel SA, as well as the basic core configuration (see Figure 2.2), were defined based upon neutronics investigations (i.e. sensitivity and representativity analysis) performed with ERANOS, in order to obtain a neutron spectrum as close as possible to that of the GFR reference with the constraint of using only the available fuel. For illustration, the fundamental-mode direct and adjoint fluxes are depicted in Figure 2.3 and Figure 2.4, respectively.

The SA rodlet-configuration for the reference core contains, as shown in Figure 2.5, 24 rodlets of $(U,Pu)O_2$, 8 rodlets of UO_2, 16 rodlets of C and 16 voided regions. The core has a fuel height of 91 cm and a diameter of approximately 108 cm [58]. The fuel SAs are in square geometry, while the geometry in the GFR core is hexagonal.

In particular, the use of C rodlets increases the spectrum softening, while the introduction of UO_2 rodlets helps to reduce the high-Pu concentration of the available $(U,Pu)O_2$ rods. As seen in Figure 2.3, showing the spectrum comparison for a typically envisaged GFR and the ENIGMA reference core, a good agreement is obtained. Nevertheless, the Si scattering resonance at 200 keV is not reproduced and the local flux depression due to the scattering resonances in steel nuclides is still present in MASURCA as the fuel pin cladding and SA tubes are made of steel.

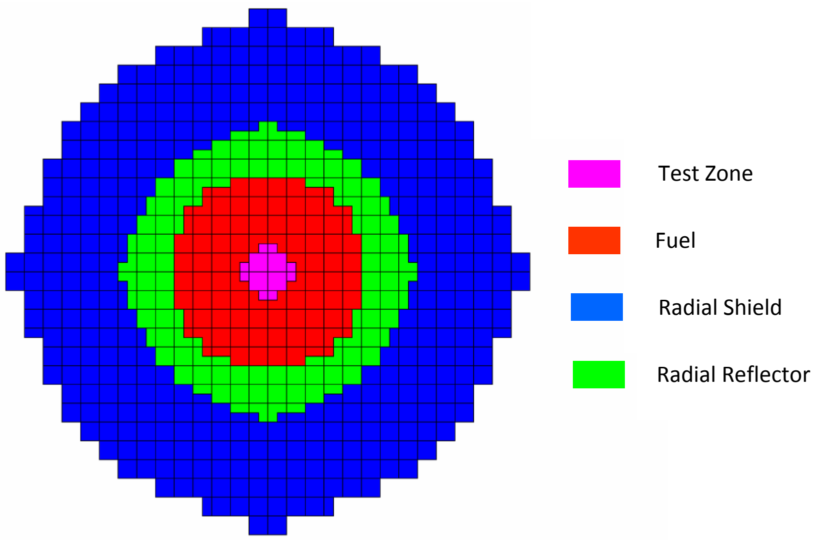

Figure 2.2 The reference ENIGMA core

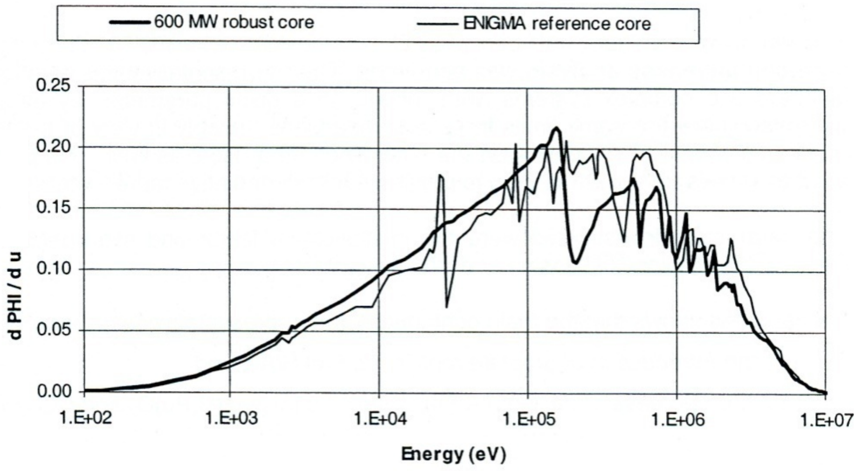

Figure 2.3 Fundamental mode direct flux (175 energy groups, normalized to 1) [57]

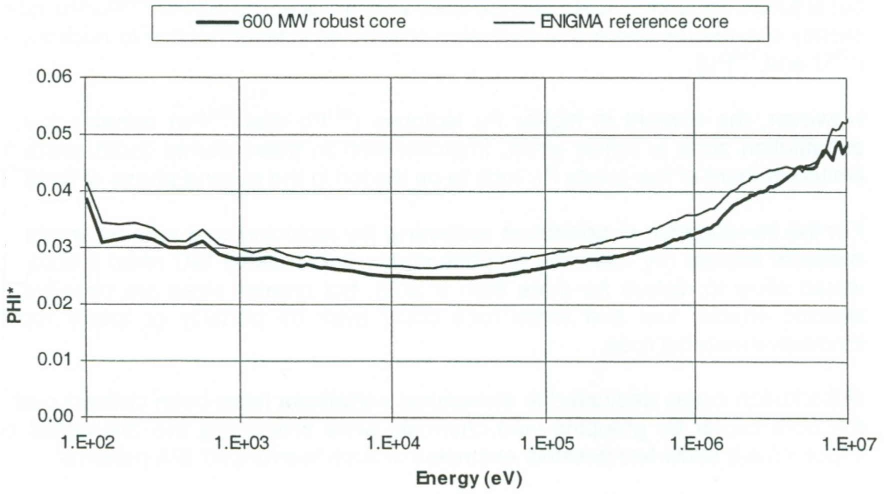

Figure 2.4 Fundamental mode adjoint flux (175 energy groups, normalized to 1) [57]

As seen in Figure 2.2, the central core region (in the range of six to nine SAs in order, principally, to limit the quantities of special materials needed) represents the actual test zone where the specific neutronics features of the GFR will be simulated. For example, for the investigation of spectrum softening or of innovative materials, void regions in the central SAs could be replaced by graphite rods or by SiC rods, respectively (see Figure 2.6). Additional test zones, dedicated to streaming variations, have been defined over appropriate 3X3 SA patterns at the core centre; with void channels grouped together while preserving the global SA composition balance (see Figure 2.7 and Figure 2.8).

Innovative reflector materials will also be studied by substituting a central part of the axial steel reflectors by innovative ones (Zr_3Si_2 or ZrC if available, or a mixture of Zr and C or SiC rods), an experimental assessment being carried out of the substitution reactivity effect and of axial reaction rate profiles. Finally, while concluding the ENIGMA experimental program overview, it needs to be stressed that control rod heterogeneity effects are important in a fast reactor (up to 30% for a sodium-cooled system, depending essentially on the spatial configuration and the ^{10}B content) and require special calculation procedures (such as those described in Chapter 4). Accordingly, it is planned to implement a few B_4C rod patterns within the ENIGMA core to check the validity of the equivalence algorithms used in softened spectra.

Additional information, e.g. regarding the sensitivity and representativity studies performed with ERANOS in support of the ENIGMA experimental program, can be found in the literature [57; 58; 59; 60; 61; 62; 63].

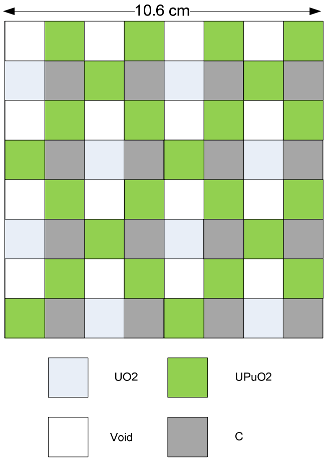

Figure 2.5 The reference ENIGMA fuel SA

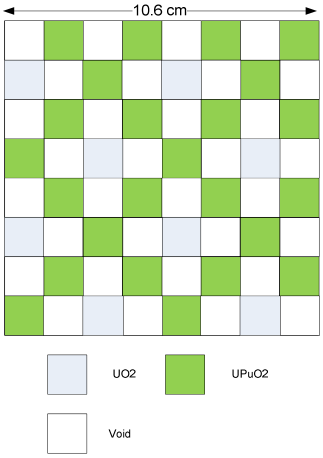

Figure 2.6 SA pattern for spectrum hardening studies: graphite is replaced by void

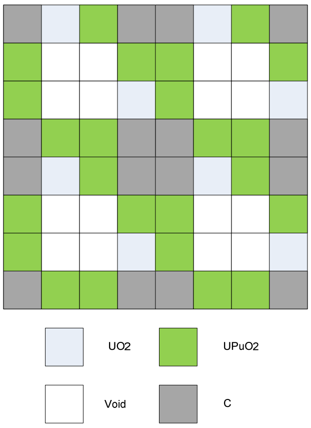

Figure 2.7 SA pattern for streaming studies: 2x2 void channel grouping

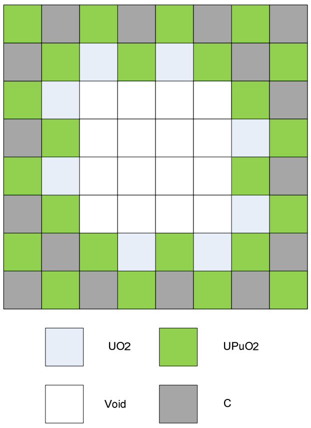

Figure 2.8 SA pattern for streaming studies: 4x4 void channel grouping

2.3 The first GFR prototype: ETDR

Complementary to the work on the ENIGMA experimental program, international R&D efforts are currently under way to study and design a GFR with a thermal power of 50 MW: the

Experimental Technology Demonstration Reactor (ETDR). ETDR represents a unique and flexible GFR prototype, which will link the existing experimental database for gas-cooled reactors, as also the ENIGMA program, to the first GFR demonstrator. The R&D activities were launched in 2000 as part of the European Commission's Gas-Cooled Fast Reactor project under the European Commission's 5th Framework Program. These have been continued, since March 2005 [64; 65; 66], under the current four-year project within the 6th Framework Program [67]. The ETDR would be the first ever gas-cooled fast reactor to be constructed, thus serving as a crucial test for GFR technology.

It is envisaged to build the ETDR reactor in about ten years, for a start of operation around 2020 [67]. As indicated, the primary goal of the prototype is to test and demonstrate the viability of the specific advanced and innovative features of the GFR, e.g. the new fuel technology for the heterogeneous ceramic fuel in plate geometry. Thus, the second core ("demonstration" core [67]) will not only investigate the fuel behavior under irradiation but also verify the feasibility of the processes envisaged for closing the fuel cycle, i.e. reprocessing and fuel re-fabrication, etc. Furthermore, the ETDR will also contribute to demonstration of the safety features of the GFR, e.g. the DHR systems.

Apart from the technology demonstration role of the ETDR, it will also provide valuable experimental data for core physics validation, the target being to extend the validation domain of the computational tools, especially of the deterministic code ERANOS-2.1. The measurement of integral parameters – mainly critical mass, neutron balance components, control rod worths, and reactivity feedback effects (Doppler, thermal expansion, depressurization, etc.) – will adequately complete the zero-power reactor experimental database.

In order to be able to initiate construction of the ETDR reactor using existing technology, it is envisaged to operate the reactor with two successive core configurations:

- *A "start-up" core*. This is based on conventional (LMFBR technology) pin-bundle SAs with (U,Pu)O_2 fuel and metallic (stainless-steel) cladding. As a consequence, the operating temperature will be relatively low (to be compatible with the cladding technology), viz. with inlet and outlet temperatures of 260°C and 560°C, respectively. This core is effectively a preparation for the next core configuration. The core geometry is represented in Figure 2.9. One sees, among other features, the six CSDs with the central DSD [68]. As a starting point, the CA pattern envisaged for the ETDR is similar to that used for the sodium-cooled EFR. For completeness, the homogeneous CA and assembly-follower volumetric fractions are given in Table 2.1. No definitive or optimized design is currently available. Complementary information can be found in [67; 69].

Table 2.1 Homogenous description of the ETDR control assembly pattern [69]

Control assembly	**Volumetric fraction, %**	**Material**
Absorber	30.2	B_4C - 75% ^{10}B
Structure	20.6	AIM1
Helium	49.2	He
Assembly follower	**Volumetric fraction, %**	**Material**
Structure	8.8	AIM1
Helium	91.2	He

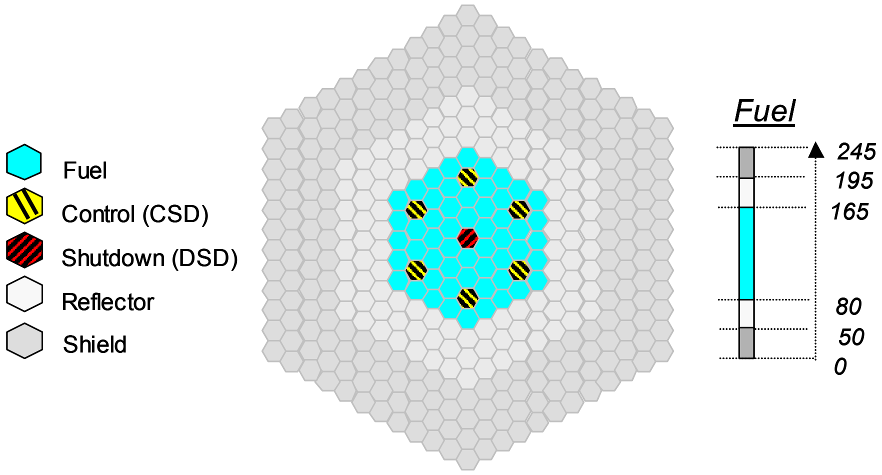

Figure 2.9 Cross-sectional view of the ETDR start-up core. An axial description is given on the right-hand side of the figure [68]

- *A "demonstration" core*. The start-up core will progressively be upgraded in order to implement new fuel SAs based on the plate-type GFR SA design with (U,Pu)C-SiC fuel. Correspondingly, the operating temperature will be increased, with 480°C and 850°C as the inlet and outlet values, respectively. This will provide representative conditions to test the material behavior.

It is planned to operate the ETDR with both cores using the same primary and secondary systems. The SA technology and diagrid have, therefore to be compatible in both cases. The main design parameters for the two ETDR cores are summarized in Table 2.2.

Apart for the core, the whole plant system has been studied for the ETDR and design options have been defined. In particular, the reactor vessel and its internal components have been given detailed consideration [70]. Other studies are in progress to design the control and instrumentation [71]. The diagrid, supporting the core, will distribute the helium mass flow according to the power distribution. In other words, a specific gagging scheme is applied at the SA inlets in order to match the flow rate to the power. A flat temperature distribution, as required for efficient plant operation, is thus obtained at the core outlet.

The ETDR will also serve as a first-of-its-kind prototype to test diverse safety-system design options.

Table 2.2 ETDR “start-up” and “demonstration” cores: main design and neutronics parameters [72]

Parameter	ETDR "Start-up" Core	ETDR "Demonstration" core
Power, MW	50	50
Power density, MW/m^3	100	100
T inlet, °C	260	480
T outlet, °C	560	850
Helium pressure, MPa	7.0	7.0
Fuel type	$(U,Pu)O_2$ pellets	CERCER
	hexagonal assemblies, metallic structure	(U,Pu)C + SiC
Fuel SA	Pins within hexagonal tube	Plates within hexagonal tube
Pin diameter (room T), mm	6.55	-
Plate thickness (room T), mm	-	6.27
Fissile height (room T), m	0.86	0.86
Fissile diameter (room T), m	0.86	0.86
Core pressure drop, MPa	0.062	0.058
Pu/(U+Pu), %	27.3	34.9
Fuel management scheme, EPFD	1705	1368
Burnup, mean/maximal (at%)	5.2 / 7.9	5.4 / 8.0
Max fast flux E > 0.1 MeV, n/cm^2/s	9.81E+14	8.53E+14
Doppler constant (EOC), pcm	-360	-523
He void effect (EOC), pcm	63	-18

2.4 Reference 2400 MWth Gas-cooled Fast Reactor Design

The large Generation IV GFR [47; 73; 74; 75; 76; 77] is the result of the renewed interest in fast-spectrum technologies – mainly for closing the fuel cycle and improving fuel utilization, which are among the principal goals of the Generation IV initiative. The large GFR design combines the experience gained during the development of mainly (a) thermal-spectrum gas-cooled reactors (see Appendix A) and (b) LMFBRs (see Section 1.3).

The benefit of combining these two different types of technology development efforts lies in the high degree of synergy which can be achieved. Considerable progress has thus been rendered possible in the context of:

(1) Gas flow under forced convection conditions (coolant thermal-hydraulics and heat transfer),
(2) Material behavior at temperatures up to 950°C, and the related use of refractory metals and ceramics,
(3) Neutronics of fast-spectrum reactors, and corresponding computational tools.

However, the advanced GFR features several unique, innovative characteristics, in terms of design (fuel geometry, spectrum, etc.) and materials (ceramic structures, Zr_3Si_2 reflectors, etc.), which were not present in previous reactors. As a direct consequence, R&D has to be performed in order to dispose of adequate computational tools for the detailed design and safety analyses.

In Subsection 2.4.1, the main GFR design constraints, in order to meet the Generation-IV requirements, are presented, while Subsection 2.4.2 gives a general overview of the design specifications. A more detailed description of specific GFR core features are presented in Chapter 4, along with the control system design studies conducted as part of the present research.

2.4.1 Design constraints

Prior to the description of the reference large 2400 MWth GFR itself, some important aspects are reviewed to justify some of the choices made in the current reference design presented in Subsection 2.4.2.

Designing a new core concept with innovative features, such as a high outlet temperature leading to a high thermal efficiency, requires technological advances relative to current-day knowledge and experience, especially in relation to the fuel and structural materials. The design options are dictated a priori also by economic considerations. Fabricating a new fuel type is highly demanding in terms of research and development, as well as establishing the needed industrial processes. As a direct consequence, the fuel becomes very expensive, which is not compatible with the Generation IV goals. To compensate for this drawback, the volumetric power density has to be high in order to maximize the energy production for a given fuel mass. Another implication of a high volumetric power density is in terms of core size reduction, and therefore of capital cost reduction. This was the approach used, for instance, for fast-spectrum sodium-cooled reactors with a power density in the order of 280 MW/m^3 [30]. Taking into account the challenge of reaching high temperatures, a volumetric power density of 100 MW/m^3 has been considered reasonable for the reference GFR design option, this value being in the order of that of LWRs.

The GFR core design should allow for operation with flexible fuel management [73], i.e. as (1) burner, (2) iso-breeder and (3) breeder. This implies that it should be possible to operate the core with different Pu contents and different amount of MAs, depending upon the fuel strategy and/or the available fuel inventory. At the present time, it is anticipated to operate the core in an iso-breeder mode, while utilizing the spent fuel from LWRs and addressing non-proliferation concerns by excluding the separation of Pu from U. Designing the GFR with iso-breeding capability is a highly challenging task in terms of neutron economy, for the main reason that blankets are not envisaged and breeding needs to be provided within the core itself. A possible strategy is that the core is fed only by natural or depleted uranium and all the minor actinides, i.e. Np, Am and Cm, are recycled entirely, along with the Pu. The fuel cycle is thus completely closed, which allows one to reduce the risk of radiotoxicity release to the environment because only the fission products need to be disposed of in a final depository.

The iso-breeding option is decisive for the GFR core design since it imposes a rather low content of Pu within the core, with a Pu/(U+Pu) ratio in the range of 15 to 20%, considering the Pu coming from the LWR fleet ("Pu-2016" grade [78]) as feed. A compromise has to be found between the ^{239}Pu fraction, which has to be high enough to obtain criticality, and the ^{238}U concentration (low Pu/(U+Pu) ratio) to ensure a breeding ratio of one. One of the ways to solve this problem is to use a high-density fuel like carbide or nitride. The reference GFR design considers at the present time only the carbide fuel option.

On the neutronics side, a large core facilitates the breeding gain, with a "cigar"-shape design to limit neutronics instabilities and neutron leakage (this aspect will be discussed in more detailed terms in Chapter 4). However, for the thermal-hydraulics, and especially to improve the natural circulation associated with DHR, the core should be rather large in diameter (~4.5 m) and relatively small in height (~1.5 m; this corresponds to a height-to-diameter ratio of 0.3), i.e. have a "pancake" shape. Such geometry permits one to obtain a low core pressure drop (in the order of 0.05 MPa). In the context of design, there is a strong coupling between the neutronics and thermal-hydraulics specifications. The coupling existing in the reference large GFR design is a principal topic addressed in the present research, with the detailed dynamics studies described in Chapter 5.

In general terms, there is coupling between neutronics and thermal-hydraulics for several physical phenomena [79]:

- *Doppler effect*. The temperature impacts the vibration state of the nuclides. These vibrations broaden the neutronic reaction resonances and then change in consequence the microscopic cross-sections for the various reaction types, i.e. fission, scattering, capture, etc. In the core of a reactor, the Doppler effect is predominant for the ^{238}U capture reaction in the fuel, an increase of the fuel temperature leading to an increase in ^{238}U absorptions, which in turns reduces the reactivity. The Doppler effect is particularly important for reactor safety, the reactivity feedback being negative and rapid, helping to stabilize the core power in case of external perturbations. In comparative terms, due to the particular materials used in the GFR and the corresponding spectrum, the absolute value of the GFR Doppler constant is much higher than in the SFR.
- *Void effect*. The temperature and pressure field within the core determines, among other things, the coolant density which in turns impacts the neutronics in terms of neutron spectrum and leakage. In the GFR, due to the low parasitic absorption cross-section of helium, the void effect is very small, although slightly positive mainly due to a hardening of the neutron spectrum, which is not counter-balanced by the loss of absorption. The value of the void coefficient for the GFR is much lower than that for the SFR.
- *Thermal expansion*. The axial and radial thermal expansions of materials, following a temperature increase, lead to a core volume expansion, which reduces the reactivity mainly due to an increase of leakage and change of relative positions between fuel and absorbers. However, this reactivity can be delayed in time: the radial expansion is governed by the expansion of the diagrid, which supports the core and reacts on the change of the coolant temperature at the core inlet. On the contrary, the axial expansion

is governed by the fuel or cladding expansion, depending on the fuel geometry configuration.

2.4.2 Design specifications

As mentioned in Chapter 1, the advanced GFR is one of the promising candidates, in the framework of the Generation IV initiative [34], to improve the various aspects of nuclear energy production: safety, economics, sustainability, non-proliferation and availability.

A schematic representation of the Generation IV helium Gas-cooled Fast Reactor is given in Figure 2.10.

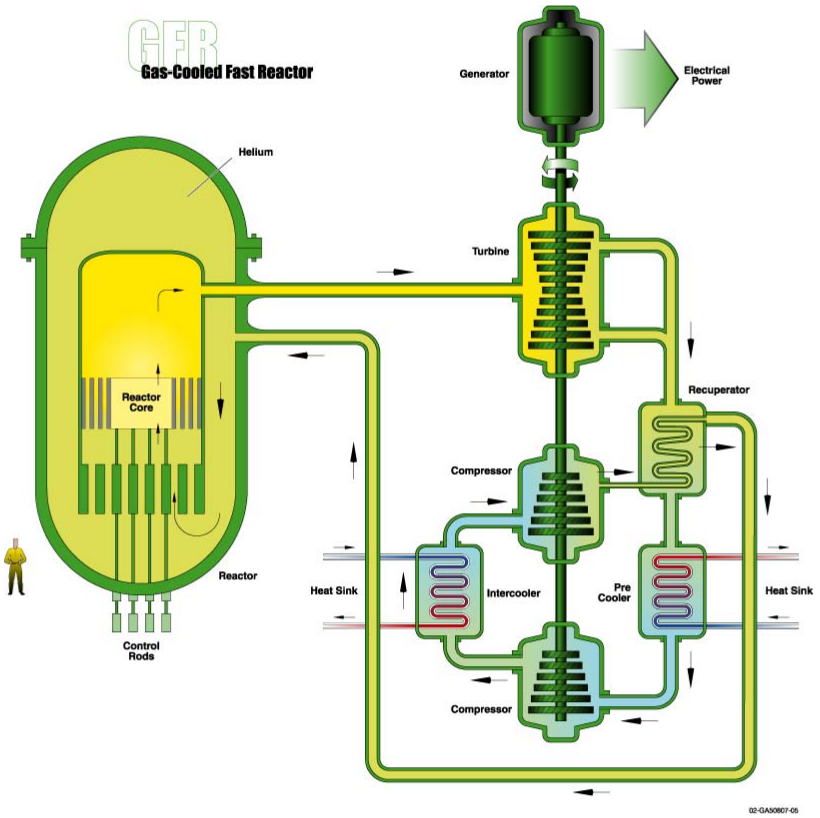

Figure 2.10 Schematic view of the Generation IV Gas-cooled Fast Reactor (direct cycle option)

It is of importance to recall the main design features of the advanced reference Generation IV GFR:

- *Fast-spectrum system*. Fast-spectrum reactor core without use of any fertile blanket due to proliferation concerns (since blankets contain high-purity fissile material).
- *Iso-breeder core*. The breeding gain is equal to zero and allows one to feed the reactor only with fertile material, since enough fissile material is bred within the core.

- *Moderate volumetric power density core*. The design volumetric power density is 100 MW/m^3, which improves core cooling capability.
- *Conversion system*. The core is cooled by a direct or indirect cycle to maximize the thermal efficiency and compensate for the relatively low volumetric power density. A Brayton-cycle is a possible option for electricity production, but other options are also considered (e.g. indirect cycle with CO_2).
- *Helium is the coolant*. Helium as the working fluid minimizes the parasitic absorption and offers good thermal properties. To obtain high thermal efficiency, a high reactor outlet temperature is necessary (in the range of 850°C), combined with a pressure of 7 MPa to compensate for the low density of the gas.
- *Ceramic material*. High gas temperatures within the core will be possible using refractory materials like SiC. The melting point of pure SiC is ~2700°C, so that the material integrity is ensured up to the high temperature reached under accidental conditions. Ceramics are also chemically inert up to dissociation temperatures.
- *Safety*. The core design is set up with a large coolant fraction (~40%) to obtain a low core pressure drop (~ 0.05 MPa). A low core pressure drop is attractive because it increases the possibility of operating the core under natural circulation for DHR conditions.
- *Fuel material*. To avoid any release of radioactive inventory into the environment, fuel pellets placed within a honeycomb ceramic structure are the preferred option over pin fuel. However, R&D for pin-type fuel is being continued and is considered as a backup plan.

To summarize the above design characteristics, the large Generation IV GFR is a fast spectrum, helium-cooled advanced reactor concept, with a thermal power of 2400 MW and an average power density of 100 MW/m^3 [41; 45; 47; 73; 75; 80; 81; 82; 83; 84]. The core contains two zones of different Pu content, these zones being almost equal in volume The use of high coolant temperatures, i.e. ~850°C, permits an optimal thermal efficiency for electricity generation (in the range of 45%), and also facilitates co-generation of heat and/or hot steam. The main design and safety challenges for the GFR are:

(1) To provide efficient DHR under accident conditions, which include depressurization,
(2) To ensure integrity of the CERCER fuel elements (relatively high fragility).

Details regarding the fuel design and core materials are given later in Subsection 4.2.1.

Figure 2.11 and Figure 2.12 illustrate the system design for the reference GFR (2400 MWth), operating in indirect-cycle mode [47].

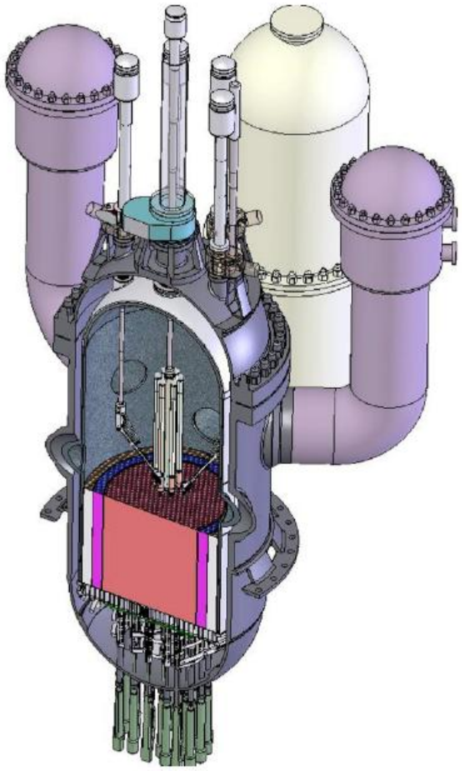

Figure 2.11 Schematic representation of the GFR vessel

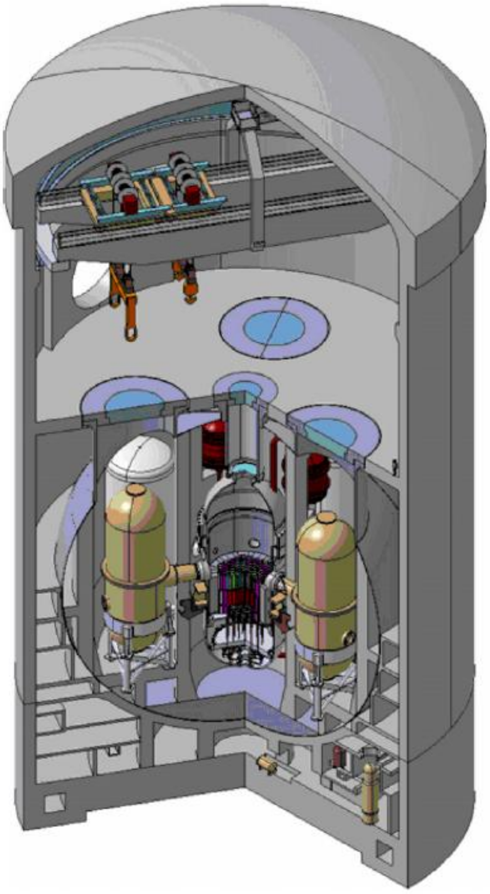

Figure 2.12 Schematic representation of the GFR reactor building

The reflector material in the GFR is a mixture of Zr_3Si_2 and helium, in different volume fractions, depending on the position. The axial reflector, above and below the fuel zones (each, 1 m thick), is made of 60%vol. Zr_3Si_2, the remaining volume being occupied by helium at 7.0 MPa. The proportion is 80/20% for the radial reflectors. In addition, the central subassembly does not contain fissile material, but instead Zr_3Si_2 and helium in equal volume proportions, allowing one to reserve room for instrumentation or specific experiments.

To control the core reactivity, the reference GFR contains a total of 33 control assemblies implemented within the core in three individual banks: two CSD banks and one DSD bank. In more detailed terms, the first CSD bank contains six assemblies, and the second one 18. There are nine DSD assemblies in the intermediate safety bank. The implementation scheme for the CAs is assumed to be similar to that of the EFR.

At the beginning of the current research, no specific and detailed control or safety assembly pattern was available. As a consequence, significant work was dedicated, in the first phase, to design a suitable CAP and then, in a second phase, to implement this pattern within the core (CA implementation scheme). Due to the similarity of reactor power and core size, the CAP developed for Superphénix and EFR were considered as the starting point. Detailed neutronic and

TH analyses were then performed in order to optimize the pattern and to help the core designers in achieving an effective CAIS (see Chapter 4).

The main design characteristics of the reference large GFR are summarized in Table 2.3.

Table 2.3 Design characteristics of the reference large 2400 MWth Gas-cooled Fast Reactor (GFR) [47; 72] (see Section 4.2.1 for details of the fuel design)

Parameter	Reference GFR "2004-Core" Design
Power, MW	2400
Volumetric Power, MW/m^3	100
T inlet, °C	480
T outlet, °C	850
Fuel type	CERCER honeycomb, (U,Pu)C$_{56\% \text{ vol.}}$ and (SiC, He$_{gap}$)$_{44\% \text{ vol.}}$
Fuel assembly	Plates in hexagonal wrapper, SiC/SiCf structures
Fissile and coolant (% core vol.fraction)	22.4 - 40.0
Total plate thickness, mm	7.00
Plate width, cm	12.0
Distance between fuel plates (channel width), mm	5.9
Fuel pellet height, mm	5.9
Lateral SiC wall thickness, mm	0.5
Number of control assemblies	33
Implementation scheme	3 banks
Number of plates per assembly	27
Flat-to-flat distance, cm	21.43
Fissile height, cm	155.0
Reflector height (axial, both sides), cm	100.0
Height over diameter ratio	0.35
Max cladding/fuel T, °C	1075 / 1210
Core pressure drop, MPa	0.06
Average Pu/U+Pu, %	17.7
Fuel management scheme, EFPD	3 X 831 = 2493
Burnup$_{mean/maximal}$, (at%)	10.1 / 14.7
Max dose (dpa in SiC)	163
Doppler constant (EOC), pcm	-1175
He void effect (EOC), pcm	253
Delayed neutron fraction (EOC), pcm	344

2.5 Computational tools

2.5.1 The FAST code system

The core neutronics and safety analysis of various advanced fast-spectrum systems is currently performed at the Paul Scherrer Institut using a new, multi-purpose analytical code system, called FAST (Fast-spectrum Advanced Systems for power production and resource managemenT) [85]. It represents a general computational tool, which allows the assessment of the static and dynamic behavior of different fast reactor systems using various coolants and different fuel types. The general structure, with the information flow between the codes, is schematically depicted in Figure 2.13.

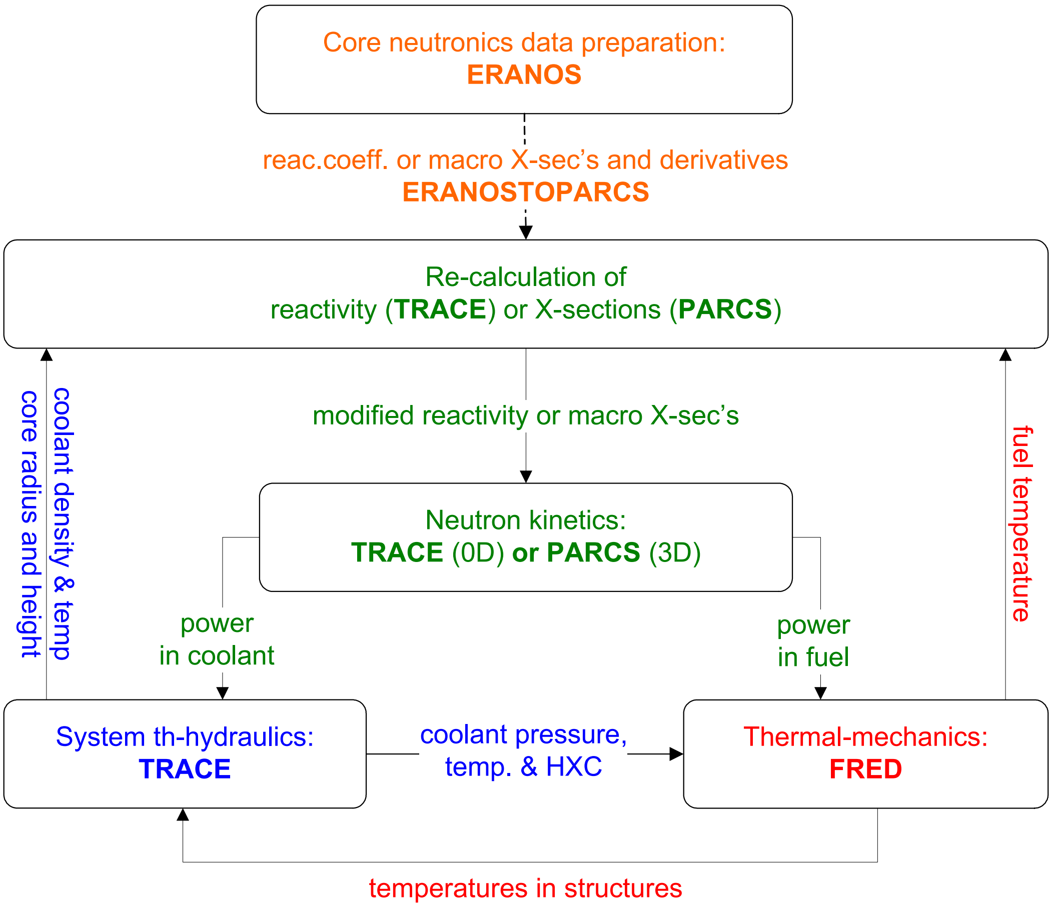

Figure 2.13 The FAST code system structure

A code system of this complexity and flexibility is particularly attractive in the context of safety related studies aimed at establishing the basic feasibility of advanced critical fast reactors being proposed by the Generation IV International Forum. It is in this context that the investigations of GFR core dynamics have been performed in the course of the present research, using primarily the FAST code system (see Chapter 5).

Not only is the reactor core simulated in FAST, but also the whole reactor system with a detailed representation of the primary circuit. This degree of modeling allows detailed safety studies of hypothetical accidents which have their origin on the side of the TH, e.g. a loss of flow, and on the side of the neutronics, e.g. CA withdrawals. Additionally to the neutronics and TH codes, the fuel rod thermal-mechanics code FRED [86] is used for simulating the fuel behavior via an internal coupling especially developed for this purpose. Furthermore, the code system makes it possible to analyze, in a systematic manner, a wide variety of transients, including those which may lead to asymmetric core conditions. Examples are the accidental withdrawal of control assemblies, the insertion of moderating material which may lead to a reactivity increase, e.g. water/steam in a gas-cooled core, the flow of gas bubbles in a liquid metal cooled core, etc.

The stand-alone codes, which are part of the code system, are state-of-the-art as regards their domain of applications. In effect, the FAST code system has been created from existing codes which, where necessary, have been modified to simulate fast reactor features, e.g. in the cross-section derivatives calculations. The code development is focused on coupling these codes together in an adequate way for advanced fast-spectrum analysis.

As seen from Figure 2.13, the core neutronics analysis and data preparation is performed using the deterministic system code ERANOS-2.0 [49; 87; 88]. ERANOS-2.0 is a neutron and gamma transport code consisting of different modules, allowing a great flexibility in its application. The code was developed within the European Fast Reactor collaboration. Among other capabilities, it performs core, shielding and fuel cycle calculations in conjunction with either non-adjusted or adjusted JEF-2.2 data and includes the most recent developments in calculational methods, e.g. the collision probability method in many groups and a 3D nodal transport theory variational method with perturbation theory and kinetics options [89]. In the context of the FAST code system, the code is used for calculating the core power distribution and reactivity coefficients in the case of point reactor kinetics, or macroscopic cross-sections and their derivatives in the case of spatial neutron kinetics in conjunction with the PARCS code [90]. The self-shielded macroscopic cross-sections and their derivatives are calculated, in particular, with the cell code ECCO [87; 91], which is included in the ERANOS package.

Thermal-hydraulics assessment is performed with the well-established computer code TRACE [92]. TRACE (Transient Reactor Analysis Code) is a best-estimate analysis, system code which can be used for steady-state and transients TH calculations of various reactor systems. It includes physical properties of numerous coolants and, in particular, He in order to perform GFR analysis. In the transient mode, the core power is evaluated using the point kinetics approximation with kinetic parameters being calculated with ERANOS. On the contrary, the TRACE code is not appropriate for transients in which there are large changing asymmetries in the reactor-core power distribution, such as would occur in a CA ejection transient, unless it is used in conjunction with the PARCS spatial kinetics module [90; 92]. The spatial neutronics response associated with the ejection of a single CA cannot be accurately modeled in conjunction with the point-kinetics approximation.

The PARCS (Purdue Advanced Reactor Core Simulator) code is a 3D reactor core simulator which solves the steady-state and time-dependent, multi-group neutron diffusion and transport equations. As indicated above, PARCS is coupled directly to the thermal-hydraulics system code TRACE which provides the core temperatures, coolant densities and core dimensions to PARCS for the transient re-calculations of the group cross sections. The primary use of PARCS involves a 3D calculation model for the realistic representation of the physical reactor.

The transient fuel-rod thermal mechanical code FRED [93; 94] has been included in the FAST code system to calculate, in 2D geometry and at each time step of the transient, the fuel and structure thermal-mechanics parameters, such as temperatures, stresses and strains in the fuel and in the structure. Specifically, in the case of the use of the TRACE code with the PARCS code (i.e. in spatial-kinetics mode), the fuel and coolant temperatures and densities, as also the axial and radial thermal expansions, calculated either by TRACE and FRED (in a more detailed manner), are transferred to PARCS to re-calculate the macroscopic cross-sections of the various materials.

More detailed information on the different codes is provided below.

2.5.2 Fast-reactor neutronics code: ERANOS

The neutronics calculations have been performed with the deterministic code, ERANOS-2.0 and -2.1, the code name denoting “European Reactor Analysis Optimized code System”. The latest version (ERANOS-2.1) was released in 2007, with significant improvements in the algorithms for analysis of advanced Generation IV systems [87; 88; 89; 91; 95]

ERANOS consists of data libraries, individual codes and calculation procedures, which have been developed and validated in an international collaboration within the European Collaboration on Fast Reactors [49], with the aim of providing a suitable analytical capability for reliable neutronics calculations of LMFR-spectrum reactor systems. The new release of the code extends the capabilities for treating advanced reactor fuel SAs (in particular, the plate-type geometry), GFRs and ADSs.

One of the main advantages of the code system consists in its high flexibility and modularity. A typical ERANOS calculation is performed using different modules, linked together in procedures using a specific language. Recommended calculational routes are also provided depending on the objectives, from fast scoping studies to reference calculations. Clearly the CPU-time needed will be considerably different depending on the desired option.

In a deterministic code like ERANOS, the core neutronics parameters (e.g. the effective multiplication factor k_{eff} or the fine flux Φ at each point modeled in the system) are computed with a two-step approach (see Figure 2.14): (1) the cell/lattice calculation performed with the ECCO code and (2) the core calculation, using either the variational nodal method TGV/VARIANT [89] for a 3D core geometry or the finite-difference S_n BISTRO method [88] for a 2D core geometry. These codes solve the homogeneous and inhomogeneous (i.e. with an external neutron source) equations. Both the direct and adjoint solutions can be computed.

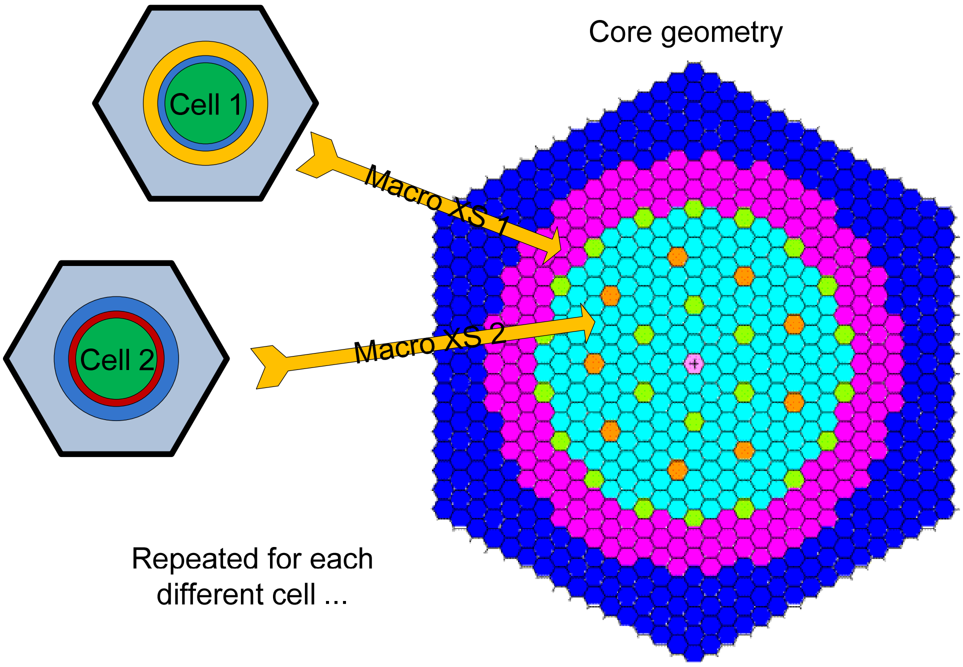

Figure 2.14 Schematic of a typical ERANOS calculations. The self-shielded macroscopic cross-sections are first computed with the ECCO code on a cell level and then the core calculations are performed combining the cells together to build the core geometry.

More particularly, in the first step of the calculation, the ECCO cell/lattice code is used for the preparation of self-shielded macroscopic cross-sections and matrices for each core region (i.e. fissile SA, reflectors, CAs, etc.) by combining the slowing-down treatment in the fine group structure (1968 groups [96]) with the collision probability method using the sub-group method. The subgroup method is a powerful method to calculate the weighted flux needed to calculate the self-shielding when computing macroscopic cross-sections. Additionally, the subgroup method can deal with highly heterogeneous lattices. The sub-group method takes into account the resonance structure for heavy nuclides by means of probability tables and assumes a uniform neutron source within a given fine energy group:

$$\Sigma_g = \frac{\int_{E_{inf}}^{E_{sup}} \Sigma(E)\Phi(E)dE}{\int_{E_{inf}}^{E_{sup}} \Phi(E)dE} \Rightarrow \Sigma_g = \frac{\int_{\Sigma_{t,inf}}^{\Sigma_{t,sup}} \Sigma(\Sigma_t)p(\Sigma_t)\Phi(\Sigma_t)d\Sigma_t}{\int_{\Sigma_{t,inf}}^{\Sigma_{t,sup}} p(\Sigma_t)\Phi(\Sigma_t)d\Sigma_t} \qquad \text{Eq. 2.1}$$

where $\Sigma_g$is the macroscopic cross-section in the g group, ϕ the fine flux and $p(\Sigma_t)$ is the probability distribution in the energy interval $[E_{inf}, E_{sup}]$. In ECCO, the cells can be described either as homogeneous or heterogeneous (typically, a fuel SA made of fuel rods arranged in a lattice) media. Several geometries are available:

(1) Homogeneous or infinite media,
(2) A 2D rectangular lattice of cylindrical rods and/or pins within a square wrapper,
(3) A 3D slab,
(4) A 2D hexagonal lattice of cylindrical pins within a hexagonal wrapper.

At the end of the ECCO cell calculations, the results (cross-sections and matrices) are usually condensed in a defined energy-group structure (typically 33 groups in the present research) for a homogenized cell used for reactor calculations.

The ERANOS-2.0 code release contains two neutron cross-section libraries, both derived from the JEF-2.2 nuclear data evaluated files: JECCOLIB2 and ERALIB1 [97]. In ERANOS-2.1, additional neutron libraries have been derived from the JEFF-3.1, JENDL3.3 and ENDFB6.8 evaluated nuclear data files [95]. Each library contains:

(1) A 1968-energy-group library (or 1/120 in lethargy), for the main nuclides (41 isotopes, including ^{235}U, ^{238}U, ^{239}U, ^{240}Pu, ^{241}Pu, ^{242}Pu, Zr, Gd, Al, ^{56}Fe, ^{58}Ni, ^{52}Cr, Na, O, C, ^{10}B, bounded H). The library is obtained by processing the JEF-2.2 data file, using a validated version of NJOY,
(2) A 33-energy-group library for fast-spectrum applications (287 isotopes),
(3) A 175-energy-group library (VITAMIN-J scheme) for shielding calculations,
(4) A 172-energy-group library (XMAS scheme) for thermal-spectrum applications (287 isotopes),
(5) A 36-energy-group library for gamma source calculations.

In the case of the ERALIB1 nuclear library, which was produced in 1996, adjustments have been made, based on 355 experimental integral-parameter values obtained from 71 different systems. The adjustments concern the elastic, inelastic, capture, (n,xn), fission and nu-bar data for the main nuclei, i.e. ^{235}U, ^{238}U, ^{239}Pu, ^{240}Pu, ^{241}Pu, ^{242}Pu, Zr, Gd, Al, ^{56}Fe, ^{58}Ni, ^{52}Cr, Na, O, C, ^{10}B and bounded H. The micro-flux weighting spectra used to collapse from the 1968 to 33 groups, and from 172 to 33 groups, have been generated from ECCO homogeneous cell calculations for a typical sodium-cooled LMFBR fuelled with (U,Pu)O_2 fuel.

The BISTRO code is particularly efficient in terms of convergence, and S_n transport and diffusion options are available. The diffusion option is also used in the transport mode to accelerate the convergence scheme. In more detailed terms, the standard S_n method is used to discretize the Boltzmann equation in two-dimensional geometries (XY or RZ). Different algorithms (viz. step, diamond and theta-weight) and a negative flux fix-up capability exist.

The variational nodal method implemented in the VARIANT code is used in the TGV/VARIANT module. This method is based on the second-order form of the even-parity transport equation. A solution is computed in the form of an expansion of the even and odd-parity fluxes. More specifically, the spatial variables are described with orthogonal polynomials, and the angular variables using spherical harmonics. Cartesian and hexagonal geometries can be modeled using TGV/VARIANT. Due to the use of the transport option, the CPU-time can be considerable and, as a consequence, the simplified transport option has been implemented and is used in the reference route. The user can specify the order of the spatial expansion of the sources, the flux within a node and the flux at the interface, conferring to the module a high flexibility.

Complementary to TGV/VARIANT, a spatial three-dimensional kinetics and perturbation theory module, called KIN3D, has also been integrated into ERANOS [98].

Cell or core burnup calculations are another ERANOS capability. This is particularly important in the context of core design and safety studies related to fuel burnup, since safety and reactivity parameters (Doppler effect, coolant void, delayed neutron fraction β_{eff}, etc.) are degraded with burnup. In ERANOS, the differential equations of evolution (Bateman equations, governing the isotopes evolution) are solved using the exponential resolution method, and a constant flux is assumed during the depletion time step, typically a few tens of days. To overcome this simplification, the flux is renormalized to keep the reactor power constant. Additionally the precision of the computation is improved by obtaining (with BISTRO or TGV/VARIANT) the flux solution corresponding to the new fuel composition, after a certain time step (typically, for every fuel batch). To further improve accuracy, the self-shielded macroscopic cross-sections are recalculated for the next burnup step. The new cell calculation makes it possible to take into account the changes in the self-shielding due to the evolution of the densities and corresponding change of spectrum. However, in the established computational scheme, this step is usually not performed, mainly because of the relatively minor corrections that it brings and also because of the additional CPU-time. More details on the burnup calculations, performed in the framework of the present thesis are provided in Appendix E.

One other feature worth mentioning here is the possibility in ERANOS to directly perform perturbation and sensitivity analysis [99]. The perturbation theory procedures are based on the use of the adjoint solutions of the reactor equation to approximate first-order derivatives of integral physical variables (k_{eff}, reaction rates, isotopic concentrations, reactivity coefficients, etc.) relative to the nuclear data library. Using the implemented modules, it is possible to calculate, using standard 1st-order, as well as exact and generalized, perturbation theory, the reactivity and sensitivity coefficients of neutronic systems. A representativity-coefficients calculation is another capability of the code, rendered possible using the sensitivity and perturbation modules. Perturbation theory has a wide range of applications, in particular the computation of reactivity coefficients needed for instance for point kinetics calculations. Sensitivity analysis (via the derivation of sensitivity coefficients *S,* which are vectors) allows one to study, in a systematic manner, the effects of the variation of basic parameters *P* (such as cross-sections, nuclear density, etc.) on an integral value *I* (e.g. effective multiplication factor k_{eff}, reaction rates, etc.). The main idea is to express:

$$\Delta I = \sum_i \frac{\partial I}{\partial P_I} \Delta P_i \qquad \text{Eq. 2.2}$$

$$S_I = \frac{\frac{\Delta I}{I}}{\frac{\Delta P_I}{P_I}} \qquad \text{Eq. 2.3}$$

One advantage of using linear perturbation theory is that the sensitivity coefficients are, in this particular case, independent of the perturbation and can be calculated quickly, compared to direct calculations involving “by-hand” changes to parameters of interest.

The sensitivity and perturbation package in ERANOS offers the possibility to calculate, based upon the formalism expressed by Eq. 2.3, the following:

- *Multiplication factor sensitivity*. The calculations are based on 1st-order perturbation theory.
- *Sensitivity of reaction rate ratios*. The calculations are based on generalized perturbation theory.

- *Reactivity coefficients sensitivity*. The calculations are based on “equivalent generalized perturbation theory” (EGPT).
- *Uncertainties (σ_I)*. In this case, the computation requires the sensitivity coefficients *S* (see Eq. 2.3) and a covariance matrix *D*, which is associated to the nuclear library. The methodology is based on linear perturbation theory [100]:

$$\sigma_I^2 = S^T \, D \, S \qquad \text{Eq. 2.4}$$

- *Representativity coefficient r_{RE}*. This parameter gives an indication of the similarity, from the nuclear data viewpoint, of a given parameter for two different situations: (1) the configuration in which experimental data are obtained and (2) the envisaged reactor. By relating the sensitivity vectors S_R for the reactor and S_E for the experiment (each expressed per energy group for the given parameter) to the covariance matrix *D* (containing nuclear data variances and covariances), it is possible to define an angle (scalar product) between the S_R and S_E vectors, relative to the metric defined by the matrix *D*:

$$r_{RE} = \frac{S_R^T D S_E}{\sqrt{(\mathrm{S}_\mathrm{R}^\mathrm{T} D S_R)(\mathrm{S}_\mathrm{E}^\mathrm{T} D S_E)}} \qquad \text{Eq. 2.5}$$

The value of r_{RE} lies between 0.0 and 1.0. The closer r_{RE} is to 1.0, the more representative is the experiment of the reactor conditions. In practical terms, the result for the r_{RE} factor is obtained in three steps:

(1) Assessment of nuclide-specific “integral sensitivities” on the basis of calculations of sensitivity coefficients S_I. Effectively, such a "relative" integral sensitivity is calculated as the square of an uncertainty, while assuming that the matrix *D* is unity,

(2) Determination of the uncertainty of *I* (due to nuclear data) using the covariance matrix *D*,

(3) Calculation of the representativity factor r_{RE}.

In summary, the parameter r_{RE} compares the sensitivity profiles of two different configurations and the closer to unity this is, the more similar can the two configurations be considered. Thus, if the first configuration is that in which experimental measurements have been carried out, and the second the studied reactor, the “transferability” of the experimental data to the system of interest is greatest for a r_{RE} value of 1.0

In Chapter 3, the representativity factors between integral data from the GCFR-PROTEUS experiments, the ETDR and the advance GFR will be presented.

2.5.3 Monte Carlo code: MCNPX

The stochastic code MCNPX version 2.5e [101; 102] has been used in the present research, mainly for the verification of certain reference cell calculations performed with the ERANOS code.

MCNPX (Monte Carlo N-Particle eXtended) is a general-purpose Monte Carlo radiation transport code for modelling the interactions of radiation with matter and is developed by Los Alamos [103; 104]. It is an extension of the capabilities of MCNP4C to nearly all particle types and to nearly all energies. It is capable of tracking 34 particle types (neutrons, protons, nucleons and light ions) and 2000 heavy ions at nearly all energies. It uses standard evaluated data libraries combined with physics models where experimental data are not available [103; 104]. MCNPX is written in FORTRAN90, supported on all UNIX, Linux and PC platforms, and can be multi-processed with PVM or MPI. The code has a wide application domain, which is rapidly growing mainly due to the increase of computational power and the cost reduction of high-performance computers.

In simple terms, a Monte Carlo code simulates the different types of interactions between atoms of a given medium and particles (neutrons in our case) injected into the system. Complex geometries can be treated explicitly, the system being modelled as a three-dimensional configuration of materials in geometric cells bounded by, usually, first- and second-degree surfaces. In neutronics calculations, continuous-energy neutron data libraries can be used [105], as basis for deciding statistically, with minimal loss of modelling accuracy, on the particular interactions taking place (capture, fission, scattering, etc.). To improve the problem convergence, a variety of variance reduction techniques are included, e.g. weight cut-off, geometry splitting, Russian roulette and weight windows.

An important justification for performing MCNPX calculations currently is the possibility of using, in its context, different modern nuclear data libraries, viz. JEF-2.2, JEFF-3.0, ENDF/B-VI.r8, and JENDL-3.3. These official libraries are made available to PSI by the OECD/NEA Nuclear Data Bank. Thus, through the use of the MCNPX code, in conjunction with these libraries, it has been possible to study the nuclear-data sensitivity of certain neutronics parameters of interest (mainly, infinite and effective multiplication factors, neutron balance components such as reaction rate ratios, etc.).

2.5.4 Thermal-hydraulics code: COPERNIC

COPERNIC is a thermal-hydraulics code developed at CEA to study, in a simplified manner, the thermal-hydraulics characteristics of the reactor core, as also the nuclear power plant system as a whole [106]. It allows the user to calculate, quickly using EXCEL sheets and Visual Basic for Applications (VBA) macros with implemented correlations (HTCs) and geometries, thermal-hydraulics parameters of interest for core and plant designers, e.g. the fuel or cladding temperature. The calculations are performed in the steady-state mode, using 1D elements to represent the core. Different heat transfer correlations are implemented for the heat transfer from the source (fuel) to the coolant. The code is essentially used for scoping calculations and the design phase, where rapidity of the calculations is most important.

In this thesis, COPERNIC has been used to calculate the maximal cladding temperature of the absorber pins constituting a CA. A model of a CA was developed in COPERNIC to compute the axial temperature distribution due to the nuclear reactions taking place within the core, mainly the (n,α) reaction in ^{10}B and inelastic scattering in ^{56}Fe in the case of a metallic wrapper/cladding.

The boundary conditions used by the code are the volumetric heat generation imposed as a function of the axial mesh, supposing an upward flow of helium at a given inlet temperature. Different heat transfer correlations and mass flow rates associated with different CAPs have been tested in order to determine, for a given coolant flow area (which should be minimized in order to maximize the B_4C fraction), the temperatures reached by the materials.

The investigations performed with COPERNIC, in conjunction with the neutronics constraints, are described in Chapter 4.

2.5.5 3D neutron-kinetics code: PARCS

PARCS (Purdue Advanced Reactor Core Simulator) is a 3D reactor core simulator which solves the steady-state and time-dependent, multi-group neutron diffusion and transport equations in orthogonal and non-orthogonal geometries (HEX-Z) [90]. The PARCS code was initially released in 1981 (v1.01) and since then, constant progress have been made, the current released version used in the FAST code system being the version 2.7, allowing both square and hexagonal geometry, as well as a multi-group cross-sections representation.

As shown in Section 2.5.1, the manner in which PARCS is integrated within the FAST code system implies that it is coupled directly to the TH system code TRACE, which provides the temperature and flow-field information needed during the steady-state and transient calculations, performed either in the point kinetics or spatial kinetics mode. Spatial kinetics calculations involve the solution of the eigenvalue problem and the time-dependent neutron transport equations. To solve these equations, it is necessary to discretize the balance equations in both time and space. For the temporal discretization, the theta-method with exponential transformation is employed in PARCS, along with a second-order analytic precursor integration technique. The temporal discretization scheme allows sufficiently large time-step sizes, even in very fast transients involving super-prompt critical reactivity insertion. For spatial discretization, the efficient nonlinear nodal method is employed, in which the coarse-mesh finite difference (CMFD) problems and the local two-node problems are repetitively solved during the course of the non-linear iteration.

A hexagonal, multigroup nodal diffusion kernel is implemented in PARCS, based on the Triangular Polynomial Expansion Method (TPEN) [107], an appropriate acceleration technique being applied to improve the convergence, and hence the computational efficiency. Other features of the code include the ability to perform xenon transient calculations, decay heat calculations, pin power calculations, and adjoint calculations for commercial LWRs. Realistic representation of the physical reactor is ensured using the 3D calculation model. However, various 1D modelling features are available as well, essentially to offer the possibility to perform faster simulations.

A restart option is also available in PARCS and helps to reduce the computational time. This option is used, for instance, to perform different transient analyses that are initiated at a certain time. The transient history before the new transient conditions can be, using the restart capability, simulated just once and the needed information stored in a file. Many edit options are available as well, allowing one to display different aspects of the calculation results.

Generally, advanced numerical methods have been implemented in the code to minimize the numerical complexity. In practice, a variety of kernels for spatial discretization are available, including the two-group nodal methods ANM [108] and NEM. The solution of the Coarse Mesh Finite Difference (CMFD) linear system is obtained using a Krylov subspace method which utilizes a pre-conditioner [109]. Additionally, the eigenvalue calculation to establish the initial steady-state is performed using the Wielandt eigenvalue shift method [110].

In PARCS, the original cross-section parameterisation was developed for LWR applications, and this has been reviewed for fast-spectrum system analysis. In particular, the dominant reactivity feedback effects in LWR transients are the Doppler effect and the change in coolant (moderator) density or void, while in fast-spectrum systems, partly because of the relatively smaller magnitude of these, other feedback effects are of equal importance, e.g. fuel and core structure thermal expansion, which changes both the core dimensions and the effective fuel density, influencing the neutron leakage and core reactivity. As a consequence, the original LWR PARCS model uses the following procedure for re-calculating macroscopic cross-sections:

$$\Sigma(T_{Fuel}, \rho_M, T_M, B) = \Sigma_0 + \left[\frac{\partial\Sigma}{\partial Z}\right]_{Z_0}(Z - Z_0) + \left[\frac{\partial\Sigma}{\partial\sqrt{T_{Fuel}}}\right]_{T_{Fo}}\left(\sqrt{T_{Fuel}} - \sqrt{T_{Fuel,0}}\right)$$

$$+ \left[\frac{\partial\Sigma}{\partial\rho_M}\right]_{\rho_{M,0}}\left(\rho_M - \rho_{M,0}\right) + \left[\frac{\partial\Sigma}{\partial T_M}\right]_{T_{M,0}}\left(T_M - T_{M,0}\right) + \left[\frac{\partial\Sigma}{\partial B}\right]_{B_0}(B - B_0) \qquad \text{Eq. 2.6}$$

where Σ is the macroscopic cross-section, Z the control rod position, T_{fuel} the fuel temperature, ρ_M the moderator density, T_M the moderator temperature and B the boron concentration. The subscript ‘‘0’’ refers to reference conditions.

A simple way to functionalize the cross-sections for fast-spectrum systems, in order to additionally take into account the dependence of cross-sections on fuel temperature and core expansion effects, is:

$$\Sigma(T_{Fuel}, \rho_C, \mathrm{R}, H) = \Sigma_0 + \left[\frac{\partial\Sigma}{\partial Z}\right]_{Z_0}(Z - Z_0) + \left[\frac{\partial\Sigma}{\partial \ln T_{Fuel}}\right]_{T_{Fo}}\left(\ln T_{Fuel} - \ln T_{Fuel,0}\right)$$

$$+ \left[\frac{\partial\Sigma}{\partial\rho_C}\right]_{\rho_{C,0}}\left(\rho_C - \rho_{\mathrm{C},0}\right) + \left[\frac{\partial\Sigma}{\partial \mathrm{R}}\right]_{\mathrm{R}_0}(\mathrm{R} - R_0) + \left[\frac{\partial\Sigma}{\partial H}\right]_{H_0}(H - H_0) \qquad \text{Eq. 2.7}$$

where ρ_C is the coolant density, *R* the average core radius and *H* the average core height. Eq. 2.7 represents the current status of cross-section parameterisation as used in the PARCS code.

PARCS makes use of macroscopic cross-sections (typically in 33 groups) which have to be separately calculated and introduced as input parameters. The self-shielded macroscopic cross-sections and their derivatives with respect to state variables, i.e. the fuel temperature T_f, coolant density ρ_c, and thermal radial δ_r and axial expansions δ_z, were produced using the cell code ECCO in association with homogeneous cells and the adjusted neutron data library ERALIB1 [97]. They were then transferred to PARCS, using for this purpose a specially developed, in-house routine ERANOS2PARCS [111] to convert the cross-section format in an appropriate manner. The data format is schematically represented in Figure 2.15. This scheme has to be repeated for each different material zone of the GFR core. Complementarily, the kinetics parameters, i.e. the delayed neutron fraction of the i^th^ group β_i, the decay constant of the i^th^ group λ_i and the delayed-neutron fission spectrum, have to be provided in the input deck using the appropriate format for each neutron group. These are also prepared by ERANOS.

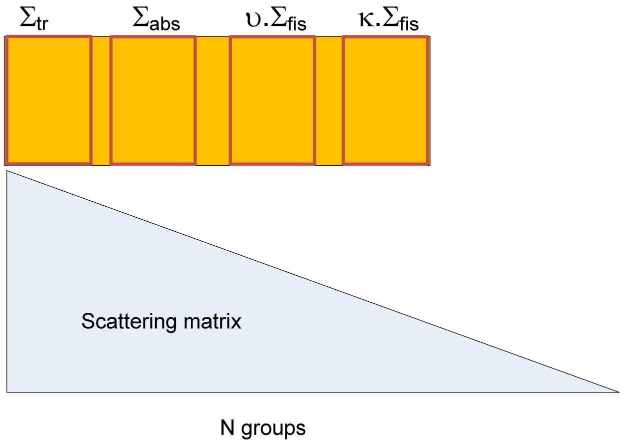

Figure 2.15 Schematic of the macroscopic cross-section structure, given as input to PARCS for each material zone

2.5.6 Thermal-hydraulics code: TRACE

TRACE (TRAC/RELAP Advanced Computational Engine) [92] is the latest in a series of best-estimate reactor systems codes developed by the U.S. Nuclear Regulatory Commission (NRC) for analyzing steady-state and transient neutronics/thermal-hydraulics behavior, originally for LWRs. TRACE integrates, in the current version, the combined capabilities of the NRC's four main system codes (TRAC-P, TRAC-B, RELAP5 and RAMONA). TRACE has been designed to perform best-estimate analysis of LOCAs, operational transients, and other accident scenarios in LWRs. It can also model phenomena occurring in experimental facilities designed to simulate transients in reactor systems.

The models used mainly include 1D two-phase flow, non-equilibrium thermo-dynamics, generalized heat transfer, re-flood, level tracking, and reactor kinetics. For each phase of the fluid, the classical three thermal-hydraulics equations are solved by advanced numerical methods [112]. The 3 equations are: (1) the energy conservation, (2) the momentum conservation and (3) the mass conservation. Automatic steady-state and dump/restart capabilities are also provided to reduce the computation time. The partial differential equations that describe two-phase flow and heat transfer are solved using finite-volume numerical methods. The heat-transfer equations are evaluated using a semi-implicit time-differencing technique. The fluid-dynamics equations in the spatial one-dimensional (1D), two-dimensional (2D), and three-dimensional (3D) components use, by default, a multi-step time-differencing procedure that allows the material Courant-limit to be exceeded.

The TRACE code is used in this thesis for the dynamic analysis of CA driven transients in the large Generation IV GFR. The physical fluid properties built into the code include correlations for the following:

(1) light water,
(2) heavy water,
(3) helium,
(4) air,
(5) CO_2,
(6) lead-bismuth,
(7) sodium.

TRACE takes a component-based approach to modeling a reactor system. Each physical piece of equipment in a flow loop can be represented as some type of component (pipe, T-junction, heat-structure, etc.) and each component can be further nodalized into a certain number of physical volumes (called cells), over which the fluid, conduction and kinetics equations are averaged. The number of reactor components in the problem and the manner in which they are coupled are arbitrary, which provides a high flexibility to the code. There is no built-in limit on the number of components or volumes that can be modeled; the size of a problem is theoretically limited only by the available computer memory.

Reactor hydraulic components in TRACE include [92]:

(1) PIPEs,
(2) PLENUMs,
(3) PRIZERs (pressurizers),
(4) CHANs (BWR fuel channels),
(5) PUMPs,
(6) JETPs (jet pumps),
(7) SEPDs (separators),
(8) TEEs, TURBs (turbines),
(9) HEATRs (feed water heaters),
(10) CONTANs (containment),
(11) VALVEs,
(12) VESSELs (with associated internals),
(13) HTSTR (heat structure) and REPEAT-HTSTR components modeling fuel elements or heated walls in the reactor system are available to compute 2D conduction and surface-convection heat transfer in Cartesian or cylindrical geometries.
(14) POWER components are available as a means for delivering energy to the fluid via the HTSTR or hydraulic component walls.
(15) FLPOWER (fluid power) components are capable of delivering energy directly to the fluid.
(16) RADENC (radiation enclosure) components may be used to simulate radiation heat transfer between multiple arbitrary surfaces. FILL and BREAK components are used to apply the desired coolant-flow and pressure boundary conditions, respectively, on the reactor system to perform steady-state and transient calculations.

(17) EXTERIOR components are available to facilitate the development of input models designed to exploit TRACE's parallel-execution features.

The code's computer execution time is highly problem dependent and is a function of the total number of mesh cells, the maximum allowable time-step size, and the rate of change of the neutronics and thermal-hydraulics phenomena being evaluated. The stability-enhancing, two-step (SETS) numerics for hydraulic components allows the material Courant-limit to be exceeded. This allows very large time steps to be used for slow transients. This, in turn, can lead to significant speedups in simulations (one or two orders of magnitude) of slow-developing accidents and operational transients.

The complete GFR core TH model developed and used in the present research is schematically represented in Figure 2.16. The hydraulic components used (see Figure 2.17) are described below in more detail. 0D and 1D components have been used for the modelling and, as a direct consequence, only the core has been explicitly modelled (i.e. not the primary and secondary circuits).

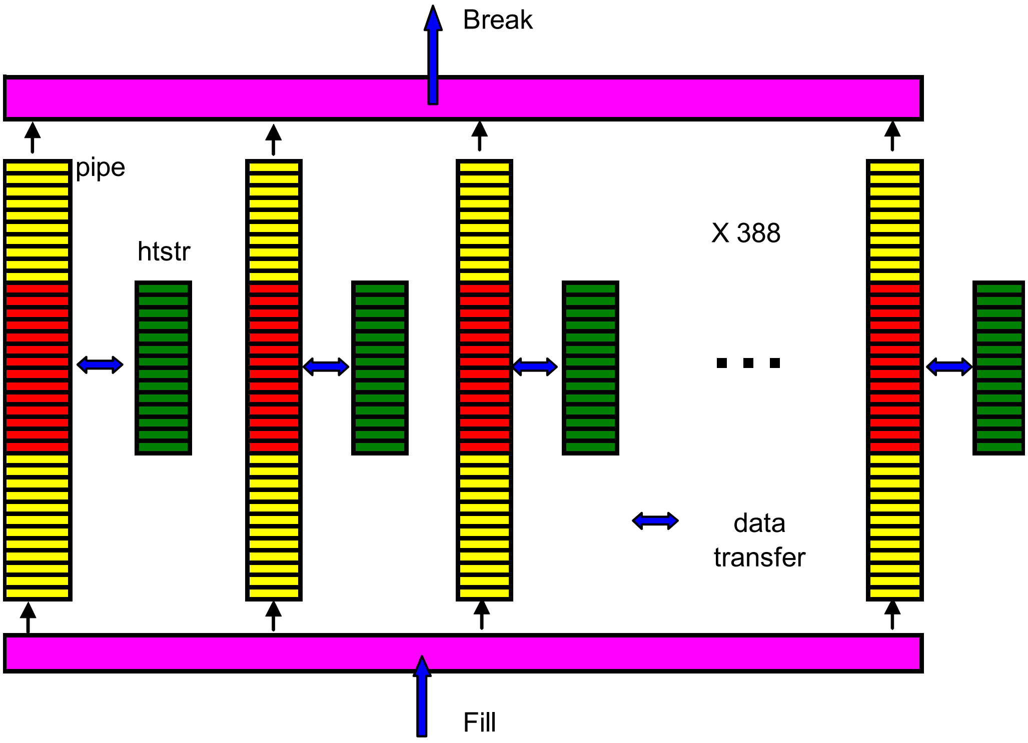

Figure 2.16 Schematic of the TRACE model of the GFR

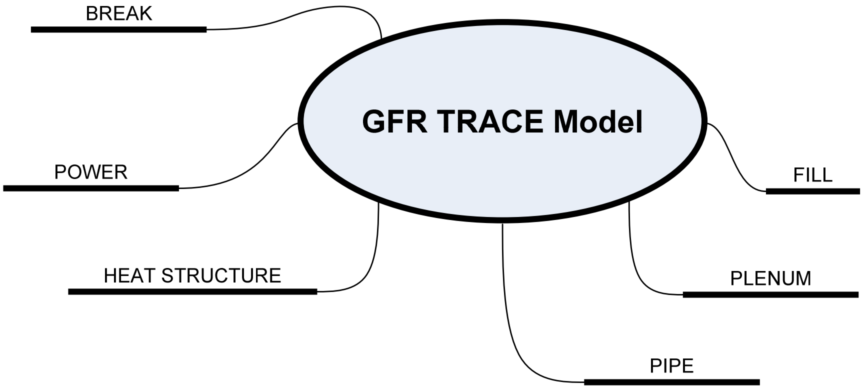

Figure 2.17 Schematic view of the hydraulic components used in TRACE to implement the GFR core model

The TRACE components used are described below:

FILL

The core model starts with a FILL component, which is used to impose the inlet boundary conditions, i.e., the helium mass flow rate and the inlet temperature. The component is used in connection with a 1D pipe.

BREAK

On the outlet side of the core model, the coolant pressure is imposed in the upper plenum by means of a break component.

PLENUM

A PLENUM component consists of a single 0D hydraulic cell with an unlimited number of connections to 1D hydraulic components. The PLENUM component allows one to transport the momentum across the cell from one side to the other.

PIPE

A PIPE component is used to model the flow of fluid in a 1D element, e.g. a duct, a channel or a pipe. The PIPES can be linked to a FILL or a BREAK component, which is precisely the manner adopted here. In the GFR, the pipes are used to model the helium channels between the fuel plates and are all connected together to a lower and an upper plenum. To improve the accuracy of the results, a PIPE component can be subdivided into smaller volumes, called cells, for which the solutions are computed. The results are provided in the output file and include, for each cell of the PIPE, the pressure, coolant temperature, liquid and gas temperatures, material densities, velocities and Reynolds number. The total power transferred to the pipe, from the connected HEAT STRUCTURE components, is also calculated.

HEAT STRUCTURE

The heat generation resulting from nuclear fission is calculated and imposed externally by the POWER component. The core region producing the heat, e.g. fuel, has to be modelled in

TRACE using the HEAT STRUCTURE (HTSTR) component. This 2D component calculates, in either cylindrical (RZ) or Cartesian (x,z) geometry, the heat transfer by conduction, convection or radiation in a fuel element, which in the present research corresponds to slab geometry. This is accordingly the geometry in which TRACE currently solves the heat-conduction equation:

$$\frac{\partial(\rho c_p \cdot T)}{\partial t} + \nabla \cdot \vec{q} = q''' \qquad \text{Eq. 2.8}$$

where ρ is the density, c_p the specific heat of the material, T the temperature, $\vec{q}$ the heat flux vector, and q''' the heat generation rate per unit volume.

The above equation can be simplified by replacing the heat flux vector $\vec{q}$ with the temperature gradient ∇T (Fourier's law of conduction):

$$\vec{q} = -k\nabla T \qquad \text{Eq. 2.9}$$

where k stands for the thermal conductivity of the material.

Substituting Eq. 2.9 in Eq. 2.8, one gets:

$$\rho c_p \frac{\partial T}{\partial t} = \nabla \cdot (k\nabla T) + q''' \qquad \text{Eq. 2.10}$$

Within the HTSTR component, the fuel-cladding gap conductance is of particular importance. Specific routines of TRACE calculate the conductance. Physically, the temperatures obtained are dependent on the gas thermal properties, in particular the thermal conductivity *k* and the roughness of the plates.

In TRACE, the gas gap conductance can be calculated by two different options: (1) a constant gas gap conductance during the duration of the transient and (2) a value which is recalculated during the transient allowing one to take into account the thermal expansion of the fuel during the duration of the transient. The latter option was used in the thesis.

Finally, the HTSTR is linked to a hydraulic component, in the present case, to a pipe. The HTSTR represents the fuel plate, while the helium channels surrounding the fuel plate are modelled by the pipes. The heat exchange coefficients and the temperature fields are calculated by the TRACE thermal-hydraulics solution for the coolant. Later, in Chapter 5, the two different mappings, of the heat structures and of the pipes, to the neutronics nodes will be presented in detail.

A fuel SA is modelled, assuming 27 plates within the SA, by 54 half-plates (thanks to the symmetry) and 27 pipes (see Section 4.2.1), the whole being regrouped in one HTSTR linked to PIPE components. All the HTSTRs and the PIPEs are linked together using junctions to a lower and upper plenum.

More details about the SA model and the numerical methods used to solve the conductance equation are provided in Chapter 5.

POWER

The fission reaction in the core generates energy inside the fuel that has to be correctly calculated and transferred to the different component of the system. This energy is transferred to the primary fluid and reaches the secondary fluid, if any. The code has to calculate the heat conduction in the fuel to correctly simulate the heat-transfer processes involved in the thermal-energy transport.

In TRACE, the energy distribution is specified with a POWER component. Specifically, for a transient calculation, the core power can be imposed (e.g. by using a power table) or the code itself calculates the power solving the point-kinetics equations. The power can also be calculated in PARCS using the spatial-kinetics mode.

Chapter 3

3 Validation of computational tools

This chapter provides an overview of certain relevant results concerning neutronic investigations performed in the context of the GCFR-PROTEUS experimental program. The following aspects are addressed in this chapter:

1. Motivation and procedural steps for the re-analysis of the experimental data (see Section 3.1)
2. Brief description of the GCFR-PROTEUS experimental program (see Section 3.2)
3. Validation of the ERANOS cell calculations against GCFR-PROTEUS data and MCNPX calculations (see Section 3.3)
4. Investigation of the effects of ERANOS data-library adjustments on k_∞ of the GCFR-PROTEUS reference lattice (see Section 3.4)
5. Transferability of the data to advanced GFR reactor concepts (see Section 3.5)
6. Conclusions and recommendations (see Section 3.6)

Supplementary investigations are presented in Appendix B.

Some of the investigations were reported at the PHYSOR'2006 conference [113] and in PSI internal reports [114; 115; 116].

3.1 Motivation and procedural steps

As mentioned earlier, the deterministic fast system code ERANOS-2.0 was developed within an international collaboration in order to create a numerical tool for analysis of fast-spectrum reactors, mainly Na-cooled systems operating with MOX fuel. The neutron cross-section library ERALIB1, which is derived from the JEF-2.2 nuclear data evaluation, has been adjusted based upon integral measurements obtained in many different systems but essentially in sodium-cooled systems [97]. The reference GFR studied in this thesis is not a sodium-cooled system fuelled with MOX and, therefore, the GFR spectrum is not really comprised within the validation domain of ERANOS. The performance of ERANOS-2.0/ERALIB1 needs to be evaluated in this context, since the first legitimate question is as to whether neutronics analysis related to the characterisation and development of the GFR can be reliably performed using the ERANOS-2.0/ERALIB1 code, or whether other computational schemes linked to other nuclear data libraries have to be found.

To address the validity of the computational schemes in ERANOS with the adjusted ERALIB1 data library, called here the "reference calculational route", use has been made of the integral data obtained at PSI during the GCFR-PROTEUS experimental program.

As a first step, the literature concerning this program was reviewed and sorted according to the relevance as regards the GFR, as also the completeness of the data. After a certain selection phase, one particular PROTEUS core configuration of the program (GCFR-PROTEUS Core 3) was selected for re-analysis. In a second step, the reference test lattice investigated in this reactor configuration was re-analyzed with the ERANOS code. The calculational results (for the integral reaction rate ratios measured in the centre of the test lattice) were essentially obtained with the ECCO cell code, which is part of the ERANOS code system. Sensitivity studies of reaction rate ratios, as a function of (1) the nuclear data adjustment (ERALIB1) and (2) the computational options, were also performed in detail, essentially to derive a reference scheme for the calculations.

In order to explain the library-dependent differences, i.e. between the ERANOS-2.0/ERALIB1 and ERANOS-2.0/JECCOLIB2 results, generalized perturbation theory was applied to decompose the reactivity effects in terms of isotopes, energy groups and reactions. Afterwards, Monte Carlo simulations with different modern nuclear data libraries were performed, first to compare the results obtained with the deterministic code and then to compare with the experimental values. Following this analysis, additional investigations were carried out to evaluate the representativity of the data with respect to three Generation IV-type gas-cooled fast-spectrum systems, namely the MOX start-up core of the ETDR, the reference GFR and the CAPRA-CADRA core using MOX fuel and CO_2 coolant. The representativity analysis allows to situate the GCFR-PROTEUS program in a larger context and to draw recommendations about the potential use of the data.

Finally, it should be mentioned that an important aspect of the present re-analysis of these earlier experiments is that of knowledge preservation.

3.2 The experimental program at PROTEUS

The experiments were carried out between April 1972 and April 1979. The measurements were used to examine the adequacy of the then-current calculational methods and related nuclear data libraries for the design of gas-cooled fast breeder reactors, with the final aim of trying to meet the target accuracy for predicting the multiplication factor and the breeding gain.

The overall PROTEUS reactor core configuration was designed to be highly flexible and to offer the possibility to test different fuels and lattices in its central, fast-spectrum test zone [50]. The composition and geometry of the fast reactor lattices investigated in the test zone were chosen to be typical of gas-cooled fast breeders, and it was the first time that a dedicated fuel with high plutonium content in the form of rods was employed, enabling the investigation of streaming effects in a representative manner.

The experimental program was divided into two phases. In the first phase, the fuel consisted of 6.7 mm diameter pellets of typical fast breeder reactor fuel, $(U,Pu)O_2$ containing 15% Pu, the fissile Pu fractional content being 82%. In the second phase, a series of test zone configurations was employed to investigate the characteristics of thorium-based fast breeders, e.g. a test lattice in which one third of the $(U,Pu)O_2$ rods were replaced by ThO_2 rods in order to provide benchmark results for thorium reaction rates.

A complete description of the two phases and the corresponding core configurations are presented in Appendix B, Sections B.1 and B.2, describing the first and second phase, respectively.

3.2.1 Reactor description

The central test zone in each of the zero-power, GCFR-PROTEUS reactor configurations was surrounded by two thermal-driver regions, viz. a D_2O-driver and a C-driver (with C-reflector), in order to drive the reactor critical. A natural-U buffer region was located between the fast and thermal zones An overall view of the PROTEUS reactor, essentially cylindrical in shape, is presented in Figure 3.1, while Figure 3.2 and Figure 3.3 give horizontal and vertical cross-sectional views [50; 54].

The dry (unmoderated) buffer zone, consisting of natural U-metal rods and positioned between the fast and thermal spectrum regions, served to modify the thermal neutron flux emerging from the driver regions and entering the test zone. As a result, the neutron spectrum in the central part of the test lattice was very close to that in a critical reactor with the same composition. The primary function of the buffer was to effectively generate fast fission neutrons from thermal neutrons originating in the D_2O- and C-driver regions.

The full experimental program consisted of 16 individual configurations [54; 117; 118; 119; 120; 121; 122]. For completeness, each of these is described briefly in Appendix B. The reference GCFR-PROTEUS test lattice, which is the main object of the current detailed analysis, was installed with the finally chosen buffer zone (natural-U metal rods) in the third reactor configuration (Core 3). This is described in greater detail in the following subsection.

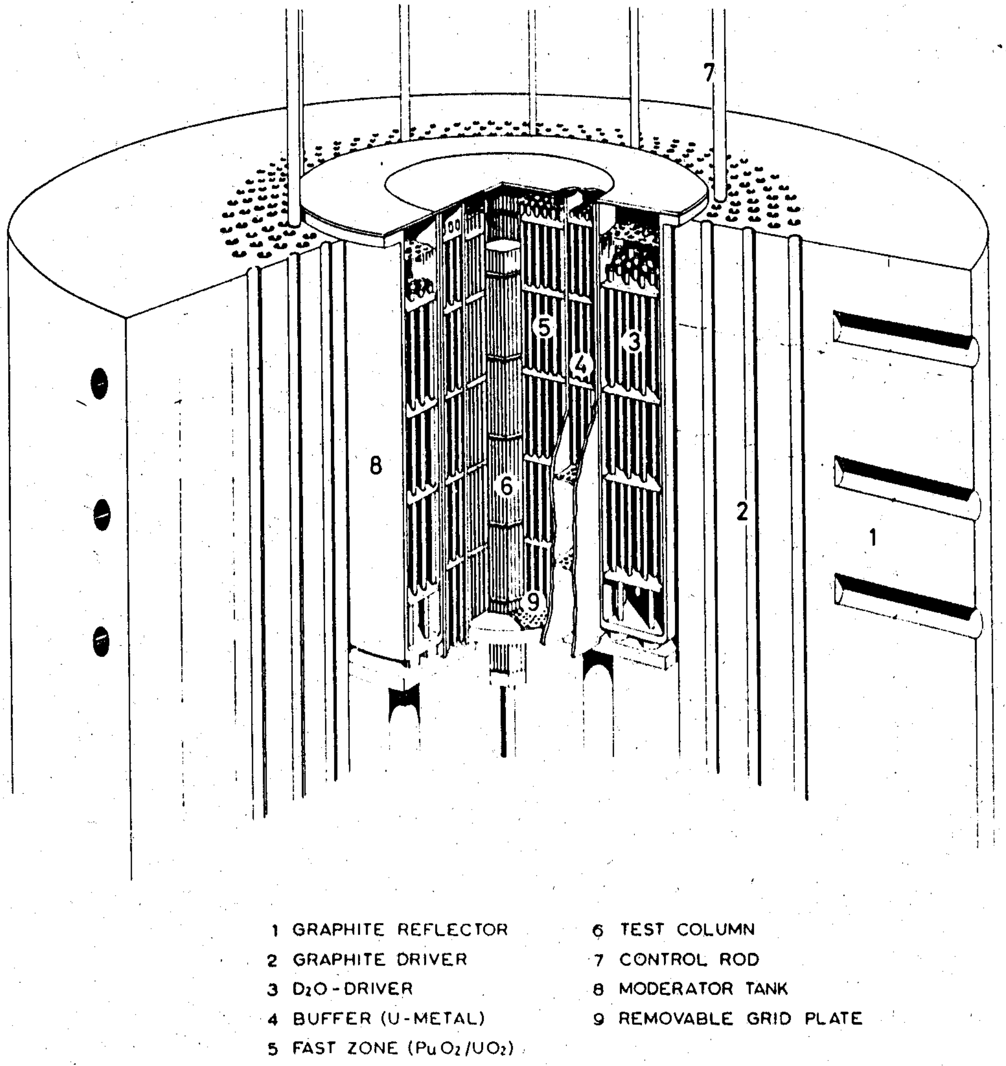

Figure 3.1 A general view of the multizone, zero-power facility PROTEUS at PSI

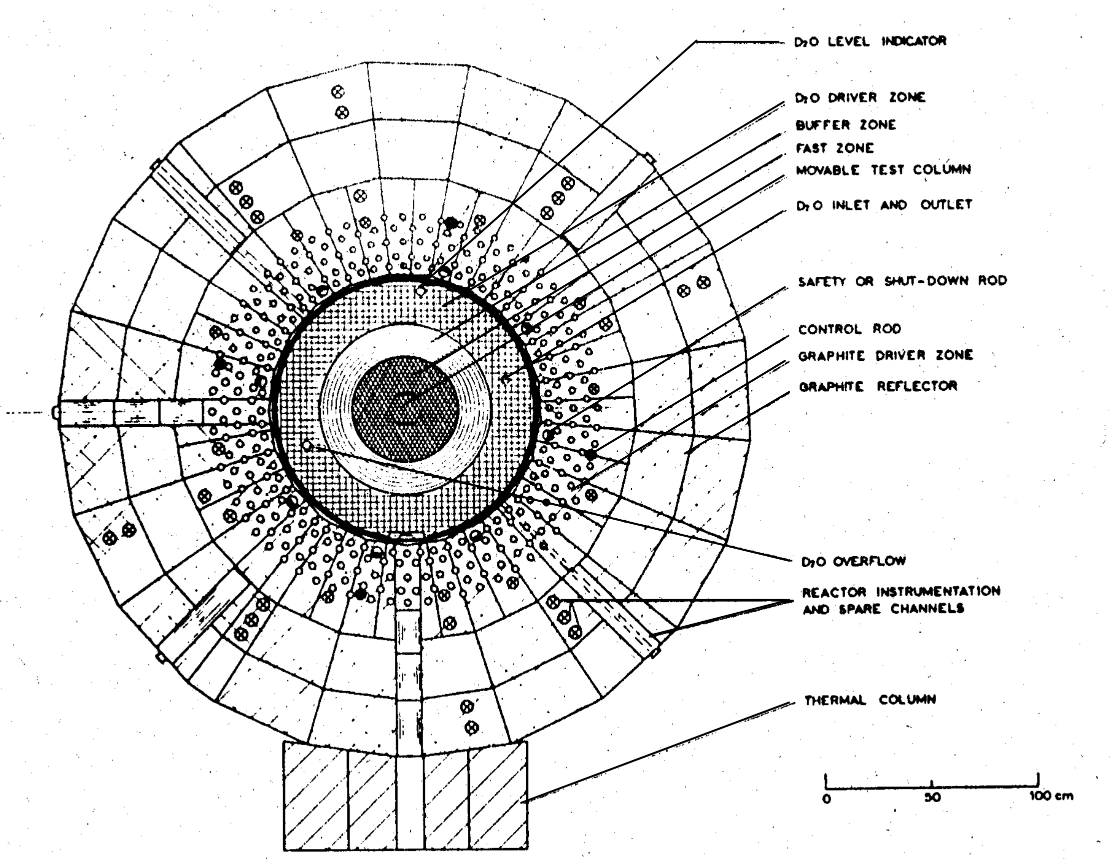

Figure 3.2 Horizontal cross-sectional view of the PROTEUS reactor

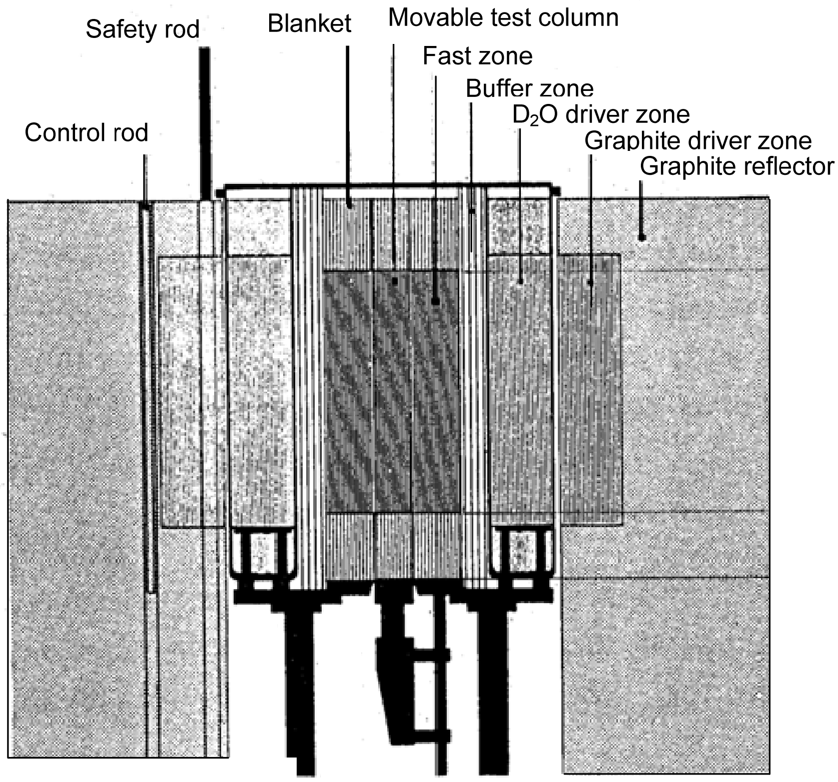

Figure 3.3 Vertical cross-sectional view of the PROTEUS Reactor

3.2.2 GCFR-PROTEUS Core 3

The central fast zone, i.e. the test lattice in which the measurements took place, had a diameter of 50 cm and contained over 2000 fuel rods arranged in a lattice of 10 mm hexagonal pitch [123]. The central part of the test zone was a hexagonal column of 13 cm across flats, which could be moved in and out of the core (see index 6 in Figure 3.1).

The $(U,Pu)O_2$ fuel pellets, containing 15% Pu with a fissile fraction of 82%, were put into thin aluminum “cigars”, before being loaded into steel cladding tubes with an outer diameter of 8.2 mm. The active fuel height was 88.9 cm and the total rod height was 140 cm (including 22.7 cm of top and bottom depleted UO_2-pellet regions).

In the first two GCFR-PROTEUS configurations, the 10 cm thick, buffer zone consisted of closely packed natural-UO_2 rods. This was not found to be the optimal buffer material and starting from Core 3 (containing the reference test lattice), the buffer was a zone of tightly packed natural-U metal rods, each 2.2 cm in diameter and 150 cm long [99]. There were 398 U-metal rods (fuel density: 18.96 $g.cm^{-3}$) in the buffer.

The D_2O-driver region was 17 cm thick. The fuel rods were of the same type as used for the C-driver (see below) and were arranged in a square pitch of 6 cm.

The outer PROTEUS graphite block is ring-shaped with a mean inner diameter of 125 cm, a mean outer diameter of 326 cm and a height of 318 cm. In the GCFR-PROTEUS experiments, it contained the C-driver and also provided the function of reflector. Furthermore, the reactor safety, shutdown and control rods are all located in the outer graphite block. A large number of UO_2 fuel rods (~300), with an enrichment of 5% and a diameter of 10 mm, were inserted into the graphite driver, up to an outer radius of ~90 cm (see Figure 3.2). As can be seen in Figure 3.3, there was an axial blanket in the central core region, above and below the fast zone. The fuel and axial blanket materials are described in Table 3.1.

Table 3.1 Description of the fuel and axial blanket materials, each clad in stainless steel

Parameter	Fuel $(U,Pu)O_2$	Blanket UO_2
Pu/(U+Pu), w-%	14.96	-
^{240}Pu/Pu, w-%	17.69	-
^{241}Pu/Pu, w-%	2.15	-
^{235}U/U, w-%	0.42	0.42
Density, g.cm^{-3}	10.60	10.50
Pellet diameter, mm	6.70	6.70
Pellet length, mm	6.90	7.10
Cigar can material	Al	Al
Cigar wall thickness, mm	0.09	0.09
Fuel heigth in cigar, mm	55.40	56.90

3.2.3 Reference MOX fuel cell and experimental results

The cell calculations presented in this chapter were performed based upon the hexagonal reference fuel cell, corresponding to the reference GCFR-PROTEUS test lattice occupying the test zone in Core 3 of the program. This unit cell is depicted in Figure 3.4. Due to its simplicity, no further geometrical simplification has been required. The material specifications can be found in Appendix B.4. The fuel cell model described here was used consistently, i.e. for the calculations with both ERANOS-2.0 and MCNPX-2.5e.

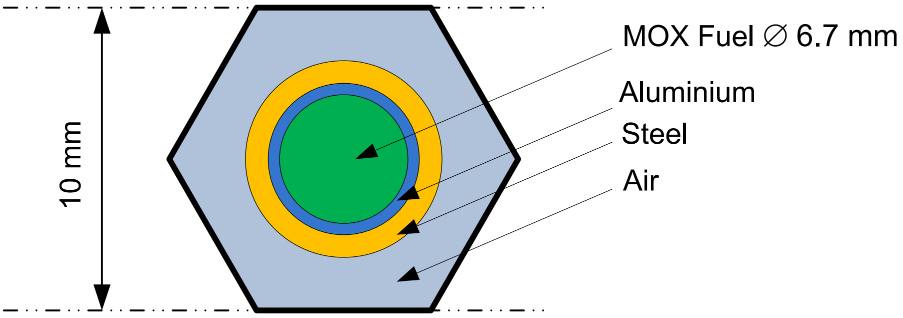

Figure 3.4 Schematic of the MOX fuel cell representing the reference test lattice of GCFR-PROTEUS Core 3

The main experimental investigations carried out in the centre of the GCFR-PROTEUS reference test lattice were:

- The neutron spectrum, measured by the proton-recoil technique; these results are not considered explicitly in the current validation study.
- As neutron balance components[1], the integral reaction rate ratios C8/F9, F8/F9 and F5/F9, i.e. the capture and fission rate in ^{238}U (C8 and F8) and the fission rate in ^{235}U (F5), each expressed relative to the fission rate in ^{239}Pu (F9),
- As spectral indices[2] relevant to certain investigations carried out later in the GCFR-PROTEUS program, the integral reaction rate ratios C2/F9, F2/F9, C7/F9, F7/F9 and F3/F9, where the numerators here denote the infinite-dilution capture and fission rates in ^{232}Th (C2 and F2), the capture and fission rates in ^{237}Np (C7 and F7) and the fission rate in ^{233}U (F3).
- Also measured as spectral index was the (n,2n)2/C2 ratio, where (n,2n)2 denotes the infinite-dilution (n,2n) reaction rate in ^{232}Th. This particular spectral index was the only one which, for reasons related to experimental accuracy, was not measured relative to the ^{239}Pu fission rate in the MOX, the numerator and denominator in this case being both infinite-dilution reaction rates in ^{232}Th.

All reaction rate ratios were measured applying appropriate foil activation techniques [124], in conjunction with the use of calibrated fission chambers (for the fission rates).

In order to be able to directly compare the experimental data with the results of fundamental-mode lattice calculations, the experimental values have been corrected by means of correction factors quantifying the influence of the outer PROTEUS regions on the neutron

---

[1] implying that the reactions represented in the numerator and denominator actually contribute to the neutron balance in the lattice.

[2] implying that, here, the nuclide represented in the numerator does not actually occur in the lattice, so that the parameter is simply being used to characterize the corresponding infinite-dilution cross-section, averaged over the given spectrum.

spectrum at the centre of the test zone. The measured experimental reaction rate ratios are provided in Table 3.2.

The correction factor, for a given reaction rate ratio, is defined as the ratio of the reaction rate ratio value obtained from whole-reactor PROTEUS calculations (i.e. calculations for the full, multizone PROTEUS configuration) and that obtained from fundamental-mode calculations (i.e. single-zone critical, cell calculations for the reference lattice):

$$C_{corr} = \frac{\text{Reaction rate ratio}_{\text{whole-reactor calculation}}}{\text{Reaction rate ratio}_{\text{cell calculation}}} \qquad \text{Eq. 3.1}$$

The corrections factors are applied to the measured experimental values ($E_{measured}$) in order to obtain adjusted experimental values ($E_{adjusted}$):

$$E_{adjusted} = \frac{E_{measured}}{C_{corr}} \qquad \text{Eq. 3.2}$$

The cell calculations performed in the framework of this study can be compared to the adjusted experimental values obtained after applying the provided correction factors. This procedure is rather unusual since, nowadays, one generally corrects, by convention, the calculated values. We have chosen, in this analysis, exactly the same way as was originally presented in the literature, i.e. to correct the experimental values.

The original analysis was based on cell calculations performed with a fine neutron energy group structure in association with nuclear data obtained from the UK Nuclear Data Library (FGL 4). This library was established for use with the collision-probability lattice code MURAL [54; 125].

As mentioned above, the correction factors given in Table 3.2, and used in the current study, have been taken directly from the available literature [54; 117; 118]. The second-last column of the table, which gives the 1σ experimental uncertainty in each case, is the propagated value combining the measurement errors and the uncertainty on the correction factor. In order to compare the performance of the new calculations, which will be presented in Section 3.3, with those performed during the original project, the relative deviations between calculation (C) and adjusted experiment (E), as obtained from [54], are also presented in Table 3.2 (last column).

Table 3.2 Measured (unadjusted) reaction rate ratios, correction factors, the propagated 1σ experimental uncertainty and, in the last column, the relative deviation of the original MURAL-calculated reaction rate ratio (C-value) from the adjusted experimental result (E-value).

Ratio	Experimental value	Correction factor	1σ, %	(C-E)/E, %
C8/F9	0.13270 ± 1.1 %	0.994 ± 0.5 %	1.2	-1.1
F8/F9	0.03111 ± 1.3 %	0.974 ± 0.5 %	1.4	-3.7
F5/F9	1.0100 ± 1.4 %	1.004 ± 0.5 %	1.5	1.9
C2/F9	0.2000 ± 1.3 %	1.022 ± 0.5 %	1.4	-2.8
F2/F9	8.061E-03 ± 2.0 %	0.979 ± 0.5 %	2.1	-11.2
F3/F9	1.5190 ± 1.3 %	1.027 ± 0.5 %	1.4	-1.0
(n,2n)2/C2	6.840E-03 ± 2.5 %	0.973 ± 0.5 %	2.6	1.9
C7/F9	0.8260 ± 2.3 %	1.020 ± 1 %	2.5	10.2
F7/F9	0.2270 ± 1.8 %	0.975 ± 1 %	2.1	-1.7

3.3 Validation of ERANOS results against experiment and MCNPX simulations

All the measured reaction rate ratios (C8/F9, F8/F9, F5/F9, C2/F9, F2/F9, (n,2n)2/C2, F3/F9, C7/F9 and F7/F9) have been calculated using the established ECCO and MCNPX Reference Computational Schemes (RCSs) and have been compared to the adjusted experimental values. For the sake of clarity, the investigations performed in order to derive the RCS (both for ECCO and MCNPX) are presented, together with the related sensitivity studies, in Appendix B, Section B.3.

In Table 3.3, four cases are considered for the ERANOS/ECCO calculations. These combine the use of two nuclear data libraries, viz. ERALIB1 and JECCOLIB2, with two different treatments of the self-shielding, viz. a reference route (calculated in the fine-group structure using the sub-group method) and a design route (calculated in the broad-group energy structure):

(1) ERALIB1 library and reference route,
(2) ERALIB1 library and design route,
(3) JECCOLIB2 library and reference route,
(4) JECCOLIB2 library and design route.

Table 3.4 presents MCNPX results, the different cases corresponding to the full range of continuous-energy data libraries used currently in conjunction with the Monte Carlo code (see Section 3.3.2). In both Table 3.3 and Table 3.4, the results are presented in the form of C/E-values.

For the sake of easier comparisons, Table 3.5 provides the relative deviations of the reaction rate ratios for all the considered cases, i.e. as (C-E)/E, obtained with both ECCO and MCNPX. In this table, out-of-range values (where the discrepancy is 3σ or more) are displayed in red, the first column indicating the corresponding 1σ experimental uncertainty. The second column gives the relative deviations of the original calculations (OC), i.e. with MURAL/FGL4 [54].

For the sake of completeness, Table 3.3 and Table 3.4 also give, at the bottom of each column, the corresponding calculated k_∞–value for the infinite-lattice cell, even though there is no direct experimental information available for this parameter. In each case, k_∞ was calculated by setting mirror boundary conditions, i.e. the ECCO calculations were performed by setting the buckling value to zero.

Table 3.3 C/E-values for the measured reaction rate ratios, and calculated k_∞-values, obtained using ECCO with the 4 defined computational options: (1) Reference route and ERALIB1, (2) Design route and ERALIB1, (3) Reference route and JECCOLIB2, and (4) Design route and JECCOLIB2. Relative changes in the C/E-values are given with respect to the Reference route and ERALIB1 values (1st column).

	Reference, ERALIB1	**Design, ERALIB1**		**Reference, JECCOLIB2**		**Design, JECCOLIB2**	
Ratios	**C/E**	**C/E**	**Rel. change, %**	**C/E**	**Rel. change, %**	**C/E**	**Rel. change, %**
C8/F9	0.996	0.992	-0.33	1.004	0.85	1.001	0.52
F8/F9	1.011	1.012	0.09	1.040	2.94	1.041	3.04
F5/F9	0.998	0.998	-0.03	1.013	1.45	1.013	1.42
C2/F9	0.959	0.959	0.07	0.970	1.23	0.971	1.30
F2/F9	0.964	0.964	0.04	0.979	1.60	0.979	1.64
(n,2n)2/C2	0.990	0.990	-0.02	0.998	0.81	0.998	0.79
F3/F9	1.004	1.003	-0.05	1.013	0.93	1.013	0.89
C7/F9	0.947	0.948	0.06	0.959	1.27	0.960	1.33
F7/F9	0.954	0.960	0.60	0.958	0.44	0.964	1.06
	C-value	C-value		C-value		C-value	
k_∞	1.3591	1.3610	0.15	1.3516	-0.55	1.3536	-0.40

Table 3.4 C/E-values for the measured reaction rate ratios, and calculated k_∞-values, obtained with MCNPX and the 4 different nuclear libraries described in Section 3.3.2: (1) JEF-2.2, (2) JENDL-3.3, (3) ENDF/B-VI.r8, and (4) JEFF-3.0. Relative changes in the C/E-values are given with respect to the JEF-2.2 values.

	JEF-2.2	JENDL-3.3		JEFF-3.0		ENDF/B-VI.r8	
Ratios	**C/E**	**C/E**	**Rel. Change, %**	**C/E**	**Rel. change, %**	**C/E**	**Rel. change, %**
C8/F9	1.011	1.000	-1.03	1.025	1.47	0.977	-3.38
F8/F9	1.010	1.028	1.28	1.032	1.92	1.061	4.70
F5/F9	0.994	1.006	1.19	1.012	1.77	1.000	0.58
C2/F9	0.994	0.917	-7.54	0.920	-7.24	0.941	-4.98
F2/F9	0.899	0.997	10.47	1.012	12.49	0.986	9.57
(n,2n)2/C2	1.242	1.093	-12.43	1.039	-16.53	0.988	-18.00
F3/F9	0.997	0.990	-0.86	0.999	0.20	1.002	0.34
C7/F9	0.934	0.938	0.35	0.950	1.75	0.922	-1.22
F7/F9	0.944	1.001	5.98	0.979	3.710	1.033	9.31
	C-value	C-value		C-value		C-value	
k_∞	1.3480	1.3576	0.71	1.3449	-0.23	1.3766	2.12

Table 3.5 Relative deviations of the reaction rate ratios, i.e. $\frac{(C-E)}{E}$, calculated with ECCO in conjunction with the reference route (ERALIB1 and JECCOLIB2 nuclear data libraries) and with MCNPX using its different nuclear data libraries, viz. JEF-2.2, JENDL-3.3, JEFF-3.0 and ENDF/B-VI.r8.

	Data		ECCO		MCNPX			
	Exp.	**OC**	**ERALIB1**	**JECCOLIB2**	**JEF-2.2**	**JENDL-3.3**	**JEFF-3.0**	**ENDF/B-VI**
Ratios	**1σ, %**	**(C-E)/E, %**	**(C-E)/E, %**		**(C-E)/E, %**			
C8/F9	1.2	-1.1	-0.4	0.4	1.1	0.0	2.5	-2.3
F8/F9	1.4	-3.7	1.1	4.0	1.0	2.8	3.2	6.0
F5/F9	1.5	1.9	-0.2	1.3	-0.6	0.6	1.2	0.0
C2/F9	1.4	-2.8	-4.1	-3.0	-0.6	-8.3	-8.0	-5.9
F2/F9	2.1	-11.2	-3.6	-2.1	-10.1	-0.3	1.2	-1.4
(n,2n)2/C2	2.6	1.9	-1.0	-0.2	24.2	9.3	3.9	-1.2
F3/F9	1.4	-1.0	-0.4	-1.3	-0.3	-1.0	-0.1	0.2
C7/F9	2.5	10.2	-5.3	-4.1	-6.6	-6.2	-5.0	-7.8
F7/F9	2.1	-1.7	-4.6	-4.2	-5.6	0.1	-2.1	3.3

3.3.1 Analysis of the ECCO results

The reaction rate ratios obtained by means of the RCS are very similar when using the two different calculational routes (reference and design route), and this is independent of which library is used (see Table 3.3). The impact of the self-shielding treatment (see Appendix B.3 for details) is seen for instance in Table 3.3 (Column 3), which shows the relative difference between the reference and design routes with the ERALIB1 library. There is a very good agreement for all parameters, the maximal discrepancy being for F7/F9 with a value of 0.6%, i.e. one third of the 1σ experimental uncertainty. Based on these results, we can assume that the specific self-shielding treatment, as computed in the reference route or in the design route, does not substantially influence the calculated parameters of interest for this study.

A comparison between the two libraries concerning the measured neutron balance components (i.e. reaction rate ratios involving reactions actually occurring in the MOX), indicates that there are no important differences, with the single exception of F8/F9. Thus, for C8/F9 and F5/F9, both libraries yield results in good agreement with experiment (within 1σ). For F8/F9, however, the ERALIB1 based result is much better: it agrees with experiment in a similar manner as for the other ratios, while the JECCOLIB2-value is more than 2σ higher than the measured value.

Among the reaction rate ratios measured as relevant spectral indices in the GCFR-PROTEUS reference lattice (i.e. corresponding to infinite-dilution reactions of interest in the numerator), the ECCO results for F3/F9 are seen to be in good agreement with experiment, i.e. within 1σ, with both libraries, the difference between the two individual results being only 0.9%.

Concerning the capture and fission rates in ^{232}Th, relative to F9, the ratios are underpredicted both with ERALIB1 and JECCOLIB2. The underprediction is, on average, 3.9% with ERALIB1 and 2.6% with JECCOLIB2, indicating that the latter library performs slightly better for the spectral indices involving ^{232}Th. The results with both libraries, however, are within 3σ of the experimental values, for both C2/F9 and F2/F9.

Similar observations can be made for the reaction rate ratios involving ^{237}Np. The underprediction, on average, is ~5% with ERALIB1 and ~4% with JECOLIB2. Again, both libraries yield results (here, for C7/F9 and F7/F9) within 3σ of the experimental values.

As regards the last spectral index considered, viz. (n,2n)2/C2, the calculational results for both libraries are in remarkably good agreement with experiment, lying well within the 1σ uncertainty.

To conclude with this part of the analysis, it is seen that the ERALIB1 based results show good agreement with the experimental data for most reaction rate ratios that have been considered currently, especially for C8/F9, F8/F9 and F5/F9. Considering that the latter directly reflect the neutron balance in the lattice, the ERALIB1 library can be considered more preferable than JECCOLIB2.

3.3.2 Analysis of the MCNPX results

For the main reaction rate ratios, the MCNPX calculations with the reference library JEF-2.2 (see Table 3.4) give accurate predictions (within 1σ of the experimental results). These results are also in very good agreement with those obtained with ECCO/ERALIB1 (see Table 3.3).

For other libraries, a trend to overestimate F8/F9 is observed. The overestimation is by about 2.8% (2σ) for JENDL-3.3, 3.2% (2.3σ) for JEFF-3.0 and even higher, by about 6% (4.3σ) for ENDF/B-VI.r8, respectively. While the MCNPX results for F5/F9 are good, almost independently of the library used, the result for the important neutron balance component C8/F9 seems to be somewhat overpredicted with JEFF 3.0 (by ~2σ) and underpredicted (by a similar amount) with ENDF/B-VI.

As regards the other reaction rate ratios, measured as spectral indices, one can make various observations:

(1) Looking first at just the JEF-2.2 based results, the agreement between MCNPX and the experimental values is within 1σ for C2/F9 and F3/F9. For F2/F9, C7/F9 and F7/F9, however, one has significant underpredictions, viz. by 10.1% (4.8σ), 6.6% (2.6σ) and 5.6% (2.7σ), respectively. For (n,2n)2/C2, there is a very large overprediction with JEF-2.2 (by as much as 24%, i.e. 9.3σ).

(2) The quality of the F3/F9 prediction is almost independent of the data library (agreement with experiment to within 1σ in all cases).

(3) A very high dependence on the data library is observed for the MCNPX results involving ^{232}Th reaction rates. The largest effect is for (n,2n)2/C2, the (C-E)/E value for this ratio varying from +24.2% with JEF-2.2 to -1.2% with ENDF/B-VI. For F2/F9, the range of variation of (C-E)/E is from -10.1 % with JEF-2.2 to +1.2% with JEFF-3.0, while, for C2/F9, it is from -0.6% with JEF-2.2 to -8.3% with JENDL-3.3. This large sensitivity between the libraries is somewhat surprising. On the other hand, the use of newer libraries does lead to a real improvement, the MCNPX prediction of F2/F9, for instance, being within 1σ of the experimental value for all the three libraries JENDL-3.3, JEFF-3.0 and ENDF/B-VI.

(4) As far as the ratios involving ^{237}Np reaction rates are concerned, C7/F9 is systematically underpredicted by between about 2σ and 3σ with all four libraries. For F7/F9, good agreement between calculation and experiment, i.e. within 1σ, is seen for JENDL-3.3 and JEFF-3.0. Overestimation by nearly 2σ and underestimation by nearly 3σ are noticed for the ENDF/B-VI.r8 and JEF-2.2 libraries, respectively.

3.3.3 Analysis of the k_∞-results

The k_∞-values calculated by ECCO with the different libraries are in relatively good agreement with each other (see Table 3.3). First, a value of ~200 pcm (i.e. 0.15%) is found for the effect of the calculational route. This is obtained by comparing, for either of the two libraries, the k_∞-values resulting from the reference route and the design route. Second, a decrease of ~740 pcm (0.55%) is obtained for the library effect on k_∞, i.e. in going from ERALIB1 to JECCOLIB2.

Despite the relatively good agreement between the k_∞-values obtained with MCNPX/JEF-2.2 and ECCO/JECCOLIB2 (the Monte Carlo method yielding a value lower by ~360 pcm), the spread in the MCNPX results obtained for k_∞ with the different libraries is very significant. There is a large discrepancy (~3160 pcm or 2.4%) between the extreme values, viz. those obtained using ENDF/B-VI.r8 (k_∞=1.3766) and JEFF-3.0 (k_∞=1.3449). This may, to a significant extent, be explained by the fact that the important neutron-balance component C8/F9 is calculated to be nearly 5% lower with ENDF/B-VI than with JEFF-3.0 (see Table 3.5).

Concerning the inter-code comparison, it is seen that the ERALIB1/reference route k_∞-value is very close to the JENDL-3.3 k_∞-value, with a discrepancy of only ~140 pcm. The JECCOLIB2 k_∞-value, on the other hand, deviates more significantly from the JENDL-3.3 result, viz. by ~600 pcm.

All in all, there is some indication that the adjusted library (ERALIB1) performs better than the non-adjusted library (JECCOLIB2).

3.3.4 Main findings

Based upon the results obtained with ECCO and MCNPX for the different neutron data libraries presented above, the following statements can be made concerning the re-analysis of the GCFR-PROTEUS reference lattice:

(1) Globally, relatively good agreement, i.e. within 3σ, is found between the different calculations and experimental values for the three principal reaction rate ratios. More specifically, the relative agreement of these reaction rate ratios is within the 1σ experimental uncertainty with ERANOS-2.0/ERALIB1 and MCNPX-2.5e/JEF-2.2, and within 2σ with MCNPX-2.5e/JENDL-3.3.

(2) The above indicates that the overall neutron balance, as calculated with ECCO/ERALIB1, is in good agreement not only with the experimental results, but also with MCNPX used in conjunction with modern libraries. This is valuable supporting evidence for the use of ERANOS-2.0/ERALIB1 in design studies for advanced gas-cooled fast reactors using conventional MOX fuel pins.

(3) Regarding the reaction rate ratios involving infinite-dilution reactions, i.e. for nuclides of interest which did not actually occur in the experimental lattice, less satisfactory agreement between the codes is obtained. The capture reactions in ^{232}Th and ^{237}Np, i.e. C2/F9 and C7/F9, appear to be systematically underpredicted by several 1σ experimental uncertainties, and large relative discrepancies between the computations are observed.

(4) The somewhat surprisingly large spread of the different calculations for the reaction rates ratios involving ^{232}Th and ^{237}Np is a clear indication that, in the libraries being considered, the data for these nuclides has undergone significant independent reassessments in the specific energy range of interest for this study. The need for revisiting the data of ^{232}Th and ^{237}Np, particularly in the context of analyzing transmuting gas-cooled fast-spectrum systems, is thus clearly highlighted.

3.4 Effects of the ERALIB1 data adjustment on k_∞

In order to understand the source of the discrepancy in the k_∞ results between the two neutron libraries in ERANOS (the reactivity effect is $\Delta\rho = \rho_{ERALIB1} - \rho_{JECCOLIB2}$ = 404 pcm), the

Extended Generalized Perturbation Theory (EGPT) capability available in ERANOS-2.0 has been used. The analysis has been carried out in an exact manner by decomposing the reactivity effect into partial effects for (1) the nuclide, (2) reaction type and (3) energy.

The calculations have been performed with the perturbation theory modules of ERANOS-2.0 [99] (see Section 2.5.2). The computational scheme is described in Subsection 3.4.1.

3.4.1 Computational scheme

First, 172-energy-group macroscopic cross-sections for the homogenized cell were prepared with the ECCO RCS both for the perturbed (ERALIB1) and reference (JECCOLIB2) case, respectively. To be consistent with the k_∞ results presented above, the calculations consider an infinite test lattice, i.e. the cell buckling is 0.0.

Then, equivalent homogeneous models of the infinite system were set up in terms of a cylinder with mirror boundary conditions. The material constituting this cylinder has the same macroscopic cross sections as the homogenized fuel cell resulting from ECCO calculations in conjunction with ERALIB1 and JECCOLIB2, respectively. Clearly, for such homogeneous infinite systems, the results of subsequent transport- and diffusion-theory treatment would be identical and independent of the number of meshes used. Accordingly, transport theory and one mesh each in the radial and axial directions were selected currently. In a consistent manner, the adjoint solution was obtained with BISTRO for the unperturbed case, along with the direct solution for the perturbed case.

The next step was accomplished by creating the dispersion matrix, i.e. a unit covariance matrix including the nuclides of interest in conjunction with specific reactions, viz. capture, fission, production (simulated with ν and diagonal-matrix elements equal to 0, in this case), elastic and inelastic scattering, as well as (n,xn). A further step was the perturbation integral calculation on the system volume with a specific module, which provides all integrals needed for evaluating the numerator and the denominator of the perturbation expression (direct as well as indirect terms).

The macroscopic cross-section variations for all the reactions were then evaluated. This was done in terms of nuclide-dependent microscopic cross-sections and/or number densities (constant in the present case). Finally, the analysis was completed by computing $\Delta\rho$ and its individual components. The reactivity variation obtained in this way is, as reported below, 415 pcm.

3.4.2 Results

The reactivity variations are expressed as $10^5\Delta k_\infty/k_{\infty,\mathrm{ERALIB1}}/k_{\infty,\ \mathrm{JECCOLIB2}}$. By analogy to the reactivity used for a critical reactor, we use the unit “pcm” in the following for expressing the reactivity differences.

The results are shown in Table 3.6, which presents the individual reactivity effects (for a total of +415 pcm) corresponding to the different isotopes and their specific reactions. Globally, the most important contributions to the k_∞ change can be attributed to the heavy isotopes for which data have primarily been adjusted, namely ^{239}Pu, ^{238}U, ^{240}Pu and (to a lesser extent) ^{241}Pu, as also to ^{16}O. More specifically, the principal contributors are, with decreasing magnitude, the fission related data (fission cross-section and ν (5)) for ^{239}Pu (+429 pcm), followed by cross-sections for ^{16}O(n,α) (+170 pcm), ^{239}Pu capture (-164 pcm), ^{238}U inelastic scattering (-133 pcm) and ^{240}Pu capture (+119 pcm), as illustrated in Figure 3.5. Smaller contributions are found to come from ^{241}Pu fission (-35 pcm), ^{238}U capture (-33 pcm), ^{16}O elastic scattering (+33 pcm), ^{240}Pu fission (-31 pcm) and ^{241}Pu capture (+25 pcm). The adjustments made to the data for structural materials appear to play a less important role, e.g. ^{58}Ni capture and ^{56}Fe inelastic scattering cross-sections account for only +39 and +24 pcm, respectively, all other effects being found negligibly small.

The energy-dependent differential variations are displayed in the form of histograms for the five major contributions (see Figure 3.6 to Figure 3.10). From these plots, it is seen that:

- The ^{239}Pu fission cross-section is modified over a wide range, from 10^3 to 10^7 eV.
- The ^{16}O(n,α) cross-section was adjusted only above a threshold of 10^5 eV.
- The ^{239}Pu capture cross-section was adjusted between 100 to 10^6 eV.
- The ^{238}U inelastic scattering cross-section varies mainly above 10^6 eV.
- The ^{240}Pu capture cross-section was adjusted between 100 to 10^6 eV.
- The ^{240}Pu and ^{241}Pu fission cross-sections were adjusted between 10^3 and 10^6 eV.
- The ^{238}U fission cross-section was adjusted above 10^6 eV.
- The remaining cross-sections, for ^{56}Fe, ^{52}Cr, ^{58}Ni and ^{27}Al, were all slightly adjusted above 10^5 eV.

Table 3.6 Decomposition, by isotopes and reactions, of the ERALIB1 data adjustment effect on the k_∞-value for the reference GCFR-PROTEUS lattice. The total effect (in terms of reactivity) is 415 pcm.

ISOTOPE	CAPTURE	FISSION	ELASTIC	INELASTIC	N,XN	SUM
^{239}Pu	-164	429	0	5	1	270
^{240}Pu	119	-31	0	-5	0	83
^{241}Pu	25	-35	0	0	0	-9
^{242}Pu	3	-1	0	0	0	1
^{241}Am	0	0	0	0	0	0
O	170	0	33	-7	0	197
^{235}U	-9	1	0	-1	0	-8
^{238}U	-33	-2	-19	-133	0	-187
bdH	0	0	6	0	0	6
^{54}Fe	0	0	0	0	0	0
^{56}Fe	-9	0	4	24	0	18
^{57}Fe	0	0	0	0	0	0
^{58}Fe	0	0	0	0	0	0
^{50}Cr	0	0	0	0	0	0
^{52}Cr	-3	0	14	-4	0	7
^{53}Cr	0	0	0	0	0	0
^{54}Cr	0	0	0	0	0	0
^{58}Ni	39	0	2	0	0	40
^{60}Ni	0	0	0	0	0	0
^{61}Ni	0	0	0	0	0	0
^{62}Ni	0	0	0	0	0	0
^{64}Ni	0	0	0	0	0	0
Mo	0	0	0	0	0	0
Al	0	0	-3	0	0	-3
Mn	0	0	0	0	0	0
Mo	0	0	0	0	0	0
^{14}N	0	0	0	0	0	0
^{15}N	0	0	0	0	0	0
SUM	138	362	36	-121	1	415

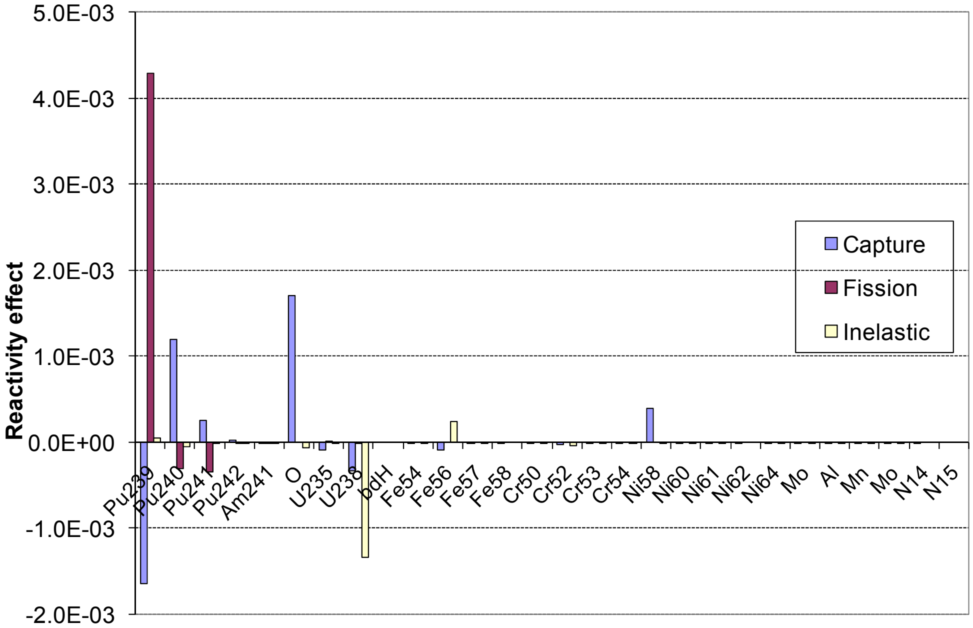

Figure 3.5 Data adjustment effects on k_∞ in terms of individual reactions (capture, fission and inelastic scattering) in the different isotopes

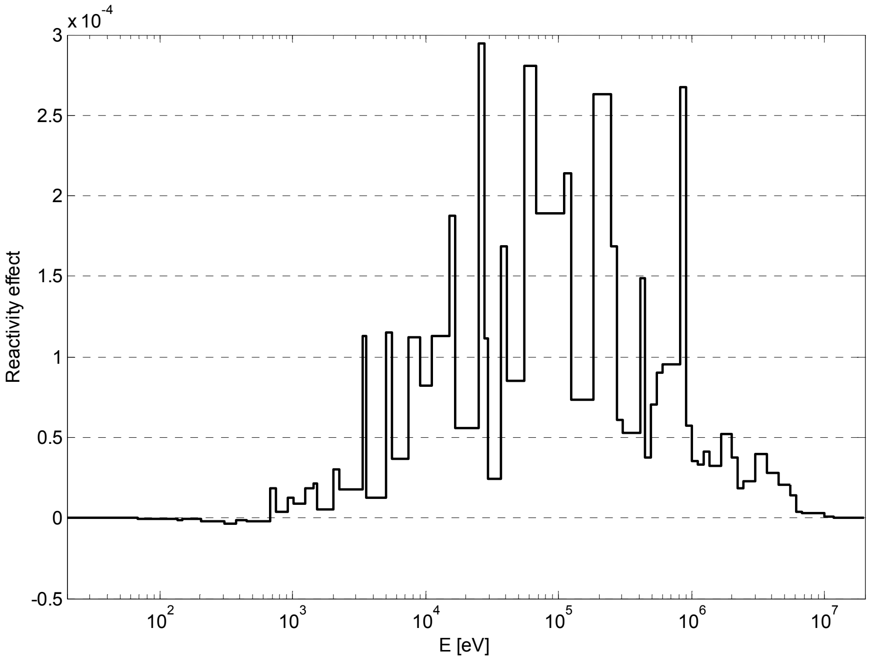

Figure 3.6 Energy dependence of the ^{239}Pu fission cross-section effect (10^5 pcm)

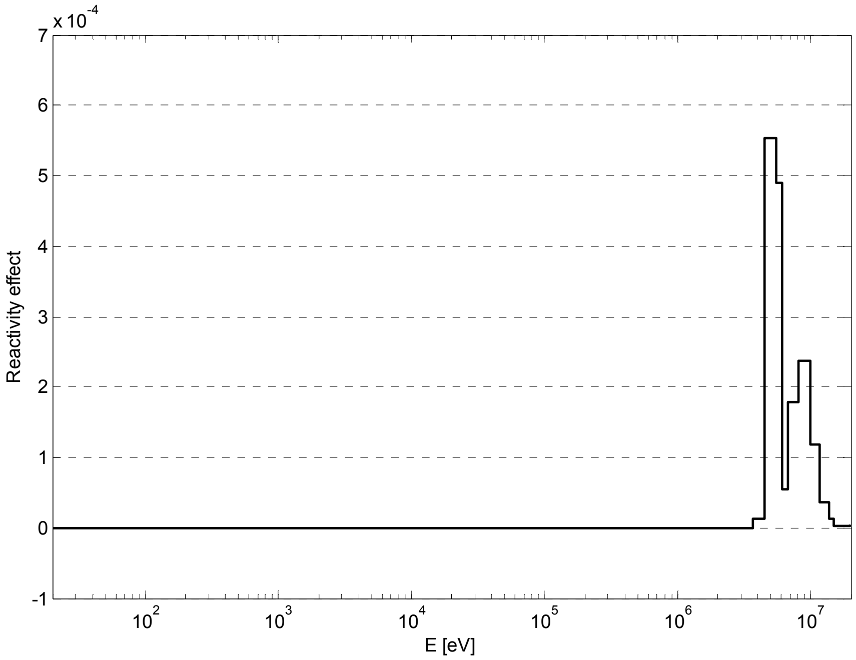

Figure 3.7 Energy dependence of the ^{16}O(n,α) cross-section effect (10^5 pcm)

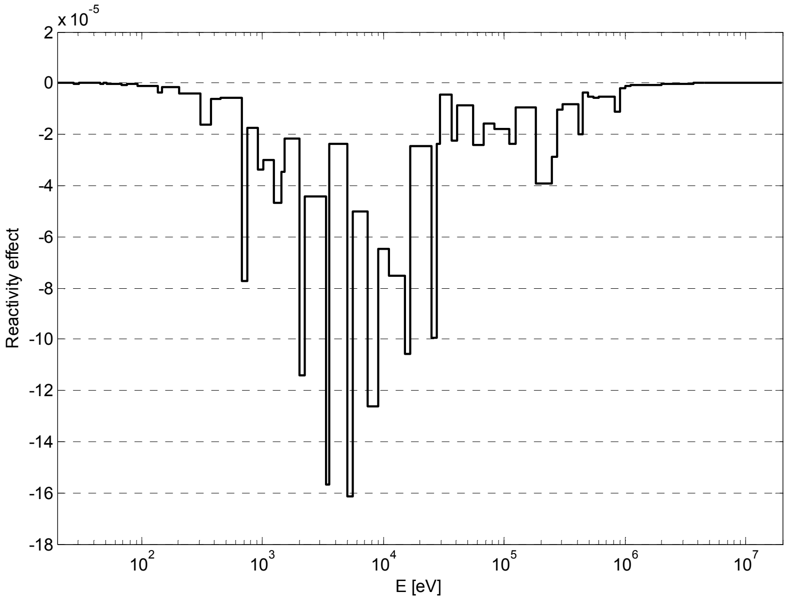

Figure 3.8 Energy dependence of the ^{239}Pu capture cross-section effect (10^5 pcm)

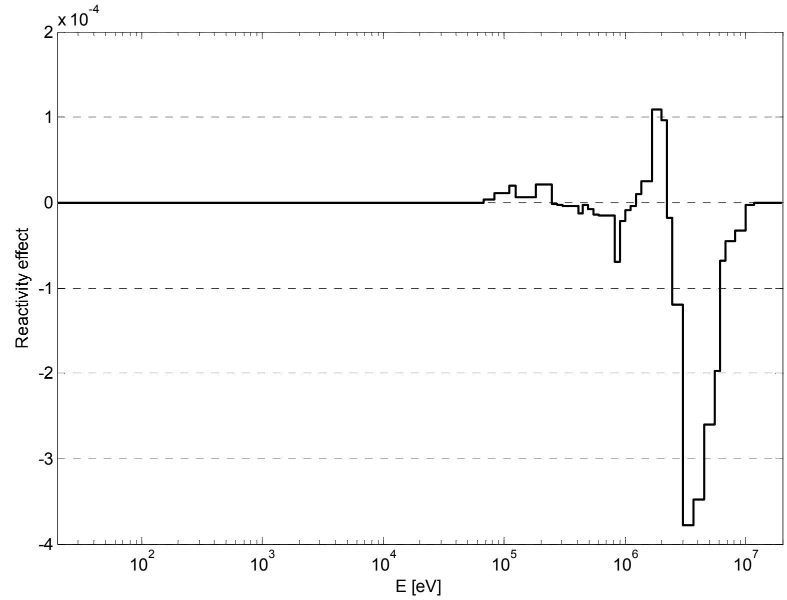

Figure 3.9 Energy dependence of the ^{238}U inelastic scattering cross-section effect (10^5 pcm)

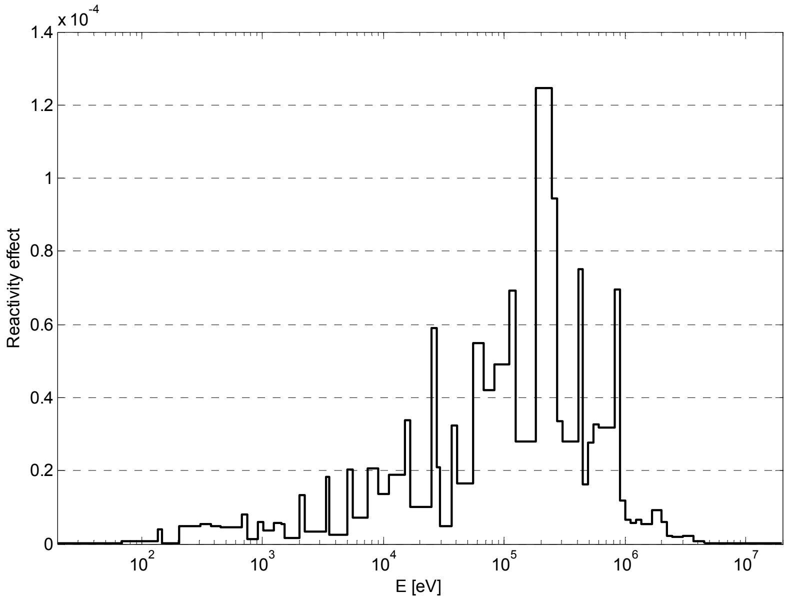

Figure 3.10 Energy dependence of the ^{240}Pu capture cross-section effect (10^5 pcm)

3.5 Transferability of the GCFR-PROTEUS data to Gen-IV systems

This section presents the transferability of the GCFR-PROTEUS experimental data to Generation IV systems. First, the spectra of different systems, viz. GCFR-PROTEUS, GFR, SFR and ETDR, are analyzed, and the origin of the differences is discussed (Subsection 3.5.1). In

Subsection 3.5.2, use is made of perturbation theory to compute the representativity factors of the GCFR-PROTEUS data for the fast reactor systems of current interest.

3.5.1 Spectrum considerations

The fine-group neutron spectrum of the GCFR-PROTEUS reference lattice, as computed by the ECCO cell code in conjunction with the ERALIB1 adjusted data library, is shown in Figure 3.11.

Figure 3.11 Fine-group neutron spectrum of the GCFR-PROTEUS reference lattice

Figure 3.12 compares the spectra of different systems, viz. GCFR-PROTEUS, GFR SFR and ETDR. There is clearly a more dominant slowing-down tail in the GFR case, as compared to the other systems, largely due to the higher moderation induced by the greater amount of light materials present (SiC in particular). Additionally, different resonances are visible in the SFR spectrum (which result from materials no longer envisaged for the GFR): the scattering resonance of ^{23}Na at 2.85 keV (see Figure 3.13) and the large resonance at 435 keV for ^{16}O (see Figure 3.14). On the contrary, a flux depression is observed in the GFR at 200 keV (see Figure 3.12), due to the large scattering resonance of Si at 200 keV. The elastic scattering cross-section of natural Si is depicted in Figure 3.15, and a broad resonance is seen there at 200 keV, which is important for the GFR since this energy corresponds to the average energy.

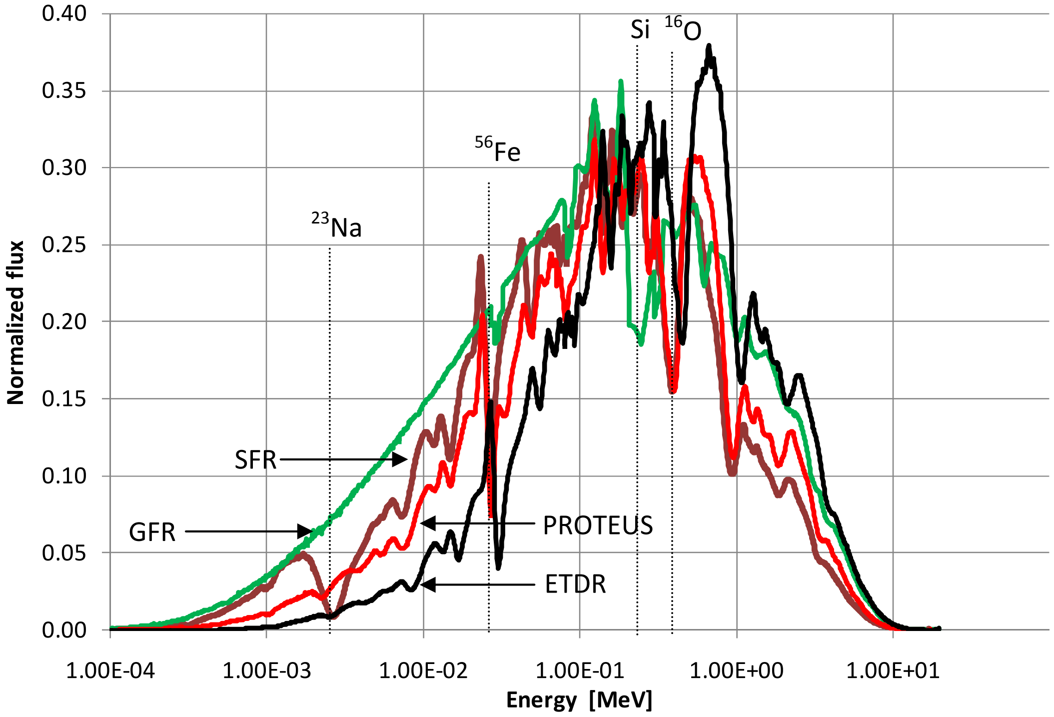

Figure 3.12 Spectra comparison for different systems: GCFR-PROTEUS, GFR, SFR and ETDR

Two other isotopes contribute, in a significant manner, to features of both the SFR and GCFR-PROTEUS spectra, viz. ^{56}Fe and ^{16}O, with important resonances at 28 keV (see Figure 3.16) and 435 keV (see Figure 3.14) for Fe and O, respectively. In the case of Fe, additional resonances above 30 keV are visible in the spectrum. The envisaged GFR fuel matrix does not contain any oxygen or iron. As a direct consequence, these resonances are not present in the GFR spectrum.

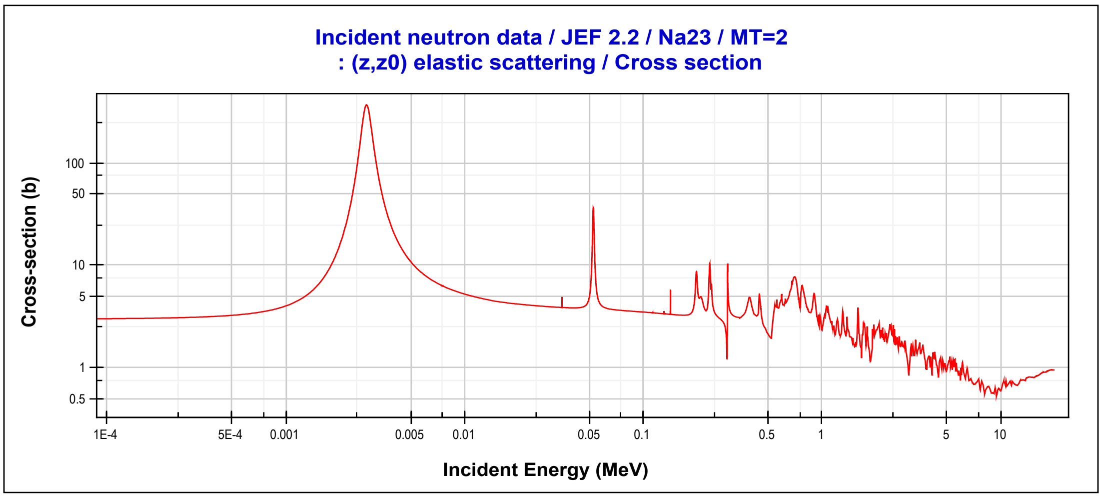

Figure 3.13 Elastic scattering cross-section of ^{23}Na, obtained with JANIS and JEF-2.2 data

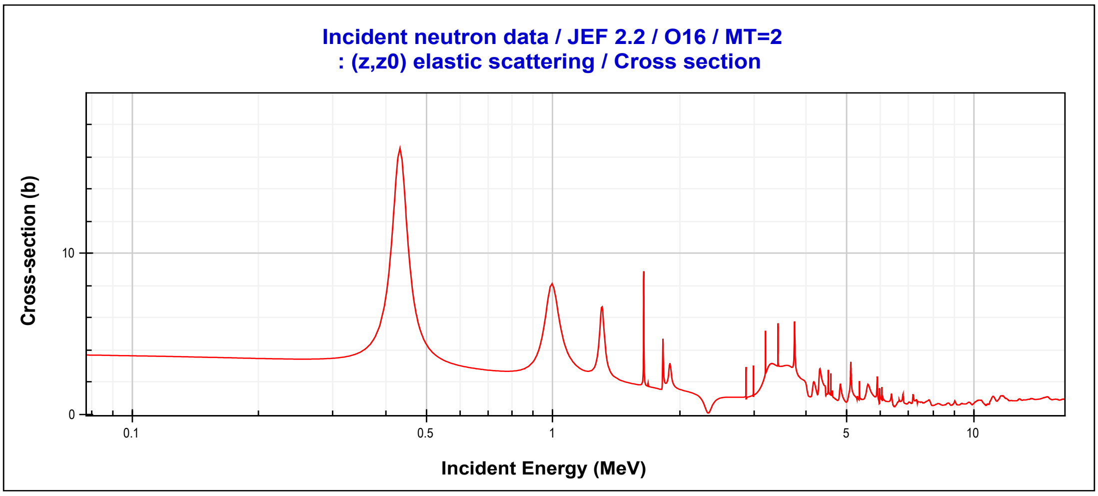

Figure 3.14 Elastic scattering cross-section of ^{16}O, obtained with JANIS and JEF-2.2 data

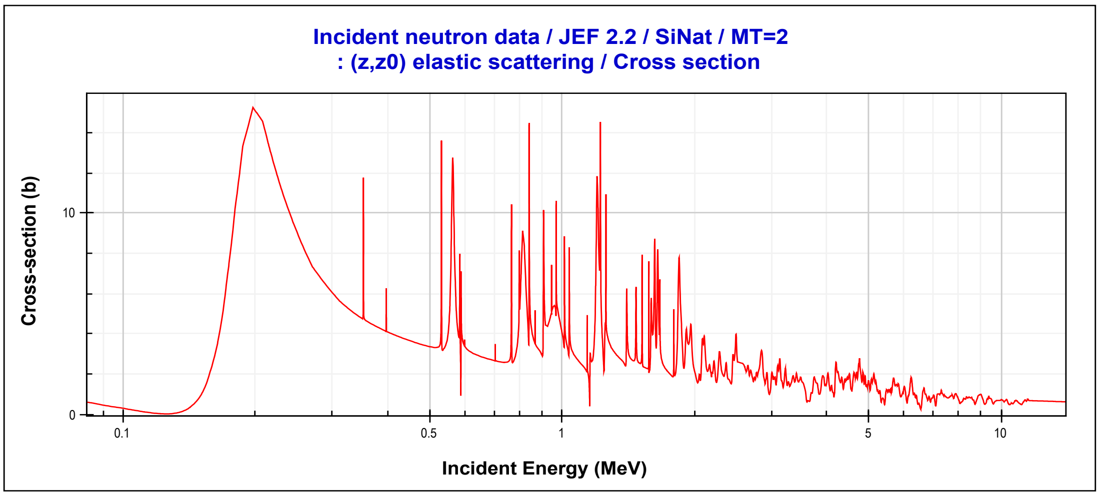

Figure 3.15 Elastic scattering cross-section of natural Si, obtained with JANIS and JEF-2.2 data

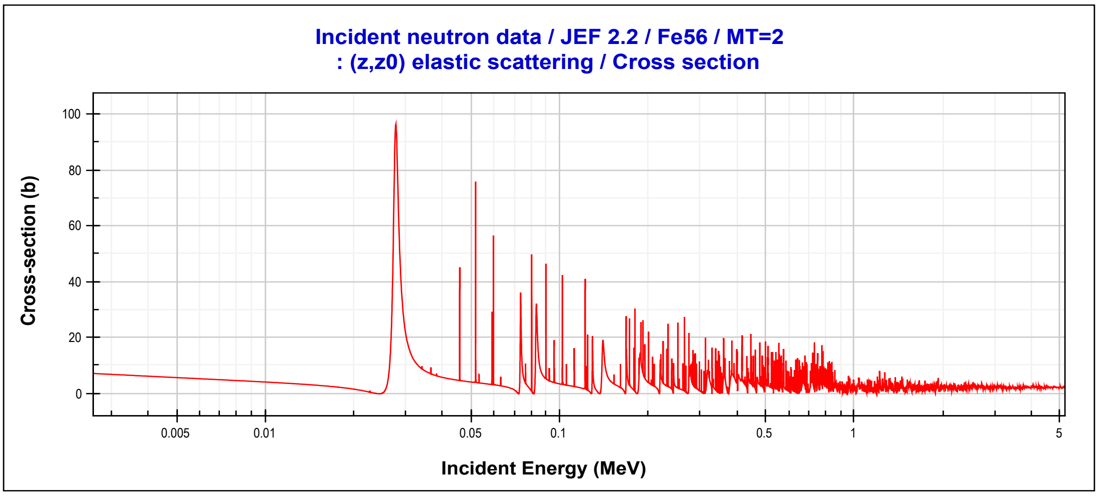

Figure 3.16 Elastic scattering cross-section of ^{56}Fe, obtained with JANIS and JEF-2.2 data

Based on the spectra comparison presented in Figure 3.12, it is found that the GFR spectrum is reasonably close to that of the GCFR-PROTEUS reference lattice, allowing one to perform relevant code validation with the currently employed integral data. Mainly, differences are observed due to the presence in the GFR of new materials (Si, C) and the absence of others which occurred in GCFR-PROTEUS (O, Fe). More detailed analysis is performed below, based on the use of representativity factors.

3.5.2 Representativity analysis

Investigations have been conducted to quantitatively assess the representativity of the GCFR-PROTEUS reference lattice as regards the corresponding integral parameters for different types of gas-cooled fast-spectrum systems. Data sensitivity/uncertainty (see Eq. 2.4 in Chapter 2, Section 2.5) and representativity calculations have been performed using the reference computational scheme associated with ERANOS-2.0/ERALIB1. The established methodology based on linear perturbation theory has been used for computing representativity factors r_{RE} (See Eq. 2.5 given in Chapter 2, Section 2.5) relating the reference MOX cell to three advanced systems:

1. The start-up core of the 50 MWth ETDR, with ~30% Pu content in the (U,Pu) mixture (see Section 2.3),
2. The large reference GFR core, with ~17% Pu content in the (U,Pu) mixture (see Section 2.4),
3. The reference 3600 MWth, CO_2 cooled CAPRA-CADRA core, fuelled with pin-type MOX with ~20% Pu content in the (U,Pu) mixture [126] (see Section 2.1).

First, sensitivity coefficients have been calculated for the four systems and representativity factors computed between the test lattice and the three advanced systems mentioned above. The parameters considered are the measured reaction rate ratios and the infinite multiplication factor k_∞. For greater clarity, the results are presented and discussed separately for k_∞ and for the reaction rate ratios. The results obtained for k_∞ (relative integral sensitivity to the data for the various nuclides, total uncertainty and representativity factor) are provided in Table 3.7. The nuclide-dependent, relative integral sensitivity is deduced from the calculated sensitivity coefficients S_I, the sum over all the nuclides being normalized to 100%.

Table 3.7 Break-down of the relative integral sensitivity to nuclear data and the total uncertainty on k_∞ for the four systems studied: (1) GCFR-PROTEUS, (2) ETDR, (3) GFR and (4) CAPRA-CADRA. The representativity factors relating (1) to the other three are given in the last row.

Nuclide	GCFR-PROTEUS	ETDR	GFR	CAPRA-CADRA
	Rel. integral sensitivity (%)	Rel. integral sensitivity (%)	Rel. integral sensitivity (%)	Rel. integral sensitivity (%)
^{235}U	-	-	0.4	-
^{238}U	16.1	8.0	28.4	14.1
^{238}Pu	-	0.1	0.1	0.1
^{239}Pu	82.7	86.2	64.7	77.9
^{240}Pu	0.5	3.1	1.1	4.5
^{241}Pu	0.1	2.2	2.6	1.9
^{242}Pu	-	0.1	0.1	0.1
C	-	-	2.2	-
O	0.5	-	-	1.1
Si	-	-	0.4	-
^{56}Fe	-	0.1	-	0.1
others	0.1	0.1	0.0	0.1
k_∞ Total uncertainty, ‰	1.4	2.5	3.0	2.3
$r_{RE}(k_\infty)$	-	0.89	0.85	0.90

It is seen from these results that the highest sensitivity of k_∞ is, systematically, to uncertainties in the data for ^{239}Pu. In the case of the GFR, the second largest sensitivity, which is to ^{238}U, is enhanced, relative to ^{239}Pu, due to the softer neutron spectrum resulting from the combination of carbide fuel and SiC structural material. In all cases, the contributions of all the other nuclides are much smaller, making up less than 10% of the total effect.

As regards the total uncertainty on k_∞ in the individual systems, it is seen that the values are rather small relative to the delayed neutron fraction, which amounts to 350-400 pcm in the different cases. The k_∞ uncertainty is somewhat higher for the GFR (3‰), mainly due to the softer neutron spectrum, which leads to a larger contribution of ^{238}U (~28%).

As regards the representativity factors, it is seen that, for k_∞, the GCFR-PROTEUS reference lattice is well representative of CAPRA-CADRA and ETDR, the corresponding r_{RE} values being close to 0.9. This is not surprising, since CAPRA-CADRA and the ETDR demonstrator both use MOX fuel with similar Pu-content and stainless-steel structural material. The impact on the spectrum and adjoint function of the different coolants, i.e. CO_2 and He, is only marginal in this context. The k_∞ representativity also appears quite satisfactory in the case of the GFR, in spite of it being a significantly different system from the neutronics viewpoint. However, the representativity factor (~0.85) is clearly smaller in this case, primarily as a result of the different material composition and softer neutron spectrum.

The same basic methodology has been used to compute the uncertainties (due to the nuclear data) on the reaction rate ratios measured in the GCFR-PROTEUS reference lattice. In this analysis, a less dominant effect is found for ^{239}Pu than in the case of k_∞. Results, in terms of the total uncertainties and the main contributing isotopes, are provided in Table 3.8. In these calculations, only the principal ratios C8/F9, F8/F9, F5/F9, were analyzed.

The uncertainties on the reaction rate ratios are significantly higher than those obtained for k_∞, which can be explained by the more integral nature of the latter parameter. The calculated values are very similar and consistent for the three MOX fuel systems, with values in the range of 1%. That the values for the principal ratios (C8/F9, F8/F9, F5/F9) are smaller than the 1σ uncertainties in the experimental results used currently may be explained by the adjusted nature of the ERALIB1 library.

Table 3.8 Nuclear data uncertainties for the main reaction rate ratios, along with the main contributing isotopes, for the four systems studied: (1) GCFR-PROTEUS, (2) ETDR, (3) GFR and (4) CAPRA-CADRA.

Reaction rate ratio	**PROTEUS**		**ETDR**	
	Uncertainty, %	**Main contribution**	**Uncertainty, %**	**Main contribution**
C8/F9	0.55	^{239}Pu, ^{238}U, O	0.65	^{239}Pu, ^{238}U, O
F8/F9	0.63	^{238}U, ^{239}Pu, O	0.67	^{238}U, ^{239}Pu, O
F5/F9	0.39	^{239}Pu, ^{235}U, O	0.41	^{239}Pu, ^{235}U
Reaction rate ratio	**GFR**		**CAPRA-CADRA**	
	Uncertainty, %	**Main contribution**	**Uncertainty, %**	**Main contribution**
C8/F9	0.62	^{239}Pu, ^{238}U, C	0.56	^{239}Pu, ^{238}U, O
F8/F9	1.07	C, Si, ^{238}U	0.70	^{238}U, ^{239}Pu, O
F5/F9	0.51	^{239}Pu, ^{235}U	0.40	^{239}Pu, ^{235}U

The representativity factors, obtained for the various reaction rate ratios measured in the GCFR-PROTEUS reference lattice, are presented in Table 3.9. These r_{RE} results confirm the trend observed for k_∞, the values being systematically larger than 0.95 for CAPRA-CADRA and ETDR, and in the range of 0.86 for GFR. Particularly noticeable is the poor representativity for the (n,2n)2/C2 ratio in the latter case. This is linked to the very high energy threshold for the ^{232}Th(n,2n) reaction, viz. ~ 6.5 MeV.

Table 3.9 Representativity factors, r_{RE}, for the different reaction rate ratios measure in the GCFR-PROTEUS reference lattice.

Reaction rate ratio	ETDR	GFR	CAPRA-CADRA
C8/F9	0.99	0.83	0.97
F8/F9	0.95	0.90	0.96
F5/F9	0.99	0.87	0.98
C2/F9	0.97	0.85	0.98
F2/F9	0.95	0.86	0.96
(n,2n)2/C2	0.96	0.70	0.96
F3/F9	0.99	0.89	0.99
C7/F9	0.97	0.86	0.98
F7/F9	1.00	0.99	1.00

3.6 Conclusions and recommendations

This chapter describes the neutronics investigations performed in the context of the integral data measured in the reference lattice of the GCFR-PROTEUS experimental program.

The deterministic code ERANOS-2.0, in conjunction with its two nuclear data libraries ERALIB1 and JECCOLIB2 and different computational schemes, was used to assess, principally, the adequacy of using the adjusted ERALIB1 nuclear data library for GFR neutronics analyses. The integral parameters of interest were recalculated using ECCO/ERANOS and benchmarked against both the available experimental data and stochastic calculations using a wide range of nuclear data libraries.

The sensitivity of the ERANOS results, for the considered integral parameters, to the nuclear data available in the adjusted ERALIB1 library has been evaluated quantitatively using extended generalized perturbation theory (EGPT). Furthermore, the representativity factors for k_∞ and the measured experimental reaction rate ratios have been obtained with respect to three gas-cooled fast-spectrum systems of interest, viz. ETDR, GFR and CAPRA-CADRA. The total uncertainties in the various parameters, due to the ERALIB1 nuclear data, have also been evaluated for each of the considered systems.

It has been found that, for the main reactions rate ratios (C8/F9, F8/F9, F5/F9), the new analysis of the GCFR-PROTEUS reference lattice generally yields good agreement between experiment and the various calculations performed in conjunction with different modern libraries. The ECCO/ERANOS results obtained with ERALIB1 appear to be of a somewhat better quality than the other calculation, especially, in the prediction of F8/F9. This provides a useful indication of the adequacy of ERANOS-2.0/ERALIB1 as the principal neutronics tool for the present research.

Regarding the reaction rate ratios measured as spectral indices in the GCFR-PROTEUS reference lattice, viz. those involving infinite-dilution reaction rates, a relatively large spread in the results has been highlighted for the ratios with ^{232}Th and ^{237}Np reactions. In the context of Gen-IV GFRs fuelled with MAs, it is clear that the data for these nuclides have to be reassessed.

The EGPT analysis currently carried out has shown that the representativity factors of the GCFR-PROTEUS experiments are particularly good for the systems employing MOX fuel, the values being in the range of 0.95. The values for the GFR are somewhat lower, viz. in the range of 0.86. The ERALIB1-data dependent uncertainties k_∞have been found to be relatively small, e.g. 3‰ for the k_∞ of the GFR core. This is clearly a reflection of the adjusted nature of the data in ERALIB1.

Finally, as regard to the lower representativity factor for the GFR, it is recommended to investigate this system's specific neutronics features (softer neutron spectrum, etc.) with a dedicated, new experimental program. Clearly, in this context, the planned ENIGMA program, involving the use of new GFR-specific materials such as SiC, would be better positioned in terms of representativity than the GCFR-PROTEUS data. This program would help, additionally, to improve the nuclear data to meet target accuracies for minor actinides, as exemplified in the current investigations by ^{237}Np.

Chapter 4

4 Development of the control assembly pattern for the reference GFR Core design

This chapter presents (1) the development and optimization of the control assembly pattern for the reference GFR core ("2004-Core" design), and (2) its neutronic characterization.

The general context and the global procedure adopted for the current design work are first described (see Section 4.1), followed by a description of the GFR core and models (2D and 3D) (see Section 4.2). The detailed design development and optimization considerations made are presented in Section 4.3, along with the resulting CA pattern.

Characterization of the CA, in terms of the shadowing and anti-shadowing interactions occurring within the core, is presented in Section 4.4. Section 4.5 gives the methodology used to compute the CA worth, while Section 4.6 provides the reactivity requirements for the GFR and the corresponding CA implementation scheme adopted for the core. Section 4.7 gives the summary and conclusions of the present chapter.

4.1 General context and scope

At the time the present research was initiated, the GFR core design was defined as a 2-zone core [84], for which only a simplified description was available. Later came a more detailed description, along with a preliminary suggestion for the CA [127]. All materials were specified as homogeneous mixtures within the core regions. In particular, neither a specific CA pattern nor a CA implementation scheme (number and position of the CAs within the core) was available. In this context, the investigations and developments presented in this chapter have to be seen as a direct contribution to the overall GFR core development effort.

The currently described research was structured in several phases and combined, in parallel, analyses related to the CA design work and to the neutronic characterization. First, the 2D and 3D ERANOS neutronics models of the GFR core were developed based upon the computational scheme validated by the PROTEUS investigations (presented in Chapter 3). The 2D model was used to perform simplified analysis, while the more detailed GFR physics investigations were carried out with the 3D core model.

The second part of the design development involved the calculation of the Heat Generation (HG) within the absorber assemblies (a key parameter in the CA design process) and the determination of the optimal absorber pin diameter. This was achieved via coupled neutronic and thermal-hydraulic analysis, effectively an iterative process. The predicted temperatures of the materials (of particular concern for the safety) mainly depend on the coolant mass flow rate and the employed HTC. The optimal mass flow rate was determined based upon the neutronic/thermal-hydraulic results, with account taken for limitations imposed on the maximal cladding temperatures. Additionally, parametric studies were performed regarding the HTC.

HG values for different positions of absorber allow one to dimension the CA appropriately and, in an iterative process, to compute and optimize the material temperatures. The optimization was focused on maximizing the absorber fraction while minimizing the neutronic interactions (i.e. the self-shielding in, as also the shadowing effects between, the individual absorber pins). Supporting Monte Carlo simulations were also performed in this optimization phase.

Since strong interactions were observed not only within the CAs but, even more important, between the individual CAs in the GFR core, detailed neutronics calculations were undertaken in a third step to obtain a better understanding of the latter phenomenon. Thus, while the within-assembly interactions essentially impact the efficiency and performance of the developed CA pattern, the mutual CA effects are more directly of concern for the core safety since the available reactivity worth is rendered dependent on the CA positions. These interactions, and the way to reduce them, were investigated also via parametric and sensitivity studies.

Once the optimization process was complete, supplementary analyses were performed to characterize the design in terms of reactivity worth.

The final implementation of the CA scheme for the GFR core was carried out by taking into account not only the neutronic interactions and the CA reactivity worth values, but also the safety relevant, reactivity requirements derived from the operation of earlier (sodium-cooled) fast reactors. It will be shown that, as compared to these previous commercial fast reactors, significant improvement have currently been obtained in the CA design, particularly regarding the neutronic penalties which result from heterogeneity effects.

The results of the present investigations have also contributed to GFR design improvements in a global sense. In particular, the CA interaction studies have allowed one to anticipate such effects, while optimizing the core design itself. The various studies have been documented in both CEA and PSI technical documents, as well in two conference proceedings [128; 129; 130; 131; 132; 133]. Finally, the work has been published in a journal [134].

4.2 GFR core design description and modelling

4.2.1 Core design description

The reference GFR core, which has been chosen for the present research, is the so-called “2004-Core” design (also called “06/4” in the CEA terminology), being developed by the French Commissariat à l’Energie Atomique (CEA) at Cadarache. This design neutronic, thermal-hydraulic and fuel considerations encompasses [42; 45; 47; 63; 78; 81; 82].

The core description presented below complements the specifications given in Section 2.4, which was focused more on the overall GFR system design.

The GFR core is a flattened cylinder, 1.55 m in height and 4.44 m in diameter (see Figure 4.1), with 2 different Pu-content zones, the Pu content being higher in the outer region (values of 16.3% in the inner zone and 19.2% in the outer). The ratio of the Pu content of the inner zone to that of the outer zone was adjusted such as to flatten the power distribution at BOL, while keeping the two fuel zones equivalent in volume. The absolute Pu-content values were adjusted to provide the envisaged core management, namely 2493 EFPD, corresponding to a burnup of ~10% FIMA. While increasing the Pu content, allows higher burnup to be reached, the $^{Pu}/_{U+Pu}$ ratio has to be kept low enough to ensure the targeted breeding gain.

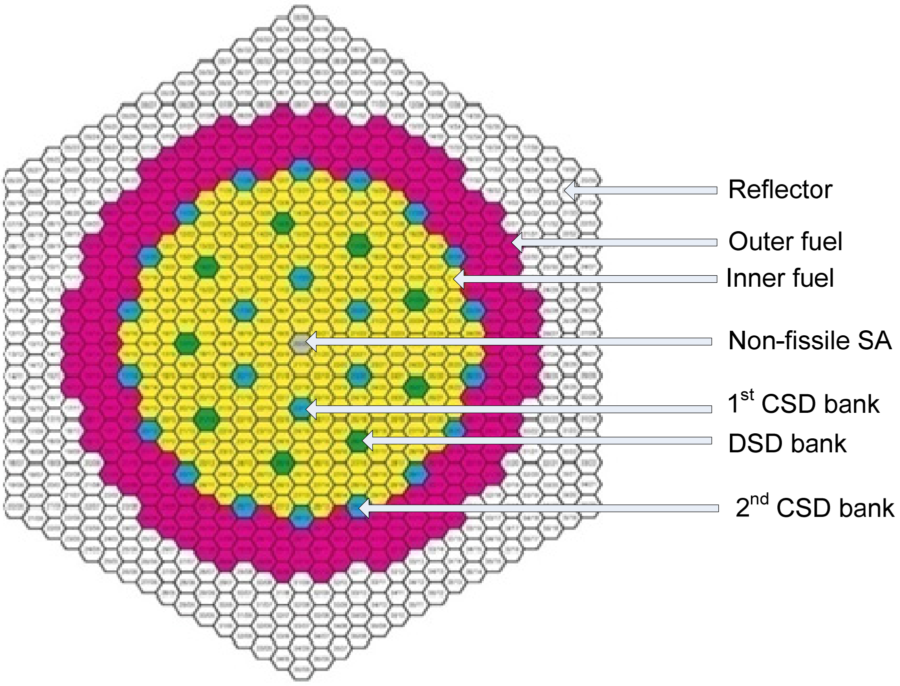

Figure 4.1 3D HEX-Z model of the GFR core

The core contains hexagonal fuel SAs, based on a new design compared to previous commercial FRs and made of (U,Pu)C ceramic materials. In total, the core contains 387 SAs implemented in 12 rings. The homogenized volume fractions of the different materials of a fuel SA (see Figure 4.2) are given in Table 4.1.

Table 4.1 Homogenized volume fractions of the fuel SA materials for the reference GFR core

Material	Volume fraction, %vol.
(U,Pu)C	22.4
Coolant	40.0
Structural SiC material	20.0
SiC matrix	6.4
He, within and between the plates	11.2

The total fuel assembly length is 3.55 m (this value includes the reflectors), the fuel height being 1.55 m, corresponding to the axial coordinates z=1.00 to 2.55 m. Radial and axial thermal expansion due to operating conditions have been accounted for, axially assuming that the thermal expansion of the core is imposed by that of the ceramic material [135], and radially as governed by dilatation of the diagrid. The determination of the new dimensions corresponding to operating conditions has been done in ERANOS itself, using a specific module [136] with the linear thermal expansion coefficient of SiC specified in the input for that purpose. The operating GFR conditions, in terms of the core material temperatures, are summarized in Table 4.2.

Table 4.2 Operating conditions: temperatures of the different materials

Material	Temperature, °C
He (Inlet/Outlet)	480/850
Fuel	990
Structures	665

A SA consists of three different regions (see Figure 4.2), each containing nine parallel fuel plates. The plates are placed in a parallel manner to allow the flow of helium, on each side of the fuel. More precisely, a plate is made of a CERCER material consisting of ceramic fuel pellets (U,Pu)C placed in a honeycomb SiC matrix, enclosed by two thin covers (see Figure 4.3), each fuel pellet being separated from the others. Between the fuel pellets and the honeycomb matrix, there is a gap filled with helium at 0.1 MPa to accommodate fuel expansion and fission gas release. The plate material composition is given in Table 4.3. To accommodate the high temperature (in the range of 850°C), SiCf[3]-SiC ceramic material is envisaged. While the bulk of this material is made of silicon, it is reinforced by SiC fibers woven in 2D patterns. It may be added that such materials are already used in space technology, but there is little related experience in nuclear technology.

---

[3] SiC fibers

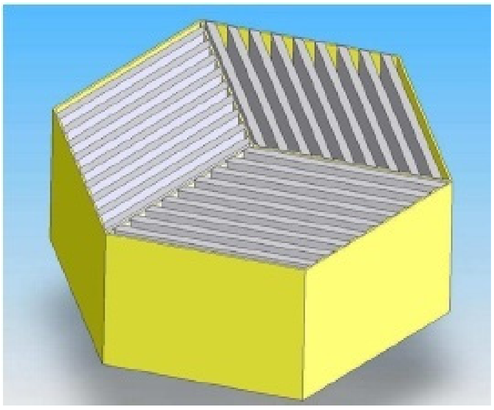

Figure 4.2 A hexagonal fuel assembly (section)

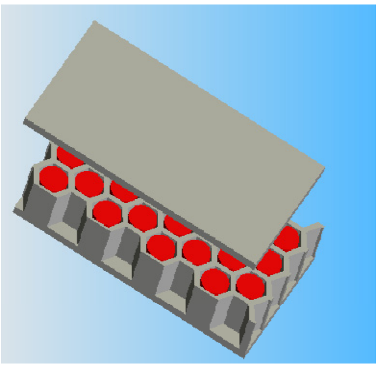

Figure 4.3 A GFR fuel plate

Table 4.3 Volume fractions of fuel-plate materials

Material	Volume fraction, %vol.
(U,Pu)C	56.0
SiC matrix	16.0
He gap (between matrix and fuel pellet)	28.0

As indicated in Figure 4.1, the early design strategy for control of the GFR core reactivity was to have a total of 33 CAs implemented within the core in three individual banks: two CSDs and one DSD. In more detailed terms, the first CSD bank contains six assemblies, symmetrically centered and placed at ~64 cm from the core center in the inner fuel zone, and the second one contains eighteen assemblies and is located at the interface between the inner and outer fuel zone, at a radius of 171 cm. Complementary to these CAs, there are nine DSD assemblies in the intermediate safety bank, at an average distance of 118 cm. The control command of this bank is totally independent of that for the CSDs. In the absence of a specific CA design, the present design work started by assuming a homogeneous CA based on the CSD design for EFR, as described below.

For EFR, the reactivity change during normal operation is large and is compensated by using two independent banks of CSD CAs, the first one being placed in the inner fuel region while the second bank is located at the interface between inner and outer core. Additionally, DSDs are placed between the two banks of CSDs. Moreover, each CSD assembly design is composed of 37 high-enriched (90%-^{10}B) boron carbide (B_4C) absorber pins, surrounded by a hexagonal stainless steel wrapper (see Figure 4.5). The cladding material is stainless steel (AIM1-type). The remaining volume – about 40% – is filled with sodium for cooling the absorbers. Table 4.4 provides the volume fractions of the materials constituting CSD and DSD assemblies in the EFR.

Table 4.4 Volume fractions of the materials constituting CSD and DSD assemblies in the EFR. The follower is the same in both cases.

Assembly type	Material	Fraction, %vol.
CSD	B4C-^{10}B 90%	30.2
	Steel (1515-type)	20.6
	Coolant	49.2
DSD	B4C-^{10}B 90%	26.3
	Steel (1515-type)	21.4
	Coolant	52.3
Follower	Coolant	8.8
	Steel (1515-type)	91.2

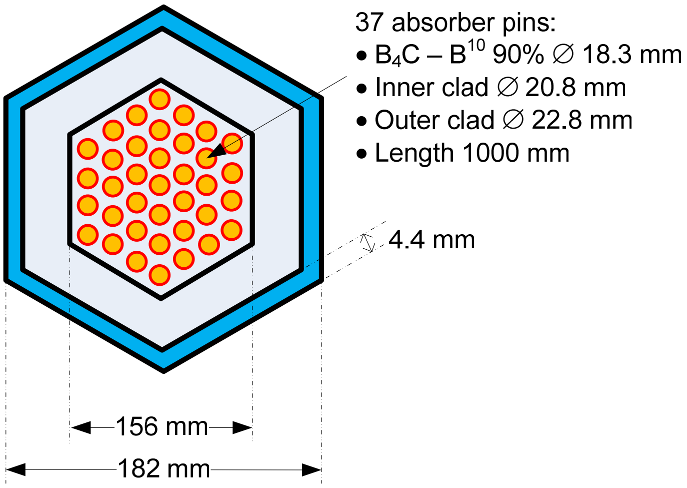

Figure 4.4 Schematic of an EFR CA

4.2.2 RZ GFR core model

Detailed information was not available at the start of the present work and the lack of data made it necessary to start the analysis with a simplified RZ model [84]. Subsequently, this model was used to permit the application of perturbation theory and gamma source calculations, ERANOS options which are available only for a RZ description.

In the model, the three CA banks were implemented in independent concentric rings, by adjusting the thickness such as to preserve absorber volumes. Figure 4.5 depicts the scheme adopted for the reference RZ GFR model.

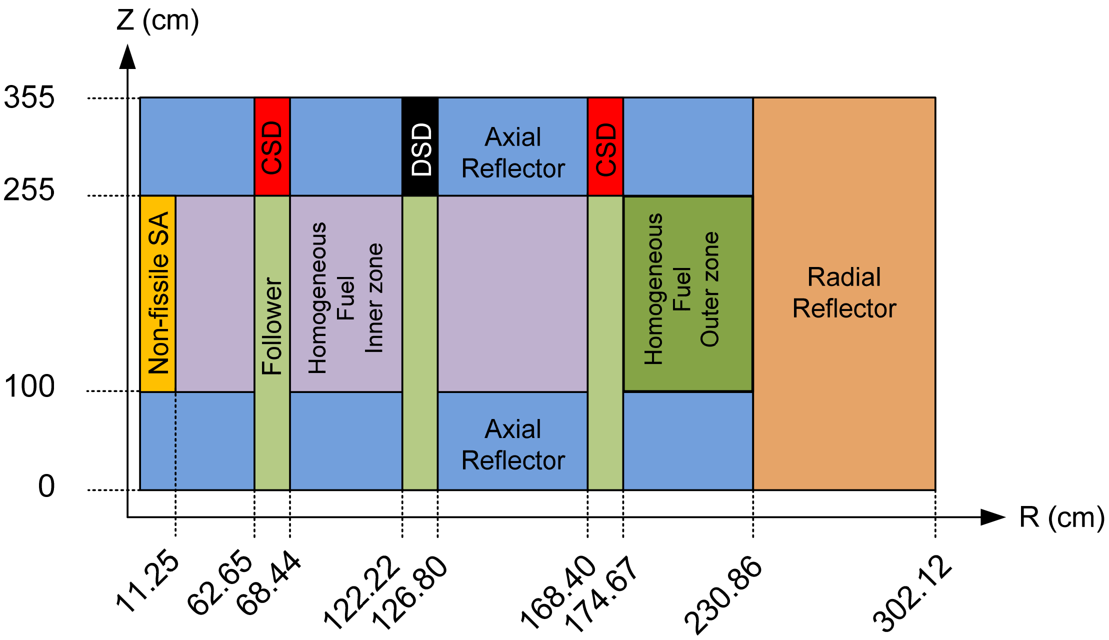

Figure 4.5 Schematic of the RZ representation of the GFR "2004-Core" design

The fuel SAs are considered to be a homogeneous mixture of the different materials. As mentioned, the GFR SAs are made of parallel plates containing a honeycomb lattice of pellets, and such a sophisticated geometry is not implemented in the ECCO cell code of ERANOS-2.0. For the CAs, the same approach is used, the assemblies being represented as a homogeneous mixture of boron carbide, stainless steel and helium, for the absorber part, and a homogeneous mixture of steel (drive mechanism) and helium, for the CA follower.

Due to the RZ modeling, the axial position of each CA within a bank has to be set to the same value, i.e. the positions of the absorbers are given by simply two coordinates. It has been considered, thereby, that a CA is fully inserted when the absorber is at the bottom of the fuel, i.e. at the coordinate z=1.00 m, and that it is in the parking position with the absorber at the top of the fuel, i.e. at z=2.55 m.

In brief, the RZ model was used for a number of purposes:

(1) Perturbation and sensitivity studies,
(2) Heat generation calculations,
(3) Burnup calculations, in association with the dynamic analysis (see Chapter 5).

4.2.3 HEX-Z GFR core model

Consecutive to the early studies performed for the GFR and to the implementation, in a first approach, of the EFR CAs within the GFR core [127], it became possible to develop a 3D HEX-Z GFR core model for use with ERANOS. This development was carried out in conjunction with use of the 3D nodal variational code VARIANT, enabling the modeling of each SA individually and permitting each CA to be represented explicitly.

This model has offered new possibilities in terms of detailed analysis. In particular, the interactions between the CAs could be investigated. Additionally, it was possible to study the CA implementation scheme, in order to derive the exact number of CAs needed for the GFR (see Section 4.6.6). Recommendations in terms of design improvements were also derived from the use of the 3D model (new CA implementation scheme for instance). In the context of the transient analysis performed to characterize the dynamic behavior of the "2004-Core" design (see Chapter 5), benchmarking of the employed PARCS models was performed against the HEX-Z ERANOS/VARIANT model.

4.2.4 Calculational scheme in ERANOS-2.0

The calculational scheme used in association with the ERANOS code, for the neutronics characterization and the CA development work, is reviewed in this subsection. To make the analysis systematic, different routines were implemented to compute the parameters of interest, e.g. effective multiplication factors, eigenvalue harmonics, reaction rates, flux, kinetic and safety parameters, etc. Of interest are the computational options used in the cell code ECCO. In a first step, self-shielded macroscopic cross-sections were produced with ECCO in conjunction with homogeneous cells. A total of eight homogeneous cells are needed to describe the core. These cells are:

(1) Inner zone fuel,
(2) Outer zone fuel,
(3) Central non-fissile region,
(4) Axial reflector,
(5) Radial reflector,
(6) CSD,
(7) DSD,
(8) Assembly follower (CA drive mechanism).

The reference calculational scheme consists of two phases, viz. the cell and the core calculations. The computational options correspond to those derived from the analysis of the GCFR-PROTEUS experimental data (see Chapter 3).

For the first phase, four steps were used in ECCO for the fissile cells:

(1) *First step*. The fission source is calculated using the ERALIB1 [97] neutron data library in conjunction with the XMAS structure. The buckling value is searched for to be used in the subsequent steps (fundamental mode).
(2) *Second step*. The self-shielding is calculated in the fine 1968-group structure with the sub-group method. A linear dependence is assumed for the anisotropy of the scattering source [91]. The losses are treated without directional treatment.

(3) *Third step*. The cross-sections are condensed into the broad-group structure (33 energy groups), using the flux computed during the previous step. The self-shielded macroscopic cross-sections and the scattering matrices are saved in an archive file for use in the following core calculations.
(4) *Fourth step*. The self-shielded macroscopic cross-sections are condensed in energy into a single group for verification purposes.

In the case of non-fissile cells (CSD, for instance), the procedure was different. The source was taken from an already calculated, fissile fuel cell and an empirical buckling value $B^2 = \frac{5}{8} \cdot \left(\frac{\pi}{L}\right)^2$ was used[4] [59].

The second phase of the ERANOS analysis was the core calculation. The computations were performed both with the RZ Sn BISTRO Code and the HEX-Z TGV/VARIANT code, in either diffusion- or transport-theory approximation (see the GFR core models presented in Subsection 4.2.2 and 4.2.3). The numerical approximations used in BISTRO were P1 for the anisotropy of scattering and S16 for the angular discretization of the flux. The geometry was discretized in fine meshes of approximately 3 cm. In the case of VARIANT, broad meshes of approx. 10 cm were used, and the numerical approximations for the flux calculations were those of set "601", viz.:

(1) Transport calculation with simplified spherical harmonics,
(2) Order of polynomial expansion for even flux of 6,
(3) Order of polynomial expansion for partial current (leakage) of 0,
(4) Order of polynomial expansion for nodal source of 1.

In particular, the integral CA worth from the core calculations was obtained as the difference of the reactivity $\rho = \frac{k-1}{k}$ between the case of the CA at the parking position and that with the CA inserted.

4.2.5 Sensitivity of eigenvalues and CA worths to computational options

The sensitivity of the eigenvalues and CA worths to the modeling and computational options was assessed via investigations detailed in Appendix C, Section C.1. The principal results are provided below in a condensed form.

For the purpose of the comparison of eigenvalues, four configurations associated to different CA positions were defined:

(1) All CAs withdrawn (CAs at their parking position),
(2) All CSDs fully inserted,

---

[4] *L* is a characteristic distance for the cell, the flat-to-flat distance being considered as such in the present analysis.

(3) The first CSD bank inserted and the second withdrawn,
(4) The second CSD bank inserted and the first withdrawn.

The selected configurations correspond to a wide range of CA positions, allowing testing of the calculational scheme for different degrees of asymmetry of the neutron flux distribution in the core. During this analysis, the safety bank was maintained at the parking position. For the four configurations defined above, the following computational options were compared:

(1) Nuclear data library: the adjusted ERALIB1 and the JECCOLIB2 data libraries,
(2) Operating conditions: operating temperatures and room temperature (zero power), in association with the HEX-Z VARIANT model,
(3) Calculations in transport and diffusion theory, in association with the RZ BISTRO model,
(4) Calculations in transport theory, in HEX-Z vs. RZ geometry,
(5) For the nodal flux calculation in VARIANT, different numerical approximations (polynomial expansion for nodal flux, even flux and partial current were tested as regards the flux and current expansion orders),
(6) Heterogeneity treatment in ECCO for the fuel cell calculation.

Based upon the results obtained from the sensitivity analysis (see Appendix C, Section C.1.), the following statements can be made:

(1) The sensitivity of the CA worth to the choice of the nuclear data library is rather limited (see Table C.1 in Appendix C.1) and amounts to ~0.3% (as difference obtained using JECCOLIB2 relative to ERALIB1).
(2) The sensitivity to the operating conditions of the CA worth is negligible (see Table C.2 in Appendix C.1): ~0.1% (in the case of “cold” conditions, relative to “hot”).
(3) The eigenvalues and the CA worths are very sensitive to the core modeling, i.e. RZ vs. HEX-Z (see Table C.5 in Appendix C.1), as also to computational options, i.e. diffusion vs. transport theory (see Table C.4 in Appendix C.1). Typical sensitivities for the bank worth are ~20% for RZ compared to HEX-Z, and 6% for RZ-diffusion compared to RZ-transport.
(4) The reactivity effect of the thermal expansions and the fuel Doppler effect are sensitive to the CA positions, the differences being in the range of 20%. This has some importance for transient analyses performed, for instance, in the point kinetics approximation, for which the fuel Doppler constant has to be provided.
(5) The sensitivity of the flux to the polynomial expansion is rather limited (~45 pcm) with respect to the tested domain. A good compromise is found with the reference options set “601”, which was adopted for all the ERANOS/VARIANT calculations.
(6) The homogeneous ECCO treatment of the fuel plates making up the GFR SAs, along with the adoption of the fuel temperature as the “homogeneous” temperature - which is the basis for the RCS - yields reactivity values which are in good agreement with a more sophisticated treatment.

The large CA-worth sensitivity underlines the need to use an accurate method to compute the CA worth, in conjunction with fine-group flux calculations in the transport theory approximation. In the presented cases, the CAs have been modeled as a homogeneous mixture of the different materials, which is an approximation. Later in this chapter, we will show the impact of this approximation. For this purpose, a more sophisticated, approach was used, based on perturbation theory, allowing the CA heterogeneity to be taken fully into account (see Section 4.5).

4.3 Control assembly pattern development

The different steps of the CAP development methodology are summarized in this section. Since CAs should be properly cooled, the starting point was the determination of the HG resulting from the nuclear reactions, especially the reaction $^{10}B(n, \alpha)^{7}Li$. The methodology applied has first focused on the HG within the absorber material, since this is what largely impacts the design and the safety. Too high temperatures within the CA will damage them and might lead to CA failures, which are unacceptable. The later investigations of transients driven by CA withdrawals (see Chapter 5) have been complementary to the current steady-state considerations, in that one has thereby evaluated the temperatures reached by the materials under abnormal hypothetical conditions.

4.3.1 Heat generation methodology in ERANOS

The HG calculations were performed using the RZ core model, thus allowing one to calculate the gamma source and the gamma-transport using the existing calculational routines in ERANOS, viz. using BISTRO.

The DSD assemblies were placed at their parking position, while the two CSD banks were inserted at different level of insertion. The reference insertion has been fixed at 33%, i.e. at an axial position of z=2.03 m. In the light of previous fast reactor studies, a 33%-insertion has been judged representative of inserted CAs during full nominal-power operation.

Specific procedures were used to compute the volumic heat generation, both for the absorber and the follower part. In order to better understand these values, analysis has been performed to break-down the integral values into the individual neutron-capture and gamma-ray components (gammas from fission, capture and inelastic scattering, essentially, with consideration of the gamma-transport effect). Finally, the axial distribution has been analyzed, mainly, for three different position of insertion, i.e., 33%, 50% and 100%.

There are several ways of computing the energy generation in ERANOS, depending on the required accuracy. A first method is the use of separate energy terms for the fission Q_f and for the capture Q_c. In this method, not only fissile isotopes release energy but also all other isotopes via capture contributions. A correction is then applied for energy loss in scattering and leakage, and subtracted from the energy released by fission and capture:

$$E = \sum_g \sum_e N^e \left\{ Q_c^e \sigma_{cg}^e + Q_f^e \sigma_{fg}^e - \left[(\upsilon - 1)\sigma_{fg}^e - \sigma_{cg}^e \right] \overline{E} \right\} \phi_g \qquad \text{Eq. 4.1}$$

where *e* denotes the nuclide and *g* the energy group, σ_c is the microscopic capture cross-section and σ_f the microscopic fission cross-section, ϕ_g stands for the total flux in the gth group, υ for the number of neutron emitted per fission and N^e is the nuclide number density. $\bar{E}$ is defined as follows:

$$\bar{E} = \frac{\sum_g \overline{E_g} \varphi_g}{\sum_g \varphi_g} \qquad \text{Eq. 4.2}$$

where $\overline{E_g}$ is defined by:

$$\overline{E_g} = \frac{E_{g+1} - E_g}{Log \dfrac{E_{g+1}}{E_g}} \qquad \text{Eq. 4.3}$$

The term $Q_c^e \sigma_{cg}^e + Q_f^e \sigma_{fg}^e - \left[(\upsilon - 1)\sigma_{fg}^e - \sigma_{cg}^e \right]$ is called the KERMA^{g,e} (Kinetic Energy Release per MAterial) factor, and the power rate P^g is calculated as:

$$\mathrm{P_g} = \sum\nolimits_{\mathrm{e}} N^e KERMA^{g,e} \phi_g \qquad \text{Eq. 4.4}$$

A second method (used in the present work) is more sophisticated and computes the energy release through the use of group-dependant energy values, KERMA^{e,g,x} values per material *e*, per group *g* and per reaction *x* [137]. To be consistent with the self-shielding treatment in ECCO, all KERMA values are self-shielded for each reaction considered (fission, capture, elastic and inelastic scattering). This is done by dividing the KERMA values by the corresponding cross-sections, which produce reduced KERMA values, independent of the spectrum and self-shielding [138].

The energy release is calculated by using the reaction rates for each group and each isotope:

$$P_g = \sum\nolimits_e \sum\nolimits_x Q_x^{g,e} N^e \sigma_x^{g,e} \phi_g \qquad \text{Eq. 4.5}$$

$$Q_x^{g,e} = \frac{KERMA_x^{g,e}}{\sigma_x^g}$$

The gamma contribution has been treated separately with another specific ERANOS module [139]. The advantage of this level of treatment is that the energy is released in the system where the gamma annihilation occurs, and not at the neutronic interaction location (the so-called gamma-transport effect).

The calculation of gamma-transport effects requires the computation of the gamma source and flux within the core, which requires the use of BISTRO and thus a GFR RZ model in ERANOS. In practice, the gamma source is first obtained by means of the computed neutron flux. The gamma flux is then obtained from the source term, while considering the (γ, γ) reactions. Finally, the gamma energy release is obtained using the gamma KERMA values. In ERANOS, use is made of [139]:

1. Gamma emission spectra in 33x36 groups (33 neutron energy groups and 36 gamma energy groups),
2. Gamma KERMA values in 36 energy groups,
3. A gamma-gamma macroscopic library in 36 energy groups.

For the gamma propagation calculation, use is made of BISTRO in the transport theory approximation. The gamma-gamma interactions exhibit a strong anisotropic behavior, the BISTRO core calculations being performed using P5, S16 approximations (anisotropy of scattering and angular discretization, respectively). In the model, the CSD was divided axially in 10 cm meshes, allowing one to compute the axial distribution.

It is important to mention that the gamma-transport method is particularly important for shielding (not covered in the present work) and also for SAs containing non-fissile materials such as diluents or absorbers. The gamma-transport effect is also a dominating factor in the presence of large flux gradients and highly heterogeneous assemblies. For homogeneous materials, on the other hand, it is expected that the transport term will be negligible since, at any particular location, there exists an equilibrium between the energy deposited by gammas arriving from the surroundings and the energy transported by gammas leaving that location. This is only valid if the material is homogeneous, which is of course not the case for a CA.

One limitation of the method is the fact that not all isotopes of current interest are available in the KERMA library, viz. Mo, Mn, Zr, Si, Ti, ^{4}He, ^{237}Np, ^{239}Np and ^{238}Pu. These isotopes are missing in the file for the reason they were considered of less interest at the time of the development of the procedure. However, Zr and Si are envisaged to be used in the GFR, for instance in the fuel matrix and in the reflector (Zr_3Si_2). In particular, the HG in the reflectors cannot be evaluated currently, the KERMA values being simply set to zero since the required isotopes are missing in the KERMA library.

Benchmarking of the GFR RZ model to compute the HG and the related transport effects, has been done directly against the HEX-Z model, with the limitation that the gamma-transport term had to be neglected. The neutronic contribution was compared, and good agreement obtained (see Section 4.3.2).

4.3.2 Neutronic considerations

Heat Generation (HG)

The described methodology has been applied to a homogeneous CSD assembly for three positions of insertion: 33%, 50%, and 100%. The HG are volumic values (see Table 4.5), taking into account all materials within the CA. The values for the absorber regions are given separately for the three different CA insertions considered. That for the assembly follower, on the contrary, is only for the 33% case. Due to the large volume of the follower and, more important, the absence of absorber material, the heat generation within the follower is not sensitive to the position of the CA. Therefore, only the one case is shown in Table 4.5.

Table 4.5 Heat generation within the control assembly for the three insertion values, as also in the assembly follower (latter results shown for the case corresponding to 33% insertion).

Parameter	33%	50%	100%	Follower
Integrated power, kW	284	437	879	72
Volume, cm^3	6.05E+04	7.06E+04	1.01E+05	4.10E+04
Average power density, W/cm^3	4.7	6.2	8.7	1.8
Gamma power density, W/cm^3	0.8	1.1	1.5	1.6
Gamma fraction, %	17	18	17	92

Consideration of 50% and 100% insertion, in addition to the reference 33% case, allows one to examine the sensitivity to the CA position. From the results of Table 4.5, it is observed that the average volumic power shows an increase of 32% for the 50% case and of 85% for a fully inserted CA, relative to the reference insertion, which is of importance.

The presence of the absorber modifies the axial neutron flux shape and, consequently, impacts the axial distribution of the heat generation within the assembly (as it does also the dependence of the CA worth on the position of insertion). At the end, this also impacts the CA surface temperature reached at the maximal-flux location. To illustrate this aspect, the axial distribution of the neutron flux is depicted in Figure 4.6 for the 100% insertion case.

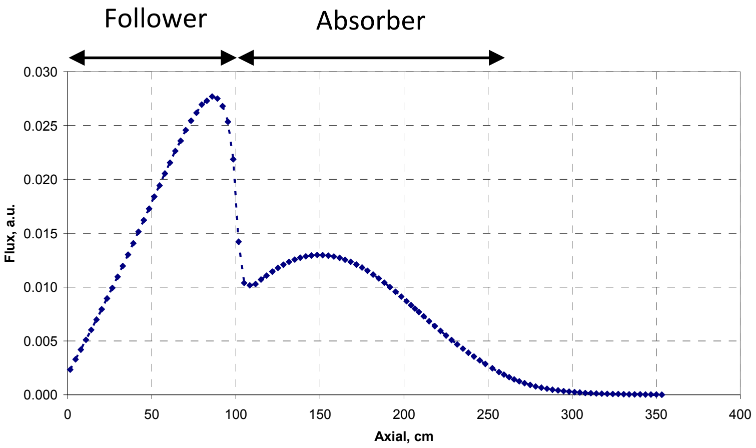

Figure 4.6 Axial distribution of the neutron flux within the control assembly and follower (100% insertion)

A large neutron flux increase is seen in Figure 4.6, under the absorber part of the CA , i.e. within the follower. As expected, the heat generation profile in the absorber (see Figure 4.7) largely coincides with the corresponding flux profile. The peak located towards the end of the absorber region, i.e., at the interface between the CA and the follower, results from the large flux values in the follower. This peak will also produce a large local increase in the CA surface temperature.

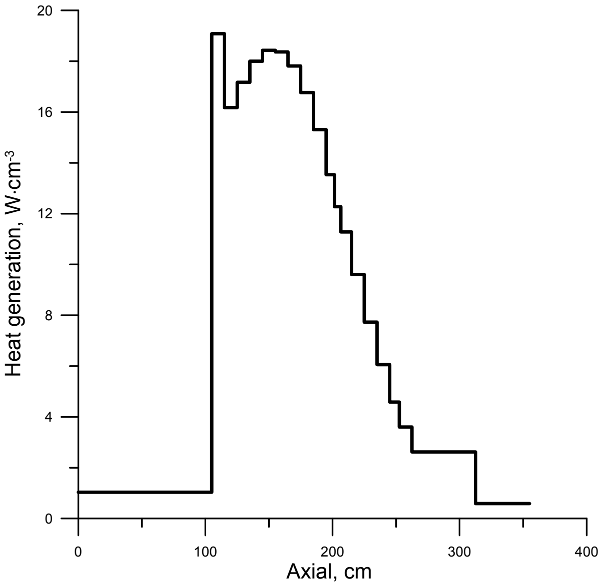

Figure 4.7 Axial heat generation profile (100% insertion). The heat within the follower (0 – 100 cm) and above z=255 cm are averaged values for 0 to z=100 cm and for z=255 to 355 cm, respectively

To complete this analysis, the main contributions, viz. those from the ^{10}B and ^{56}Fe capture reactions, are shown in normalized form in Figure 4.8. The boron reaction rate goes to zero in the follower region (since there is no boron in it), and the peak, at the interface between absorber and follower, is clearly observed. The ^{56}Fe capture rate shows, on the contrary, a similar variation to that of the neutron flux throughout the length of the CA, i.e. with a large increase within the follower.

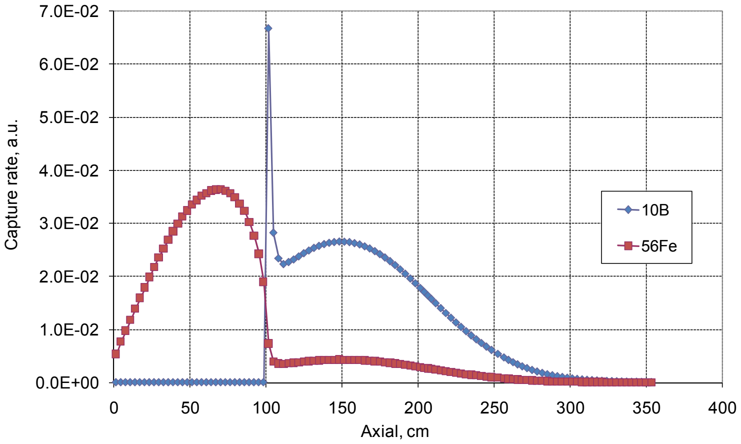

Figure 4.8 Axial distributions of the ^{10}B and ^{56}Fe capture rates within the control assembly

As indicated earlier, detailed consideration has currently been made of the individual components of the heat generation, i.e. neutron capture and gamma absorption. The relative terms are provided in Table 4.6, the %-values in brackets being the fraction of the gamma energy deposition resulting from gamma-transport effects.

Table 4.6 Relative contributions (%) – neutron capture and gamma-rays – to the heat generation within the control assembly and follower. The value in brackets, in each case, represents the fraction of the gamma energy deposition resulting from gamma-transport effects.

Region	Neutrons, %	Gamma-rays, %
CSD	82	18 (15)
Follower	8	92 (77)

For the CSD, it is seen that the gamma-ray contribution represents ~18% of the total heat generation. Moreover, the transport term contributes only ~15% to the total gamma power, i.e. the transport effect is relatively negligible. This is partly due the fact that both the fuel and the absorber assemblies are modeled as homogeneous mixtures, limiting the consideration of spatial effects (flux gradients). On the other hand, within the assembly follower, the gamma power represents 92% of the total and the transport term, in this case, is as high as 77%. This implies that transport effects can by no means be neglected for the follower region.

To complete the detailed analysis, the neutronic power has been decomposed in terms of the contributions from individual isotopes (see Table 4.7).

Table 4.7 Main contributions to the heat generation in absorber regions from different neutron capture reactions (contributions > 0.5%)

Nuclide	Rel. Contribution, %	Reaction
^{10}B	83.2	(n,α)
^{56}Fe	9.4	Capture and inelastic scattering
^{58}Ni	2.0	Capture and inelastic scattering
^{52}Cr	1.8	Principally inelastic scattering
^{54}Fe	0.8	Capture and inelastic scattering
^{60}Ni	0.8	Capture and inelastic scattering

As is seen from Table 4.7, the main contribution (83%) is due to the ^{10}B (n,α) reaction, followed by ^{56}Fe capture and inelastic scattering with 9%, the two together representing of 92% of the total. These results confirm that stainless steel (AIM1-type), used here as structural material for clad and wrapper, is of some importance. However, for the new developed design, steel is no longer envisaged for the wrapper, due to the high temperature expected (see Subsection 4.3.4). As a consequence, use of the same boron carbide volume fraction may be expected to imply a decrease in the heat generation when steel is replaced by ceramic. On the other hand, this might lead to a softer neutron spectrum, with other indirect effects. Verification and sensitivity studies were performed to address this point and no large differences were observed, i.e. in the current case compensation was found between the lower heat generation produced by the absence of steel and the higher rate resulting from the increase in the ^{10}B capture due to the softer spectrum.

Consideration of penetration distance

An important parameter to be considered for a CA is the penetration distance of neutrons into the boron carbide pellet. This distance provides an indication of the optimal pellet diameter and such an analysis was used to help choosing the optimal absorber pin radius. If the radius is significantly larger than the penetration distance, the inner part of the pellet will not contribute to the neutron absorption due to the heavy self-shielding effects, which lead to a decrease in the absorption per ^{10}B atom (corresponding, in other words, to an increase in the heterogeneity effect). The self-shielding effects occurring within two pellet diameters (large and small) are illustrated in Figure 4.9. Clearly the pellet fraction contributing to neutron absorption is larger for a small pellet diameter than for a large value (relative to the penetration distance).

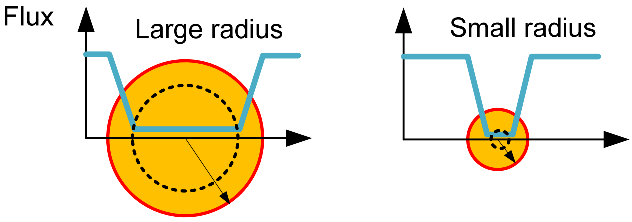

Figure 4.9 Illustration of self-shielding effects for two absorber pellet sizes: large diameter on the left hand-side and small diameter on the right hand-side

Furthermore, the spatial arrangement of the absorber pins is important from the viewpoint of shadowing effects between the pins. This point is treated in more detail in Section 4.4.

In the current study, the neutron mean free path (MFP) has been calculated to assess the neutron penetration distance within the B_4C pellets, in order to recommend the absorber pin diameter. The analysis was performed with MCNPX-2.5e [101], using a specially developed, 3D HEX-Z GFR core model in conjunction with a one pin-equivalent heterogeneous EFR-type CA (see Figure 4.10), derived from the material volume fractions of the EFR assembly. Except for this specific CA, all materials were homogeneous, as in the HEX-Z ERANOS model.

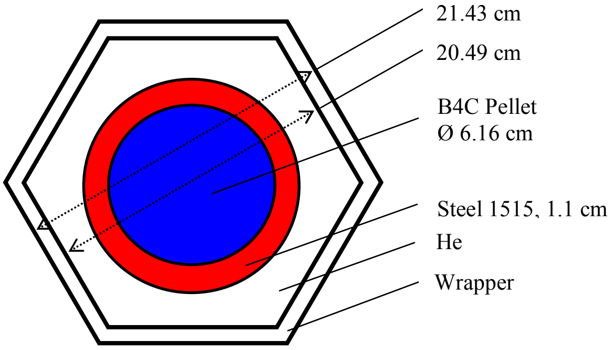

Figure 4.10 Heterogeneous control assembly model used in MCNPX to assess the mean free path within the B_4C pellets (not to scale drawing)

The purpose of the study being to assess the penetration distance in the boron, no detailed modeling of the CA (and especially of the absorber pins) was necessary. We may also recall that, at this stage of the development, the heterogeneous pattern was not available.

The MFP in the B_4C has been calculated to be ~26 mm. This value gives an indication that the neutron absorption is highly reduced after this distance, reducing the efficiency of the CA design. The relative flux within the various materials (arbitrarily normalized to 100% in the cladding) is depicted in Figure 4.11. It is observed that the flux is not suppressed significantly in the wrapper and the coolant. The suppression is, however, seen to be strong in the central absorber and confirms the value given above for the MFP.

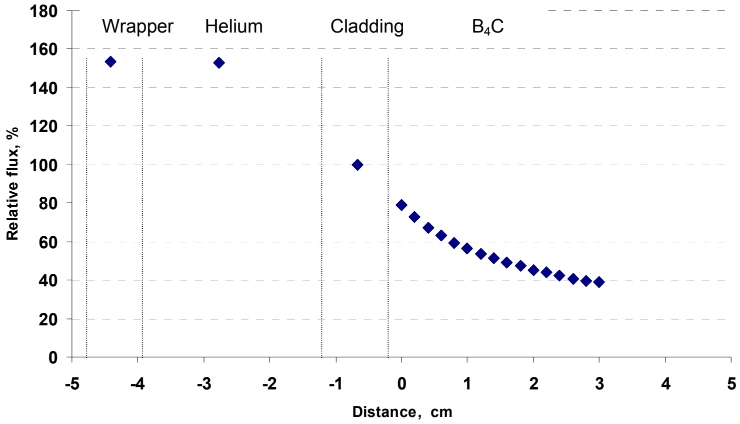

Figure 4.11 Neutron flux within an equivalent heterogeneous, EFR-based CA. Analysis performed with MCNPX. The distance is expressed from the absorber pellet

Based upon the results of the mean free path assessment with Monte Carlo simulations, additional investigations were made on the MFP sensitivity to the ^{10}B content. It was observed that the MFP is not highly modified (28 mm compared to 26 mm) with a lower ^{10}B content (48% instead of 90%), while the CA worth reduces significantly, i.e. by ~20%.

On the basis of these results, and, taking into account the wish to maximize the absorption for a given CA size, absorber pins, consisting of 20 mm diameter cladding tubes filled with high-enriched boron carbide (90%), were chosen, the diameter being slightly lower than the mean free path due to a better integration of the pins within the available cross-sectional area. This diameter ensures that, in addition to a high heat transfer between the pins and the coolant, there is no excessive self-shielding within the pellets, nor large shadowing effects within the CAs. The minimization of these undesired effects, mainly for assuring a high efficiency of the CAs, was an important part of the design requirements and optimization.

For verification purposes, the MCNPX mean free path value for the homogeneous CA was compared to that directly deduced from the total macroscopic cross-section ($1/\Sigma_{total}$), as calculated by ECCO. The two values (4.7 cm from MCNP, 4.1 cm from ECCO) were found to agree reasonably well.

Benchmarking against the HEX-Z model

For verification purposes, the HG (without the gamma-transport term) has been calculated within a first CSD bank of CAs, inserted at 33%, using the HEX-Z core model. The average power density obtained was $P_{average} = 13.4$ W.cm^{-3}.

To be consistent, this value has to be compared with the equivalent result from the RZ model, i.e. the value without the gamma-transport term. This was $P_{average} = 12.7$ W.cm^{3}, showing that the comparison agrees within about 5%. It has to be noted that these values are given for the HG fraction within the fuel region of the CAs and do not include gamma heating. As such, they are not to be directly compared with the values of Table 4.5, which give the total CA power density.

Benchmarking of the methodology against the TRIPOLI4 code

The above presented methodology has been applied additionally to the ETDR startup core, in order to enable a comparison with results obtained using the CEA's Monte Carlo code, TRIPOLI4. The results are presented in Appendix C, Section C.2, agreement being obtained in the range of 4%, and hence further confirming the adequacy of the methods used in the present work.

4.3.3 Thermal-hydraulic considerations

Once the neutronics results had been determined, a first-iteration, heterogeneous-CA design was implemented, assuming a certain volumic coolant-fraction and a lattice of pin absorbers. Consequently, a 2D model was developed for use with the CEA code COPERNIC, in order to evaluate the thermal-hydraulic parameters, in particular, the material temperature at CA outlet, with the mass flow rate being imposed as a boundary condition. The calculations were performed for 10 cm axial meshes and, within each mesh, the heat source was imposed by the heat generation results provided by the neutronics analysis (see Figure 4.7). As indicated earlier, CA design calculations need to be performed in an iterative process to converge upon an optimized design that fulfills both thermal-hydraulics and neutronic constraints. In particular these constraints are:

(1) Maximization of the absorber volumic fraction,
(2) Minimization of the coolant flow rate,
(3) Minimization of the neutronic interactions between pins within the assembly, which requires an adequate spatial dispersion of the absorber pins allowing a minimization of the self-shielding effects.

The design process, depicting the coupled neutronics and TH calculations, is illustrated in Figure 4.12. The loop represents the successive iterations from the first design (iteration 0) to the final optimized design.

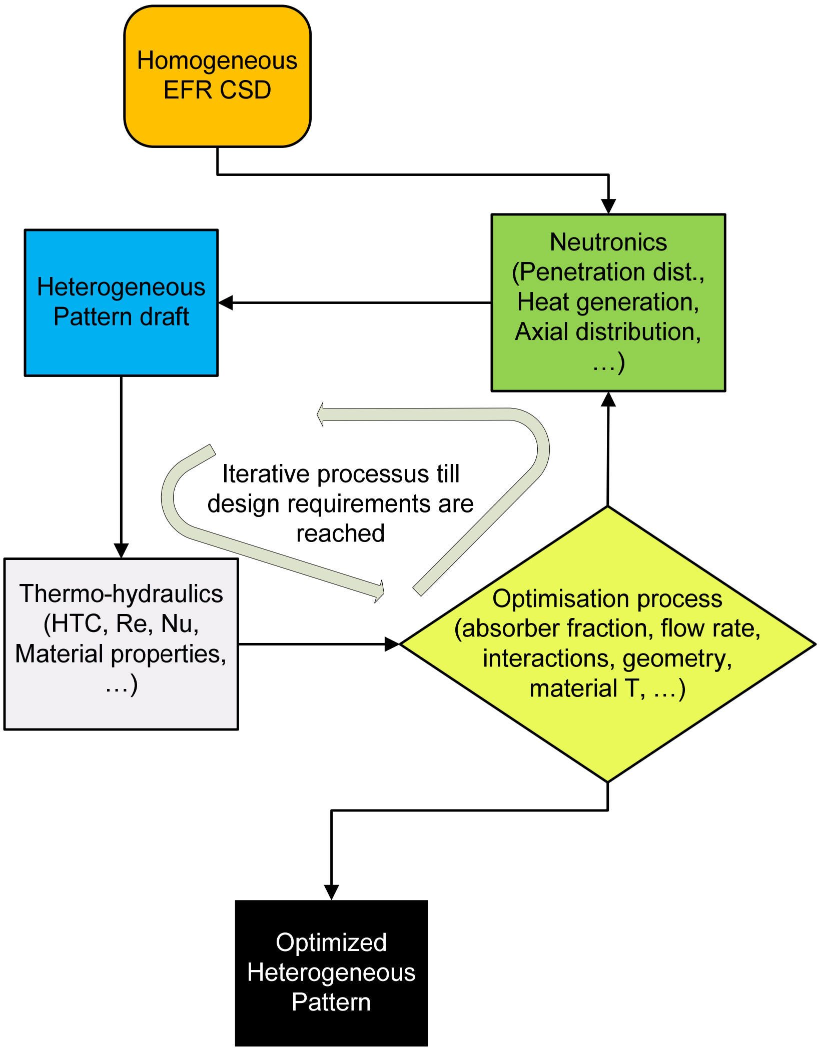

Figure 4.12 Illustration of the coupled neutronic and thermal-hydraulics calculations. The optimization process is made via an iterative scheme.

The temperature profiles were computed, for the successively developed CAPs, for three positions of insertion and different helium mass flow rates, using the corresponding HG values (in particular, results from Table 4.5). Selected results, corresponding to three different helium mass flow rates (0.4, 0.8 and 1.0 kg/s) are shown in Figure 4.13, Figure 4.14 and Figure 4.15, for three different CA-insertion cases, viz. 33% (reference), 50% and 100%, respectively. These plots consider the optimized and finally developed CA.

As seen, each of the figures shows two sets of curves computed with the COPERNIC code. These correspond to different assumptions for the contact surface between the cladding and the coolant: “smooth” and “rough”, referring to the cladding surface roughness. The heat transfer coefficient is derived with the Dittus-Boelter correlation for forced convection of developed turbulent flow. In the “smooth” case, a typical value for the cladding roughness is considered to compute the heat transfer coefficient. On the contrary, for the “rough” case, the heat exchange between the absorber pins and the coolant was increased using an artificial increase of the cladding roughness, the effective increase in contact area and fluid turbulence leading to lower cladding temperature.

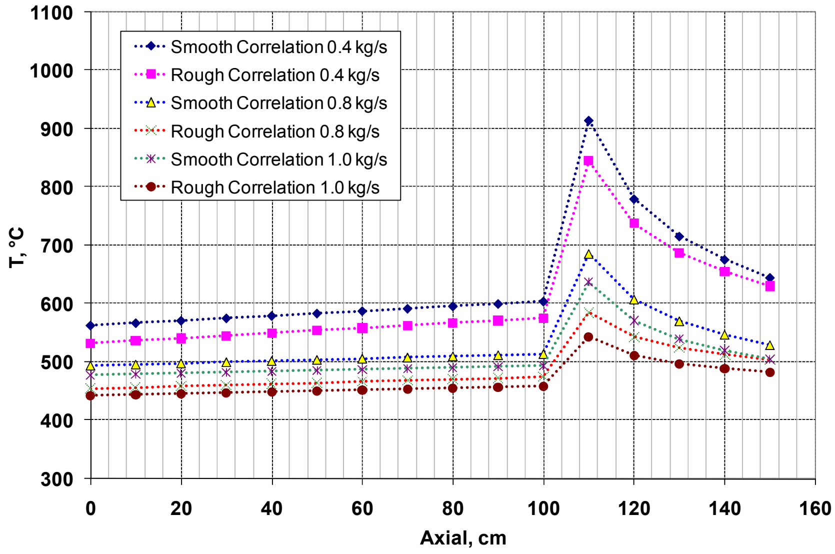

Figure 4.13 Absorber pin cladding temperature for the heterogeneous CA-pattern, 33% insertion. The CA follower is below z=103 cm

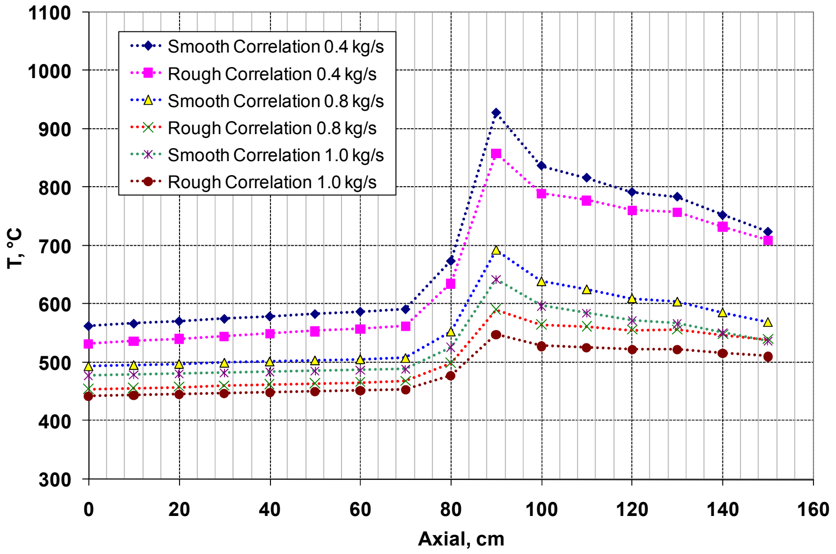

Figure 4.14 Absorber pin cladding temperature for the heterogeneous CA-pattern, 50% insertion

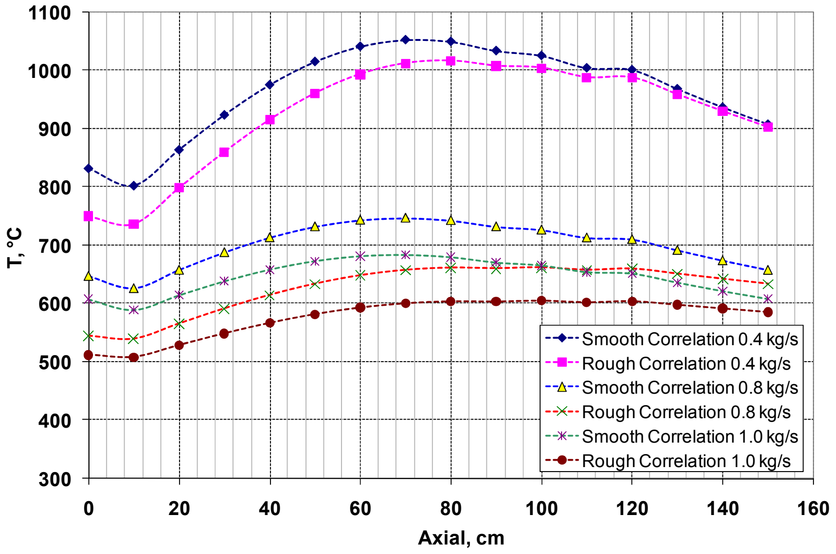

Figure 4.15 Absorber pin cladding temperature for the heterogeneous CA-pattern, 100% insertion

An important parameter to be determined in the design process is the He flow area, which impacts the heat transfer coefficient indirectly. In the proposed design, the fractional area to be dedicated to the coolant is 40% and was minimized, as indicated earlier, in an iterative process, to maximize the absorber fraction. The coolant fraction value is consequently lower than it was for EFR (~50%) and this allow a large volumic fraction of the absorber material.

The temperatures increase only slightly along the assembly follower (see Figure 4.13 for instance). However, there is a large increase of the assembly temperature when the absorber region is reached, i.e. at ~1.1 m for the 33% insertion case, which reflects the large increase in the heat generation rates.

One of the innovative features of the CA design (see Subsection 4.3.4) is the central part (so-called static zone), which is filled with static helium (i.e. not acting as coolant), in order to increase the heat transfer in the helium surrounding the pins. This increase was achieved via the effectively reduced flow area of the coolant, leading to an increase in the coolant velocity. Compared to a design without the central static zone, the resulting decrease in material temperatures was between 50 and 100°C, depending on the relative insertion of the CAs and the HTC used.

Considering the most conservative case, viz. that of 100% CA-insertion, it was found (in association with use of the "rough surface" correlation) that a coolant flow rate of ~1.0 kg/s is needed per CA, in order to maintain the cladding temperature below ~630°C (assuming AIM1-type steel as cladding material, as recommended in the Phénix safety dossier). For the two CA banks together, this corresponds to ~2.5% of the total mass flow rate, a reasonable low fraction for cooling the CAs. The upper plenum temperature is not influenced significantly by this mass flow rate, the temperature effect being in the range of only a few degrees.

4.3.4 Description of the GFR CA design

The final design arrived at for the CA of the reference large GFR is presented in this subsection, the principal calculation steps having already been discussed in detail in the previous sections.

The developed CA (see Figure 4.16) consists of 54 absorber pins, 20 mm in diameter, within a triangular lattice. To complete the representation, a 3D view is shown in Figure 4.17. The pins are held together by metallic grids fixed upon a central drive mechanism which passes through the core from below. The non-moving part consists of a dual-layer hexagonal wrapper made of SiC, the thickness being 9 mm. Compared to a fuel SA, the thickness of the wrapper has been significantly increased to reinforce its strength and thus avoid, in case of core compaction after severe mechanical core deformation, the deformation of the CA channel. This ensures that the channels stay free and non-deformed, allowing CA insertions if needed.

As indicated earlier, the central static-He zone of the CA allows a reduction of 50 to 100°C to be achieved for the cladding temperature. From the neutronics viewpoint, the presence of this zone contributes to reducing self-shielding effects between the absorber pins (see Section 4.5).

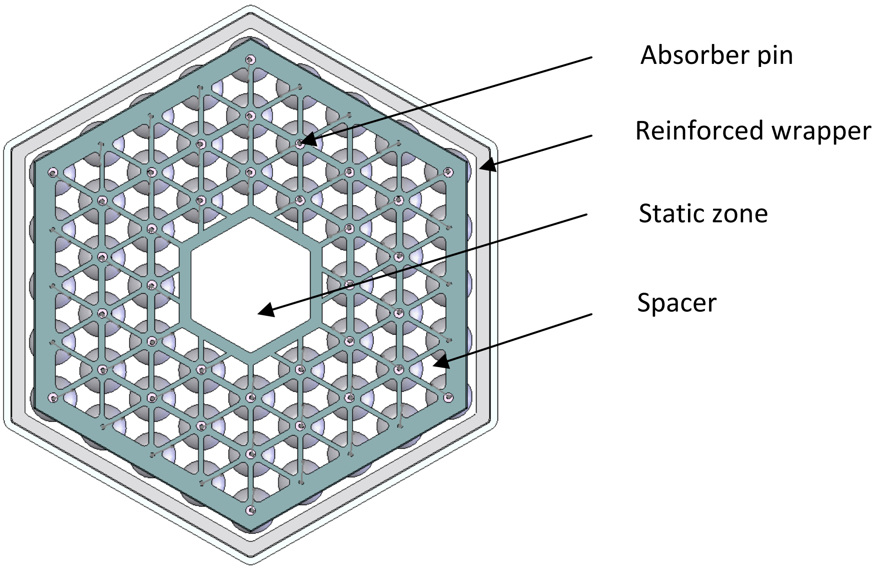

Figure 4.16 XY cut of the CA pattern for the GFR

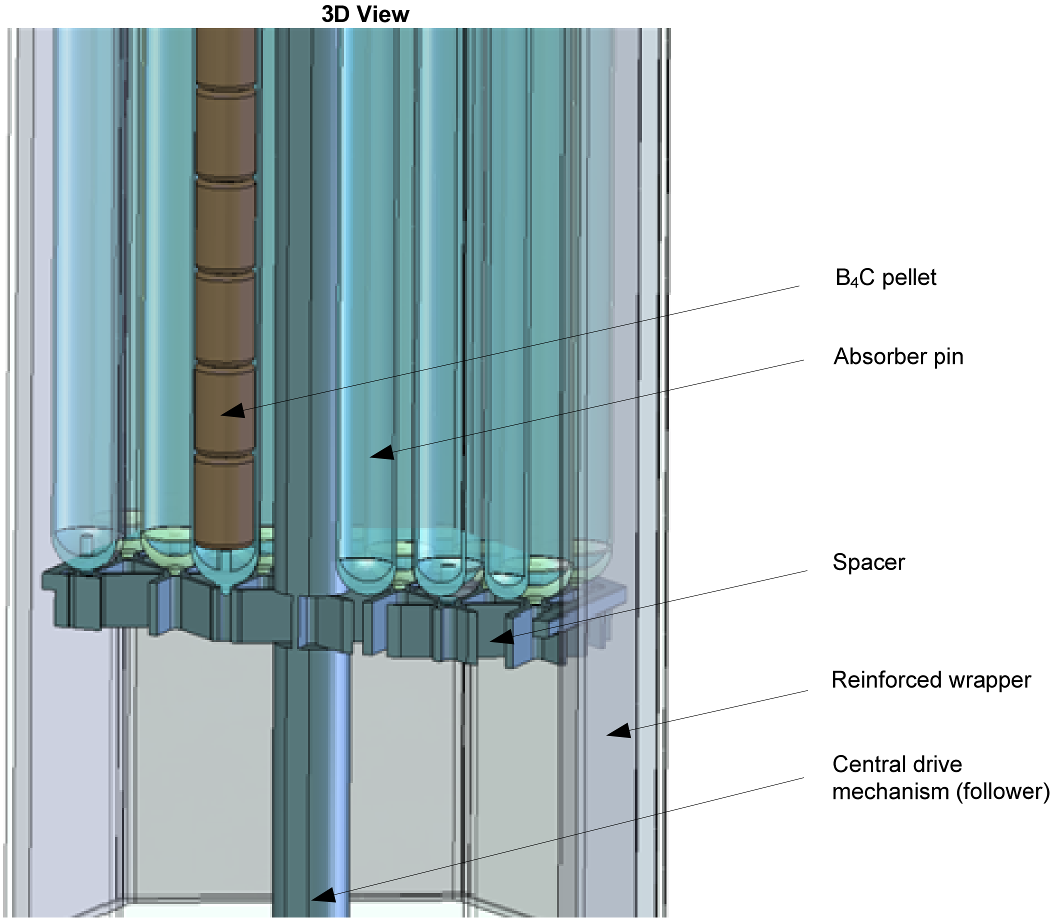

Figure 4.17 3D view of the control assembly (absorber part)

The volume fraction of B_4C is 35%, instead of 30% as in the EFR design, implying that the spatial arrangement of the pins has also been optimized. Moreover, the CA movement is from the bottom of the core, by means of a central metallic shaft (see Section 4.3.5) – the CA follower – which passes through the core. The main design characteristics of the CA pattern are summarized in Table 4.8.

One particular remark should be made regarding the design. It was mentioned that the cladding material and the central drive mechanism are made of stainless steel. Despite the high coolant core temperature, in the range of 850°C, this option appears acceptable since the coolant mass flow rate was carefully adjusted to deal with the temperature limit for steel. Additionally, the coolant mass flow rate, derived from the present study, considers a fully inserted CA combined to full power operation, which is clearly a conservative case. Nevertheless, neutronics investigations have been performed to assess the impact of, for instance, replacing the stainless steel of the absorber pin cladding and the central mechanism drive with ferritic alloys, such as ferritic superalloy Alloy 800H [140]. No significant differences in the neutron spectrum or heat generation rate were observed, while the CA worth was somewhat more sensitive.

Table 4.8 Main characteristics of the optimized control assembly pattern

Heterogeneous design	**Characteristics**
Wrapper	SiC, 9 mm thick
Absorber Pin	54 absorber pins, 20 mm in diameter, 1 mm thick AIM1-cladding, triangular lattice of pitch 24.5 mm
Absorber material	B_4C - 90% ^{10}B
Absorber cooling surface	5.43 m^2
Hydraulic diameter	13.1 mm
Central static zone	60 mm across inner structure with static helium
Total surface and assembly size	389.2 cm^2, 21.2 cm (across flats), and 1.15 mm He gap
Material	Volumic fraction, %
SiC	15.9
AIM1	9.5
B_4C	34.6
Helium	40.0

4.3.5 CA drive mechanism

Complementary to the CA design, the CA drive mechanism (or follower) was studied in a preliminary manner. The SiC wrapper is 9 mm thick. At the current time, the CA follower is assumed to be made of AIM1-steel and 60 mm in diameter, radially centered within the assembly. Once again, all these materials have been considered smeared into an equivalent homogeneous mixture. The corresponding volumic fractions are given in Table 4.9.

Table 4.9 Volumic fractions of the homogenized CA follower

Material	Volumic fraction, %
SiC	15.9
AIM1-steel	7.8
Helium	76.3

4.4 Control assembly interactions

In the course of the development of the final CA pattern for the large GFR core, significant interactions were observed between the individual CAs, as also between the banks (see Figure 4.1 for the GFR core description with the positions of the corresponding CAs). These have been investigated in detail while studying possible implementation schemes (starting from that used in the EFR) using the HEX-Z model. It is important to note that the results provided below have been obtained in conjunction with homogenized EFR-type CAs, the neutronic characterization and the CA design work (see Section 4.3) having partly been carried out in parallel. This implies that differences in the CA worths are possible when comparing the different tables of results[5].

4.4.1 Definitions

The two main parameters used for characterizing the interactions are:

(1) The assembly interaction effect δ,
(2) The amplification factor *A*.

In effect, shadowing and anti-shadowing effects, or interactions between CAs leading to a decrease or increase of the CA efficiency, are associated with the modification, as a consequence of the presence of other CAs, of the nominal worth of a given CA. The origins of the modifications have to be seen in the spatial perturbation of the neutron flux (see, for instance, Figure 4.18). The CA interaction is defined as the relative difference between the value of the total worth of a group of CAs and the sum of the individual worths. Thus, if there are N CAs (or banks), each with a reactivity worth $\Delta\rho_i$, then the assembly (or bank) interaction effect [141] δ is given by:

$$\delta \equiv \frac{\Delta\rho_{1,2,\ldots N} - \sum_{i=1}^{N} \Delta\rho_i}{\Delta\rho_{1,2,\ldots N}} \qquad \text{Eq. 4.6}$$

---

[5] Some differences also occur because of modifications adopted in material compositions for instance.

where $\Delta\rho_{1,2,\ldots N}$ is the total worth of all N assemblies (defined positive) and $\Delta\rho_i$ is the worth of an individual assembly *i*.

If $\delta \neq 0$, then there is some interaction, and in this case there are two possibilities, viz. $\delta < 0$ and $\delta > 0$. The case $\delta < 0$ corresponds to a shadowing effect, where a CA in a certain location can reduce the reactivity worth of another CA. The situation with $\delta > 0$ corresponds to anti-shadowing, the combined worth being greater than the sum of the individual worths.

In addition to δ, another parameter called the amplification factor (A_J) of control assembly J, is defined by:

$$A_J = \frac{\Delta\rho_{1,2,\ldots J} - \Delta\rho_{1,2,\ldots J-1}}{\Delta\rho_J} \qquad \text{Eq. 4.7}$$

where $\Delta\rho_{1,\ldots,J}$ is the total worth of all assemblies (1 to J), $\Delta\rho_{1,\ldots,J-1}$ the total assembly worth of the assemblies 1 to *J-1* and $\Delta\rho_J$ the worth of the single assembly *J*. If $A_J > 1$, the CA worth is amplified, and this corresponds to an anti-shadowing effect, while if $A_J < 1$, the CA worth is reduced and one has a shadowing effect.

4.4.2 Interactions within the reference GFR Core

Both the above parameters permit the quantification of the degree of interaction in the GFR core, between the different CA banks, as well as between the individual assemblies within a given bank. Consequently, calculations have been carried out for various combinations of inserted CA banks (see Table 4.10), the corresponding inserted-bank reactivity worths allowing one to quantify the diverse interactions in terms of δ and A_J values. The CA-bank interactions are presented in Table 4.11 and show quite different effects for the different cases. Thus, large anti-shadowing effects take place between the two CSD banks (δ = 46%), as well as between the DSD and the two CSD banks taken separately (δ = 31%). For the interaction between the DSD and the second CSD alone, the effects are more limited (δ = 8%).

Table 4.10 Control assembly bank configurations and corresponding worths (EFR-type control assemblies and operating conditions)

Configurations	1st CSD	DSD	2nd CSD	Worth, pcm
Both CSD inserted	in	out	in	15598
1st CSD inserted	in	out	out	2372
2nd CSD inserted	out	out	in	6052
DSD inserted	out	in	out	4788
Both CSD and DSD	in	in	in	19171
1st CSD and DSD	in	in	out	5553
2nd CSD and DSD	out	in	in	11818

Table 4.11 Control assembly bank interactions (δ)

Bank interaction	δ, %
Between 1st CSD and 2nd CSD	46
Between DSD and both CSD	31
Between DSD and 1st CSD	-29
Between DSD and 2nd CSD	8

For the largest interaction case, i.e. that between the two CSD banks (δ = 46%), the total worth (15598 pcm) is increased by a factor of almost 2, as compared to the sum (8424 pcm) of the individual bank values (2372 pcm for the first CSD bank and 6052 pcm for the second). In the case of the interaction between the DSD and the first CSD bank on its own, one has a large shadowing effect (δ = -29%). Table 4.12 gives the amplification factors for the individual banks for selected cases.

Table 4.12 Amplification factors (A_j) for selected cases

Bank	Case	A_J
1st CSD	In conjunction with 2nd CSD	4.0
2nd CSD	In conjunction with 1st CSD	2.2
DSD	In conjunction with both CSDs	0.7

The values in Table 4.12 confirm the fact that each CSD bank amplifies the worth of the other CSD bank (A_J = 4.0 and 2.2). On the other hand, the amplification factor of the safety bank, viewed in conjunction with both CSDs, is 0.7. This implies a shadowing effect and is consistent with the corresponding negative δ value in Table 4.11.

Table 4.13 shows the interactions at the level of individual assemblies within the different CA banks. Shadowing effects are observed for the assemblies within the first CSD bank (δ = -34%), while anti-shadowing effects are seen for the other two cases (δ = 11% for the effects within the 2nd CSD bank, and δ = 20% for the DSD assemblies). For the first CSD bank, the shadowing leads to a reduction of the individual CA worth from 530 pcm (the value derived from the insertion of a single CSD assembly) to 395 pcm, the average worth per assembly considering insertion of the entire bank ($\Delta\rho$= 2370 pcm for all 6 CSDs inserted).

Table 4.13 Interactions (δ) for individual assemblies in the different banks

Configuration	δ, %
1st CSD bank	-34
2nd CSD bank	11
DSD bank	20

From a study of Tables 4.11 to 4.13, it is seen that the various interactions, at both bank and individual assembly levels, are dependent, in a complex manner, on several different factors, e.g. location, number of assemblies, type of other bank/assembly, etc.

Large interactions between the CAs are not favorable for the core safety, since the level of reactivity is then dependent on the position of other CAs and individual movements of CAs can lead to local increase of power. Moreover, the interactions impact the number of CAs and the individual CA worth allowed in the core. For example, in the presence of large interactions, it is necessary to reduce the reactivity worth of a CA, in order to limit its impact on the other CAs. The amplifications take their origin in the largely decoupled neutronic zones of the core. To avoid any local power peak, the density of CAs has to be sufficiently high allowing better control of each zone of the core. Finally, it is also necessary to have independent CA drives, to counter-balance any local power disturbance.

Certain supplementary studies showed that there are, in principle, possible ways to reduce the interaction effects drastically, but these are not practical in most cases. Thus, for example, if one were to group the control assemblies belonging to the two CSD banks, such that half the 1st-CSD-bank assemblies were grouped with half the 2nd-CSD-bank assemblies, one would have two new "banks", for which the anti-shadowing would be as low as 5%. However, such a cross-linking of assemblies belonging to different "rings" would not be able to meet power flattening requirements associated to burnup in a satisfactory manner.

4.4.3 Radial traverses

The introduction of the different CA banks significantly affects the radial neutron flux profile, which is essentially the basic reason for the amplification of bank worths indicated in Table 4.10. To investigate the origin of these large interactions more closely, radial traverses of the neutron flux and fission power were computed for the four main configurations:

1. All assemblies withdrawn,
2. All CSD assemblies inserted,
3. Only the first CSD bank inserted,
4. Only the second CSD bank inserted.

Figure 4.18 and Figure 4.19 show the radial traverses of flux and power, respectively, for the different cases and illustrate that the movement of an individual CSD bank leads to a large displacement in the neutron flux (Arbitrarily, in these two figures, the core power is assumed to be constant). The effect on the flux is clearest for the second CSD bank, where there is a strong shift from the core periphery towards the centre. In Figure 4.19, it is seen that the form factor becomes very high (about 3) when the second CSD bank is introduced.

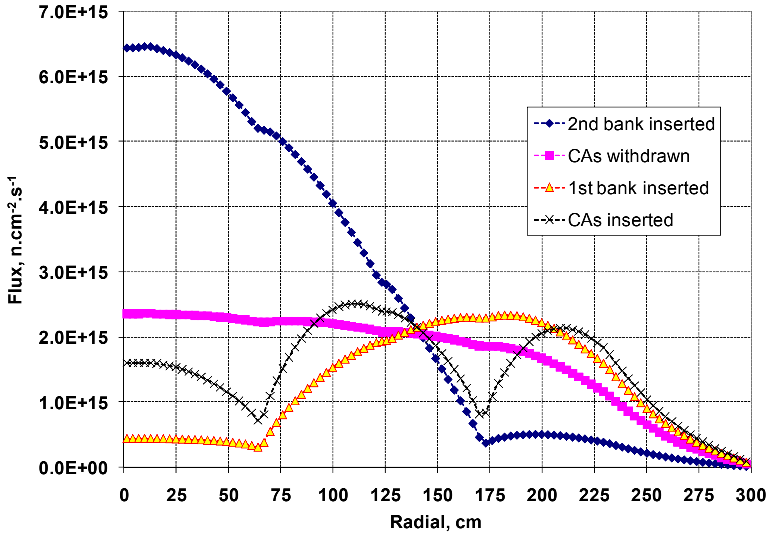

Figure 4.18 Radial traverses of the neutron flux at mid-core with respect to four CA bank positions (identical core power): (1) all assemblies withdrawn, (2) all CSD assemblies inserted, (3) only the first CSD bank inserted, and (4) only the second CSD bank inserted

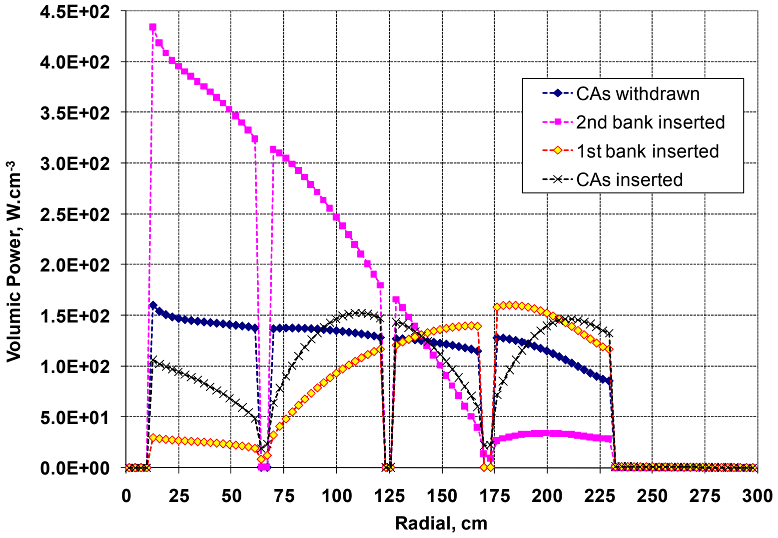

Figure 4.19 Radial traverses of the fission power at mid-core with respect to the four control assembly bank positions considered in Figure 4.18 (identical core power)

It is important to stress that these observations (shift of the flux) are qualitatively consistent with measurements made in Superphénix, confirming the existence of the phenomenon. Similar observations, albeit at different amplitude levels, have also been made for various test reactors [142; 143].

4.4.4 Eigenvalue separation analysis

One important aspect of this work has been to identify and apply an easy method that allows one to anticipate the existence of CA amplification effects without performing time consuming calculations, viz. application of the so-called eigenvalue separation (SVP) approach. Thus, additional investigations have been performed, using the RZ 2D BISTRO model, to determine the 1st order eigenvalue and the SVP, defined by the following equation [144]:

$$SVP \equiv \frac{1}{1-\frac{k_{Order1}}{k_{Fundamental}}} \qquad \text{Eq. 4.8}$$

where k_{order1} is the eigenvalue corresponding to the first harmonic of the Boltzmann equation and $k_{fundamental}$ is the fundamental eigenvalue.

A large SVP value means that the magnitude of the first order eigenvalue is comparable to the fundamental eigenvalue and consequently leads to neutronic instabilities and power oscillations [144; 145] for the reason that the neutronics zones of the core are weakly coupled. In other words, a local perturbation can be propagated at high range when the SVP value is high (about 10 or more). The importance of harmonics is principally correlated to the overall core dimensions or to the height-to-diameter ratio (H/D), as also to the average mean free path over the whole core. With a low H/D ratio, the harmonics can be propagated more easily radially within the core. The SVP values have been computed for two control assembly bank configurations:

(1) All assemblies withdrawn,
(2) Only the second CSD bank inserted.

The results are presented in Table 4.14, mainly to confirm that the harmonics propagation can be lower when absorbing materials (low mean free path in absorber) are introduced within the core. It is seen that the SVP value of 8.2 (all assemblies withdrawn) is large and is reduced when the absorbers are inserted, with a SVP value of 7.0 for the configuration with the 2nd CSD bank inserted. This reduction is to be expected since the insertion of an absorber would inhibit the propagation of harmonics within the core, corroborating the statement made above.

Table 4.14 Eigenvalue separation (SVP) with respect to two control assembly bank configurations: (1) All CAs withdrawn, and (2) only the second CSD bank inserted

Configuration	SVP	$k_{eff, fund.}$	$k_{eff, 1st order}$
All CAs withdrawn	8.2	1.1030	0.9688
2nd CSD bank inserted	7.0	1.0336	0.8865

In previous studies, performed for Superphénix, the SVP value calculated was 10.5. Large CA interactions were measured (of the same order of magnitude, in between the banks) and instabilities problems were encountered. For the EFR, the SVP value is even higher at 13.6.

As a consequence, and taking into account the current GFR analysis, one has a clear confirmation that a high SVP (in the range of 8 or higher) value is a good indicator of the potential existence of large CA interactions. The advantage of such a criterion is that it provides an easy method to assess the likelihood of interactions and core instabilities.

The SVP value impacts the number of CAs. For instance, to limit the power oscillations due to the movement of a CA, it is necessary, to implement a high number of absorbers and to limit the speed of movement of these assemblies. Finally, the SVP also impacts the core instrumentation, with the need to measure the flux at a large number of locations in order to detect rapid changes in the power distribution.

Supplementary to the SVP values, the radial power distributions of the fundamental and first order eigenvalue for the two studied configurations are depicted in Figure 4.20 and Figure 4.21**.**

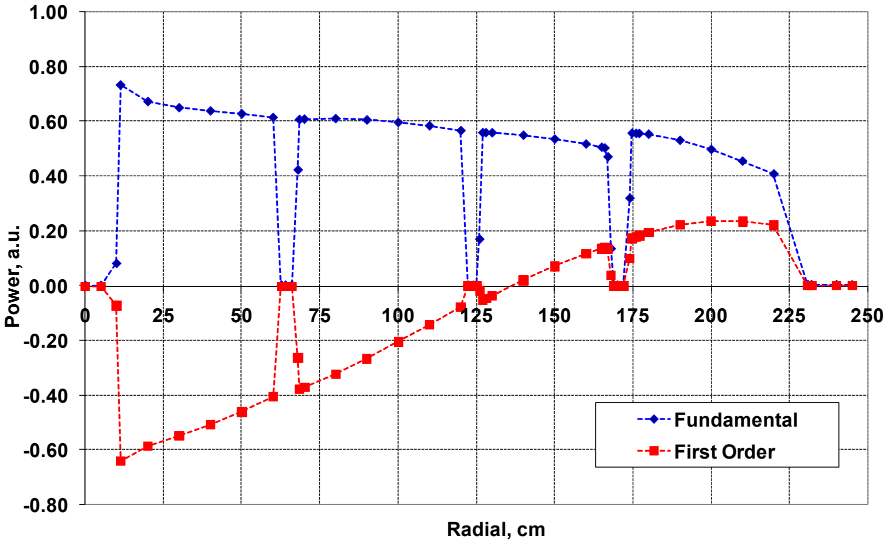

Figure 4.20 Radial power distribution at mid-core of the fundamental and first order eigenvalues for the "CAs withdrawn" configuration.

A differential behavior is observed for the first order eigenvalue, with a negative contribution in the inner core region, which then crosses the axis and becomes positive. An interesting finding is that the sign changes at the current location of the DSD assemblies, which means that the amplitude of the harmonics is minimal at that location. This suggests that the DSD assemblies, placed at 1.18 m (r/R = 0.53) from the core centre, minimize the interactions with other control assemblies. The amplification factor for the DSD assemblies, viz. 0.7, confirms this finding (see Table 4.12), this value being the smallest of the amplification factors computed.

At this stage of the study, one may indeed conclude that the implementation scheme currently adopted for the large GFR core, i.e. identical to that of the EFR, is adequate in terms of CA bank location. Further optimizations have been carried out for the number of CA (see Subsection 4.6.6).

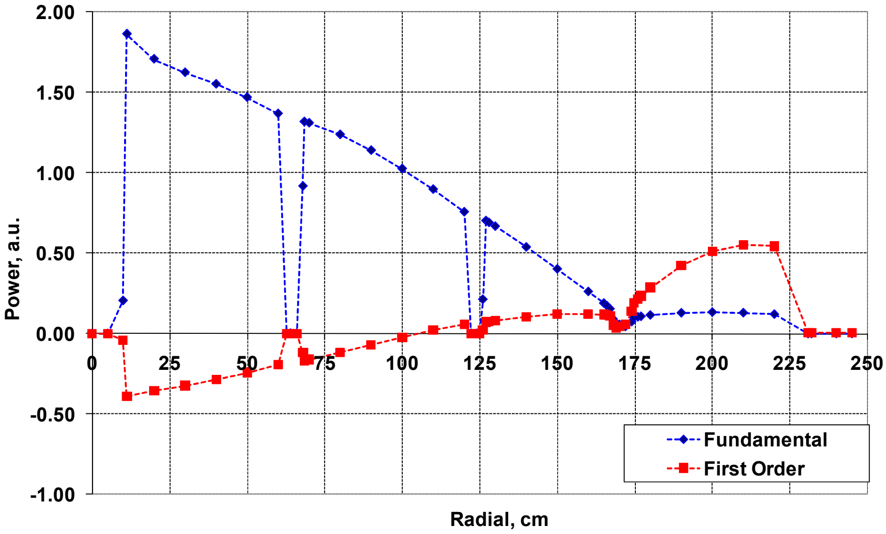

Figure 4.21 Radial power distribution at mid-core of the fundamental and first order eigenvalues for the "2nd CSD bank inserted" configuration.

More generally, the neutronic investigations presented in the present chapter have directly contributed to refining the neutronic GFR core design to suggesting an alternative core layout, the so-called "2007-Core" design. The main difference is the core geometry, viz. the height-to-diameter (H/D) ratio which was increased to 0.6 (from the value of 0.3 for the "2004-Core").

To complement the insights obtained from the SVP analysis presented above, this core variant has been studied as well, enabling one to assess the impact on the neutronic stability of the increase in H/D ratio. In general terms, a better neutronic stability was observed as a result of the reduced core radius, which is favorable. However, a core geometry change impacts other parameters (fuel plate design, SA size, etc.) and other criteria have also to be taken in to account such as an increased ΔP over the core, which is less favorable for establishing natural circulation in a loss-of-coolant scenario.

It is also important to mention that the "2007-Core" design is the result of detailed fuel, neutronic and thermal-hydraulic considerations, mainly performed at CEA-Cadarache. At the time of writing this thesis, the design is still not finalized. Nevertheless, at the current stage, the "2007-Core" design may be considered as a relevant basis for extended analysis. Accordingly, both GFR cores ("2004-Core" and "2007-Core") have been considered while performing three-dimensional core behavior analysis related to hypothetical CA fast movements or ejections.

4.4.5 Parametric study

A parametric study was performed to examine the impact of the following parameters on the shadowing and anti-shadowing effects and to recommend an optimal CAIS:

(1) The location of the CSD banks,
(2) The number of CSDs within the core,

(3) The absorber pin length.

The principal goal of this analysis was to try to reduce, due to safety considerations, the large anti-shadowing effects occurring between the two CSD banks.

Location of the CSD banks

Regarding the displacement of CSD banks, a constraint is to preserve a sufficiently large number of fuel SAs in the surroundings of a given CA. The reason is to be able to control each fuel zone via one or several CAs. The second CSD bank offers higher flexibility than the first, and consequently modifications to the former were examined. Particularly, two cases were analyzed, viz. by moving the bank one fuel row either towards or away from the core centre. The results are presented in Table 4.15, together with the values for the reference core design.

Table 4.15 Impact of the CA locations on the interaction effect δ, on the amplification factors $A_{1st\ bank}$, $A_{2nd\ bank}$ and on the CA worth, for a displacement of the 2nd CSD bank towards the core centre (case “-1”) and towards the core periphery (case “+1”). The CA worth difference is expressed relative to the reference core (ρ=15598 pcm).

Configuration	δ, %	A_1	A_2	CA worth difference, pcm
Reference	46	4.0	2.2	-
Case “+1”	43	3.0	2.2	-3986
Case “-1”	5	1.3	1.1	-5060

The results show a large decrease in the total worth for both modifications, in addition to a reduction in the interactions δ. However, the case “+1” offers no real improvement: δ=43% and A_1=3.0. In the second case “-1”, the interactions are highly reduced at first sight, since the δ value is only 5% and the amplification factors A_1 and A_2 are 1.3 and 1.1, respectively. However, when looking at the radial flux distribution (see Figure 4.22), it is seen that both CSD banks lead to large power peaking factors that compensate the global anti-shadowing effects. As a consequence, the interactions between both CA banks are only lower due to compensatory effects.

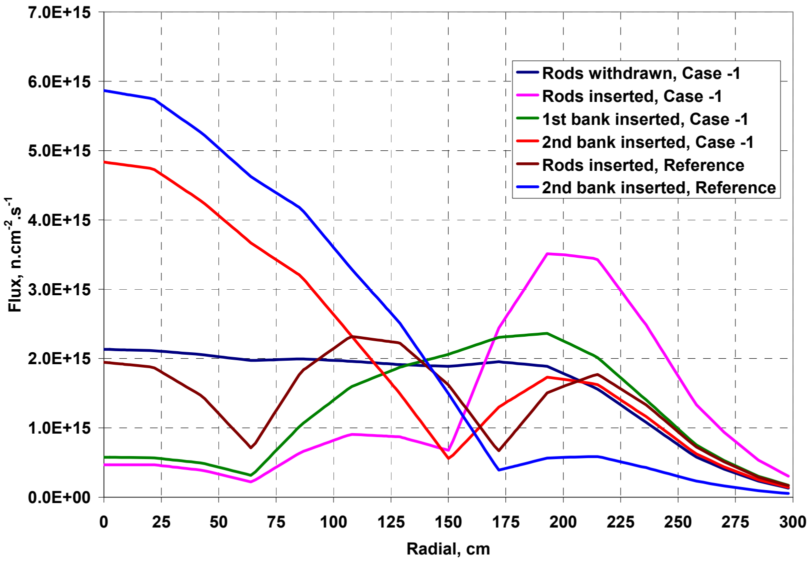

Figure 4.22 Radial distribution of the neutron flux at mid-core height (identical core power). Both the reference case and the case considering a displacement of the 2nd CSD bank towards the core centre (case “-1”) are shown.

Number of CSDs

A reduction in the number of CSDs in the second bank has been assessed. Starting from the reference core design with a total of 18 CAs, a reduction to 15, 12, 9 and finally 6 CAs was considered (see Table 4.16). The results show that the shadowing and anti-shadowing effects are correlated with the total CA worth of the two CSD banks. The diminution of the absorption leads to a decrease in the perturbations within the core, resulting in lower values of δ, A_1 and A_2. A linear relation between the interaction effect δ and the total CA worth can be observed (Figure 4.23).

Table 4.16 Impact of the number of CAs in the 2nd CSD bank, with results shown for 18 (reference), 15, 12, 9 and 6 CAs. The CA worth difference is expressed relative to the reference core (ρ=15598 pcm).

	Number of CAs on 2nd CSD Bank				
Parameter	**18**	**15**	**12**	**9**	**6**
δ, %	46	34	31	25	17
A_1	4.0	2.9	2.6	2.1	1.5
A_2	2.2	1.7	1.6	1.5	1.3
CA worth difference, pcm	-	-3880	-5291	-7360	-10168

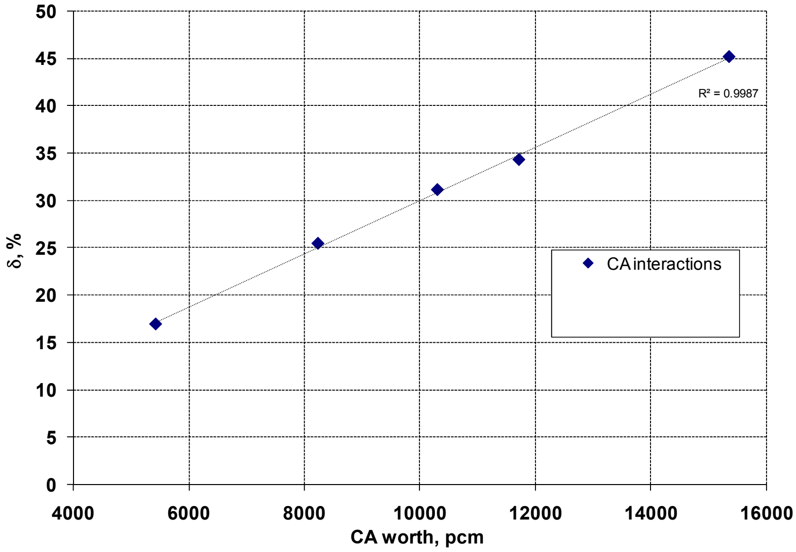

Figure 4.23 CA shadowing effects vs. CA worth for the 2nd bank

These results show that the interactions are correlated with the CA worth, which is of importance in terms of the CAIS. Avoiding having a large excess CAs will contribute to lowering the CA interactions. In this context, the reactivity requirements needed to operate the GFR core were carefully assessed (see Section 4.6). It was observed from this analysis that the number of CAs can indeed be reduced, which is favorable in terms of lower CA interactions.

Absorber length

In the reference design, a CSD has an absorber length of 1.55 m, which corresponds to the fissile core height. Sensitivity calculations were performed for CSD heights of 1.45 m, 1.35 m, 1.25 m and 1.1 m. The results (see Table 4.17) show that the interaction effects are correlated with the active length. This leads to a decrease in the interaction parameter δ from 46% to 35%, while a similar trend is observed for the amplification factors.

Table 4.17 CA interaction δ, amplification factors A_J and CA worth for assembly lengths of 1.55 m (reference), 1.45 m. 1.35 m, 1.25 m and 1.10 m. The CA worth difference is expressed relative to the reference core (ρ=15598 pcm).

	CA length				
Parameter	**1.55m**	**1.45m**	**1.35m**	**1.25m**	**1.10m**
δ, %	46	44	43	41	35
A_1	4.0	4.0	3.8	3.5	3.0
A_2	2.2	2.1	2.0	1.9	1.7
CA worth difference, pcm	-	-658	-1351	-2376	-4455

Additional investigations have shown that the reduced length, even if better in terms of mutual interactions, impacts the axial flux distribution within the CA, leading to a larger power peak beneath the absorber (see Figure 4.24). The peak amplitude is correlated with the absorber length and implications for the peak material temperatures have to be accounted for. In view of such considerations, the reduced CA length option does not appear to be an attractive solution for reducing the interactions.

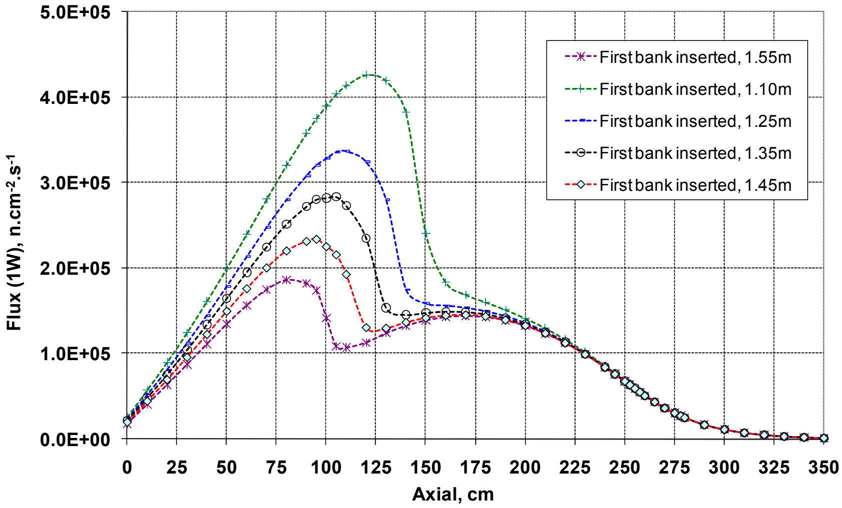

Figure 4.25 Axial flux distribution for five different absorber pin lengths (between 1.10 m and the reference value of 1.55 m)

4.5 Control assembly worth

Supplementary to the CA pattern development, another important part of the work was the computation of the reactivity worths in a precise manner, in order to meet the target accuracies for safety margins, once the reactivity requirements for the GFR core had been adequately assessed (see Section 4.6). According to [146], the target accuracy for the CA worth, in the Gen IV “performance phase”, has to be below 10%.

Due to the design complexity, it has been necessary, as regards the already presented values, to simplify the CA geometry by homogenization techniques. This approach gives generally satisfactory results for scoping studies. However, inaccurate values (worth, reaction rates etc.) are expected, e.g. in the presence of strong flux gradients. To reduce the potential discrepancies, the CA heterogeneity has been taken into account by applying a methodology based on reactivity equivalence, derived from perturbation theory [147]. A more detailed description of the procedure used in ERANOS is provided in Appendix C, Section C.3, while the basic principles are presented below.

The calculation methodology consists of two steps. First, a complete 2D XY CA model, surrounded by fuel is implemented in order to compute adjusted macroscopic cross-sections, i.e. cross-sections producing the same reactivity worth as that obtained from a core calculation in association with a homogeneous CA model. To compute the cross-sections, an iterative algorithm is used. From experience, one knows that heterogeneity effects are large for sodium systems and can lead, depending on the design, to an overestimation of the CA worth in the order of 20% due to homogenization by volume [148]. The assessment of the heterogeneity effects has to be linked to a measure of the shielding effects within the absorber pins and the interactions between the CAs.

Due to the complex CA design, simplifications were made in the XY modeling. These are:

(1) The wrapper is cylindrical in shape,
(2) The absorber pin cladding is smeared with the coolant.

The methodology is CPU-time consuming, due to the small mesh size required. Moreover, the algorithm (in ERANOS) is iterative and has to be repeated until a desired accuracy ε is reached (e.g. 10 pcm). The CA worths are obtained in association with a 3D HEX-Z full core model and transport theory (see Table 4.18), along with, for comparison, the worths obtained with the homogeneous model (by volume).

Table 4.18 CSD control assembly worths (in association with operating conditions)

Configuration	Assembly worth, pcm	Heterogeneity effect, %
Homog., Total	16304	-
Homog., 1st bank	2323	-
Homog., 2nd bank	5987	-
Heterog., Total	14189	-13.0
Heterog., 1st bank	2183	-6.0
Heterog., 2nd bank	5637	-5.8

The CA worth calculated for all CSD assemblies inserted is $\rho = 14189$ pcm, which corresponds to a heterogeneity effect of -13%, a value significantly lower than the corresponding difference calculated for Superphénix (~-20 to 30%) [149]. The explanation for this reduction is associated with the spatial distribution of the absorber pins, which is somewhat away from the centre of the CA, leading, first, to a reduction of the shadowing effect and, second, to an increase of the solid angle for an individual absorber pin. The design "efficiency" is therefore better than that for the Superphénix CA system.

The reactivity curve as a function of the relative CA insertion (CSDs) is given in Figure 4.26. This curve is used later for defining the critical CA position and in the CA-driven transient analysis (see Chapter 5).

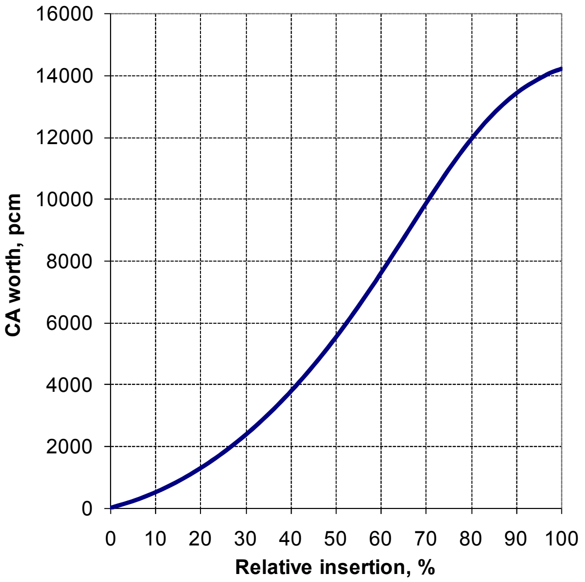

Figure 4.26 CA worth vs. relative insertion ("S-Curve")

4.6 Reactivity requirements for the GFR

In this section are presented the reactivity requirements for the "2004-Core" GFR, the assessment of the uncertainties on the reactivity values and the different safety cases associated with CAs. Finally, a revised implementation scheme is introduced as a result of the investigations.

4.6.1 Reactivity criteria

Supplementary to the development of the CA design and its neutronic characterization, investigations were performed to assess the reactivity needs to control and operate the GFR core, in a safe and suitable manner. In the absence of specific safety studies conducted for the GFR, reactivity criteria derived for previous systems have been considered by analogy. More particularly, the combined EFR [150], CAPRA [151] and Superphénix [26] safety criteria have been applied to the GFR core.

Physical effects modify the reactivity of the core and have to be controlled by an appropriate implementation of CAs (number and position) within the core. As mentioned earlier, the present studies started by considering, by analogy, a 3-bank scheme identical to that of the EFR. The different reactivity effects considered for the GFR are detailed below, and the values obtained are provided in Table 4.19:

(1) The total reactivity effect due to operating conditions is the sum of the contributions of the fuel Doppler reactivity and of the radial and axial thermal expansion effects.

(2) After the core shutdown, the long-term reactivity of the core will increase due to the ^{239}Np decay effect, the half-life of ^{239}Np being 2.3 days. The reactivity effect was

obtained by performing a fine burnup analysis of the core, covering a period of 25 days.

(3) The movement of the core located in the vessel, relative to the CAs fixed to mechanism drives, induces a reactivity effect, consecutive to a differential thermal expansion (insertion or withdrawal) of the CAs relative to the fuel. The reactivity effect is dependent on the materials used and, more important, on the mechanism type used to displace the absorbers. In the absence of a precise design choice concerning the mechanism, it was assumed that the CAs are driven from the bottom of the core with a stainless steel drive. For the core at critical insertion of the CAs, the inlet coolant temperature increase can induce a relative withdrawal due to a higher linear thermal expansion coefficient of steel compared to ceramic. Reactivity effects were computed taking into account the relative CA movements. In the absence of precise calculations, the value provided is only an indication.

(4) The reactivity at BOC corresponds to the reactivity swing over an averaged fuel cycle (831 EFPD), assuming a three-batch fuel management scheme. The positions of the two CSD banks were adjusted to the critical insertion position. For the reference GFR core, the critical position is +2.15 m relative to the bottom reflector, derived from the S-curve (see Figure 4.26). More details on the fuel cycle analysis are provided in Appendix E.

(5) Identical to the value quoted in the safety report for the Superphénix reactor, a 300 pcm reactivity margin was added to the reactivity needs for operating the GFR core.

Table 4.19 Reactivity effects for the “2004-Design” GFR. Values are given in pcm and in $ in brackets.

Parameter	Reactivity effect, pcm and $
Operating conditions	1453 (3.8)
Np-effect	73 (0.2)
Differential dilatation	100 (0.3)
Reactivity swing (average cycle)	2150 (5.6)
Control margin	300 (0.8)
Total	4076 (10.6)

The total reactivity needs of 4076 pcm, as detailed in Table 4.19, represent the total reactivity effect that the CSDs have to be able to control during one fuel batch. To this value, uncertainties have to be added, and different CA hypothetical failures have to been considered when determining the CA worth (see following subsections). The use of the CAs to scram the core has to be differentiated, depending on whether the core is at HFP or at CZP. The net reactivity balance - between positive (Doppler, expansion, neptunium-effect, etc) and negative (CA worth) effects - has to be considered for different hypothetical scenarios. A positive margin indicates that the CA implementation could be further optimized, while, on the other hand, a negative value indicates an insufficient reactivity margin taking the uncertainties into account. Depending on the situation, a possible solution would then be to implement more (or less) CAs within the core, or to reconsider the implementation scheme completely. Under all conditions (operation at

FHP, FZP or CZP; CA or CA-drive failure; refuelling, etc.) a sufficient subcriticality margin has to be provided by the available CAs [152].

Uncertainties have been taken into account based upon past studies and are associated with the following parameters, the conservative values assumed being given in brackets [42; 78]:

1. The reactivity swing (20%),
2. The CA worth heterogeneity effects (15%),
3. The CA reactivity worth (16%),
4. The neptunium decay (10%),
5. The fuel Doppler effect (30%),
6. The delayed neutron fraction (5%),
7. The thermal expansion effect (30%),
8. The computational methods uncertainty in k_{eff} at BOL, based on benchmarking against MCNPX values. This amounts to approximately 300 pcm (see Appendix C, Section C.4.),
9. The ERALIB1 nuclear data uncertainty in k_{eff}. This amounts to approximately 300 pcm and was estimated in the light of the GCFR-PROTEUS investigations (see in particular Table 3.8 of Chapter 3).

The total uncertainty associated with the parameters listed above is the quadratic sum of the partial contributions in the case of independent uncertainties. For dependent effects (assumed to be the case for methods and nuclear data, for instance), the partial uncertainties are summed linearly. Based on the numerical values for the different terms, a large contribution is found to come from the uncertainty associated with the CA worth.

As mentioned, the designed CA and the corresponding implementation scheme have, in all cases, to be able to provide enough subcriticality level to the core in order to shut it down. Based on previous safety reports, especially for the Superphénix reactor, four cases have been considered, based on hypothetical CA unavailability or failure. The results are presented and discussed in the Subsections 4.6.2 – 4.6.5. Somewhat arbitrarily, the isothermal temperature associated to CZP conditions is assumed to be 180°C.

The four safety cases used to dimension the control and safety systems are:

- At cold conditions (CZP):
  1. Reactivity insertion (10 \$),
  2. Fuel handling error,
  3. Reactor shutdown with unavailability of half the CSDs and all the DSDs,
- At operating conditions (HFP):
  4. Reactor shutdown with safety system (DSDs) and unavailability of 1 DSD.

4.6.2 Reactivity insertion (10 \$)

We verify that the GFR core – as was done for the Superphénix reactor – is still easily controllable, at cold conditions, consecutive to a reactivity insertion of 10 \$. The results are presented in Table 4.20. The table shows the reactivity effects to be considered (see Table 4.19) and the associated uncertainties (right column).

In this case, the core is assumed to have been critical with the CSDs inserted at the critical position corresponding to HFP conditions at BOC. Thus, the CA worth (in Table 4.20) of the CSDs is the reactivity difference between this critical position and the fully inserted state. To this CA worth is added the worth of the DSD, which also gets inserted in this scenario. The results show that the 10 $ reactivity-insertion criterion is fulfilled with a reactivity margin of 7502 pcm, with account taken of the 2916 pcm total uncertainty (Due to the conservative assumptions made, the total uncertainty is relatively high.).

Table 4.20 10 $ reactivity insertion safety criterion

Parameter	Reactivity effect, pcm	Uncertainties, pcm
Reactivity margin	300	-
Operating conditions	1453	436
Np effect	73	7
CA worth	-16094	2877
10 $	3850	193
Total	-10418	2916
Margin without uncertainties	10418	
Margin with uncertainties	7502	

4.6.3 Fuel handling error

The second safety criterion refers to a fuel handling error, which considers a mistake when refuelling the core and, more specifically, during the replacement of one CSD. Due to the nature of the refuelling, the core is considered to be at CZP. We consider the most penalizing case (i.e. the largest reactivity effect) which is the loading of an outer-zone fuel SA into the 2nd CSD bank, while all other CSDs and DSDs are fully inserted. The results are presented in Table 4.21. A similarly large reactivity margin is obtained as in the previous case, viz. 6612 pcm (while accounting for the uncertainty of ~2100 pcm).

Table 4.21 Fuel handling error safety criterion

Parameter	Reactivity effect, pcm	Uncertainties, pcm
Reactivity margin	300	-
Operating conditions	1453	436
Np effect	73	7
CA worth	-10539	2055
Total	-8713	2101
Margin without uncertainties	8713	
Margin with uncertainties	6612	

4.6.4 Reactor shutdown with availability of half CSDs and eight DSDs

In this criterion, considered from the EFR safety report, the core is first in a critical state, with the CSDs inserted at the critical position. The core has to be shutdown to cold conditions considering the unavailability of half of the CSDs and a single one of the DSDs. It is assumed that the CSDs and DSDs are moved with mechanism drives connected to a logic control that drives several CAs at the same time. Consequently, the failure of a logic control can lead to the failure of several CAs simultaneously.

In this case, the differential thermal expansion reactivity effect between the CAs and the core vessel is applied. The results are presented in Table 4.22. A reactivity margin of 2908 pcm is obtained, with account taken of the 1556 pcm uncertainty. Thus, also this safety criterion is respected with quite a large margin, even though this is significantly lower than in the two previous cases. This is mainly due to the large CA unavailability of 50%.

Table 4.22 Shutdown at HFP conditions with partial failure of CSDs and DSDs

Parameter	Reactivity effect, pcm	Uncertainties, pcm
Reactivity margin	300	-
Operating conditions	1453	436
Thermal expansion	100	30
Np effect	73	7
CA worth	-6390	1493
Total	-4464	1556
Margin without uncertainties	4464	
Margin with uncertainties	2908	

4.6.5 Reactor shutdown with DSDs and unavailability of 1 DSD

In this case, the core is assumed to be critical at HFP condition. The CSDs are inserted at the critical positions and the core has to be shutdown to a hot isothermal state. We assume an arbitrarily temperature of 600°C and consider the total failure of the CSDs and the failure of one of the DSDs, i.e. the scram occurs only with eight DSDs.

In this case, too, the differential thermal expansion between the CAs and the vessel is applied. The results are presented in Table 4.23. It is seen that this criterion is respected with a somewhat smaller margin, viz. ~1330 pcm (while accounting for the relatively large uncertainty of 1211 pcm). This case allows one to dimension the DSD bank in terms of number of assemblies while the previous cases were more related to the two CSD banks.

The four cases presented above have shown large reactivity margins, even when accounting for the relatively large, conservative neutronic uncertainties assumed. As a direct consequence, investigations were performed to study the possibility of reducing the number of CAs (CSDs and DSDs) within the core, i.e. to arrive at a revised CA implementation scheme. The study is described in Subsection 4.6.6. A reduction of the CAs is favourable from several viewpoints. For instance, it will help reduce the constraints on the fuel, making it easier to achieve an iso-breeder core design.

Table 4.23 Shutdown with only eight DSDs

Parameter	Reactivity effect, pcm	Uncertainties, pcm
Reactivity margin	300	-
Operating conditions	728	218
Thermal expansion	100	30
Np effect	73	7
CA worth	-3744	1190
Total	-2543	1211
Margin without uncertainties	2543	
Margin with uncertainties	1332	

4.6.6 New implementation scheme

The consideration of a reduced number of CAs in the GFR core, which still fulfils the reactivity requirements for the four safety cases described in Subsections 4.6.2 to 4.6.5, has been done on the basis of preserving the location of the three CA banks. The approach taken, viz. of simply reducing the number of CAs, is in line with the eigenvalue separation analysis and the parametric study described in Subsection 4.4.4 and Subsection 4.4.5, respectively.

As presented above, the reactivity margins are different for CSDs and DSDs. The updated CA implementation scheme is as follows:

(1) For CSDs, the reactivity margin (~6000 pcm) is in the range of eight CSDs (based on an average CA worth). An important aspect to be taken into account is that each core region has to be controlled by at least one individual CA. With this in view, the 1st CSD bank remains unchanged with six CSDs. To facilitate the CA implementation, a symmetric (120°) scheme is assumed for each bank. As a consequence, it was possible to reduce the CAs in the two CSD banks from a total of 24 (6 in the 1st bank and 18 in the 2nd bank) to 18, i.e., 6 CAs in the 1st bank and 12 in the 2nd (see Appendix D, Section D.2, so-called "Variant I").

(2) For DSDs, the margin is reduced and corresponds to approximately three DSDs, based mainly on the average CA worth calculated. With the same argument (120°-symmetry implementation), the DSD bank is reduced from nine CAs to six.

Thus, in brief, the updated CA implementation scheme consists of three banks, with a total of 18 CAs in the two independent CSD banks and six CAs in the intermediate DSD bank.

As already indicated (see Section 4.4.4), during the course of the present CA development work for the reference GFR core ("2004-Core" design"), investigations were being conducted in parallel to optimize the GFR system in terms of fuel design, system design (cooling systems, etc.) and core neutronics. In particular, these investigations led to the definition of the GFR "2007-Core" variant. The updated implementation scheme proposed in this subsection has, in fact, been directly applied to the "2007-Core" design (see Appendix D, Section D.2).

4.7 Summary and conclusions

This chapter describes the control assembly pattern development, along with the associated neutronics/thermal-hydraulics studies. Starting from the CA patterns for Superphénix and EFR, a new pattern has been developed and optimized for the reference GFR, "2004-Core" design. In the course of the design development, neutronics studies of CA interactions have been performed to essentially support the design optimization.

The developed neutronics models and the associated computational scheme in ERANOS-2.0 were presented in Section 4.2. The establishment of the reference computational scheme was based on analysis of sensitivity of the multiplication factor and CA worths to diverse computational and modelling options, e.g. RZ vs. HEX-Z geometry, operating conditions, etc. In Section 4.3, the various steps of the CA-pattern development work were presented. The axial distribution of the heat generation within the absorbers was computed, as a function of the insertion position. Coupled neutronics/thermal-hydraulics calculations were performed, using the ERANOS-2.0 and COPERNIC codes, to optimize the CA design. The latter code was used to calculate the material temperatures, in particular that of the cladding, which has to be kept below a certain limit consecutive to a specific material choice. In the present work, stainless steel (AIM1-type) was selected for the cladding, under the assumption that the temperature can be kept below the corresponding limit (630°C) by an appropriate choice of the coolant mass flow rate and coolant volume fraction.

The design and optimization phases were realized in an iterative process to match the design constraints, while achieving features such as a maximization of the absorber fractions, a reduction of the shadowing effects within the absorber pins and between the control assemblies, etc.

The final CA design arrived at is presented in detail in Section 4.3.4. This corresponds to a CA consisting of 54 absorber pins, held together in a triangular lattice. The drive mechanism is considered to be in the centre of the assembly and passes through the core, from the bottom. This choice offers certain advantages for safety, e.g. location of the mechanism in the cold region of the vessel (inlet), rather than in the upper hot part. On the other hand, the structural material is exposed to a high fast neutron flux, which limits the material lifetime. This aspect was not considered in detail in this chapter, and further studies have to be performed in this context. Particular care was taken to dimension the absorber pin diameter, relative to the lattice pitch, in order to reduce, as far as possible, the influence of a given pin on the others. Each absorber pin consists of a stainless-steel tube filled with conventional, highly enriched (90% -^{10}B) B_4C pellets. In order to optimize the absorber cooling, the central region of the CA is not occupied by an absorber pin, but is filled instead with stagnant helium. In this manner, a cladding temperature reduction in the range of 50 to 100°C has been achieved.

The CA interactions were analyzed in detail and are presented in Section 4.4. The aims of this interaction analysis have been threefold. First, the studies serve to present, in a generic sense, the complex interactions, which can occur between CAs in a large fast-spectrum reactor. Second, the analysis provides a deeper understanding of these phenomena. Third, different possible ways to reduce these effects have been examined, considering that such interactions can be penalizing in terms of performance and safety requirements.

Additionally, during the neutronics characterisation of the newly developed CA design, the CA worth was calculated using an improved method based on perturbation theory, allowing one to fully take into account the heterogeneity effect (see Section 4.5). The estimated effect of ~13% was found to be significantly lower than the value of ~20% to 30% for previously considered (sodium-cooled) fast-spectrum reactors. This improvement is mainly due to the choice of an optimal absorber pin diameter and a reduction of the shadowing effects between the pins (by having them spatially distributed in a more off-centred manner).

The CAP development was completed by the determination of the reactivity-control requirements for the large GFR (see Section 4.6). A quantification of these requirements is important from the viewpoint of optimizing the CA implementation scheme in terms of the number of CAs. The assessment of the reactivity margins was mainly based on the approach taken for previous sodium-cooled systems, due to the lack of corresponding detailed studies for advanced GFRs. Thus, reactivity effects in the GFR were quantified to account for various physical phenomena such as the reactivity swing for the average fuel cycle, the impact of the operating conditions, the ^{239}Np effect, and differential thermal expansion effects. In addition, uncertainties coming from nuclear data, computational methods and design assumptions have been systematically assessed for the estimated reactivity values. A number of different, complementary safety cases (reactivity insertion, fuel handling error, shutdown with partial failure of CAs, etc.), based upon existing safety criteria, were defined to check and optimize the implementation scheme. The most penalizing case considered was core shutdown with a partial failure of the DSDs.

The GFR reactivity requirements study has revealed that the CA implementation scheme provides relatively large safety margins in the considered situations. A possible reduction in the number of CAs has been suggested (see Subsection 4.6.6). The corresponding investigations have led to an updated CA implementation scheme, containing a total of six CAs less in the two CSD banks and three CAs less in the safety bank, compared to the initial scheme. For practical reasons, the updated implementation scheme has been directly used for the GFR “2007-Core” variant.

Chapter 5

5 Control assembly driven transients

This chapter presents the 3D simulation and analysis of GFR core behavior under conditions of CA movements at operational speed, as well as during accidental withdrawals and ejections. The reported investigations concern two different GFR core designs:

(1) The reference design ("2004-Core"),
(2) The "2007-Core" variant design, referred to in the previous chapter, the main difference being the core geometry in terms of the H/D ratio.

First, the general context and main steps of the analysis are described in Section 5.1. Second, the development and validation of coupled, full-core 3D neutron kinetics (NK) and 1D thermal-hydraulics (TH) models, for both GFR core designs, are presented (see Section 5.2). The list of the considered CA transients is provided in Section 5.3. While Section 5.4 describes the transient simulations and the analysis of the results for operational speed, Section 5.5 does so for the higher speed (CA ejection) cases. Section 5.6 is dedicated to the presentation of a sensitivity analysis of the thermal-hydraulics results and of the spatial effects, to different parameters, e.g. to the fuel composition (specifically, to that of core containing burnt fuel at begin-of-equilibrium-cycle (BOEC)), the degree of detail of the TH model, the number of ejected CAs, the location of the ejected assemblies, CA speed, etc. Section 5.7 gives a summary of the results obtained, as also the conclusions for the chapter.

For the sake of clarity, the GFR "2007-Core" variant and the fuel cycle calculations carried out to obtain the BOEC core composition have been described separately in Appendices D and E, respectively.

5.1 General context and main stages of the analysis

The design development work for the CAs in the GFR core, as described in the previous chapter, has been based on static neutronic analysis and has revealed significant CA interactions, between the assemblies themselves as also between the CA banks. These interactions have been seen to significantly amplify or reduce the CA worth, and thereby influence the efficiency of the developed design. Specifically, during a CA-movement transient, the CA worth is not a constant determined from static neutronic analysis but a dynamic value depending on the position of other surrounding assemblies, as also their location within the core. To understand the impact of these interactions on the core behavior and, in particular, on the operational safety, a systematic dynamic analysis has been carried out related to CA-driven movements. Fast CA transients have also been considered, e.g. the ejection of one or several CAs, resulting from a failure of a control drive mechanism or an error in the control command system.

For obtaining an in-depth understanding of the CA interactions from a dynamic viewpoint, it has been necessary to carry out 3D coupled simulations and analysis of the core behavior. The general aim is to thereby complete the characterization of the CA pattern (developed and presented in Chapter 4) with dynamic analysis related to CA movements, both withdrawals and ejections. As indicated, these two categories of events differ essentially in the speed at which the CA is removed, i.e. positive reactivity is inserted into the core.

Performing transient analysis allows one to better understand the design parameters of importance for operational safety related to CA movements, e.g. the number of CAs which can be simultaneously in movement, the maximal operational speed and other constraints related to the control system in general. It also directly provides the necessary evidence as to whether the developed and optimized CA pattern, based upon static neutronics considerations, is adequate during transients. Effectively, this chapter highlights the complex dynamic interactions occurring between moving CAs in a large fast-spectrum core.

In effect, three different GFR core configurations have been systematically analyzed, in order to characterize the 3D core behavior more fully, viz.

(1) The reference “2004-Core” design at BOL,
(2) The core variant “2007-Core” design at BOL,
(3) The “2004-Core” design but with burnt fuel compositions corresponding to beginning of equilibrium cycle (BOEC) conditions (in order to investigate the influence of fission products and MAs on the dynamic behavior).

Two constant-speed cases have been systematically considered:

(1) CA withdrawal at operational speed (in the range of 2 mm/s),
(2) CA ejection (in the range of 20 cm/s).

The transient analysis work described in this chapter has been carried out in three stages:

1. The first step encompasses the development and validation of the full-core, coupled NK-TH models of the two different GFR core variants, i.e. the reference “2004-Core” and the “2007-Core” designs (see Section 5.2). The full-core coupled NK-TH “2007-Core” design has been developed using an identical methodology to that applied for the reference core. For this reason, specific details are provided in this chapter concerning the “2004-Core” NK-TH model alone.

   First, stand-alone neutronics and thermal-hydraulics models were developed with state-of-the-art tools, viz. (1) the PARCS code for the neutron kinetics (see Section 2.5 for the description of the codes) and (2) the TRACE code for the thermal-hydraulics. Then, the stand-alone models were coupled together using an external mapping scheme allowing the exchange of data during the simulations. Due to the complexity of the used mapping scheme, specific tools (in particular, MATLAB based) were created to automate the creation of the input decks.

   The full-core NK-TH models were validated against reference static ERANOS-VARIANT calculations for the neutronics model, for different core configurations, viz. for both “hot” and “cold” operating conditions and for different positions of the CA banks and/or individual CAs. Prior to the simulation of the CA-driven transients themselves, preparatory coupled simulations were performed by first computing the steady state, and then the null-transient solutions. The developed mapping scheme was also checked in a systematic manner with numerous tests performed to validate the correctness of the data exchange.

2. The second stage concerns the simulations of CA-driven transients for both GFR core designs. A wide range of transients was selected for analysis, in order to cover hypothetical accidents adequately and to draw the corresponding conclusions. The dynamic behavior for the two GFR core designs was systematically compared for both the different CA-speed categories indicated above, identical transients being considered in each case to ensure consistent comparisons.
3. The third stage of the analysis work is the sensitivity study. This includes the consideration of the revised CA implementation scheme (in the context of the “2007-Core” variant), the use of a simplified TH model, as also the investigation of fuel burnup effects (via the study of the reference core at BOEC conditions). The latter investigation is of special relevance, considering that burnup in fast reactors is usually associated with a deterioration of kinetics and other safety-related parameters, mainly caused by a hardening of the neutron spectrum due to the build-up of fission products and MAs. The simulations were carried out in several steps. The first step was to develop the computational tools to calculate the fuel composition. Depletion calculations were performed to obtain the equilibrium fuel composition. The second step was to compute the corresponding macroscopic cross-sections and derivatives, for implementation within the PARCS core kinetics model. The coupled NK-TH model was then developed, in conjunction with the new macroscopic cross-sections. Finally, this model was used for transient analysis, in order to compare the results with those for the core with fresh fuel (BOL).

Some of the investigations presented in this chapter have been reported in papers at the PHYSOR’08 [153] and ICONE-17 [154] conferences.

5.2 Development of the GFR full-core coupled PARCS/TRACE model

As indicated, the prime motivation for the current development of a full-core coupled model of the 2400 MWth GFR cores, using the PARCS [90] and TRACE [92], is the analysis of the 3D core behavior under transient conditions. The two GFR models, for the two different core designs, have been developed in chronological steps, based on the same basic methodology.

The cross-sections preparation is described in Subsection 5.2.1, and the standalone PARCS model is provided in Subsection 5.2.2. Subsection 5.2.3 presents the TRACE thermal-hydraulics model. The thermal expansion coefficients are given in Subsection 5.2.4, while the mapping scheme used to couple the PARCS and TRACE models is described in Subsection 5.2.5. Finally, Subsection 5.2.6 presents the validation of the coupled model. Supplementary neutronics analysis is described in Subsection 5.2.7.

5.2.1 Cross-sections preparation

In a first step, the self-shielded macroscopic cross-sections have been prepared in 33 neutron groups (a subset of the VITAMIN-J structure). Their derivatives with respect to state variables, i.e. the fuel temperature T_f, coolant density ρ_c, thermal radial δ_r and axial expansions δ_z of the core (see Eq. 2.7), were produced using the cell code ECCO [91] (included in ERANOS-2.0) in association with homogeneous cells and the adjusted neutron data library ERALIB1 [97]. The cross-sections were calculated at “cold” conditions (293 K and 7 MPa for the coolant).

Regarding the Doppler fuel reactivity calculation, room temperature (20°C) was set as reference, and the neutron slowing down calculation was performed a second time with identical geometry but with an arbitrary fuel temperature increase of 200°C. Different values for the temperature increase were tested and the logarithmic dependence of the Doppler effect was confirmed (see Figure 5.1). The value of the Doppler constant (approximately 1510 pcm) is in good agreement with reference values for fresh fuel composition (-1576 pcm, value taken from [78]. In particular, this shows that effects of the fuel temperature are correctly reproduced with the coupled NK-TH model.

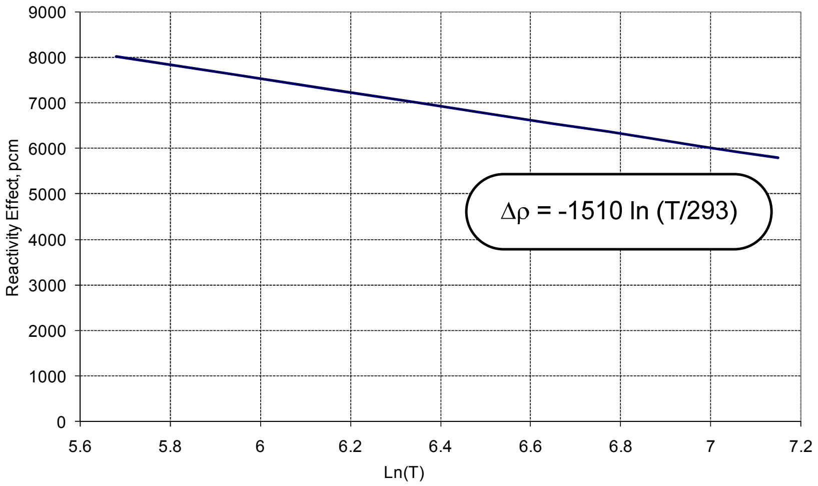

Figure 5.1 Doppler effect vs. fuel temperature, calculated with ERANOS-2.0 in association with the ERALIB1 nuclear data library.

For the coolant density, a small perturbation of +0.05% was applied to the reference value of the helium nuclear density to derive the coolant reactivity effect.

To simulate the axial thermal expansions in ECCO (homogeneous media), the material densities were adjusted by conserving the material mass of cladding and fuel for the expanded cell. Since the model was used exclusively for CA-driven transients, there was no need to consider radial core expansion effects. In the axial direction, the core expansion was driven by the SiC matrix expansion [135].

Apart from the cross-sections and their derivatives, the kinetics parameters (i.e. the delayed neutron fractions β_i and the decay constants λ_i) and the fission spectrum have to be provided in the PARCS input deck. These parameters were also obtained from ERANOS-2.0 using the adjusted ERALIB1 neutron data library (see Table 5.1).

As final preparation, the self-shielded macroscopic cross-sections, the scattering matrices and the corresponding derivatives were processed in a format adapted to PARCS using a special FORTRAN procedure, viz. ERANOS2PARCS [111; 155]. More details about the format specifications are given in Section 2.5.1 and in [135]. The self-shielded macroscopic cross-sections and the corresponding derivatives need to be processed by the ERANOS2PARCS routine for each physical zone used in the core, i.e. inner and outer fuel regions, radial reflector, CAs, inert assemblies, etc.

5.2.2 PARCS models

In a second step, the full-core PARCS 3D neutronics models (nodal diffusion theory in hexagonal geometry) were developed (with 387 fuel SAs for the “2004-Core” and 246 SAs for the “2007-Core”, along with 334 reflector and control sub-assemblies in each case). This was first done in a standalone mode (not coupled to TRACE), using the macroscopic cross-sections obtained from step one. Complementary to the neutron cross-sections in 33 groups, the kinetics parameters (β_i, λ_i) were calculated, for both fuel (inner and outer) regions, in a 6-group structure derived from the nuclear data library. Table 5.1 provides the kinetics parameters for the “2004-Core” design.

Table 5.1 Kinetics parameters for the reference GFR “2004-Core” design

	Group					
Decay constant λ_i, 1/s	1.33E-02	3.05E-02	1.19E-01	3.17E-01	9.61E-01	3.02E+00
Inner fuel zone	1	2	3	4	5	6
Delayed neutron fraction β_i	1.07E-04	9.02E-04	7.96E-04	1.78E-03	9.40E-04	3.30E-04
Outer fuel zone	1	2	3	4	5	6
Delayed neutron fraction β_i	1.04E-04	8.86E-04	7.74E-04	1.72E-03	8.99E-04	3.12E-04

The axial nodalization consists of 10 cm meshes within the reflectors and 10.333 cm within the homogeneous fuel region (see Figure 5.2).

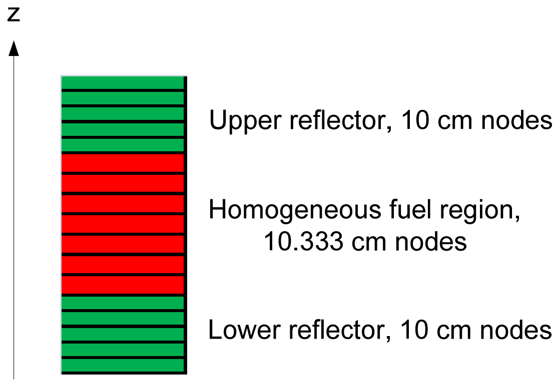

Figure 5.2 Schematic showing the axial nodalization used in PARCS; “2004-Core” design

The core geometry was set up for room temperature conditions, the dimensions being identical to those defined in ERANOS-2.0 in association with the 3D nodal code VARIANT [89]. This allowed a code-to-code comparison, before the coupled calculations were performed. The choice of room temperature as reference was also motivated by the observation of improved convergence when the PARCS code is coupled to the TRACE code, allowing smoother feedbacks when the power component is switched on in TRACE. The other option, i.e. with “hot” operating conditions set as the reference, was also tried. In case of convergence, identical computed values were obtained.

It is important to note that the CA movement was modelled using macroscopic cross-sections for the follower region (the region below the absorber), in conjunction with derivatives simulating the change of cross-sections due to the presence of the absorber. The time-dependent position of the absorber during the transient is specified by the user, in the PARCS input deck. This “transient” model was validated against “static” modelling for different core configurations, i.e. calculations performed for different CA positions. In the “static” model, the actual axial CA position was defined by applying the follower cross-sections set below the CA position, and the absorber cross-sections set above (see Figure 5.3).

The results for validation of this modelling, in terms of a comparison of the effective multiplication factors computed with the two models, are given in Table 5.2, and a good agreement is seen.

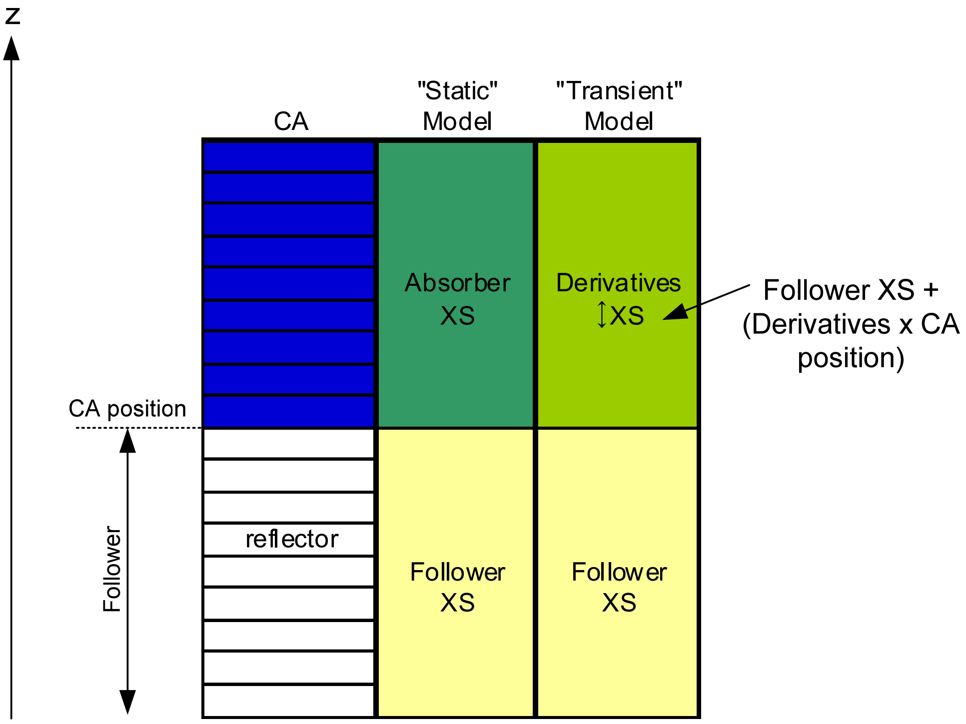

Figure 5.3 Axial description of the control assembly; use of “transient” and “static” models to simulate the control assembly position

Table 5.2 Effective multiplication factors using “transient” and “static” models for the CA position; “2004-Core” design

	"Static"	**"Transient"**	
Core configuration	**k_{eff}**	**k_{eff}**	**Difference, pcm**
All CAs parking Position	1.06106	1.06097	-8
1st CSD bank 50% insertion	1.04416	1.04455	36
1st CSD bank inserted	1.03386	1.03414	27
2nd CSD bank inserted	0.99375	0.99359	-16
DSD bank inserted	1.00742	1.00738	-4
All CSDs inserted	0.90541	0.90562	25

One point worth mentioning is that heat generation within the CAs was not calculated in PARCS. This is an acceptable approximation for transient calculations, considering that the contribution of these non-fissile assemblies, even in fully inserted position, is lower than 1% of the nominal power (see the studies presented in Chapter 4). Concerning the CAs themselves, one may assume that the steady-state calculations, performed for designing the CA pattern, provide a sufficient basis to ensure their coolability under transient conditions.

Using the developed models, the CA worths were computed by PARCS and compared with reference static VARIANT/ERANOS-2.0 calculations. Table 5.3 shows the results. It is seen that quite good agreement is obtained concerning the CA worths, the average discrepancy being in the range of 6% with diffusion theory (caused mainly by the use of different nodal schemes in the two codes) and 9% with transport theory. This provides sufficient verification of the PARCS models from the viewpoint of the present application.

Table 5.3 Control assembly worths calculated with PARCS in the stand-alone mode (first column) and differences – PARCS minus ERANOS – with respect to VARIANT/ERANOS results obtained with diffusion (3rd column) and transport (4th column) theory; "2004-Core" design.

	PARCS	Difference relative to ERANOS-2.0, pcm	
Core configuration	Worth, pcm	Diffusion	Transport
1st CSD bank inserted	2692	193	381
2nd CSD bank inserted	6747	364	583
All CSDs inserted	15730	-770	312

Of particular interest are the CA interactions occurring between the banks (see Chapter 4). The results in the 2nd column of Table 5.3 show that these complex interactions are well reproduced. Thus, the parameter $\delta = (\rho_{tot} - \rho_{1st\text{-}CSD} + \rho_{2nd\text{-}CSD})/\rho_{tot})$, characterising the interaction between the two CSD banks is ~40% with PARCS, compared to ~46% with ERANOS-2.0. This again confirms that such control assembly interactions indeed represent important physical effects occurring within the GFR core.

5.2.3 TRACE models

The next step corresponds to setting up the full-core TRACE models with parallel thermal-hydraulic channels. Each of the individual fuel SAs is modelled individually by a heat-structure and a coolant channel, an additional channel being used to model the core bypass, i.e. the reflectors and the CAs. More details about the TRACE code can be found in Section 2.5.6, and therefore only the description of the GFR model is provided in this subsection. As already stated, the purpose of this study is to analyze the 3D core behavior induced by local reactivity insertion. Accordingly, only the core has been modelled with TRACE, appropriate boundary conditions being applied to take into account the rest of the primary circuit. Figure 5.4 shows a schematic of the TRACE model for the GFR "2004-Core" design.

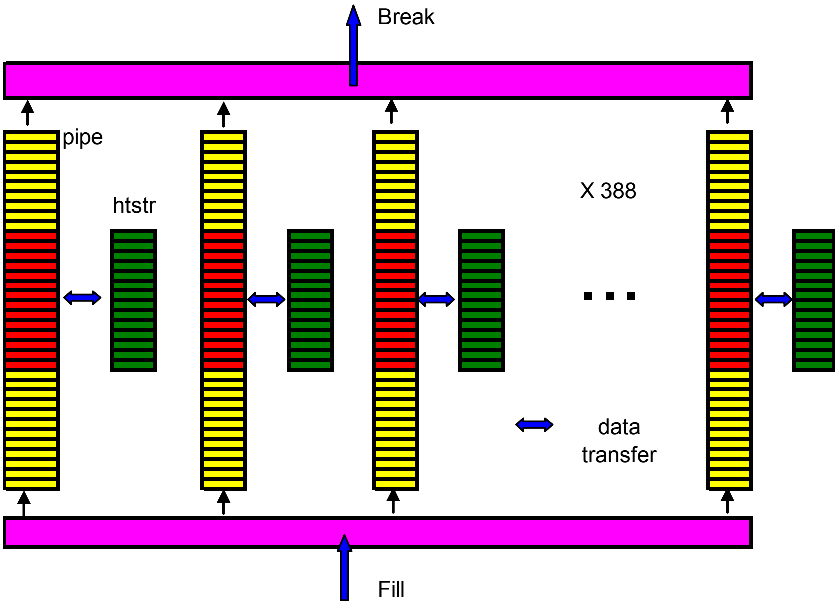

Figure 5.4 Schematic of the TRACE model for the GFR "2004-Core" design

For the TH channels, the axial nodalization consists of 33 nodes, while the heat-structure is sub-divided in 23 nodes, which is consistent with the neutronic nodalization used. Due to the large number of TH channels, the model is quite complex to handle and, accordingly, specific MATLAB routines were developed to automate the creation of the input deck. This also had the advantage of permitting changes to be made quite easily, e.g. to take into account the geometry and fuel composition specifications corresponding to the different GFR core configurations studied.

The MATLAB routines (see Figure 5.5) were particularly efficient and useful for implementing the input deck in terms of the pipes, heat-structures and junctions, the model containing more than 700 components.

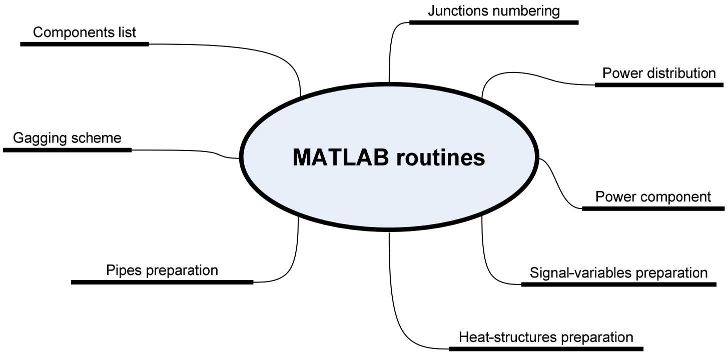

Figure 5.5 Schematic of the MATLAB routines developed to automate the input deck creation in TRACE

The fuel plate model

As described earlier, the GFR fuel plates [127] consist of an internal SiC honeycomb structure, each constituted cell containing a (U,Pu)C fuel pellet closed on both sides by flat SiC plates (see Figure 4.3). The volume between the honeycomb structure and the fuel pellet is filled with static helium (not considered as coolant) at 0.1 MPa (under cold conditions). Figure 5.6 depicts the fuel pellet and the honeycomb structure. A fuel sub-assembly consists of 3 identical regions of 9 thin parallel plates (27 plates in total per fuel sub-assembly; see Figure 4.2), with helium flowing between the plates. The fuel plate dimensions are given in Table 2.3.

Due to the complex hexagonal geometry of the sub-assembly and the fuel plates themselves, a simplified 1D fuel model with smeared (U,Pu)C and SiC material in the centre, a helium gap and a SiC cover was implemented in TRACE using the plate geometry. More details about the GFR fuel simulation can be found in [135][6].

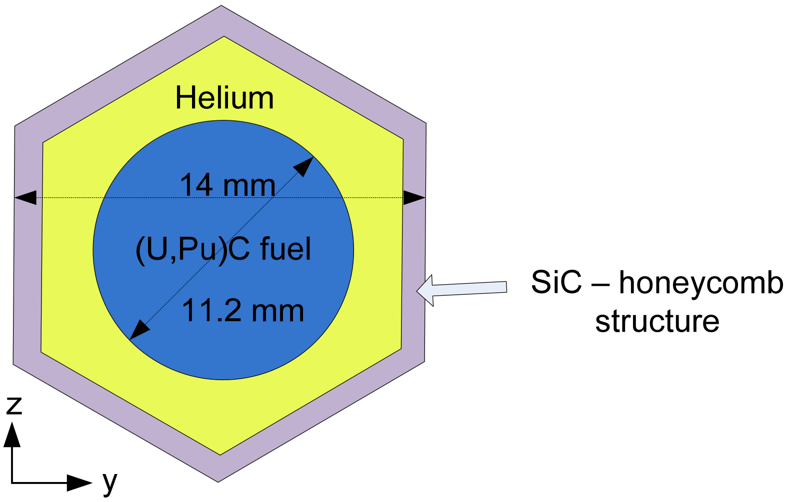

Figure 5.6 Fuel pellet within the honeycomb structure. The dimensions are given for the "2004-Core" design

The homogenized fuel plate model is shown in Figure 5.7. As indicated, only half of the plate needs to be modelled in TRACE, thanks to the central symmetry. In more detailed terms, the fuel plate is composed of three regions (see Figure 5.8):

(1) The homogenized fuel with (U,Pu)C, helium gap and SiC honeycomb structure,
(2) The helium gaps,
(3) The covers made of SiC.

---

[6] The recommendations provided in [135] for a 1D simulation of the GFR fuel were taken into account.

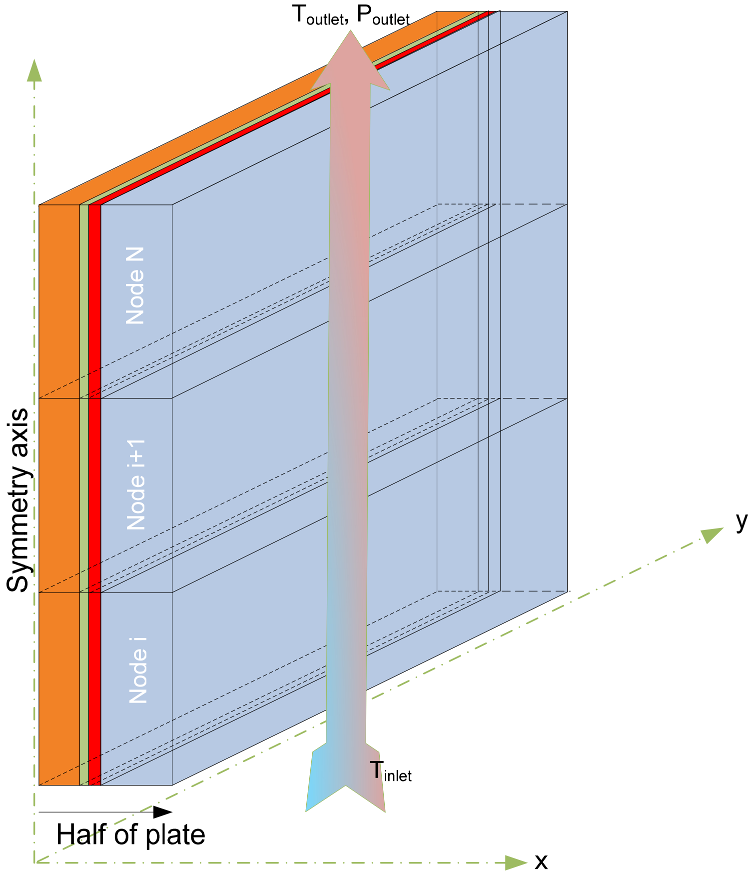

Figure 5.7 Schematic representation of the GFR fuel plate model implemented in TRACE. The axial nodalization consists of N nodes

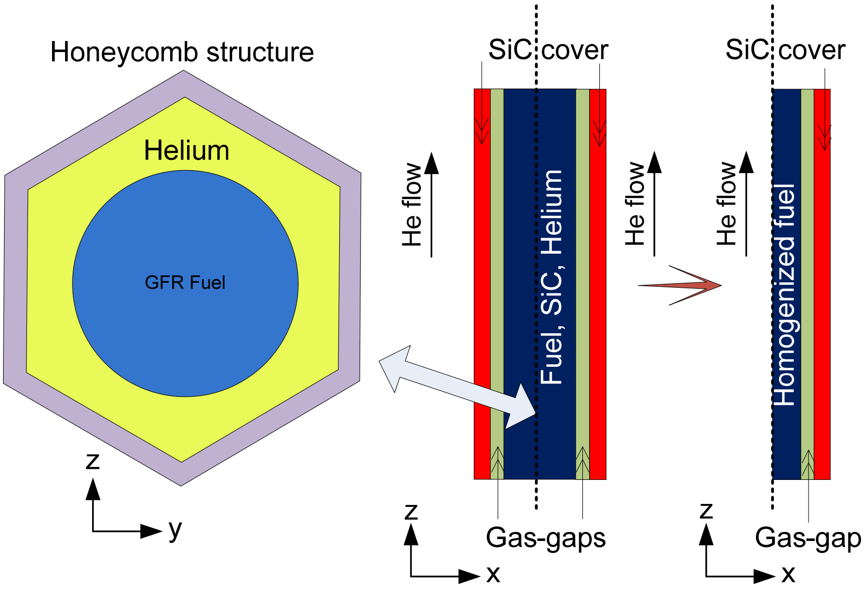

Figure 5.8 Schematic of fuel pellet within the honeycomb structure (left), the fuel plate (middle) and the ½ plate model implemented in TRACE (right)

The thermal properties for the homogeneous material representing the central fuel-plate region ((U,Pu)C fuel pellets, SiC structural material and helium) have been taken from [135]. The assumptions made are as follows:

(1) The thermal conductivity λ is set equal to that of the fuel: $\lambda_{hom} = \lambda_{fuel}$,
(2) The density and specific heat are calculated as follows:

$$\rho_{\mathrm{hom}} = \frac{\rho_{fuel} \cdot V_{fuel} + \rho_{He} \cdot V_{He} + \rho_{SiC} \cdot V_{SiC}}{V_{fuel} + V_{He} + V_{SiC}}$$

$$c_p^{\mathrm{hom}} = \frac{\rho_{fuel} \cdot V_{fuel} \cdot c_{p,fuel} + \rho_{He} \cdot V_{He} \cdot c_{p,He} + \rho_{SiC} \cdot V_{SiC} \cdot c_{p,SiC}}{\rho_{fuel} \cdot V_{fuel} + \rho_{He} \cdot V_{He} + \rho_{SiC} \cdot V_{SiC}} \qquad \text{Eq. 5.1}$$

where ρ is the density, V the volume and c_p the specific heat.

In the used fuel model, validation for which has been detailed in [135], the heat transfer is calculated along X and Z directions, according to the coordinate system depicted in Figure 5.7. For the surface perpendicular to the Y-axis, adiabatic conditions are assumed, each plate being located in an environment with equivalent rates of helium flow and heat generation. For the thermal-hydraulic analysis, it is effectively the width of the plate which is used for calculating the material volumes and corresponding heat transfer areas.

Power distributions and boundary conditions

In the stand-alone TRACE model, or in the case of point-kinetics transient simulations, the axial and radial power distributions are provided in the input deck. In case of spatial-kinetics simulations, they are calculated at each time step.

The axial power distribution obtained from ERANOS is shown in Figure 5.9. The effect of the CAs, which are in the parking position, is clearly visible.

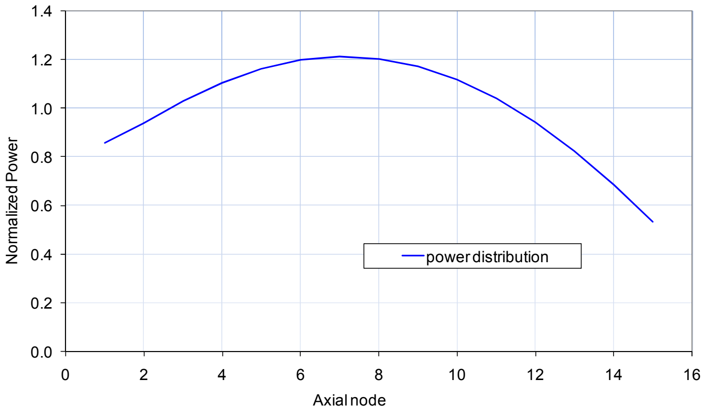

Figure 5.9 Axial power distribution for the "2004-Core" design (the axial nodes are shown numbered from the core bottom)

As mentioned earlier, with only the core being modelled in TRACE, appropriate boundary conditions were applied at the core inlet and outlet, viz. the helium mass flow rate and inlet temperature. A BREAK component was used at the core outlet to specify the outlet pressure (7 MPa). The operating conditions for the two GFR core designs are provided in Table 5.4.

Table 5.4 Operating conditions for the two GFR core designs

Design	Inlet T, K	Helium mass flow rate, kg/s
"2004-Core"	753	1244
"2007-Core"	673	925

Heat-transfer correlations

As shown in Figure 5.8, there is a gas gap between the fuel pellet and the walls of the SiC structure. The gas-gap conductance plays a major role in the fuel temperature profiles calculated in TRACE. The conductance additionally takes into account the surface roughness in the axial direction and the heat transfer by radiation.

In the calculations, the gas gap conductance in TRACE (expansion model) is derived from:

$$h_{gas} = \frac{k_{gas}}{(\Delta r_{gap} + \delta_r)} \qquad \text{Eq. 5.2}$$

where k_{gas} is the inner gas thermal conductivity, Δr_{gap} is the fuel-cladding gas-gap width and δ_r is the effective surface roughness (a built-in value of 4.4 x 10^{-6} m [92] has been used, corresponding to the mean surface roughness for the fuel and the cladding).

The heat generation rate per unit volume is calculated by PARCS, and the heat is removed by linking the heat-structure component to a thermal-hydraulic channel allowing to calculate, first, the heat-exchange coefficient between the plates and the coolant and, second, the coolant temperature.

The heat transfer coefficient is calculated in TRACE by means of different correlations. Specifically, the wall-to-gas heat-transfer coefficient for forced convection is assumed to be the maximum between the values for the laminar and turbulent regimes, i.e.:

$$Nu = \max\,(Nu_{laminar}; Nu_{turbulent}) \qquad \text{Eq. 5.3}$$

where Nu is the Nusselt number, the heat transfer coefficient being given by:

$$\alpha = \frac{Nu\,\lambda_{gas}}{D} \qquad \text{Eq. 5.4}$$

where λ_{gas} is the coolant thermal conductivity and D the hydraulic diameter.

In Eq. 5.5, the Nusselt number is shown calculated for laminar-flow convection in terms of the maximum between the values from correlations for low (Kim and Li model [156]) and high (El-Genk et al. model [157]) Reynolds numbers:

$$Nu_{laminar} = \left[\left(\max\left(Nu_{lowRE}; Nu_{hi\,\mathrm{Re}}\right) \right)^3 + \left(0.7 \cdot (Gr \cdot \mathrm{Pr})^{1/4} \right)^3 \right]^{1/3}$$
$$Nu_{lowRE} = -5.6605 \cdot pdrat^2 + 31.061 \cdot pdrat - 24.473$$
$$Nu_{hi\,\mathrm{Re}} = (2.97 - 1.76 \cdot pdrat) \cdot \mathrm{Re}^{0.56 \cdot pdrat - 0.3} \cdot \mathrm{Pr}^{0.33} \qquad \text{Eq. 5.5}$$

The Churchill superposition method is used to combine the effects of natural and forced convection [158], *pdrat* being the pitch-to-diameter ratio. *Gr* is the Grashof number and *Re* the Reynolds number.

In Eq. 5.5, the Nusselt number in the case of turbulent-flow convection is given by the modified Dittus-Boelter correlation, which accounts for the entrance length effect of Mills [159]:

$$Nu_{turbulent} = (0.028 \cdot pdrat - 0.006) \cdot \mathrm{Re}^{0.8} \cdot \mathrm{Pr}^{0.33} \cdot \left(\frac{T_{wall}}{T_{gas}} \right)^n \cdot \left[1 + \frac{2.4254}{\max(3.0; L_{entrance})^{0.676}} \right]$$
$$n = \begin{cases} -\left[\log_{10}\left(\dfrac{T_{wall}}{T_{gas}} \right) \right]^{1/4} + 0.3, & \text{for } T_{wall} > T_{gas} \\ -0.36, & \text{for } T_{wall} \le T_{gas} \end{cases} \qquad \text{Eq. 5.6}$$

where Pr is the Prandtl number, T_{wall} is the plate surface temperature and T_{gas} is the helium temperature. $L_{entrance}$ corresponds to the entrance length, i.e. the characteristic distance after which the flow regime is established. In the code, the value is set to 1.10^6, i.e. the correction for the entrance length is not considered.

It is important to stress that these correlations have been developed for tube bundles and are used in the present work because of the lack of experimental data on rectangular channels. Further validation work will clearly be needed for more accurate studies.

The gagging scheme

An important aspect of the TH model development has been the calculation of an adequate gagging scheme allowing one to render the core outlet temperature uniform. As mentioned, each fuel SA was simulated by an individual TH channel associated with a specific different heat generation rate provided by PARCS. Consequently, the flow rate in each channel had to be adjusted by applying singular, channel-specific pressure losses at the inlet of each channel. These factors were implemented by means of k-factors within the input deck. The tolerance for the temperature increase was set at +/- 15 K, relative to the value corresponding to the average upper plenum temperature, thus ensuring a uniform distribution. The channel-specific pressure losses applied to match the flow to the radial power distribution calculated in PARCS (assuming the CAs in the parking position) are depicted in Figure 5.10, while the channel numbering is given in Figure 5.11. A higher singular pressure loss has been set for the channel representing the core bypass, in order to have approximately 10% of the total mass flow passing through the bypass.

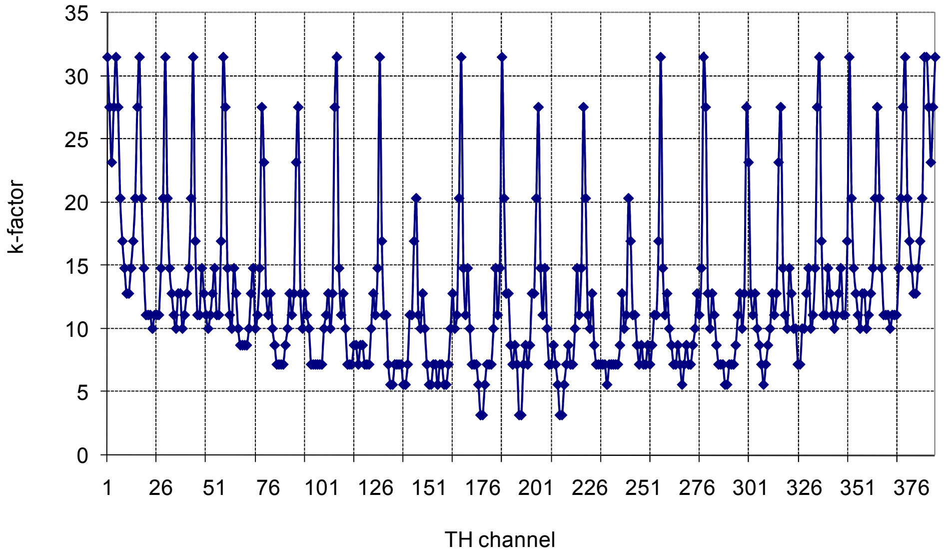

Figure 5.10 Channel-specific, pressure-loss k-factors (gagging scheme); "2004-Core"

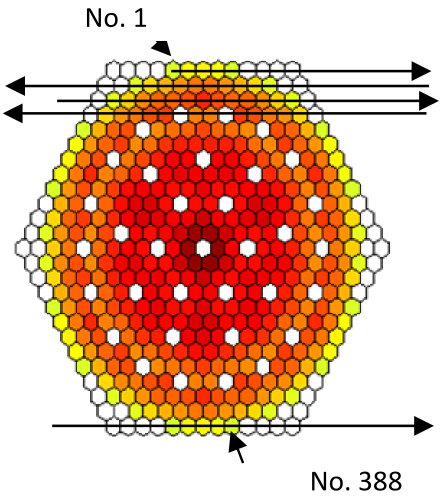

Figure 5.11 Channel numbering used in the "2004-Core" GFR

The computation of the gagging scheme was done automatically using an iterative MATLAB algorithm developed for this task. Effectively, the k-factor k_{i+1} in the $(i+1)^{th}$ iteration is calculated using:

$$k_{i+1} = k_i \cdot - C\left[T_i - T_{p,i}\right] \cdot \left[\frac{k_i - k_{i-1}}{T_{\cdot} - T_{p,i} - T_{i-1} + T_{p,i-1}} \right] \qquad \text{Eq. 5.7}$$

$$k_{i+1} = k_i \qquad \text{if } T_i - T_{p,i} > 0$$

where i is the iteration index, C is an appropriately chosen adjustment constant and the subscript p stands for plenum.

While verifying the TRACE model, one of the points checked was that the upper plenum temperature (T_{out}=850°C in the reference core) and the core pressure drop (ΔP=0.07 MPa; reference core) were in agreement with the design specifications computed with the French thermal-hydraulics code CATHARE [160; 161]. As an illustration, the axial coolant and peak fuel temperatures are represented in Figure 5.12 for the peak-power SA.

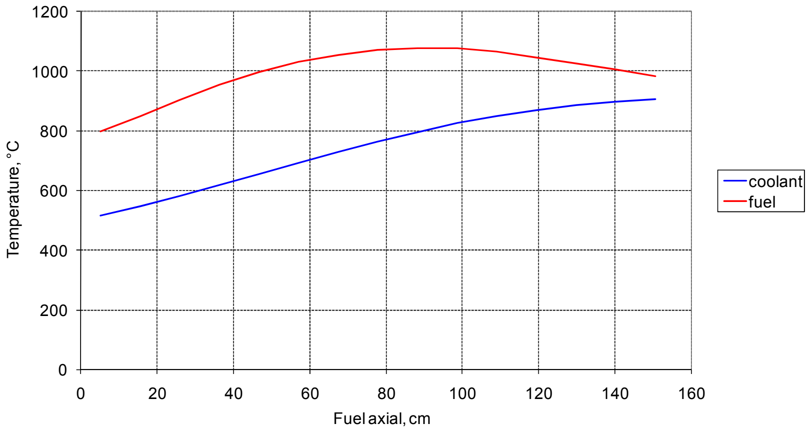

Figure 5.12 Axial distributions of coolant and peak fuel temperatures; "2004-Core" design

More generally, agreement in the energy balance between the coolant and the fuel is a good indication that the model was successfully implemented, i.e.:

$$\mathrm{Q} = \dot{\mathrm{m}}\mathrm{c_p}\Delta\mathrm{T} \qquad \text{Eq. 5.8}$$

where Q is the reactor power, $\dot{m}$ is the core mass flow rate, c_p the helium specific heat and ΔT the temperature difference between the outlet and inlet. For a power of 2400 MWth, the mass flow rate is 1244 kg/s, the temperature difference amounts to 370 K and, finally, the helium specific heat obtained is 5210 $\mathrm{J.kg^{-1}.K^{-1}}$. These values are for the "2004-Core".

5.2.4 Thermal expansion coefficients

Another important step in the model development was the calculation of the radial and axial thermal expansion coefficients needed by PARCS to calculate the changes of the macroscopic cross-sections – feedbacks – with respect to the axial and radial core thermal expansion. In practical terms, this allows one to convert a change in the temperature δT into changes in the axial and radial core sizes (δ_z, δ_r), for applying the corresponding thermal expansion feedbacks using the cross-section derivatives $\delta\Sigma/\delta_z$ and $\delta\Sigma/\delta_r$:

$$\delta_{r,z} = L_{r,z}\alpha_{coef,r,z}\delta T \qquad \text{Eq. 5.9}$$

where the subscripts r and z are for the radial and axial dimensions, respectively. $L_{r,z}$ is the nominal size (radius or height), $\alpha_{coef,r,z}$ is the radial or axial thermal expansion coefficient, and δT is the change in temperature.

The simple model used for the core expansion effects [162], assumes that the radial expansion is driven by the core diagrid and the axial expansion is determined by the average thermal expansion of the fuel element matrix (made of SiC). Consequently, the thermal expansions coefficients are considered for SiC material at the inlet temperature for the radial core thermal expansion, and at average cladding temperature for the axial expansion. Table 5.5 gives the calculated thermal coefficients.

Table 5.5 Axial and radial thermal expansion coefficients; "2004-Core" design

Thermal expansion coefficients	Value, $10^{-6}\cdot K^{-1}$
Axial	4.8
Radial	4.5

In practical terms, TRACE provides to PARCS, at each time step, the new average core radius and height, in order for PARCS to recalculate the macroscopic cross-sections appropriately.

5.2.5 Mapping scheme

In a fifth step, the PARCS and TRACE models were coupled using an appropriate mapping scheme, containing the mapping of both the heat structures and the pipe components to the neutronic nodes. Figure 5.13 schematically depicts the two mappings used to link TRACE and PARCS together.

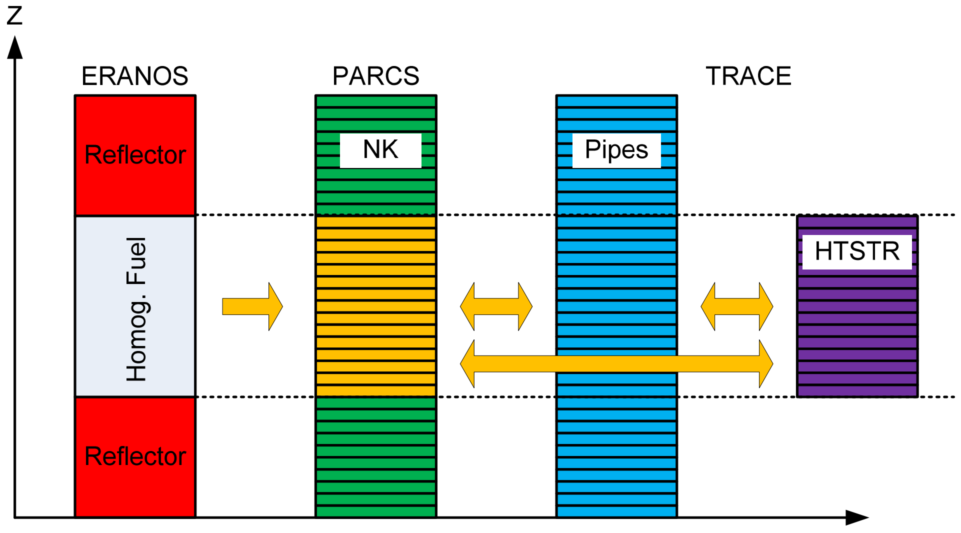

Figure 5.13 Schematic of the links between the different components of the coupled PARCS-TRACE model (mapping scheme)

The procedure is accompanied by the assignment of appropriate mapping weights w between the two meshes. The mapping weights have values from 0 to 1 and determine the distribution of the neutronic power in the thermal-hydraulic and heat-structure components. On the other hand, these factors are used to apply, in the following time step of the transient simulation, the calculation of the thermal-hydraulic feedbacks in the neutronic nodes. The mapping scheme is specified in an external input deck file (see Figure 5.14) and is read by the code at the initialization process [90]. In the mapping information file, the specification of the individual weighting factors for mapping the thermal-hydraulic and neutronic spatial regions is done through the use of cards. The two cards contain the weighting factors used for mapping a neutronic node to a component in the TRACE input deck for the thermal-hydraulic and heat structure components, respectively.

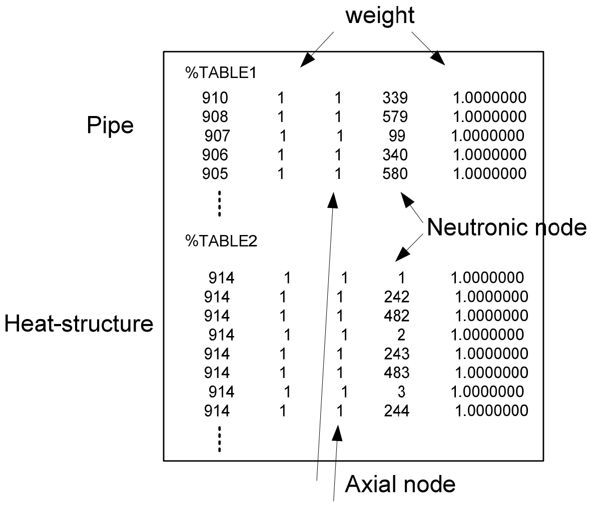

```
%TABLE1
 910    1    1   339    1.0000000
 908    1    1   579    1.0000000
 907    1    1    99    1.0000000
 906    1    1   340    1.0000000
 905    1    1   580    1.0000000
  ⋮
%TABLE2
 914    1    1     1    1.0000000
 914    1    1   242    1.0000000
 914    1    1   482    1.0000000
 914    1    1     2    1.0000000
 914    1    1   243    1.0000000
 914    1    1   483    1.0000000
 914    1    1     3    1.0000000
 914    1    1   244    1.0000000
  ⋮
```

Figure 5.14 Schematic of the external mapping scheme

Due to the complexity and repetitive nature of the mapping scheme (25515 neutronic nodes had to be linked to 13580 TH and 5820 heat-structure nodes for the “2004-Core” design), a semi-automatic procedure was developed and successfully tested. It consists of an algorithm that creates the mapping scheme, the basic information for which is given in an external file. This file contains different maps, viz. the sub-assemblies, the pipes and heat-structures and the weighting factors. The axial description for the neutronics and thermal-hydraulics is also provided. The use of this algorithm creates the necessary mapping file. Since the GFR core is modeled using a 1:1 scheme between the neutronics and the thermal-hydraulics, the mapping is facilitated in the sense that identical axial nodalizations can be chosen for the PARCS and TRACE input decks, mapping weight values of unity being assigned in both meshes.

5.2.6 Validation of the coupled models

In addition to the verification of the PARCS and TRACE standalone models, the final step of the development was the validation of the coupled models for the steady-state and the null-transient mode, which involves all the specific steps described above. The validation of the coupled TRACE/PARCS models were performed by comparing computational results against reference static ERANOS-2.0/VARIANT calculations, using the developed 3D HEX-Z core model (see Chapter 4), for different core configurations: “cold” (room temperature 20°C), and “hot” or nominal power conditions (HFP), for different CA positions. Code-to-code comparisons were made for the effective multiplication factors and the CA worths, as also for the total reactivity feedbacks (See Table 5.6).

Table 5.6 Comparisons of the effective multiplication factors (for “hot” and “cold” operating conditions), total reactivity feedbacks and CA worths, calculated with the coupled TRACE/PARCS model and with ERANOS in diffusion and transport theory (CAs in their parking position); “2004-Core” design.

"Hot" conditions	**k_{eff}**	**Difference, pcm**
PARCS/TRACE	1.0619	-
ERANOS-Diffusion	1.0633	118
ERANOS-Transport	1.0671	452
"Cold"[7] conditions	**k_{eff}**	**Difference, pcm**
PARCS/TRACE	1.0879	-
ERANOS-Diffusion	1.0871	-67
ERANOS-Transport	1.0947	571
	ERANOS	**TRACE/PARCS**
Temperature feedback effet (from room to operating temperature)	2063	2248

	Control assembly worth, pcm		
Configuration	**PARCS/TRACE**	**ERANOS-Transport**	**ERANOS-Diffusion**
1st CSD bank	2570	2293 (-10.8%)	2499 (-2.8%)
All CSDs	16091	15462 (-3.9%)	16500 (+2.5%)

---

[7] 20°C

By comparing the ERANOS effective multiplication factor results in diffusion and transport theory, it is seen that the transport effect is relatively small ($\delta\rho$= 334 pcm for “hot” conditions, 638 pcm for “cold”). The agreement for the k_{eff} value between ERANOS-2.0 in the diffusion approximation and PARCS/TRACE is excellent, the discrepancy being only 67 pcm.

The total CA worth values are also in relatively good agreement, PARCS/TRACE overestimating these in the range of 5% relative to ERANOS with transport theory. This is consistent with the trend observed between the diffusion and transport theory results within ERANOS itself.

Particular attention has been given to the validation of the reactivity feedbacks, in particular the Doppler reactivity constant:

$$C_{Dopp} = \frac{\rho_1 - \rho_2}{\ln\left(\frac{T_1}{T_2}\right)} \qquad \text{Eq. 5.10}$$

where ρ is the reactivity and *T* the temperature, the index *1* and *2* corresponding to two arbitrarily chosen fuel temperatures.

Detailed neutronic analysis was performed to breakdown the total reactivity effect, the Doppler component being found to amount to ~80% of the total feedback. The Doppler constant was calculated both with PARCS/TRACE and ERANOS (see Table 5.7). In ERANOS, two different temperatures (293 K and 493 K) were specified for the calculation. For obtaining a consistent result with PARCS/TRACE, the model was modified to a single TH-channel core model to avoid considering power, and thus temperature, distributions[8]. Thereby, the PARCS/TRACE calculations were performed at two different core powers to induce a difference of the fuel temperature.

Table 5.7 Doppler constant calculated with PARCS/TRACE and with ERANOS

Code	Doppler, pcm	Relative diff., %
ERANOS-Diffusion	-1510	6
PARCS/TRACE coupled	-1421	-

Relatively good agreement is seen to be obtained for the total feedback (see Table 5.6) and, in particular, for the Doppler reactivity constant, the discrepancy being in the order of 6% (see Table 5.7). These results show a trend for the feedbacks effects to be overestimated with the TRACE/PARCS model, particularly in the case of the thermal expansion effects. A reasonable explanation is the difference observed in the calculations of the average axial thermal expansion. In ERANOS, each region of the core is expanded according to the material temperature while, in TRACE, the core axial expansion is determined by an average (cladding) temperature. For the CA-

---

[8] considering that the ERANOS calculation corresponded to uniform fuel temperature in both radial and axial direction

driven transients being currently considered, however, the major feedback is due to the change in fuel temperature (Doppler effect), and the agreement with ERANOS in this context, as noted above, is in the range of 6%.

Similar verifications have been carried out for the “2007-Core” design. As an illustration, the code-to-code comparisons for the effective multiplication factor, the CA worth and the total reactivity feedback are provided in Table 5.8.

Table 5.8 Comparisons of the effective multiplication factors (for “hot” and “cold” operating conditions), total reactivity feedbacks and CA worths, calculated with the coupled TRACE/PARCS model and with ERANOS (CAs in their parking position); “2007-Core” design.

"Hot" conditions	k_{eff}	Difference, pcm
TRACE/PARCS	1.0401	-
ERANOS-Diffusion	1.0444	396
ERANOS-Transport	1.0466	597
"Cold" conditions	**k_{eff}**	**Temperature feedback effect, pcm**
TRACE/PARCS	1.0683	2535
ERANOS-Diffusion	1.0712	2398

	Control assembly worth, pcm		
Configuration	**PARCS/TRACE**	**ERANOS-Transport**	**ERANOS-Diffusion**
Both CSD banks	16171	17038 (+5.4%)	18168 (+12.3%)

As in the case of the reference core, good agreement is seen to be obtained for the “cold”-state effective multiplication factor ($\delta\rho$= 256 pcm), the discrepancy being somewhat larger for “hot” conditions ($\delta\rho$= 499 pcm). The total CA worth is in relatively good agreement, the discrepancies being in the range of 8%, while the agreement on the feedbacks, e.g. Doppler constant, is also good (in the range of 5%).

As indicated earlier, once the development and validation of the coupled models was terminated, coupled simulations were performed in order to compute, first, the steady-state, and then the null-transient solution as final preparation prior to considering the CA-driven transients. The normalized power map distribution in the steady-state mode is depicted in Figure 5.15. The dark blue color shows assemblies for which the power is not calculated, e.g. CAs.

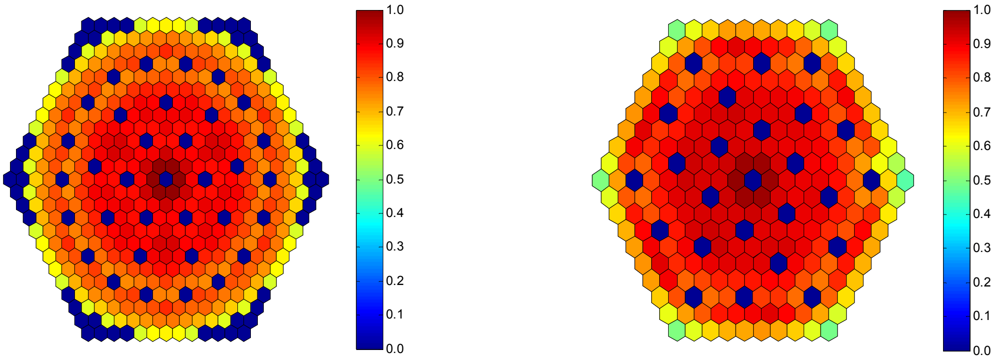

a) **b)**

Figure 5.15 Power map distribution in steady-state (normalized values);

a) "2004-Core" design and b) "2007-Core" design

The transient simulations were performed assuming that the CSD CAs are withdrawn at constant speed from the reference position (relative insertion of ~25%[9]). In each case, the reference position chosen is representative of the reactivity needs of the second batch of the fuel cycle (831 to 1662 EFPDs), related to a three-batch scheme in terms of the reactivity swing (more details about the fuel management scheme can be found in Appendix E). In this case, the CAs compensate for the reactivity swing during the average fuel cycle. The relative insertion corresponds to a reactivity worth of:

$$\delta\rho_{"2004-Core"} = \sim 2200\ pcm$$

$$\delta\rho_{"2007-Core"} = \sim 1600\ pcm$$

5.2.7 Cusping corrections

While simulating CA withdrawal, in particular at low speed, numerical oscillations of the CA worth, which are caused by "cusping effects", were observed [163]. In order to deal with this problem, certain modifications had to be made to the PARCS code.

Cusping effects are characteristic of nodal methods and are associated with the use of large axial mesh sizes (e.g. 10 cm) when there is CA movement within the nodes. In such an axial node, the CA worth of a partially inserted CA is not calculated with sufficient accuracy, due to the use of a volume-weighting approach for obtaining the absorber cross-sections. Effectively, the self-shielding effects within the node are not accurately taken into account. To overcome this numerical problem, a specific PARCS routine has been refined, such as to be able to reproduce

---

[9] a value which was found to be fortuitously the same for the two cores

the flux depression within the node more accurately. For this purpose, ERANOS/VARIANT fine-flux calculations were first carried out to obtain corrections factors $C_{i,z}^{j}$, defined by:

$$C_{i,z}^{j} = \frac{\varphi_{i,z}^{j}}{\overline{\varphi_{i}^{j}}} \qquad \text{Eq. 5.11}$$

where the subscripts are the neutron group *i*, the nodal mesh *j* and the relative insertion *z* of the CA within the mesh *j*. φ is the fine flux and $\bar{\varphi}$ is its average value within the mesh *j*.

As an illustration, Figure 5.16 compares the core power, the average-outlet coolant temperature and the peak cladding temperature in CA withdrawal accident for two cases: (1) with the original macroscopic cross-section treatment (labeled as “original treatment” in the figure) and (2) with the implemented fine-flux corrections (“with corrections”) for a CA withdrawal at low constant speed. It is seen that, in case 1), the computed values are periodically lower in between two axial nodes. The differences are rather small, since the maximal power difference amounts to only about 3%, inducing a difference of maximum 12 K and 20 K for the average-outlet coolant and peak cladding temperatures, respectively. The treatment “with corrections” was applied to simulate the CA withdrawal transients.

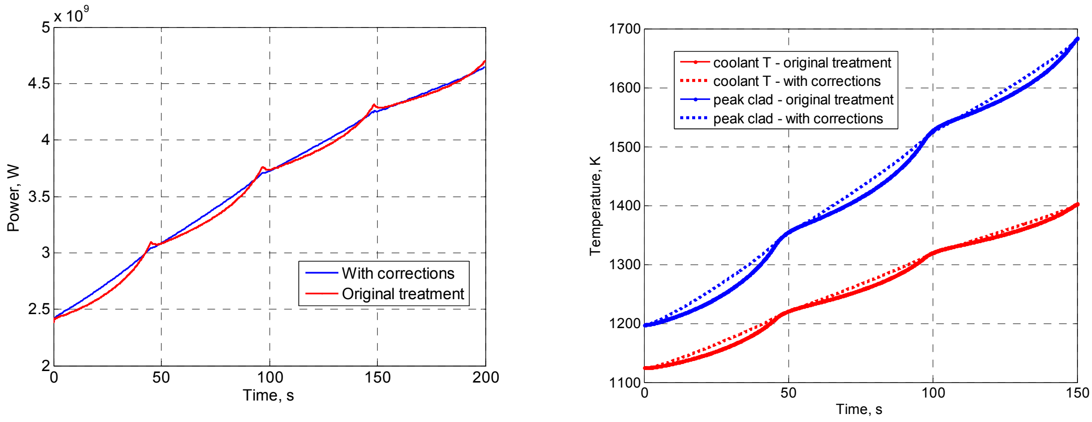

a) **b)**

Figure 5.16 a) Comparative power evolution in CA withdrawal accident, and b) thermal-hydraulics results (1) with the original CA treatment in PARCS and (2) with the cusping corrections; “2004-Core” design

5.3 Transients considered for analysis

Using the developed full-core coupled models, CA withdrawals at normal operating speed (assumed to be 2 mm/s) and at ejection speed (assumed to be up to 60 cm/s) have been simulated, in order, primarily, to study:

1. The adequacy of the developed CA pattern during operational transients.
2. The deformation of the power map (spatial effects) related to asymmetric CA movements.

The response of the core to CA withdrawal at operational speed was studied to demonstrate that the safety criteria are met in case of this relatively high-probability type of event, thus completing the qualification of the developed CA pattern.

For the sake of obtaining a detailed understanding of the 3D core dynamics, a variety of transients were studied, and a sensitivity study of the spatial effects to different parameters (viz. the CA implementation scheme, the CA speed and number being withdrawn/ejected) was carried out. Additionally, the impact of the core response to the presence of burnt fuel (BOEC conditions), as also to the use of different TH models, was investigated.

In principle, the aims of the 3D core-dynamics analysis may be considered as threefold, viz.

(1) To verify the adequacy of the CA pattern specifically developed for the GFR cores,
(2) To detect any potential safety-related problems associated with CA movements (at operating or at high speeds),
(3) To obtain further insights into the 3D spatial phenomena occurring within the core (related essentially to asymmetric reactivity insertion).

As mentioned earlier, the two GFR core designs, viz. “2004-Core” and “2007-Core”, were investigated using full-core, coupled NK-TH models developed specifically for the present dynamics and safety analysis. This has allowed one to compare the two GFR core designs in a consistent, systematic manner. In more generic terms, the GFR cores comparison was realized to better understand the correlation which exists between power map deformations and CA interactions (i.e. shadowing/anti-shadowing effects).

The conducted, GFR transient simulations may be categorized in terms of:

(1) “2004-Core” CA withdrawals,
(2) ”2007-Core” CA withdrawals,
(3) “2004-Core” CA ejections,
(4) “2007-Core” CA ejections.

As stated earlier, the transient simulations were performed assuming that the CSD CAs are withdrawn at constant speed for both GFR cores. Thereby, it is important to note that the analysis compares different operating reactors under the same CA-movement conditions from critical positions. Thus, the reactivity worth inserted during the CA withdrawal is not strictly identical.

In order to compare the different cases in a systematic manner, certain TH limits have been assumed, based upon different safety considerations [164]. The assumed limits have been ranked, depending on the frequency of occurrence of the initiating events. As such, they represent different levels of safety criteria (see Table 5.9), viz.

(1) *Safety Criterion 1:* The coolant temperature at the hot outlet reaches the limit of 1523 K.
(2) *Safety Criterion 2:* The peak cladding temperature reaches the limit of 1723 K.
(3) *Safety Criterion 3:* The fuel temperature reaches the limit of 2273 K and/or the cladding temperature reaches the limit of 1923 K.

Table 5.9 Safety criteria and associated thermal-hydraulics temperature limits

Safety Criterion	Thermal-hydraulics temperature limits Coolant, K	 Peak cladding, K	 Peak fuel, K
1	1523	-	-
2	-	1723	-
3	-	1923	2273

For defining the above safety categories and the corresponding temperature limits, various accidental situations were investigated on the basis of both deterministic and probabilistic analysis [164]. Even at an early stage, such analysis is necessary in order to:

(1) Verify that the reactor concept is safe, for a certain set of possible Initiating Events (IEs),
(2) Identify possible weakness in the basic design.

With the present research limited to the safety verification of the developed CA pattern, it is clear that a detailed safety analysis for the GFR requires, among other things, the identification of IEs, which are not covered by the presented investigations.

5.4 CA withdrawal cases at operating speed

This section presents the GFR cores (“2004-Core” and “2007-Core”) response, consecutive to CA(s) withdrawals at operating speed. The analysis has been carried out in a systematic manner for the two GFR cores. The following are the considered transient cases:

(1) Single CA withdrawal from the 1st bank,
(2) Withdrawal of three CAs from the 1st bank,
(3) Withdrawal of multiple (three and six) CAs from the 1st bank at hot zero power (HZP) conditions.

Prior to the CA-withdrawal analysis, the steady-state regime associated to HFP was analyzed, the corresponding results being presented in Subsection 5.4.1. As indicated earlier, for the transient simulations, a constant withdrawal speed of 2 mm/s was assumed. This CA speed is similar to that of earlier studied, commercial sodium reactors (e.g. Superphénix and EFR). In the absence of GFR-design specifications, this value was taken as the reference speed for the simulations, a sensitivity analysis being performed separately.

The presented results include the evolution of the following parameters:

(1) Total core power,
(2) Total (dynamic) reactivity,
(3) Peak fuel temperature,
(4) Peak cladding temperature (maximal lateral-wall inner surface),
(5) Outlet coolant temperature,

(6) Power map deformation as a function of time. The relative power map deformation, at any given time, represents the change of the power distribution relative to the steady state. It is important to stress that the steady-state distribution is determined by the gagging scheme. In a similar manner, deformations of the fuel and coolant temperature maps have been analyzed.

(7) Channel-dependent, thermal-hydraulics results (temperature). Since a full-core GFR model is being used, channel-dependent parameters can be monitored explicitly.

5.4.1 Steady-state analysis

The steady-state results for both GFR core designs are discussed in this subsection. These results serve as reference in order to compare, subsequently, the values obtained during the various transient cases examined. Since each TH channel is modeled individually in TRACE, one has access to the individual channel temperatures. The corresponding results for outlet helium and peak cladding temperatures are shown in Figure 5.17, for the reference core at steady-state conditions, a similar distribution being obtained for the "2007-Core" design.

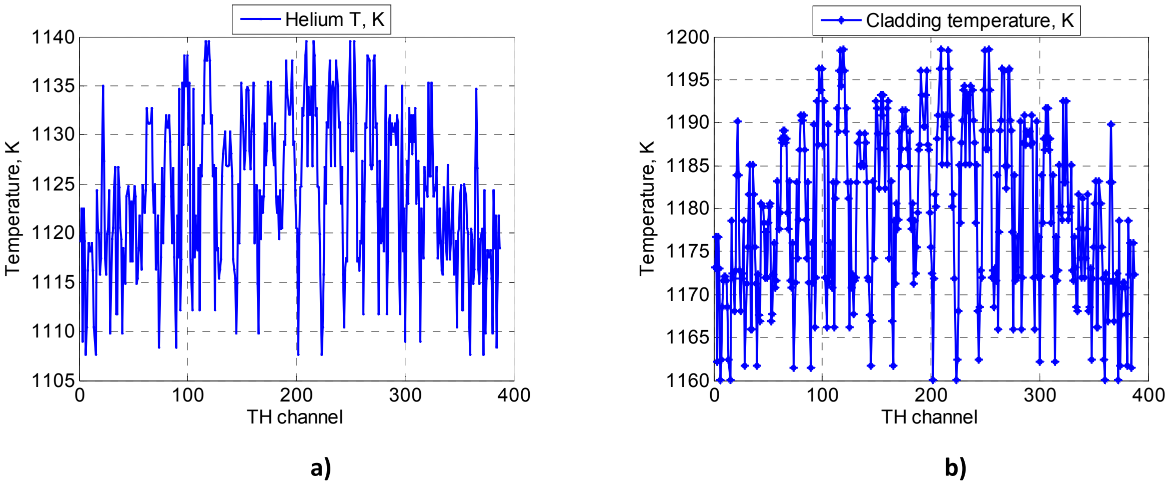

Figure 5.17 Channel-dependent a) outlet helium temperatures and b) peak cladding temperatures; "2004-Core" design

Based upon the above distributions, it is possible to verify that, in the case of the outlet-coolant temperature for example the individual channel temperatures have a rather flat Gaussian distribution centered, in this case, on a value of 1123 K. This is a clear indication of a proper gagging scheme.

The minimal, average and maximal values of the outlet coolant and peak cladding temperatures for the reference core design are shown in Figure 5.18. Similarly, Figure 5.19 shows the corresponding results for the "2007-Core" design. The temperatures correspond, in both cases, to the corresponding design specifications.

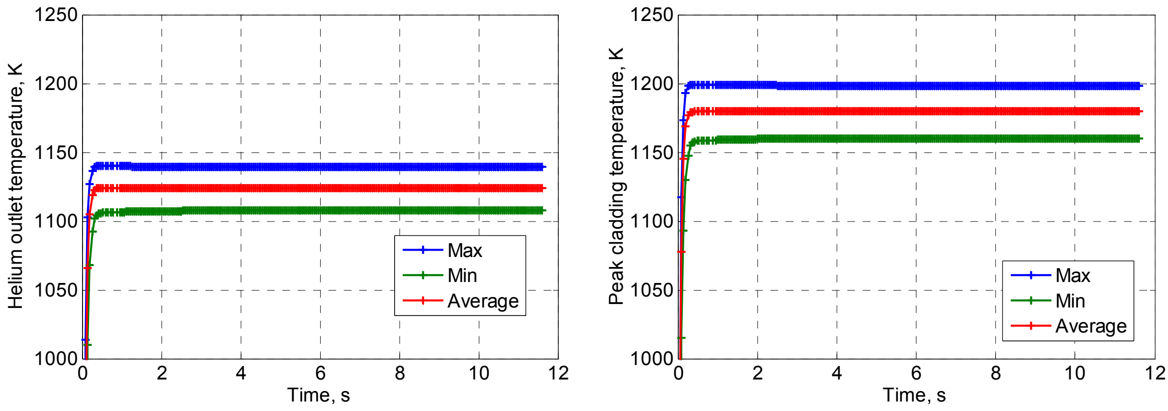

a) Channel-dependent coolant temperature

b) Channel-dependent peak cladding temperature

Figure 5.18 Thermal-hydraulics results (steady-state) for a) the coolant temperature and b) the peak cladding temperature; "2004-Core" design

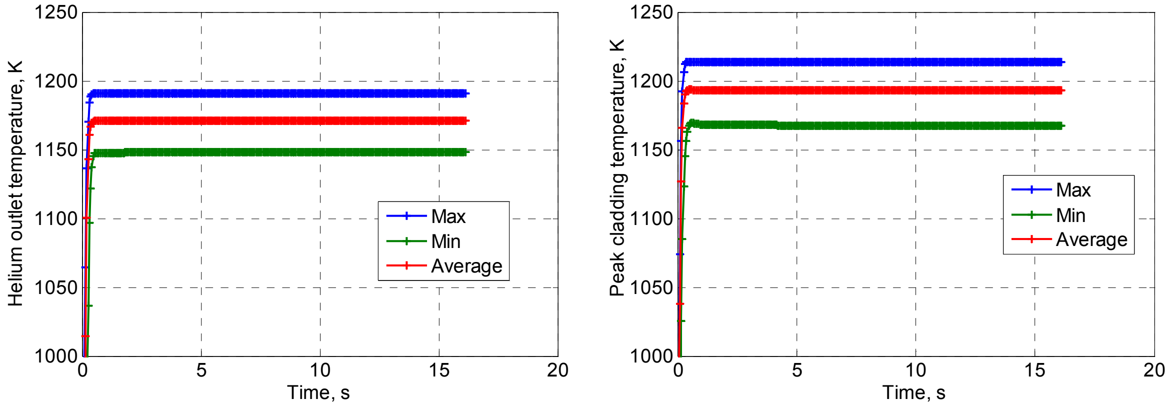

a) Channel-dependent coolant temperature

b) Channel-dependent peak cladding temperature

Figure 5.19 Thermal-hydraulics results (steady-state) for a) the coolant temperature and b) the peak cladding temperature; "2007-Core" design

To complete the results obtained from the steady-state analysis, the peak fuel temperature for the two GFR cores is shown in Figure 5.20.

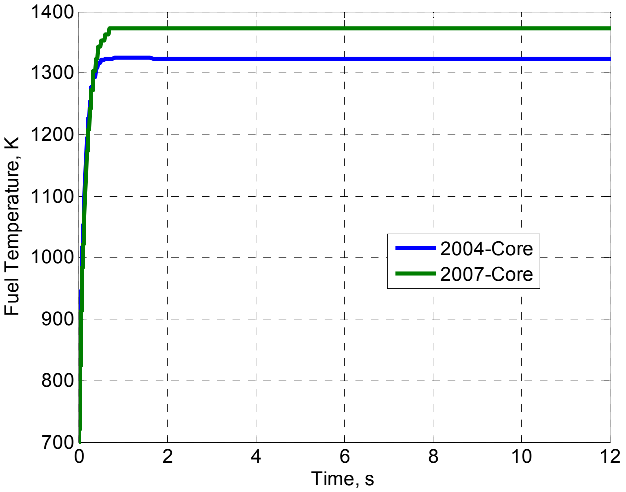

Figure 5.20 Peak fuel temperature at steady-state conditions for both GFR core designs

For the sake of clarity, only the outlet-coolant, peak cladding and peak fuel temperatures are presented in a systematic manner below.

5.4.2 Single CA withdrawal of the 1st CSD bank

A single CA of the first CSD bank is withdrawn during 200 s for the reference core, and during 300 s for the “2007-Core” design, at a constant speed of 2 mm/s and then kept at the upper parking position. This corresponds to a static reactivity insertion of approximately 0.3 $ for the “2004-Core” and 0.2 $ for the “2007-Core”. A comparison of the power evolution, as also of the total (dynamic) reactivity variation, for the two cases is shown in Figure 5.21. The thermal-hydraulics results – peak fuel, peak cladding and outlet coolant temperatures – are shown together for both cores in Figure 5.22.

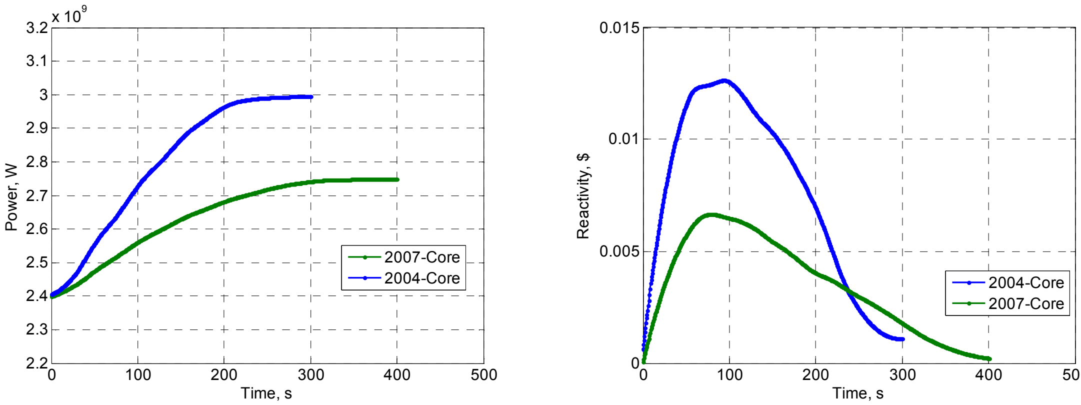

a) **b)**

Figure 5.21 a) Core power evolution and b) total dynamic reactivity for a single CA withdrawal from the "2004-Core" and the "2007-Core"; CA speed of 2 mm/s

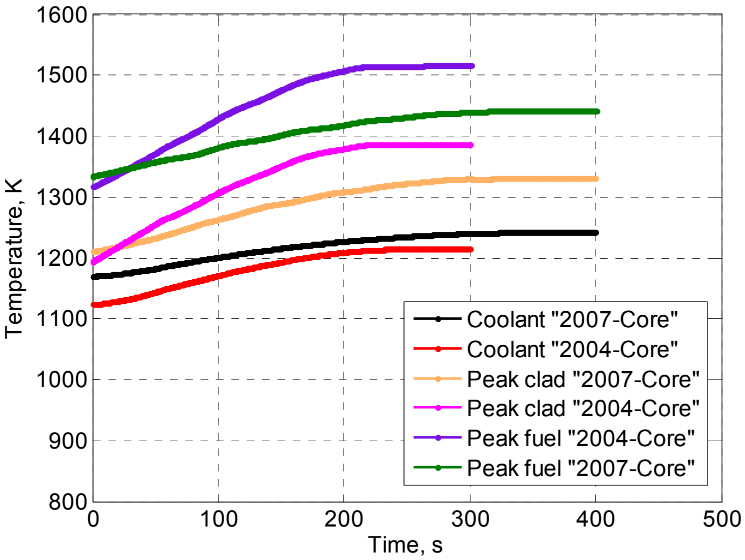

Figure 5.22 Thermal-hydraulics results for a single CA withdrawal (2 mm/s): comparison between "2004-Core" and "2007-Core"

The power map deformations at the end of the CA withdrawal, relative to steady state, are depicted in Figure 5.27 ("2004-Core") and in Figure 5.28 ("2007-Core"). The definition used for the power map deformation (PMD) of the *i*th channel, at any given time *t,* is as given in Eq. 5.12. Analogous definitions have been used to express the spatial deformation of other parameters, e.g. the outlet coolant temperature.

$$PMD_{i,t}\ (\%) = \frac{{}^{P_{i,t}}\!/\!_{P_{average}} - {}^{P_{\mathrm{i,0}}}\!/\!_{P_{average}}}{{}^{P_{\mathrm{i,0}}}\!/\!_{P_{average}}} .100 \qquad \text{Eq. 5.12}$$

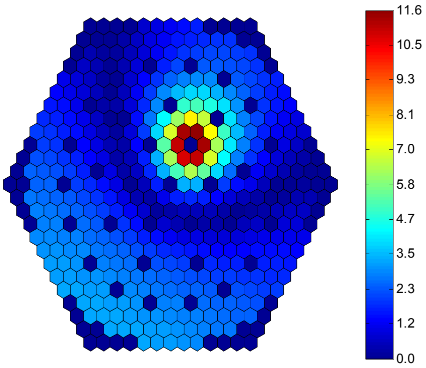

Figure 5.23 Power map deformation (expressed in %), at t=200 s, for withdrawal of a single CA from the 1st CSD bank; "2004-Core"

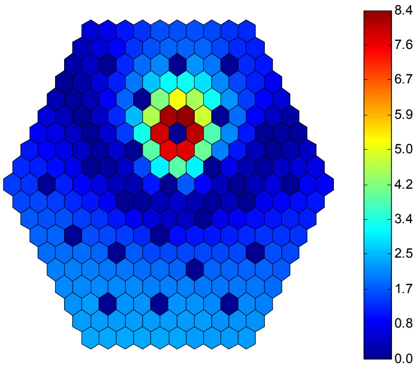

Figure 5.24 Power map deformation (expressed in %), at t=300 s, for withdrawal of a single CA from the 1st CSD bank; "2007-Core"

As can be seen, the power stabilizes at ~3 GWth at t=300 s for the reference core, and at ~2.75 GWth (lower by ~ 8%) for the second core variant due to the lower CA-worth extracted. The time to reach the stabilization is also longer in the latter case, viz. t=372 s. A consistent trend is observed for the peak fuel and cladding temperature, the values being 74 K and 55 K lower for the "2007-Core", respectively. On the contrary, the average outlet-coolant temperature is higher (by 27 K), this difference being well explained by the higher nominal outlet temperature for the "2007-Core" design (1173 K instead of 1123 K). More important is the lower rate of temperature increase observed for the "2007-Core", compared to the reference core. This shows that the time needed to reach the same ΔT will be longer, which is clearly more favorable for safety.

The results obtained for this transient case show no evidence of safety-related problems resulting from a single CA withdrawal at low speed. In particular, none of the three temperature limits specified in Section 5.3 is reached.

5.4.3 Withdrawal of three CAs of the 1st CSD bank

This transient is similar to the previous case, apart from the fact that three neighboring CAs are withdrawn simultaneously from the first CSD bank at operating speed (2 mm/s), rather than just one. Effectively, this hypothetical accident corresponds to the withdrawal of half of the first CSD bank, and to a static reactivity insertion of approximately 0.95 $ ("2004-Core") and 0.72 $ ("2007-Core"). The comparison of the power evolution for the two cores is shown in Figure 5.25, along with the dynamic reactivity variation. It can be seen that the dynamic reactivity is small, as a result of the quasi-static nature of the transient, caused in part by the low CA speed. At any given time, the fuel Doppler effect almost entirely compensates the inserted reactivity.

When the CAs reach the parking position, the core power is increased to 4.4 GWth after ~250 s in the "2004-Core", and to 3.8 GWth after ~350 s in the "2007-Core" design. The power peak is again seen to be significantly lower (-14%) in the latter case.

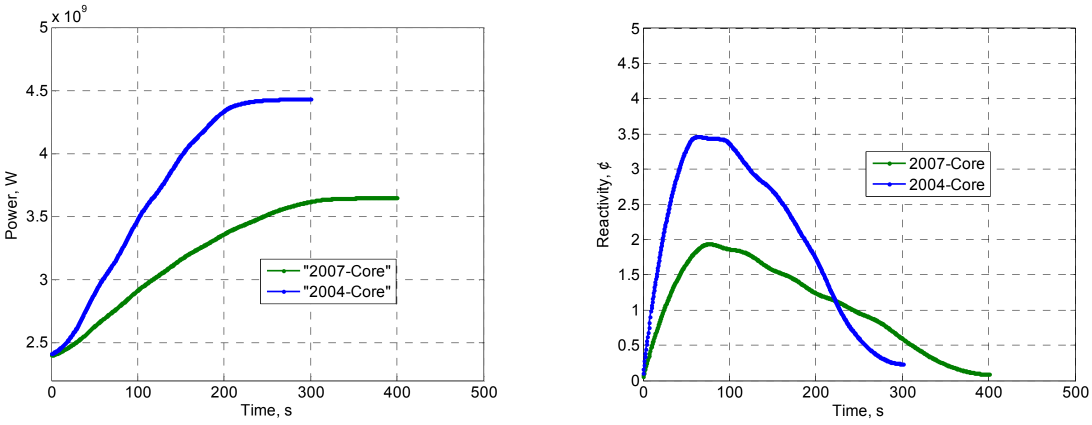

a) **b)**

Figure 5.25 a) Core power evolution and b) dynamic reactivity for the withdrawal of three CAs at a speed of 2 mm/s; "2004-Core" and "2007-Core"

The TH results obtained for both GFR cores are presented in Figure 5.26.

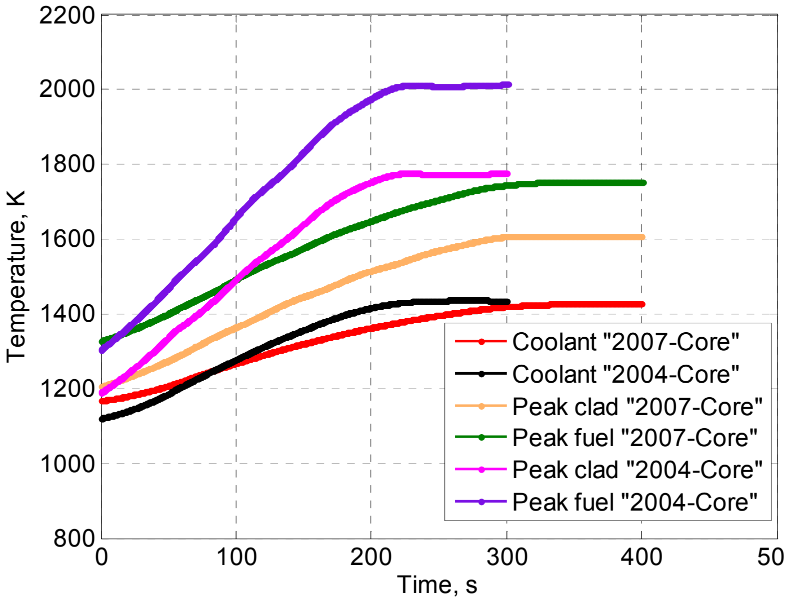

Figure 5.26 Thermal-hydraulics results for withdrawal of three CAs (2 mm/s): comparison between "2004-Core" and "2007-Core"

The power map distributions at the end of the CA withdrawal, relative to steady state, are depicted in Figure 5.27 ("2004-Core") and in Figure 5.28 ("2007-Core").

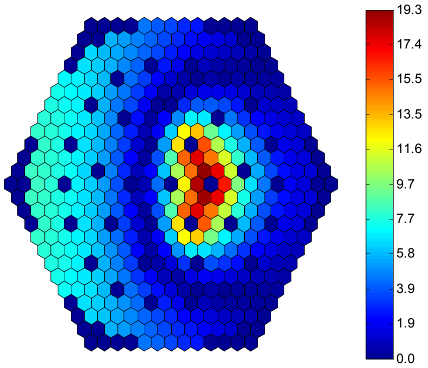

Figure 5.27 Power map deformation (expressed in %), at t=200 s, for withdrawal of three CAs from the 1st CSD bank; "2004-Core"

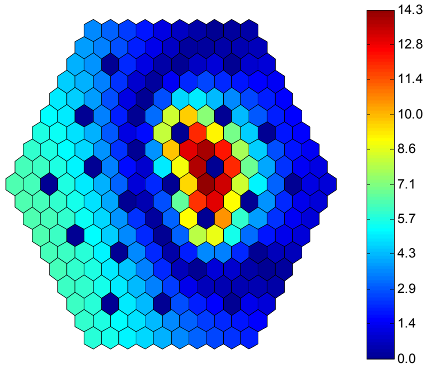

Figure 5.28 Power map deformation (expressed in %), at t=300 s, for withdrawal of three CAs from the 1st CSD bank; "2007-Core"

As seen from Figure 5.27 and Figure 5.28, a large power increase, relative to the average fission power, is observed in the two rings of fuel SAs adjacent to the withdrawn CAs. These results show the existence of large 3D spatial effects. An interesting finding is the lower spatial effects in the "2007-Core" (14% compared to 19%).

The results obtained for this transient case show that the first limiting factor is the cladding temperature for the "2004-Core". The assumed limit of 1723 K is reached at t=181 s. On the other hand, the limit is not reached for the "2007-Core", the cladding temperature being significantly lower (by 125 K) in this case. No specific limitation is imposed by the outlet coolant temperature, the values for both reactors being lower than the limit of 1523 K. The largest difference between the two cores is obtained for the peak fuel temperature, the value being 212 K lower in the case of the "2007-Core". On the contrary, the average outlet coolant temperature is higher by 23 K. As mentioned earlier, this difference can be explained by the difference in the operating temperatures.

5.4.4 Withdrawal of multiple CAs of the 1st CSD bank at hot zero power (HZP)

Here, the response of the GFR cores was analyzed for the withdrawal of CAs at hot zero power (HZP) conditions. This state is quite often realized in a power reactor, viz. when it is critical but at low power (due, for instance, to a strongly reduced electricity demand, or following a reactor shutdown). In this case, the fuel temperature is nearly the same as the helium temperature. As a consequence, one has a reduced Doppler effect, and CA withdrawals can lead to larger power excursions, causing higher temperatures to be reached.

For the sake of the analysis, two different cases were examined ("2007-Core"):

(1) Withdrawal of three consecutive CAs of the first CSD bank at operating speed,
(2) Withdrawal of all the CSDs (18 CAs) at operating speed.

The results for these two transients are presented only for the “2007-Core” design. Similar analysis was performed for the “2004-Core” design, and the core behavior found to be similar.

Prior to the initiating event, all the CSDs are inserted and HZP are established (instead of the hot full power conditions assumed in the previous cases). For the simulation, steady-state conditions are considered with a core power reduced to 0.1% of the nominal power. The transient occurs with the withdrawal of the CSDs at 2.0 mm/s during 387 s. The simulation was stopped shortly after the clad temperature reached 1723 K.

The comparative evolution of the core power is shown in Figure 5.29. The nominal power is reached after 340 s for the first case, while it takes only 132 s to reach the same power level for the “all CSDs” case. Figure 5.30 shows the corresponding peak cladding, peak fuel and outlet-coolant temperatures.

As shown by the curves, a slow increase of the temperatures is observed for the withdrawal of three CSDs. As previously, the first limit is reached for the cladding temperature (1723 K), after 362 s for the three CSDs case and 151 s for the all-CSDs case. During both these transients, the coolant temperature remains well below the specified limit.

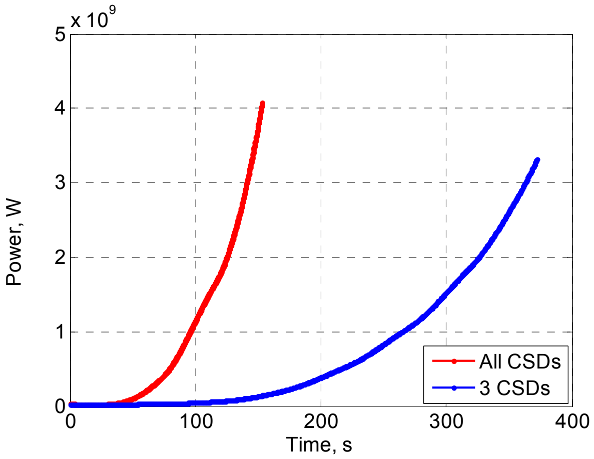

Figure 5.29 Withdrawal of (1) three CSDs and (2) all CSDs at 2.0 mm/s; “2007-Core” at hot zero power (HZP) conditions

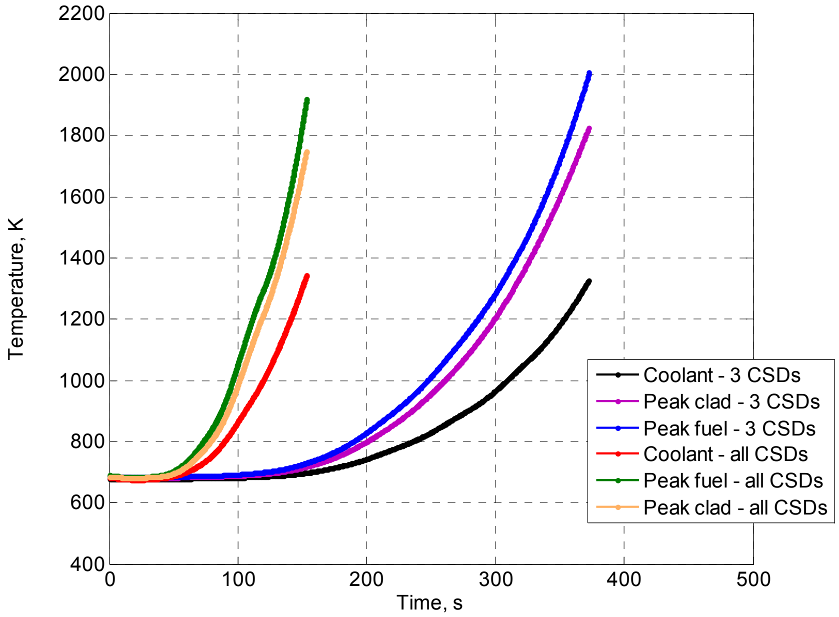

Figure 5.30 Thermal-hydraulics results for withdrawal of (1) three CDSs and (2) all CSDs at 2.0 mm/s; "2007-Core" at HZP

5.5 CA ejections and 3D spatial effects analysis

As already mentioned, the developed coupled-models were used additionally to study spatial effects for a variety of CA-driven transients at high speed, i.e. CA ejections. The same methodology for simulating the 3D core behavior was used as for the events at operating speed, CA ejection speeds of up to 60 cm/s being considered. Several cases were analyzed, in order to examine:

(1) The sensitivity of the power map deformation to the ejected CAs,
(2) The impact on the thermal-hydraulics results compared to the withdrawal cases.

For the CA-ejection transients, emphasis has been given to analysis of the spatial effects occurring within the different GFR core configurations. Accordingly, more detailed results are presented in terms of power and temperature map deformations.

The following are the three principal cases analyzed:

(1) Asymmetric ejection of a single CA of the first CSD bank,
(2) Asymmetric ejection of three CAs of the first CSD bank,
(3) Symmetric ejection of three CAs of the first CSD bank.

5.5.1 Asymmetric ejection of a single CA of the 1st CSD bank

This transient case considers the ejection of a single CSD of the first CSD bank from the reference position and corresponds approximately to a reactivity insertion of +110 pcm for the “2004-Core” and +80 pcm for the “2007-Core”. The power map deformations at t=1 s are depicted in Figure 5.31 (“2004-Core” design) and Figure 5.32 (“2007-Core” design).

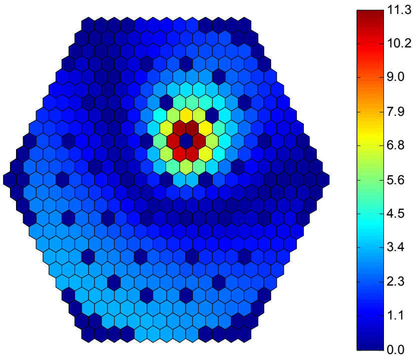

Figure 5.31 Power map deformation (expressed in %), at t=1 s, for ejection of a single CA; “2004-Core”

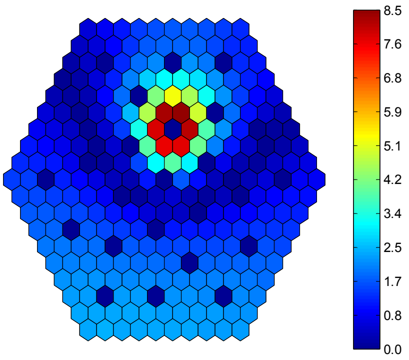

Figure 5.32 Power map deformation (expressed in %), at t=1 s, for ejection of a single CA; “2007-Core”

As observed in Figure 5.31 and Figure 5.32, considerable power map deformations, i.e. spatial effects, are observed for both GFR core designs as a result of the asymmetric reactivity insertion. The effects are in the range of +11% for the reference GFR core and are reduced to +9% for the “2007-Core” design. The differences between the two are rather small in this case.

Comparisons of the power evolutions and the total reactivity variations are shown in Figure 5.33, while the thermal-hydraulics results for the two cores are shown together in Figure 5.34. It is seen, from Figure 5.33, that the power peak is lower for the second core variant (~-7%), so that lower maximal fuel (~-70 K) and cladding (~-50 K) temperatures are reached. The differences can be explained by the lower total reactivity inserted. More important is the lower rate of temperature increase observed for the “2007-Core”, compared to the reference core. This indicates that the time needed to reach a given ΔT will be longer, which is more favorable for safety.

Of particular importance is the observation that none of the assumed temperature limits (see Table 5.9) are reached for this transient case.

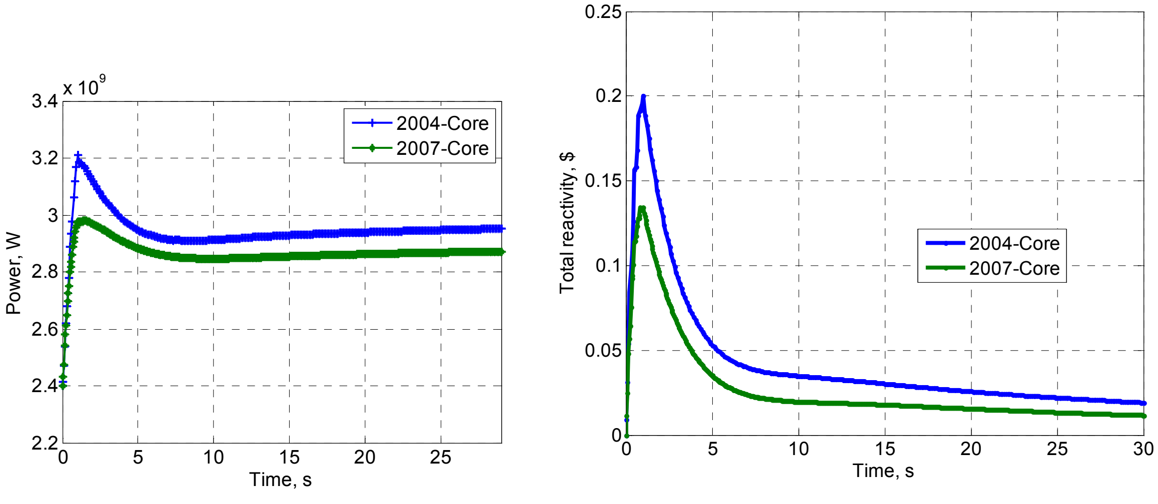

a) b)

Figure 5.33 a) Power evolution and b) total reactivity variation for ejection (within 1 s) of a single CA; "2004-Core" and "2007-Core"

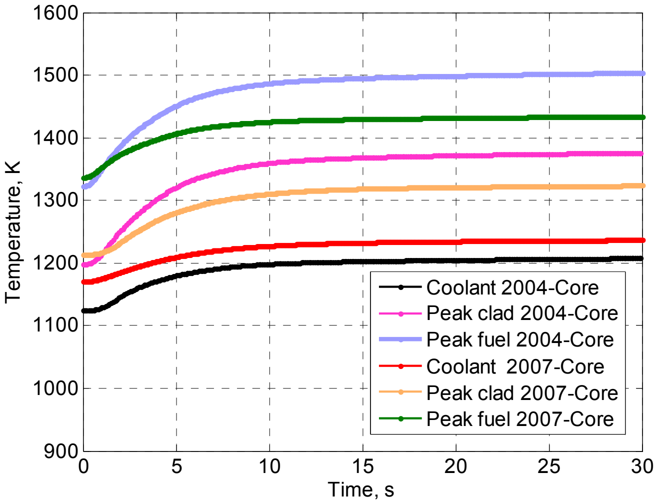

Figure 5.34 Thermal-hydraulics results for ejection (within 1 s) of a single CA of the first CSD bank. Comparison between "2004-Core" and "2007-Core"

5.5.2 Asymmetric ejection of three CAs of the 1st CSD bank

In this case, compared to the previous transient, three CAs of the first CSD bank are assumed to be ejected from the reference position within 1 s. This corresponds to a static reactivity insertion of +0.96 $ in the "2004-Core" and +0.71 $ in the "2007-Core", i.e. close to an insertion of 1 $ in each case. This hypothetical event may, as such, be considered as the reference transient in the present study.

The power map deformation at t=1 s is depicted in Figure 5.35. The spatial effects are in the range of 21% for the reference core, and are significantly reduced (to about 15%) for the “2007-Core”. The power map deformation is depicted in terms of the channel-dependent, relative power increase in Figure 5.36. It is seen that, for both cores, there are only a relatively limited number of thermal-hydraulics channels in which large power increases are observed.

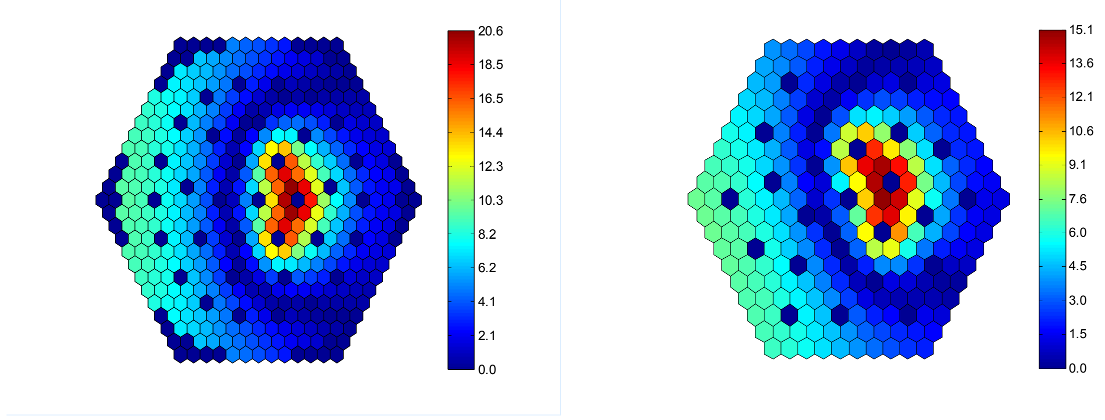

a) **b)**

Figure 5.35 Power map deformation (expressed in %), at t=1 s, for ejection of three CAs; a) “2004-Core” and b) “2007-Core”

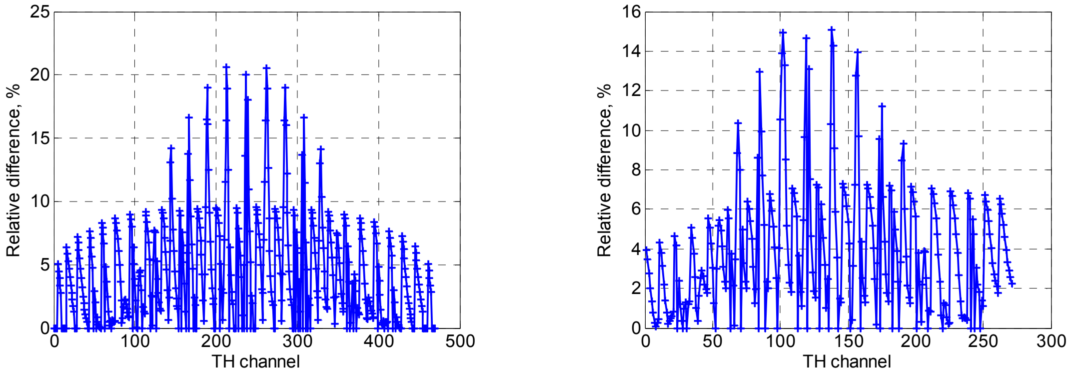

a) **b)**

Figure 5.36 Channel-dependent relative power deformation for ejection of three CAs; a) “2004-Core” and b) “2007-Core”

Comparisons of the power evolutions and the total reactivity variations are shown in Figure 5.37. To provide more detailed insight, the total reactivity is decomposed, in Figure 5.38, into its main components, viz. the CA reactivity worth, the fuel Doppler effect and the axial thermal expansion effect. As mentioned previously, the radial thermal core expansion, driven by the coolant inlet temperature, has negligible impact during the considered transients. It is seen that the core power is quickly reduced from its peak value mainly due to the large negative Doppler effect, which makes the major contribution (~90%) to the reactivity feedback.

The TH results are presented for both cores in Figure 5.39.

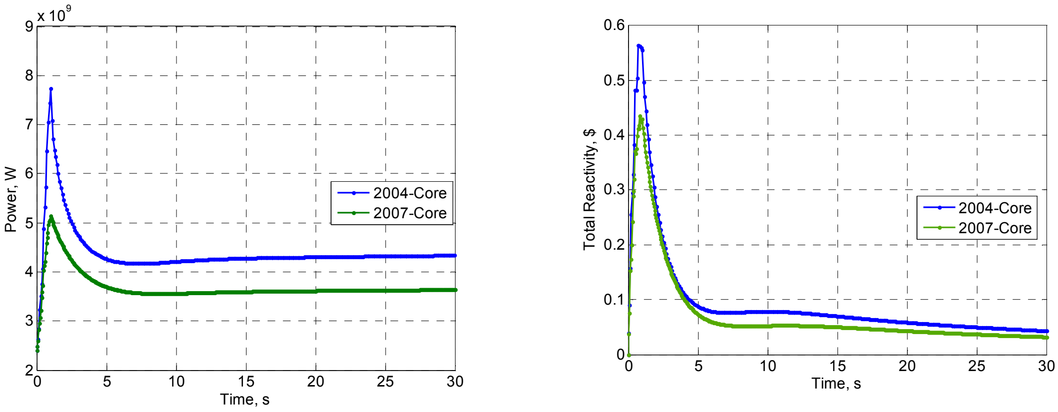

a) **b)**

Figure 5.37 a) Power evolution and b) total reactivity variation for ejection (within 1 s) of three consecutive CSDs of the first CSD bank; “2004-Core” and “2007-Core”

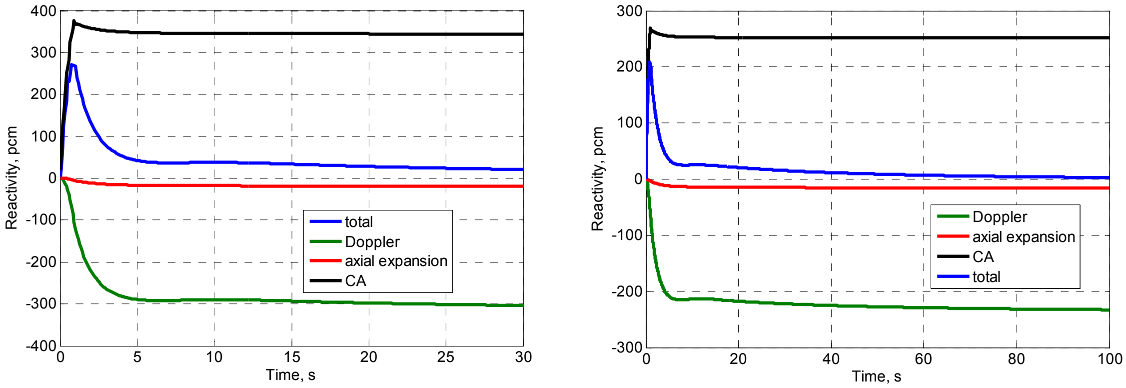

a) **b)**

Figure 5.38 Reactivity components of total reactivity: CA worth, fuel Doppler reactivity and axial core-expansion reactivity for a) “2004-Core” and b) “2007-Core”

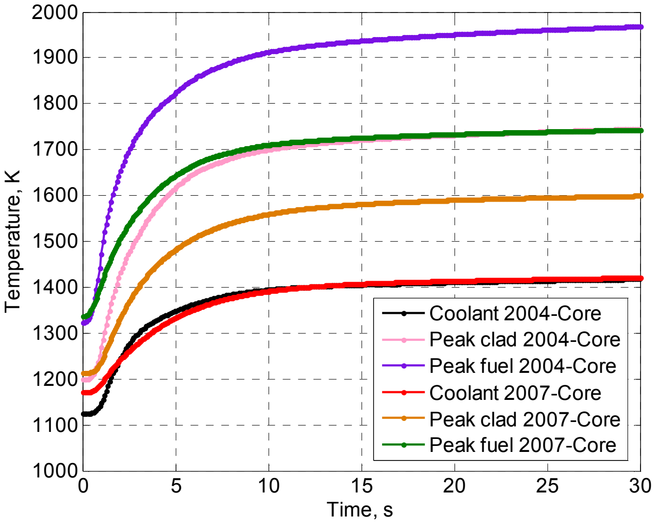

Figure 5.39 Thermal-hydraulics results for ejection (within 1 s) of three CAs of the first CSD bank. Comparison between "2004-Core" and "2007-Core"

As shown by the curves above, the first limiting factor is again the cladding temperature, with a limit of 1723 K (Safety Criterion 2). The limit is reached after ~15 s, a relatively short time. On the other hand, this limit is not reached for the "2007-Core". As in the case of the withdrawal of three CAs at operating speed, no specific limitation is caused by the outlet coolant temperature. The temperature margin is, in this case, in the range of 100 K. A lower value (by about 225 K) is obtained for the peak fuel temperature for the "2007-Core". A similar trend is observed for the peak cladding temperature, the value being significantly lower also here (by 145 K). On the contrary, the coolant temperature is slightly higher (by 2 K) for the new core.

Analysis of the axial power map deformation

The deformation of the axial power map was examined in order to evaluate the effects, not only in the radial direction, but also in the axial direction. The power map deformations as a function of the elevation are presented in Figure 5.40.

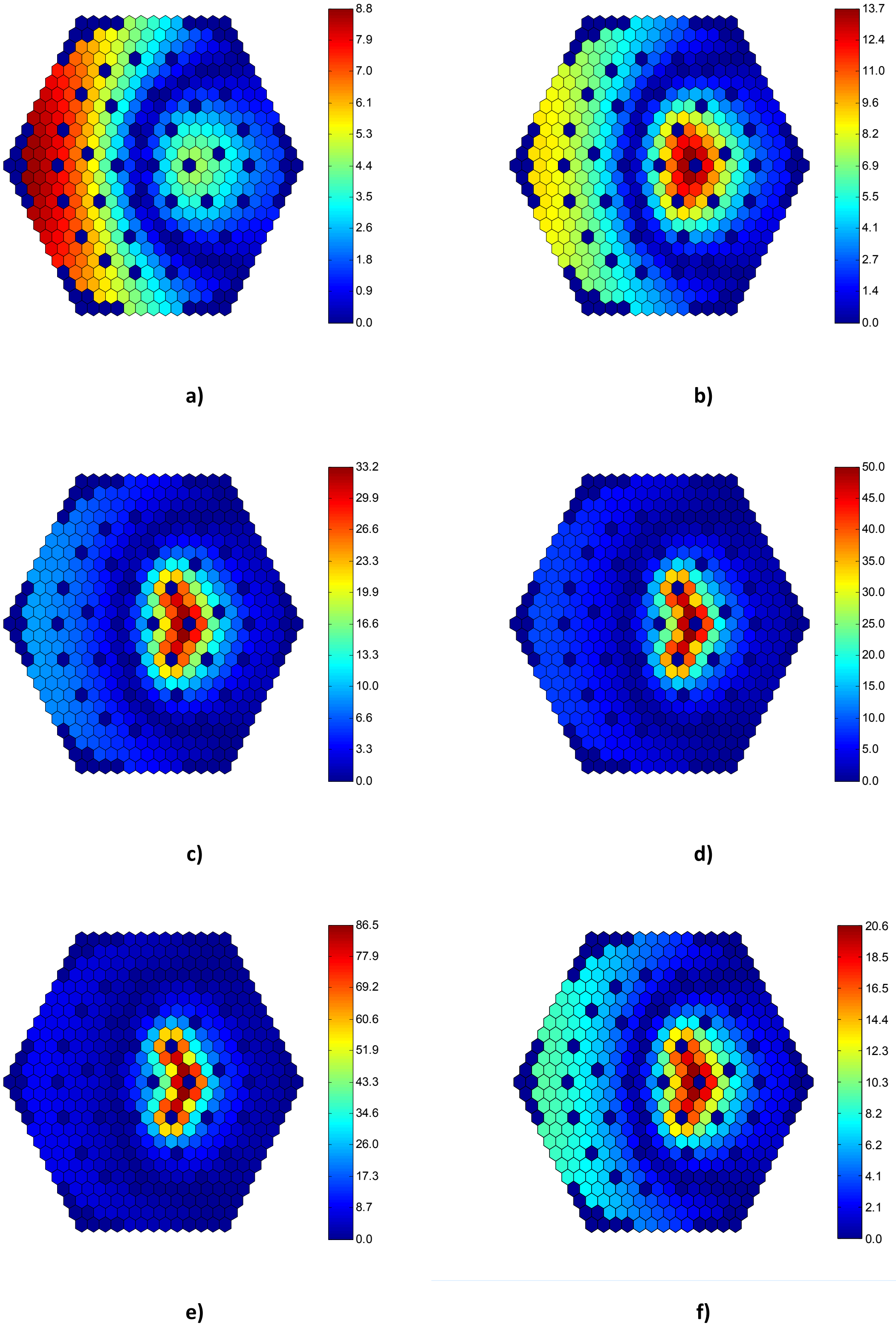

Figure 5.40 Analysis of the power map deformation, at t= 1 s, for the "2004-Core" design as a function of the elevation; a) relative height z_{rel} =0, b) relative height z_{rel} = 47%, c) relative height z_{rel} = 67%, d) relative height z_{rel} = 74%, e) relative height z_{rel} =100%, f) integral power

As previously shown, the spatial effects are in the range of +21% on average (integral power), close to the removed CAs. The axial analysis reveals that the spatial effects are, first, reduced in the lower part of the fuel height (+9% at a relative height of 0), and then increase progressively along the Z-axis to reach ~87% at the top fuel location (z_{rel}=100%). This indicates that larger temperature deformations (e.g. for peak fuel and peak cladding), relative to the core average, will occur in the upper region of the fuel where the CAs are ejected, i.e. the axial spatial effects are large. In the core regions distant from the ejected CAs, on the contrary, the power increase is significantly reduced and amounts only to a few percent.

Thermal-hydraulics map deformation analysis

As shown above, the power is increased locally in the fuel SAs close to the ejected CAs, which in turn increase the TH parameters, such as the average-outlet coolant and peak cladding temperatures. A detailed analysis has been carried out in order to evaluate the spatial effects as regards to the thermal-hydraulics results.

The outlet coolant map deformation at t=30 s, compared to the steady-state distribution, is depicted in Figure 5.41. This shows that there are large outlet coolant temperature differences between the thermal-hydraulics channels close to the ejected CAs and those more distant, the magnitude of these effects being in the range of 170 K for the “2004-Core” and 144 K for the “2007-Core”. These results also show the importance of a full (1:1) coupled model to track these large differences.

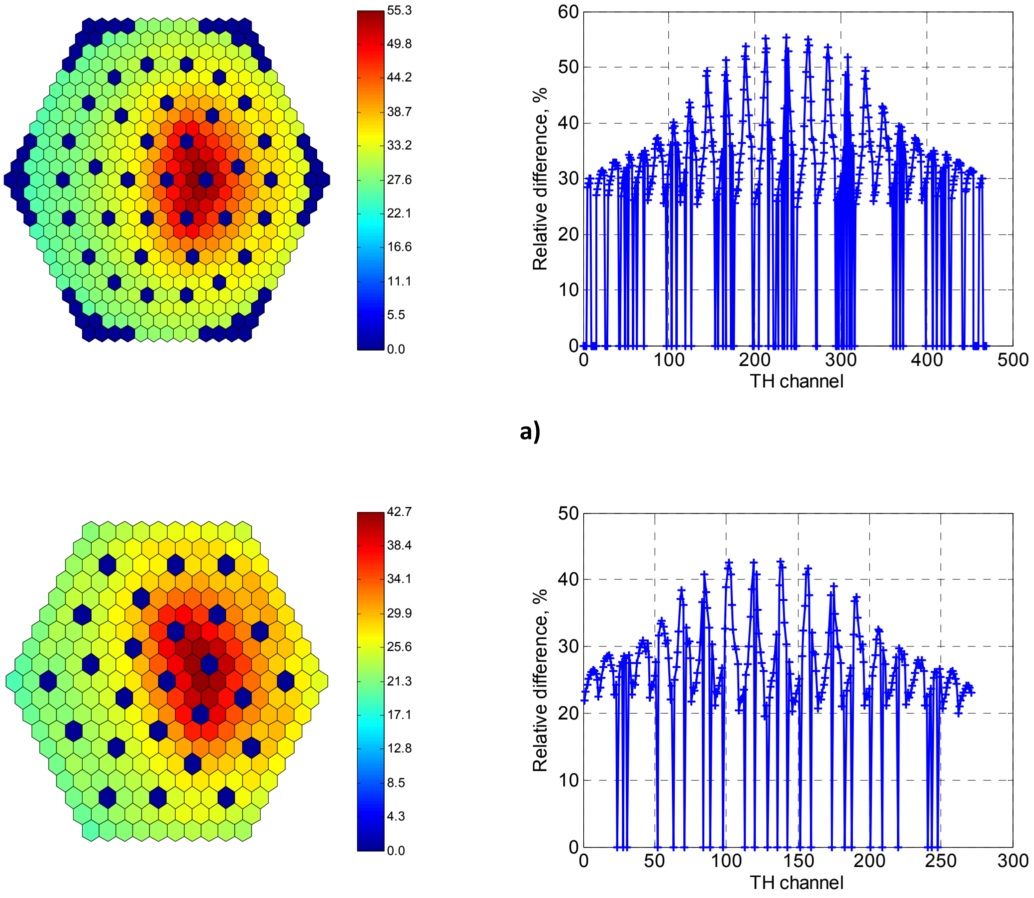

a)

b)

Figure 5.41 Outlet coolant map deformation and corresponding channel-dependent, relative increases (expressed in %) at t=30 s, for ejection of three asymmetric CAs of 1st CSD bank, for a) "2004-Core" and b) "2007-Core"

Evolution of the spatial effects

The power and TH map deformations have been shown above for the time at which the CAs have reached the upper parking position. In order to evaluate the importance of the spatial effects for the full duration of the transient, the deformations of the power and outlet coolant temperature maps are shown, for the "2004-Core", in Figure 5.42 for different times between 1 s and 10 s. Similar analysis was performed for the "2007-Core" design, and the spatial effects evolution was found to be similar.

From Figure 5.42, it is observed that:

(1) While the power map deformation increases while the CAs are in movement, the spatial effects are about at maximum (+21%) when the CAs have reached the parking position and the power peak occurs (at t=1 s). Thereafter, they remain almost constant (at about +19 %).

(2) The deformation of the outlet coolant temperature map clearly continues to increase during the transient. At the very beginning, there are almost no spatial effects (no radial or azimuthal variations), due to the thermal inertia. After the power peak occurs, the temperature differences get higher in the channels close to the ejected CAs. Thus, while the spatial effects amount to only ~3% at t=1 s, they slowly increase to reach ~52% at t=30 s.

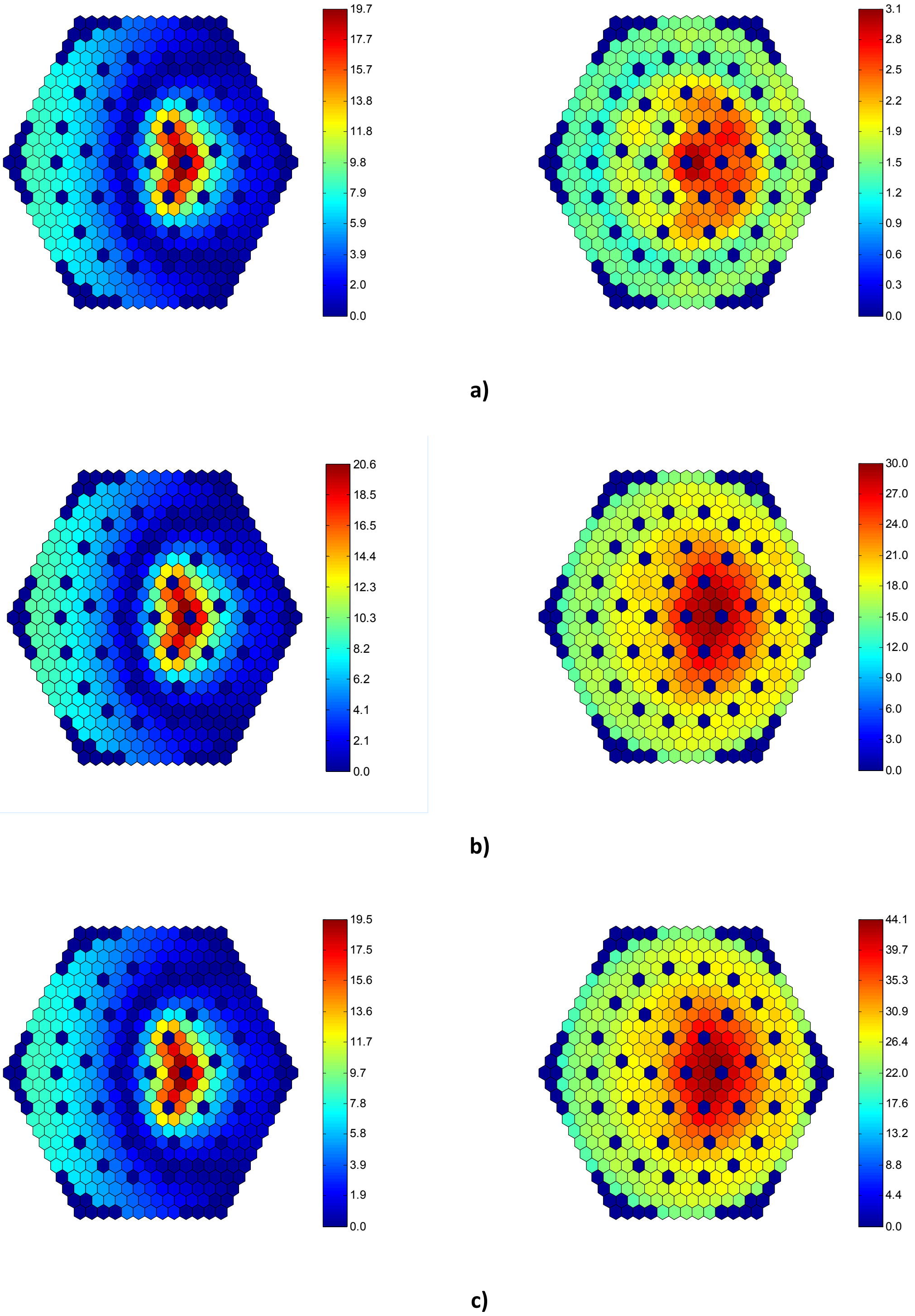

a)

b)

c)

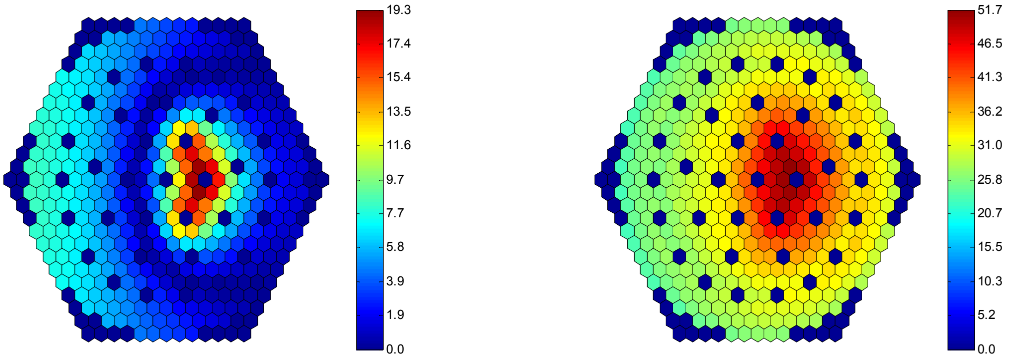

d)

Figure 5.42 Evolution of the map deformations for power (left) and outlet coolant temperature (right), for the “2004-Core” design; results shown for a) 1 s, b) 3 s, c) 5 s, d) 10 s.

5.5.3 Symmetric ejection of three CAs of the 1st CSD bank

The importance of the spatial effects has also been analyzed for the two GFR core designs in a situation corresponding to a symmetric reactivity insertion, in contrast to the previous transient cases of asymmetric CA ejections.

Starting from the steady-state hot full power conditions, three CAs of the first CSD bank with a 120° symmetry were assumed to be ejected within 1 s. Figure 5.43 shows the power map deformation at t=1 s for the two cores. The effects, in the order of 12% (“2004-Core”) and 8% (“2007-Core”), are found to be significantly lower than the corresponding values of 21% and 15%, respectively, for the case of the asymmetric ejection of three CAs (see Figure 5.35). This reveals that the power deformation is considerably reduced for a symmetric reactivity insertion, which is also qualitatively consistent with the reduction of the CA worth or inserted reactivity (by 8%), compared to the asymmetric case. Additionally, these results show the better behavior of the latter core in terms of spatial effects and neutronics stability.

As additional characterization of the transients, a comparison of the evolution of the power for the asymmetric and symmetric three-CAs ejection cases is shown in Figure 5.44 for the “2004-Core. Figure 5.45 gives the corresponding comparisons of results for the average outlet helium and peak cladding temperatures.

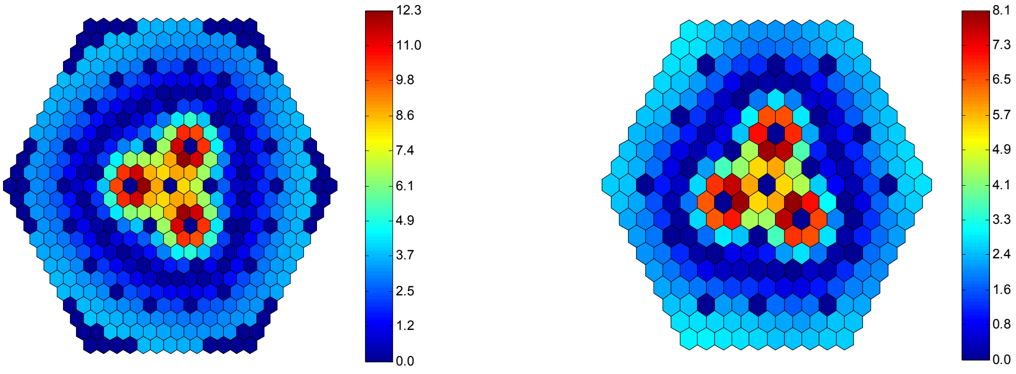

a) **b)**

Figure 5.43 Power map deformation (expressed in %) at t=1 s; reactivity insertion due to symmetric ejection of three CAs, a) for the "2004-Core" and b) the "2007-Core"

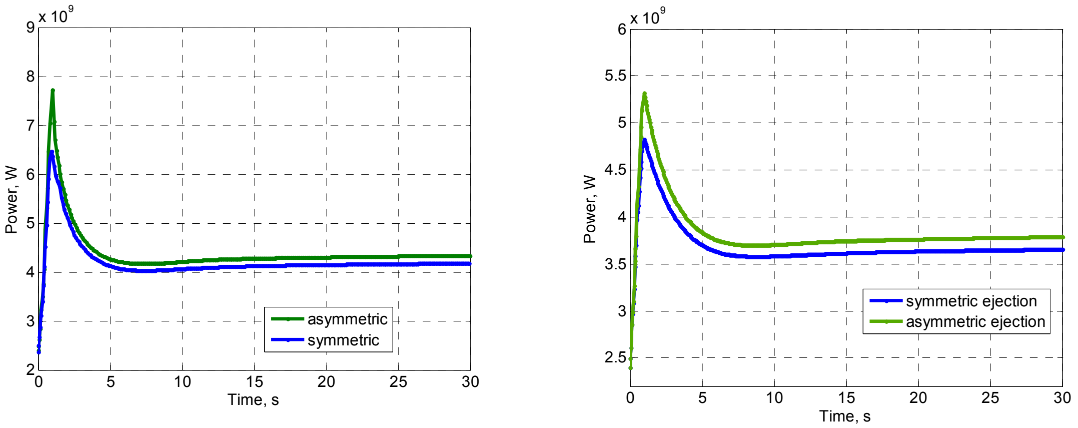

a) **b)**

Figure 5.44 Comparison of the power evolution for asymmetric and symmetric three-CAs ejection within 1 s; a) "2004-Core" and b) "2007-Core"

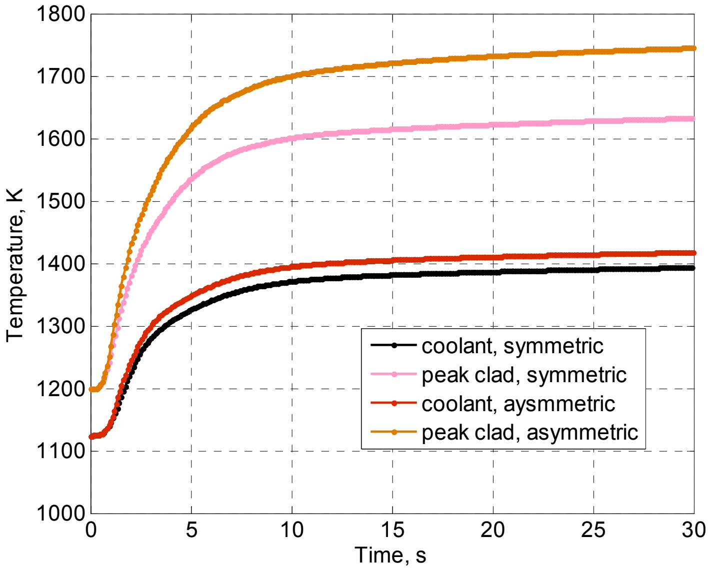

Figure 5.45 Thermal-hydraulics results for ejection of three CAs within 1 s. Comparison between asymmetric and symmetric ejections; "2004-Core"

Figure 5.46 shows the temperature differences between the peak cladding temperatures for the two simulated transients (symmetric and asymmetric CAs ejections), in the case of the "2007-Core" design. Three different curves are depicted, viz. (1) the difference in the maximal peak cladding temperature, (2) the difference in the average value, and (3) the difference in the minimal peak cladding temperature.

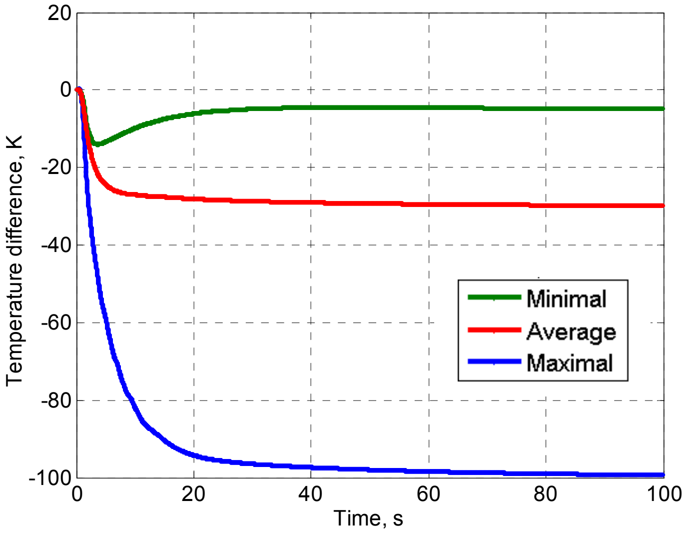

Figure 5.46 Peak cladding temperature differences between the symmetric and asymmetric ejections of three CAs within 1 s for the "2007-Core" design. Three curves are depicted, viz. the difference ("symmetric" – "asymmetric") in (1) maximal,(2) average, and (3) minimal peak cladding temperatures

As observed in Figure 5.44, the core power peak is reduced, relative to the asymmetric case, by ~32% for the symmetric three-CA ejection in the “2004-Core” and by ~10% in the “2007-Core”. As mentioned, the reduced peak can be explained by the lower inserted reactivity (by ~8%), resulting from the lower anti-shadowing effects of the CAs (see Appendix D for instance).

The temperatures reached by the materials (fuel, cladding and coolant) are higher for the asymmetric case, as to be expected from the higher integral core power and the larger spatial effects. Compared to the reference asymmetric ejection, the stabilized average-coolant and peak cladding temperatures are lower by 24 K and 113 K, respectively, for the “2004-Core”. Additionally, the assumed peak cladding temperature limit of 1723 K is reached for the asymmetric case, while this is not reached for the symmetric case.

Close observation of the evolution of the temperature differences between the two transient cases for the “2007-core” (see Figure 5.46) indicates that 1) the symmetric reactivity insertion leads to peak cladding temperatures that, on average, are lower by ~30 K (red curve) than in the asymmetric case, and 2) that the maximal peak cladding temperatures are as much as ~100 K lower at t=30 s. This relatively large temperature difference can be explained by the magnitude of the spatial effects, which are significantly reduced for the symmetric reactivity insertion.

The above results underline the possibility to limit the spatial effects by operating the CAs in a symmetric manner. For instance, the CA mechanism drive can be connected to specific logic systems in order not to allow the operation of two or more consecutive CAs of the same CA bank. The asymmetric CA withdrawal at operating speed can, with this solution, be avoided “by design”. Nevertheless, asymmetric CA ejections resulting from the failure of a CA mechanism drive would remain possible.

Neutral line

Close observation of the power map deformations, e.g. Figure 5.43, reveals the existence of a “neutral line”, i.e. a narrow region of the core in which the relative power deformation is near-to-zero (thick “line” seen in dark blue). At the corresponding locations, the steady-state power map is kept constant, which means that the power is only amplified while preserving the original power shape, i.e. there are no spatial effects.

For both GFR core designs, a correlation has been observed between the position of the “neutral line” and the minimal contribution of the first harmonic of the neutronics eigenvalues. It was shown previously that, for the reference core, the first harmonic goes to zero at approximately 1.06 m from the center (see Section 4.4.4), which in turn means that a local perturbation at this location has low impact compared to any other location.

5.6 Sensitivity analysis

In the preceding sections, spatial effects (and the corresponding checks on temperature limits, etc.) have been studied and described for a wide range of hypothetical CA-driven transients in the two different GFR core designs. Additional investigations are presented in this section, in order to provide an assessment of the sensitivity of the reported results for the 3D core behavior to various assumptions and design parameters. In particular, the sensitivity of the core power, the thermal-hydraulics results and the importance of the spatial effects has been examined with respect to the impact of:

1. Employing a revised CA-implementation scheme, viz. “Variant II” (see Subsection 5.6.1),
2. Using a simplified TH model, viz. “14-TH” (see Subsection 5.6.2),
3. Assuming non-fresh fuel conditions (consideration of BOEC conditions) (see Subsection 5.6.3),
4. Varying the assumed CA ejection speed (see Subsection 5.6.4),
5. CA “balancing”, i.e. following a CA ejection, other CAs are inserted at operational speed as a compensatory measure (see Subsection 5.6.5),
6. Ejection of a fully inserted CA (see Subsection 5.6.6),
7. Withdrawal of three CSDs of the second CSD bank (see Subsection 5.6.7).

The results of the additional transient simulations are presented mostly in terms of the evolution of the core power and associated TH parameters, in particular the outlet coolant and peak cladding temperatures. The corresponding spatial effects have also been examined systematically.

5.6.1 New CA implementation scheme (“Variant II”) for “2007-Core”

Consecutive to the neutronics analysis carried out for the “2007-Core” design, a second and revised CA implementation scheme was proposed for this GFR core (see Appendix D, Figure D.1) with, in particular, a reduction of the number of CAs from a total of 24 CSDs/DSDs to 19 CSDS/DSDs[10]. In more detailed terms, the new implementation scheme of the “2007-Core”, so-called “Variant II”, contains a total of 15 CSDS compared to 18 CSDs in the reference implementation scheme (“Variant I”).

The transient simulations were performed, for the “2007-Core” design, under conditions identical to those assumed for the “Variant I” CA implementation scheme. It was assumed that the CSDs are withdrawn at constant speed from the critical position, the latter being deduced in a similar manner as before. For the 15 CSDs at the reference position, the reactivity worth was found to be slightly (6%) reduced ($\delta\rho$ = ~1500 pcm, compared to ~1600 pcm for “Variant I”). This difference can be explained by the new implementation scheme and certain changes in core layout (e.g. fuel-SA positions).

---

[10] For more clarity, the reference implementation scheme for the reference core (“2004-Core”) contains a total of 24 CSDs and 9 DSDs. First, a reduction to 24 CSDs/DSDs was proposed (so-called “Variant I”, see Section 4.6.6 and Table D.7 in Appendix D.1). Then, in a second stage, another reduction was studied (“Variant II”), with a total of 19 CSDs/DSDs (see Table D.7).

The new CA implementation scheme (“Variant II”) has required a re-calculation of the neutronics parameters, in particular, the macroscopic cross-sections and the associated derivatives to take into account the reactivity feedbacks. The gagging and mapping schemes for the “2007-Core” were updated accordingly.

The case of the reference CA-withdrawal transient, viz. that of three neighbouring CAs being withdrawn from the first CSD bank at 2 mm/s, was then analyzed. The results, in terms of the evolutions of power, is compared with those obtained earlier for the “Variant I” scheme in Figure 5.47. Figure 5.48 compares the corresponding TH results, viz. peak fuel, peak cladding and average outlet He temperatures.

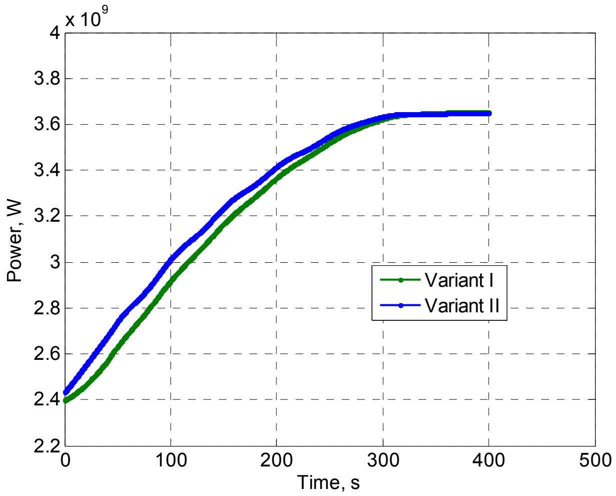

Figure 5.47 Evolution of core power; asymmetric three-CA withdrawal in “2007-Core” with reference (“Variant I”) and optimized (“Variant II”) CA implementation schemes

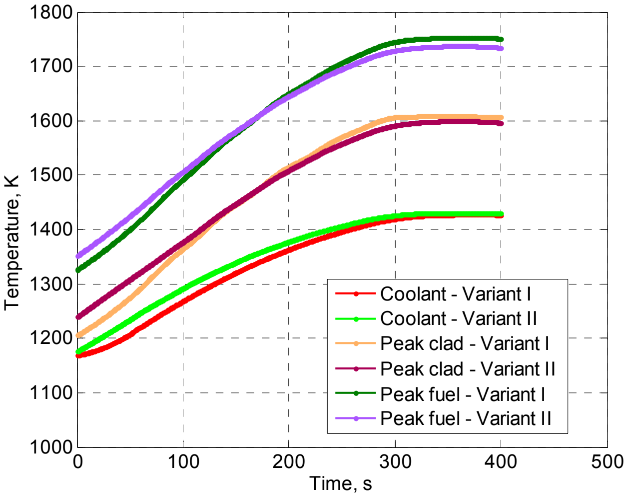

Figure 5.48 Thermal-hydraulics results for withdrawal of three CAs in “2007-Core” with reference (“Variant I”) and optimized (“Variant II”) CA implementation schemes

As shown, the power and TH results obtained with the optimized CA implementation scheme are very close to those obtained with the reference “Variant I” scheme. For instance, the power stabilizes at the same power (~3.7 GWth) as a consequence of the quasi-identical reactivity insertion. The small reactivity difference of 6%, observed between the two implementation schemes for the critical position, has relatively little impact with respect to the analyzed transient. As regard to the temperatures, the largest difference between the two schemes is obtained for the fuel temperature, the value being 16 K lower in the case of “Variant II”, which is of little importance.

The core response was also examined for other transients, e.g. the withdrawal of a single CA at operating speed, and similar results, compared to the reference scheme, were obtained. In conclusion, the “2007-Core” design with the reduced CA implementation scheme – Variant II – shows no major difference with respect to the reference implementation scheme.

5.6.2 Simplified TH model (“14-TH” model)

In order to reduce computational time and for the sake of simplicity, transient analysis is often performed based upon simplified core thermal-hydraulics models. In this case, the core is represented by a limited number of thermal-hydraulic channels representing different power levels as function of the radial power distribution [165; 166].

From the power map deformations presented earlier, it has been seen that the power perturbations are localized close to the position of the withdrawn or ejected CAs. From Figure 5.41 and Figure 5.42, for example, one sees that the spatial effects induce large local deformations in the TH maps, i.e. following the power increase, the outlet coolant and peak cladding temperatures are much higher close to the ejected-CA positions.

In order to assess the importance of the detailed (1:1) thermal-hydraulics model for capturing such effects, a simplified model was developed as well. In the latter case, the GFR core is represented by 14 parallel TH channels, each fuel assembly ring being represented by a single channel, with one additional channel for separate representation of the hot channel. The same basic methodology was applied in implementing the model as earlier. The cross-sections and derivatives were processed using the cell code ECCO and then transferred to PARCS. The mapping and gagging schemes were also updated accordingly and, once again, the results were validated against static reference ERANOS-2.0/VARIANT calculations [153].

With the simplified model (“14-TH”), there is no azimuthal dependence in the temperature fields calculated. The transient simulated for assessing the impact of this simplification is the three-CA ejection (within 1 s) with strong azimuthal asymmetry, the results compared with those of the detailed (1:1) model being for core power, as also for outlet coolant and peak cladding temperatures.

Figure 5.49 shows the relative difference in the core power at t=5.6 s, as calculated with the two models; the magnitude of the difference is ~1%. There is an overprediction (with the simplified model), mainly located in approximately a 1/6 sector of the core close to the ejected-CA position. On the other hand, the power is underpredicted (also by ~1%) in the opposite core region. The explanation lies in the reactivity feedback difference. In the core region on the left (referring to the figure), the fuel Doppler effect is larger than that observed with the detailed model.

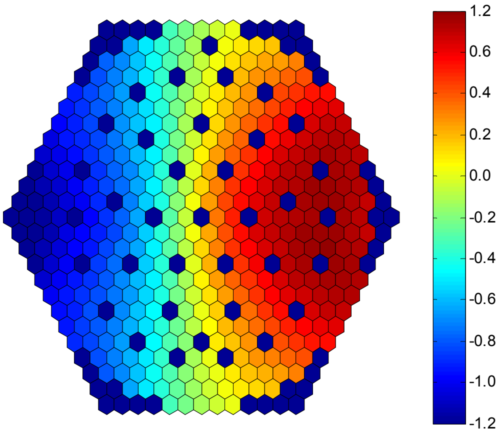

Figure 5.49 Relative differences (in %), at t=5.6 s, between the power deformation maps for the asymmetric ejection of 3 CAs, as calculated by the "14-TH" and full (1:1) models; differences expressed as ("14-TH" - full) / full

The deformations of the helium outlet temperature maps, as calculated for t=5.6 s with the two models, are presented in Figure 5.50, together with the channel-dependent, relative differences in the results. As anticipated, the coolant temperatures calculated by the "14-TH" model are symmetric in the azimuthal direction, while this is not the case with the detailed model. It is seen that the coolant temperature of the whole inner core region is increased by ~40%, as per the calculation with the 14-TH-channels model. With the full model, the coolant temperature increase is more localized (i.e. is higher close to the ejected CAs, with local values of up to 46%). The temperature differences between the model predictions are clearly visible in Figure 5.50c, amounting to ~7%, or approximately 60 K, in magnitude at this particular stage of the transient. The asymptotic temperature differences are even higher, viz. ~100 K.

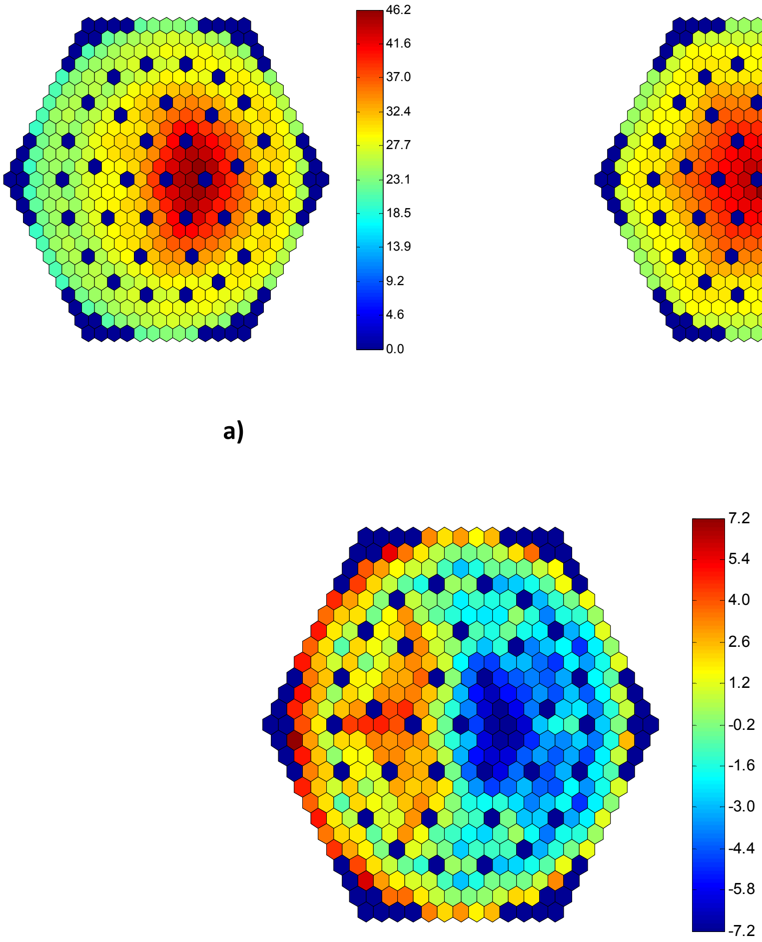

a)

b)

c)

Figure 5.50 Deformation (expressed in %), at t=5.6 s, of the helium outlet-temperature map (expressed in %) for the asymmetric ejection of 3 CAs; a) results obtained with the full (1:1) core model, b) results with the "14-TH" model, and c) relative differences, expressed as ("14-TH" - full) / full

5.6.3 Transients with BOEC fuel composition

The core response to a given transient, characterized by a given reactivity insertion, strongly depends on the kinetics parameters and reactivity feedbacks such as the Doppler effect. These parameters depend directly on the fuel composition and neutron spectrum, i.e. are strongly influenced by the plutonium isotopics and the amounts of minor actinides and fission products within the fuel. It is clearly important, in this context, to examine the GFR dynamic behavior for a representative situation with burnt fuel present in the core.

As a Generation IV system, the GFR is envisaged to operate in a fully closed fuel-cycle mode, which leads to an equilibrium fuel composition with asymptotic quantities of fission products and minor actinides within the core. Currently, the GFR is assumed to be operating under constant, HFP conditions with a three-batch reloading scheme, i.e. is periodically reloaded with fresh fuel and natural uranium as feed [167]. Thus, once equilibrium is reached, the composition of each of the three batches remains the same from cycle to cycle. Transient analysis for CA withdrawals and ejections, from the GFR core, have accordingly been performed and analyzed for a fuel composition corresponding to BOEC conditions.

It is important to stress that, for the BOEC conditions as well, the CAs are considered to be inserted at the reference position at the start. Thus, an identical methodology can be applied for the CA-driven transients, viz. the simulation of CA withdrawals or ejections from a reference position. As before, different CA transients have been simulated in terms of the speed and the number of CAs involved, and the major results are presented.

The exact context and motivation for the present investigations, together with the computations performed to determine the BOEC fuel composition, are described in Appendix E. For this reason, no particular details are provided here neither in the context of the fuel cycle analysis, nor as regard the development and validation of the coupled PARCS/TRACE model associated with the BOEC conditions.

Since the main purpose is to study the sensitivity of the GFR behavior to the fuel composition, only the reference “2004-Core” design has been analyzed. It is also important to note that the effects encompassed by the study are only those on the neutronics side, since the fuel thermal properties, in particular the thermal conductivity λ and specific heat c_p, have been assumed to be the same as for fresh fuel. This choice is partly justified by the lack of available burnup-dependent thermal data for mixed carbide fuel in the open literature. Consequently, the behavior differences observed (see below) are solely due to the differences in kinetics and other safety-related parameters. The complete comparison of these parameters is presented in Appendix E. In brief, the values at BOEC are reduced in magnitude, relative to the fresh fuel composition, viz. by approximately 13% for the delayed neutron fraction and 23% for the fuel Doppler reactivity effect (see Table E.1). The reduction of these parameters leads to less favorable dynamic responses, which in turn lead to higher power and temperature values for a given reactivity insertion caused by CA withdrawal or ejection.

Finally, it is important to note that the transients presented in this subsection consider identical reactivity ejections as in the corresponding fresh-fuel cases, rather than reduced values corresponding to the “more withdrawn” critical positions of the CAs for a core containing burnt fuel. This has been done in order to bring out the effects of the reduced safety parameters more clearly.

The transients for BOEC conditions were simulated in exactly the same manner, and the results – core power evolution, TH results and power map deformation – are presented, for comparison purposes, together with those for the fresh fuel. Four main sets of simulations have been performed for the BOEC core, viz.

(1) Asymmetric withdrawal of a single CSD of the first CSD bank at operational speed (2 mm/s),
(2) Asymmetric withdrawal of three CSDs of the first CSD bank at operational speed (2 mm/s),

(3) Asymmetric ejection of a single CSD of the first CSD bank at ejection speed of 40 cm/s,
(4) Asymmetric ejection of three CSDs of the first CSD bank at ejection speed of 40 cm/s.

Results are presented explicitly for the two bounding cases, i.e. the most moderate and the most severe of the transients. These are, respectively, the asymmetric withdrawal of a single CSD and the asymmetric ejection of three CSDs. Findings from the other two cases are included in the discussion.

Asymmetric withdrawal of a single CSD of the first CSD bank at operating speed 2 mm/s

During this transient, a CA of the first CSD bank is withdrawn during 200 s at a constant speed and then kept at the fully withdrawn position. The power peak is ~3.2 GWth, a value slightly higher (+7%) than the power reached for the reference core (see Figure 5.51). The TH results are shown in Figure 5.52, a consistent trend being observed with higher values for:

(1) Average outlet coolant temperature (+18 K, relative to the fresh-fuel core),
(2) Peak cladding temperature (+52 K, relative to the fresh-fuel core),
(3) Peak fuel temperature (+123 K, relative to the fresh-fuel core).

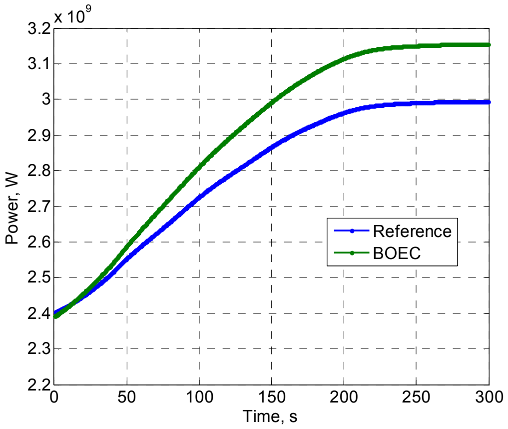

Figure 5.51 Core power evolution for a single CA withdrawal at 2 mm/s. Comparison between the reference calculation (fresh fuel) and BOEC conditions; "2004-Core" design

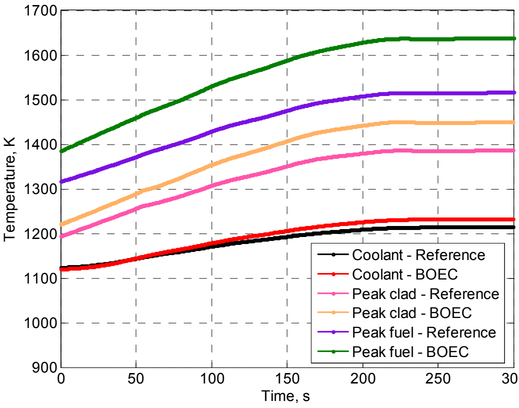

Figure 5.52 Thermal-hydraulics results for a single CA withdrawal at 2 mm/s. Comparison between the reference calculation (fresh fuel) and BOEC conditions

Even if the temperatures during this transient are higher in comparison with the reference (fresh fuel) values for the "2004-Core", the results obtained show no evidence of major safety related problems since none of the assumed temperature limits (coolant, cladding and fuel) is reached.

Asymmetric ejection of three CSDs of the first CSD bank at 40 cm/s

This case considers, as previously assumed for fresh fuel composition, the ejection of three CSDs of the first CSD bank from the reference position, which corresponds approximately to a reactivity insertion of 1 $.

The power evolutions, for the asymmetric three-CAs ejection, are compared between the reference (fresh fuel) and BOEC cases in Figure 5.53, and the thermal-hydraulics results are shown together for both fuel compositions in Figure 5.54. Additionally, the power map deformation at t=1 s for the BOEC core is represented in Figure 5.55.

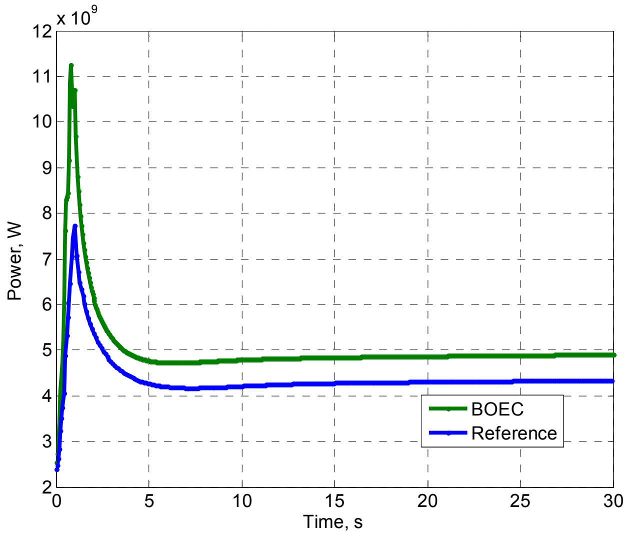

Figure 5.53 Power evolution for asymmetric ejection of three CSDs of the first CSD bank within 1 s. Comparison between the reference calculation (fresh fuel) and BOEC conditions; “2004-Core” design

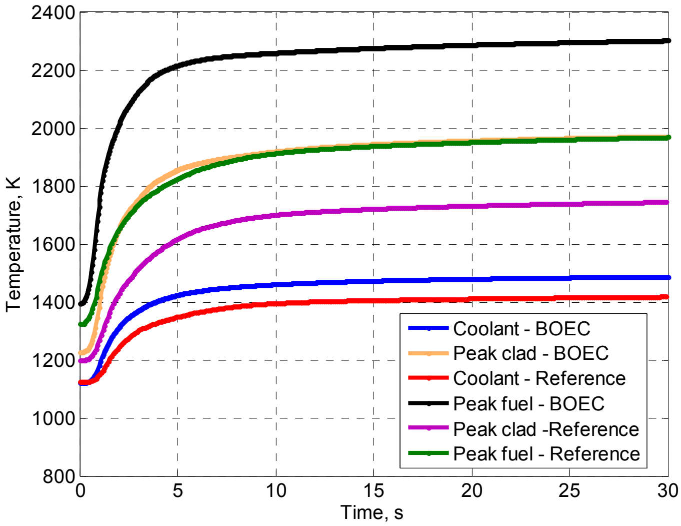

Figure 5.54 Thermal-hydraulics results for asymmetric ejection of three CSDs of the first CSD bank within 1 s. Comparison between the reference calculation (fresh fuel) and BOEC conditions; “2004-Core” design

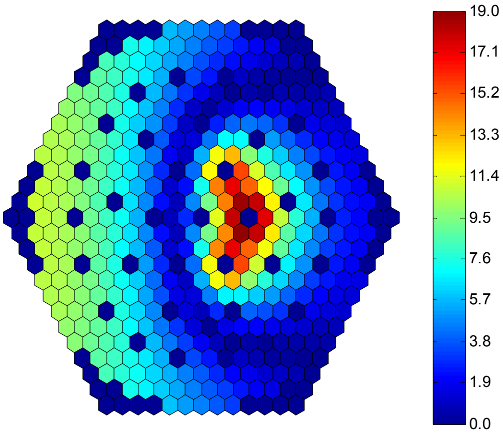

Figure 5.55 Power map deformation (expressed in %) at t=1 s, relative to steady state, for asymmetric ejection of three CSDs of the first CSD bank within 1 s; "2004-Core" design, BOEC conditions

In association with BOEC conditions, the core power peak is ~11 GWth, a significant increase (by 41%) compared to the reference fuel conditions. This high value can be explained by the reduced values of the delayed neutron fraction and fuel Doppler effect. The TH results obtained show that, once again, the first limiting factor is the cladding temperature. The assumed limit of 1723 K is reached after approximately t=15 s for the reference core, while it takes only ~2.8 s under BOEC conditions.

No specific limitation is caused by the outlet coolant temperature. However, the fuel temperature limit of 2273 K is just attained after t= 15 s, while it is not attained at all for the reference core (peak fuel temperature of ~1968 K). The analysis of the spatial effects for the BOEC core (at t= 1 s) does not reveal any particular behavior difference. The main effects are located close to the ejected CAs, and the maximum local power deformation (19%) is very similar to that for the reference core.

5.6.4 CA Speed for CA ejection transients

The sensitivity to the ejection speed was assessed for the asymmetric three-CAs ejection transient. Different cases for ejection speeds varying from 4 cm/s to 40 cm/s have been examined for the "2004-Core" design, and the two extreme speeds are compared here, viz.

(1) Asymmetric ejection of three CSD at 4 cm/s,
(2) Asymmetric ejection of three CSD at 40 cm/s (already presented in Subsection 5.5.2).

The power evolutions for the two cases are compared in Figure 5.56. It is seen that the power peak is much larger for 40 cm/s, but the asymptotic power values are nearly identical (~4.3 GWth).

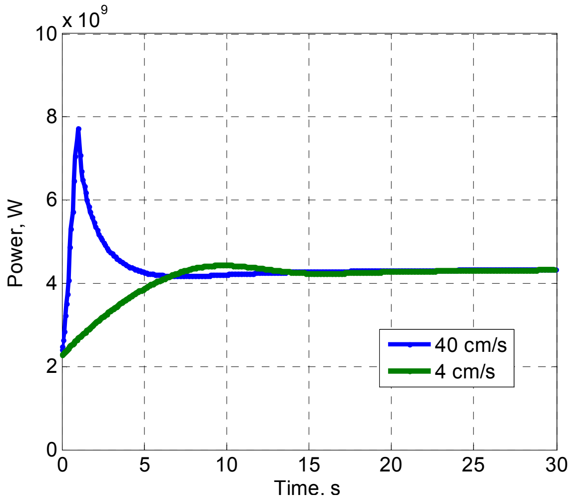

Figure 5.56 Power evolutions for asymmetric ejection of three CAs, with speeds of (1) 4 cm/s and (2) 40 cm/s; "2004-Core"

Figure 5.57 shows the comparison of the peak cladding and average outlet coolant temperatures for the two ejection speeds. While the temperature increase rate is higher for the case with higher speed, the asymptotic values are again almost identical, a consequence of the identical reactivity insertion.

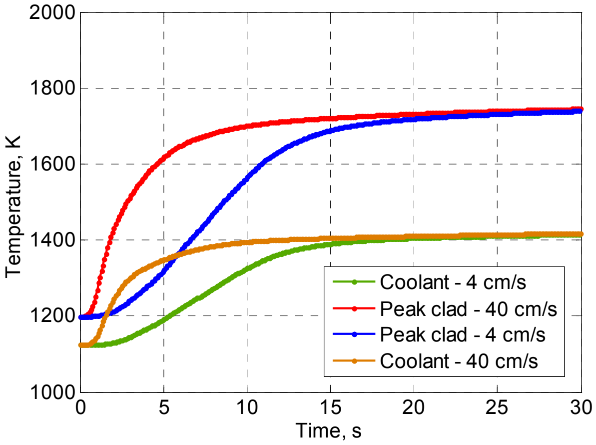

Figure 5.57 Peak cladding and average outlet coolant temperatures for asymmetric ejection of three CAs, with speeds of 1) 4 cm/s and 2) 40 cm/s; "2004-Core"

Similar analysis was performed for the "2007-Core", and the change in core behavior for a variation of the CA speed was found to be similar. A reduction of the ejection speed yields near-to identical, asymptotic values for the maximum temperatures, but the time to reach these is longer, which is particularly favourable for safety. Thus, the obtained results show that one should limit the operational speed for the developed CAs.

5.6.5 "Balancing" of reactivity

In the hypothetical case of a high-speed withdrawal of a certain number of CAs, it is in principle possible to counterbalance the effects of the transients by an insertion of other available CAs located in the second CSD bank.

To illustrate this situation, a transient case ("balancing" transient) was simulated with, as initiating event, the ejection from the critical position of three consecutive CAs of the first CSD bank. The ejected CAs are kept at the upper parking position and, after a reaction time of 1 s, three CAs of the second CSD bank (with a 120° symmetry) are inserted at higher nominal operating speed (assumed in this case to be 1.5 cm/s) during 60 s to reach an inserted position of +25 cm relative to the bottom of the fuel. The power evolution is shown in Figure 5.58, and the TH results are given in Figure 5.59.

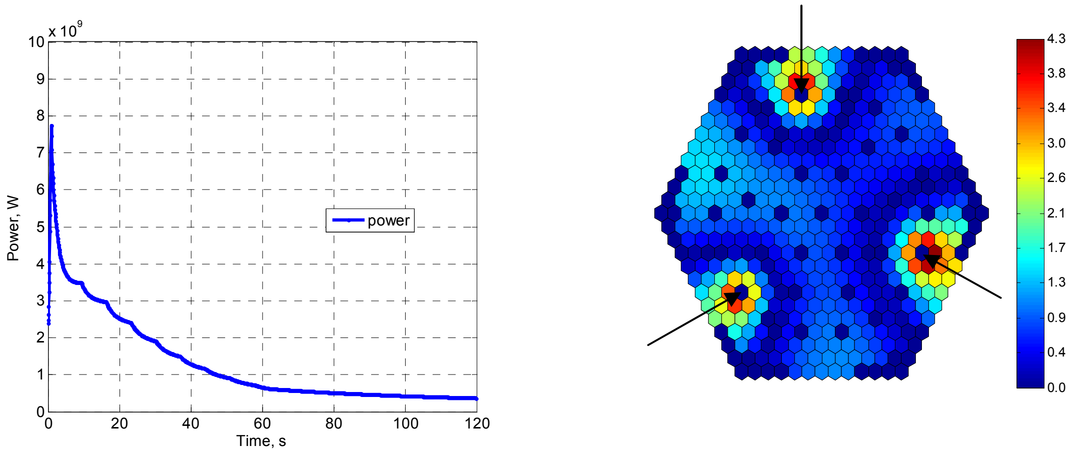

a) **b)**

Figure 5.58 a) Power evolution for "balancing" transient in "2004-Core": three CAs of the first CSD bank are ejected within 1 s and later, at t=2 s, three CAs of the second CSD bank (shown by arrows) are inserted slowly during 60 s, the DSDs being kept at their parking position; b) power map deformation between t=1 s (power peak) and t=7 s to illustrate the effects of the CA insertion

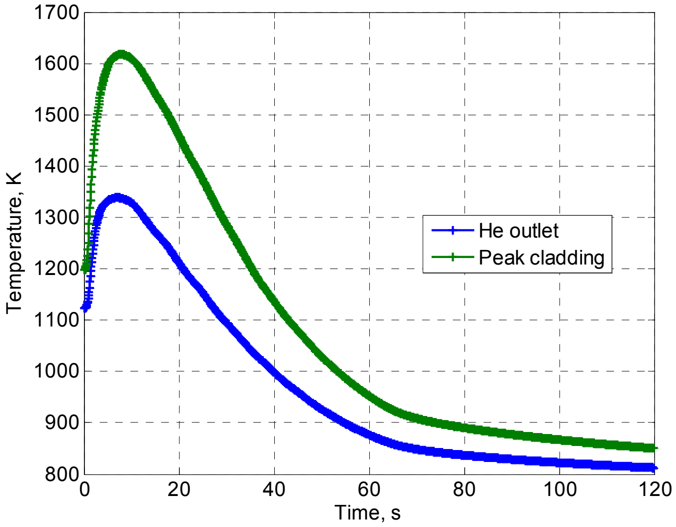

Figure 5.59 Thermal-hydraulics results for "balancing" transient in "2004-Core": three CAs of the first CSD bank are ejected within 1 s and later, at t=2 s, three CAs of the second CSD bank are inserted slowly during 60 s, the DSDs being kept at their parking position

The above results indicate that it is possible to compensate for the quick withdrawal of three CAs (approximately 1 $) by a slow insertion of three symmetric CAs of the second CSD bank. Thus, the simulation shows that, during this transient, none of the specified temperature limits (in particular, that for the peak cladding temperature) is reached. Clearly, there is an important practical requirement in this case; viz. the initiating event has to be detected rapidly via, for instance, an accurate monitoring of the core power.

5.6.6 Ejection of a fully inserted CA of the 1st CSD bank

This transient case corresponds to a situation in which a single CA is inadvertently withdrawn from a fully inserted position and the reactor not scrammed. Prior to the initiating event, all the CSDs, except for the one CA of the first CSD bank which is fully inserted, are assumed to be at the reference positions under HFP conditions. At t=0, the CA in question is fully withdrawn at operating speed. The core power evolutions for the two GFR core designs are shown in Figure 5.60. The TH results are presented in Figure 5.61.

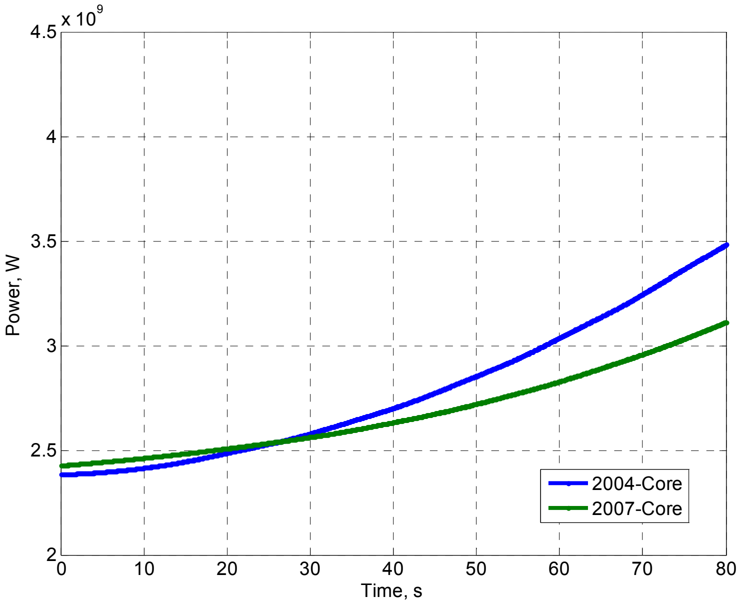

Figure 5.60 Power evolution for withdrawal of a fully inserted CA; "2004-Core" and "2007-Core"

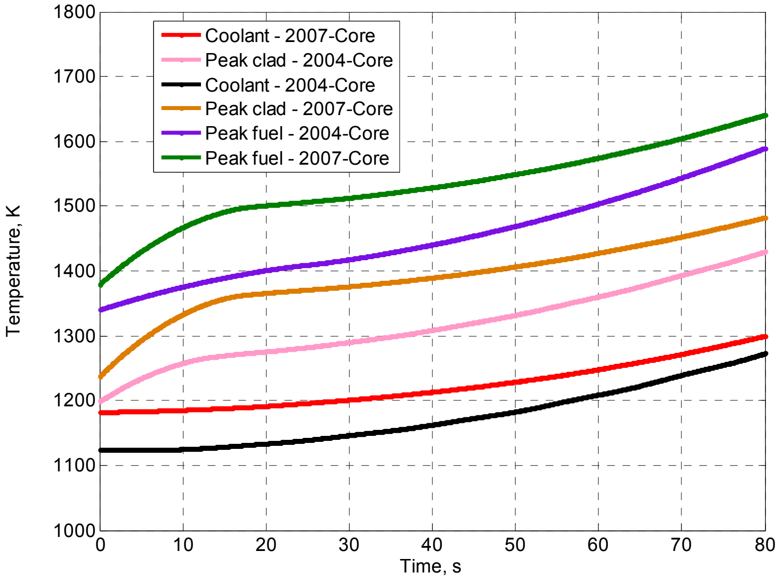

Figure 5.61 Thermal-hydraulics results for withdrawal of a fully inserted CA; "2004-Core" and "2007-Core"

Comparison of the temperature developments shows that the "2007-Core" is quicker in its response to the withdrawal of the CA, as compared to the reference "2004-Core". This reversed trend can be easily explained by the significantly higher CA worth for the new core design, the total reactivity insertion being ~1.7 $ in this case, compared to ~1.1 $ for the reference core. The difference is caused simply by the significant increase in the core height (2.35 m instead of 1.55 m).

It is worthwhile to note that, before the start of the transient considered here, relatively "cold" channels are present in the surroundings of the fully inserted CA, since the fission power is suppressed in its vicinity (see Figure 5.62). As a consequence, the nominal outlet temperature of 1123 K is not attained in these specific channels.

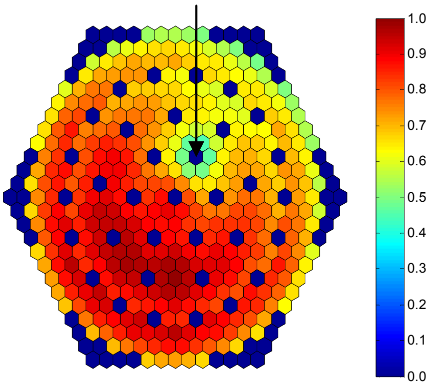

Figure 5.62 Normalized power map at steady-state conditions; "2004 with one CA fully inserted of the first CSD bank

In principle, it is possible to avoid the slightly more unfavourable behavior of the "2007-Core" during this transient by reducing the CA absorber length to a certain fraction of the core height (so as to have approximately the same reactivity worth for the fully inserted CA as for the reference core). This solution has in fact been adopted in the revised CA implementation scheme presented in Appendix D ("Variant II").

5.6.7 Withdrawal of three CSDs of the 2nd CSD bank

The reference transient considered in the present research is the asymmetric ejection of three consecutive CAs of the first CSD bank. The reactivity worth per CA is significantly higher in the first CSD bank (in the range of 360 pcm, compared to 310 pcm for the second bank), justifying this choice. However, since it has been seen on several occasions that spatial effects can lead to unexpectedly high local perturbations of the power distribution within the core, the sensitivity of the power map deformation and the TH results was also studied for different ejection and withdrawal cases for CAs of the second CSD bank.

As illustration the core response to the withdrawal (at a constant speed of 2 mm/s) of three consecutive CAs of the second CSD bank is presented here. This hypothetical incident corresponds approximately to a reactivity insertion of 0.76 $ ("2004-Core") and 0.57 $ ("2007-Core"). The power evolutions are shown in Figure 5.63, along with the TH results in Figure 5.64. For ease of comparison, each of the figures also gives the results reported in Section 5.4.3 for the withdrawal of three CAs from the first CSD bank.

As expected, the core power is lower in the case of the CAs being withdrawn from the second CSD bank, the reduction being in the range of 12% for the "2004-Core" and 7% for the

"2007-Core". Accordingly, lower outlet coolant and peak cladding temperatures are reached. The largest differences between the two different transient types is obtained for the peak cladding temperature, the value being 130 K and 81 K lower for the "2004-Core" and "2007-Core", respectively. Lower values are also obtained for the average outlet coolant temperature.

Thus, the results obtained show no evidence of safety-related problems related to CAs of the second CSD bank, which are not adequately covered by analogous considerations for the CAs of the first CSD bank.

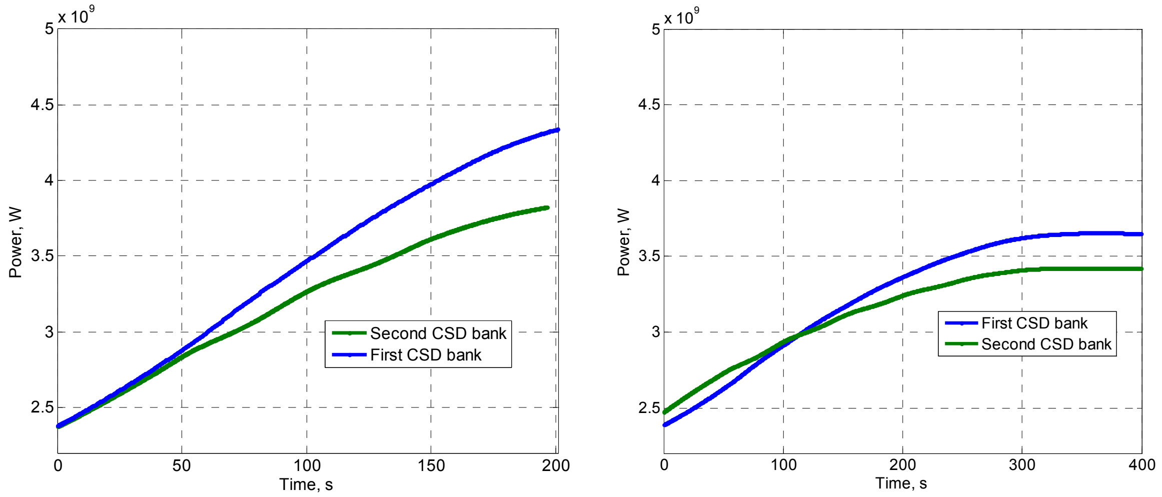

a) b)

Figure 5.63 Comparison of the power evolution for asymmetric withdrawal of three CAs (at 2 mm/s) of the first and second CSD banks; a) "2004-Core" and b) "2007-Core"

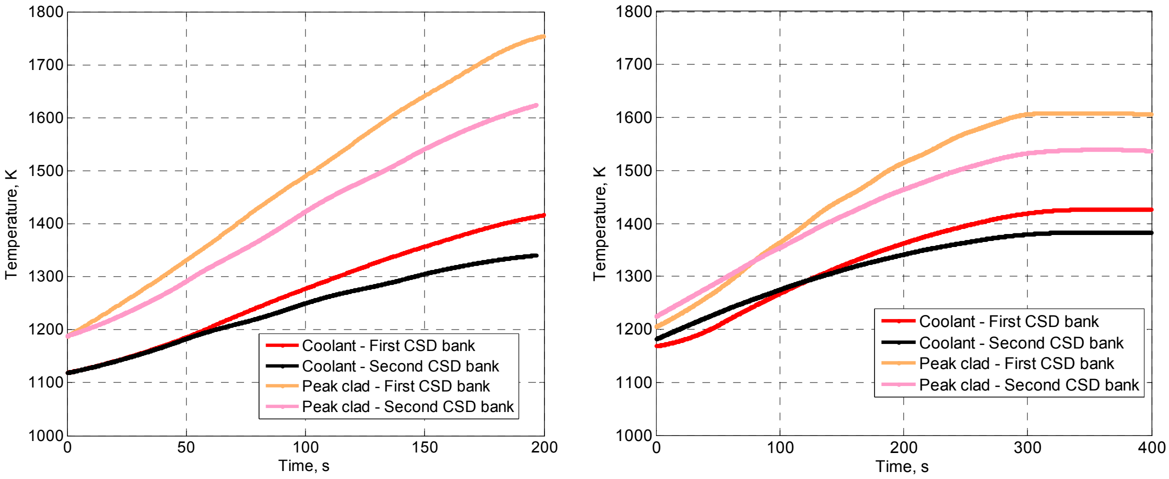

a) b)

Figure 5.64 Comparison of thermal-hydraulics results for asymmetric withdrawal of three CAs (at 2 mm/s) of the first and second CSD banks; a) "2004-Core" and b) "2007-Core"

5.7 Summary and recommendations

This chapter has been devoted to the application of the newly developed, coupled GFR full-core, 3D NK and 1D TH models to the analysis of a wide range of control assembly driven transients, i.e. CA withdrawals at operating or ejection speed. Mainly, two different GFR core designs have been considered for the analysis: (1) the reference "2004-Core", and (2) the revised "2007-Core", which differs mainly in the height-to-diameter ratio (see Appendix D).

The development of the full-core coupled (1:1) models was carried out in successive steps, starting from the preparation of self-shielded macroscopic cross-sections and derivatives for taking reactivity feedbacks into account[11]. This was done using the ECCO cell code of ERANOS-2.0 (see Section 5.2). First, the standalone neutron kinetics and thermal-hydraulics models were coupled using appropriate mapping and gagging schemes[12]. Reference static ERANOS-2.0/VARIANT calculations were then performed to validate the developed models, especially the PARCS stand-alone models. For this purpose, the CA worths and reactivity feedbacks were recalculated and good agreement was obtained, the discrepancies being in the range of 5% for the "2004-Core" and 8% for the "2007-Core".

The range of CA driven transients studied has been quite large, since the main purpose has been to obtain a detailed understanding of the 3D behavior of the GFR core (see Section 5.3). In addition, various sensitivity studies, mainly of the spatial effects to different core parameters, have been carried out. In more detailed terms, the transient analysis has considered the sensitivity of the key safety criteria to: 1) the number of CAs being withdrawn/ejected, 2) the position of the CA being withdrawn/ejected, 3) the CA implementation scheme, 4) the number of TH channels assumed in the TRACE model, 5) the fuel composition corresponding to that at beginning of equilibrium cycle (BOEC), rather than to fresh fuel, 6) the CA speed, and 7) the assumed core power level (HZP instead of HFP).

Comparisons between the two GFR cores were performed in a systematic manner, in order to understand the correlations existing between power map deformations and CA interactions (shadowing/anti-shadowing effects). These interactions were described in detail in Chapter 4.

For the current analysis, four basic sets of CA-driven transients were studied:

(1) "2004-Core" CA withdrawal cases,
(2) "2007-Core" CA withdrawal cases,
(3) "2004-Core" CA ejection cases,
(4) "2007-Core" CA ejection cases.

Thereby, the aims were multiple, viz.:

---

[11] fuel Doppler, core axial and radial thermal expansions, and coolant density

[12] The mapping allows the data exchange between the codes during the transient, while the gagging scheme was applied to match the flow to the power distribution.

(1) CA withdrawal at nominal speed (2 mm/s) allows one to verify the adequacy of the specifically developed, CA pattern for the GFR cores from the viewpoint of operational transients.
(2) Potential safety-related problems associated to CA movements (at operating or at high speeds) can be clearly identified for these innovative fast reactor cores.
(3) 3D spatial effects occurring in large cores, which are related to asymmetric reactivity insertion, can be characterized. Importance of these effects was first demonstrated via static neutronic analysis (see Chapter 4).
(4) Differences in dynamic core behavior between the two considered core designs can be analyzed.
(5) Recommendations can be made with respect to operational procedures, as imposed by the proposed CA design (speed of movement, number of assemblies simultaneously in movement, etc.).

The results obtained for CA withdrawal cases at operating speed (see Section 5.4) have clearly demonstrated that:

(1) The withdrawal of a single CA does not impact the core safety in terms of average outlet coolant, peak cladding and peak fuel temperatures.
(2) Lower values are obtained as thermal-hydraulic results (coolant, peak fuel and cladding temperatures) for the “2007-Core” design, compared to the “2004-Core” design.
(3) The rates of temperature increase are reduced for the “2007-Core” compared to the “2004-Core” design, as a consequence of lower power peaking factors.
(4) The withdrawal of CAs at HZP conditions, compared to HFP, results in a more rapid increase of all the temperatures due to the larger reactivity insertion and lower fuel temperatures (leading to lower fuel Doppler feedback). These transients have to be compensated by a scram during the first 2 minutes, in the case of a hypothetical withdrawal of all the CSDs.
(5) Spatial effects are reduced in the new “2007-Core”, which is clearly favorable for core safety.

The results obtained for ejection cases (see Section 5.5) have shown that:

(1) Asymmetric reactivity insertion induces large spatial effects (deformations of the nominal power shape up to +21%), the amplitude of these effects being correlated to the inserted reactivity.
(2) The spatial effects are significantly reduced in the “2007-Core”, which confirms the findings from the CA withdrawal cases and clearly shows the better behavior of the new GFR core design.
(3) A symmetric reactivity insertion leads to lower spatial effects, relative to the asymmetric case. This indicates that CAs need to be operated in a symmetric way.
(4) The analysis has also revealed the existence of large axial power deformations consecutive to CA ejections.

(5) The spatial effects are time-dependent, with different dynamics for the evolution of the different temperatures (due the inertia of the heat transfer from the fuel to the coolant).

Complementary to the above findings, and based on specific sensitivity analysis carried out (see Section 5.6), the following additional observations have been made:

(1) The revised CA implementation scheme ("Variant II"), corresponding to an optimized implementation (reduced number of CAs, relative to the reference "Variant I") leads to a core behavior quite similar to that with "Variant I", for identical values of the inserted reactivity. This indicates that no major safety-related problems, consecutive to the reduction of the number of CAs in "Variant II", are to be expected.

(2) The comparison of the TH results obtained with the simplified model ("14-TH" ring-wise model) has clearly brought out the importance of a detailed 1:1 assembly-wise modeling of the core for accurately simulating temperature distributions resulting from asymmetric power distributions. The simplified model has been found, for example, to underpredict the coolant temperatures by 80 – 100 K in the subassemblies close to the ejected CAs.

(3) The withdrawal or ejection of a single CA from a core with fuel corresponding to BOEC conditions, compared to the reference case of fresh fuel, has been shown to result in higher power peaking factors, and hence higher values for peak fuel, cladding and outlet coolant temperatures. This is largely due to the deterioration, with fuel burnup, of safety related parameters (delayed neutron fraction β_{eff}, fuel Doppler effect, average neutron generation time Λ). The higher temperatures, however, have still been found to remain within the allowable range, and no particular safety-related problem has been highlighted.

(4) For a higher CA withdrawal speed, the rate of temperature increase is increased due to larger power peaking factors, but the asymptotic TH results are identical. This indicates that the operational speed, for the developed CA design, has to be limited in order to provide sufficient time for taking necessary actions.

(5) Lower values were obtained as TH results for the ejection of CAs of the second CSD bank (compared to the reference cases for the first CSD bank), so that no specific safety problems have been indicated in this context. This is a consequence of the lower reactivity worth of CAs in the second bank.

Chapter 6

6 Summary and conclusions

The present research has focused on the development of the control assembly (CA) pattern, as also on carrying out the related 3D core behavior analysis, of the Generation IV Gas-cooled Fast Reactor (GFR), thus contributing to the design development and safety analysis of this advanced system.

The principal GFR core design considered in the present research is the reference design ("2004-Core"), with a thermal power of 2400 MW and a core fuelled with CERCER fuel plates. This design was, at the beginning of this research, preferred to other concepts, because it represented the most recent stage of international GFR development work at the time. It still needs to be stressed that the system design is not finalized yet and remains a subject for interdisciplinary R&D. In particular, the current investigations contributed to reconsidering the neutronics design of the core and have led to an alternative variant, viz. the new "2007-Core" design.

The present research has consisted of mainly three complementary phases, viz. (1) the neutronics tools validation, (2) the GFR CA pattern development and related static analysis, and (3) dynamic core behavior studies for hypothetical CA driven transients, i.e. CA withdrawals and ejections.

In the first phase, the CEA computer code ERANOS-2.0 and its associated neutron library ERALIB1, mainly validated earlier for sodium-cooled fast reactors, were verified against PSI experimental data for a gas-cooled fast reactor lattice. For this purpose, a detailed review of the available data was conducted and the neutronics parameters of interest, mostly reaction rate ratios, were calculated and compared to experimental values. One was thus able to demonstrate the applicability of the used neutronics tools to GFR analysis.

In the second phase, the CA pattern was developed for the GFR, followed by the study of an appropriate implementation scheme. Thereby, the interactions occurring between the absorber pins and between the CAs were investigated in detail, with the goal of optimising the control system efficiency.

During the third phase, dynamic studies were carried out for the different GFR core variants, in the context of the developed CA pattern. The practical applicability of the proposed control system could thus be established from a safety viewpoint. Thus, for example, different CA speeds and implementation schemes were investigated, allowing one to characterize the core dynamic response fully. The analysis has also contributed, in a generic sense, to the understanding of the CA related, physical phenomena which occur in such large fast-spectrum cores.

The following sections summarise the work performed, the main achievements and the recommendations for further work.

6.1 Summary

The first chapter of the thesis introduces the reader to the present doctoral research by describing the current status of nuclear energy development and the growing interest in Generation IV systems. The emphasis, in the latter context, is put on GFRs and the corresponding international R&D.

Chapter 2 provides the general background for the research and describes, in the beginning of the chapter, the past GCFR-PROTEUS experimental program. The CEA program ENIGMA and the planned GFR prototype ETDR are also described, thus serving as a link between past and future developments. Additionally, the main features of the large Generation IV GFR are provided, along with a discussion of the choices made for the current reference design. A large fraction of the chapter is dedicated to the presentation of the state-of-the-art codes currently used for fast reactor analysis. PSI’s FAST code system is presented in this context.

Chapter 3 presents the detailed re-analysis of the GCFR-PROTEUS reference test lattice. The results obtained with reference computational schemes, both using the deterministic code ERANOS and the Monte Carlo code MCNPX in association with different modern nuclear data libraries, are presented and compared with the measured reaction rate ratios. Also included in the chapter is a sensitivity analysis for assessing the impact of the ERALIB1 nuclear data library adjustments on the reference GCFR lattice calculations. Furthermore, an evaluation is made, via representativity analysis, of the transferability of the GCFR-PROTEUS experimental data to advanced GFRs. The re-analysis of the past PSI experiments has indeed provided partial validation of the currently used neutronics tools. However, it has also shown the need for performing new experimental investigations aimed at addressing the novel neutronics features of the Generation IV GFR (softer neutron spectrum, presence of minor actinides, etc.).

Chapter 4 presents, based on neutronics and thermal-hydraulics calculations, the development of the GFR CA pattern, as also the related detailed investigation of CA interaction effects. The development work has led to the establishment of an optimized CA implementation scheme, which takes appropriate account of the GFR operational needs and also provides the needed safety margins. The supplementary neutronics analysis of the interactions occurring within and between the CAs has provided a valuable in-depth understanding of the corresponding physical phenomena. For accurate characterization of the developed CA design, the reactivity worth has been calculated using a detailed treatment of the complex 3D CA pattern. Thereby, it has been shown that, compared to previous results for commercial fast reactors, a significant reduction of the heterogeneity (mainly self-shielding) effects has been achieved with the developed design, allowing one to reduce the neutronics penalties in terms of reactivity margins.

Chapter 5 is devoted to the 3D dynamic analysis of the large reference GFR, using advanced computational tools in conjunction with detailed, coupled 3D neutron kinetics (NK) and 1D thermal-hydraulics (TH) models (“2004-Core” and “2007-Core”). A wide range of hypothetical

CA driven transients have been analyzed in this context, allowing one to, first, verify the adequacy of the developed CA pattern and, second, to analyze in detail the spatial effects occurring within the GFR core in relation to asymmetric reactivity insertions. The chapter includes the results of a broad-based sensitivity analysis, with various effects having been studied, e.g. those of the CA speed, the position of the withdrawn assemblies, fuel burnup (in terms of beginning-of-equilibrium-cycle (BOEC) fuel composition), etc. This has enabled the formulation of recommendations related to CA movements, in terms of maximal speed and/or number of assemblies which can be simultaneously in movement.

6.2 Main achievements

The main results achieved in the course of the present doctoral research may be described in the frame of the three different complementary phases referred to earlier, viz.

(1) The validation of the computational tools, in particular that of the ERANOS code applied for the neutronics analysis (see Chapter 3),
(2) The development of the CA pattern and related neutronics investigations (see Chapter 4),
(3) The development and application of the 3D coupled neutron kinetics and thermal-hydraulics models of the GFR cores to study their dynamic behavior during hypothetical CA driven events, viz. operational withdrawals and accidental ejections (see Chapter 5).

6.2.1 Benchmarking of the ERANOS-2.0 reference computational scheme

It is in the context of the verification and validation of the computational tools, more specifically the deterministic neutronics code system ERANOS-2.0, that the integral data obtained at PSI during the GCFR-PROTEUS experimental program were used. To start with, the information available in the literature was sorted according to its relevance as regards the Generation IV GFR. The resulting description of the two phases of the experimental program (Appendix B) may, as such, be considered as a useful contribution to knowledge perseveration.

In a second step, the adequacy and performance of ERANOS-2.0, in association with the adjusted ERALIB1 nuclear data library, were evaluated by performing a detailed re-analysis of the reference GCFR-PROTEUS lattice configuration, first with ERANOS itself and then with Monte Carlo (MCNPX) simulations in conjunction with different modern nuclear data libraries. The aim was to re-compute neutron balance components (reaction rate ratios) with modern tools and to compare the results with experimental data, as well as with the originally performed calculations. Despite the simple hexagonal geometry of the test lattice, the comparisons were not a trivial task due to the influence of the outer reactor regions on the central fast zone, implying special care with the use of correction factors.

It has been found that, for the main reaction rate ratios (C8/F9, F8/F9 and F5/F9), the new analysis of the GCFR-PROTEUS reference lattice generally yields good agreement (within 1σ measurement uncertainty) between experimental values and the calculations performed in conjunction with different modern data libraries. Among the tested libraries, the predictions were in somewhat better agreement (especially for F8/F9) in the case of the adjusted ERALIB1 library, confirming the choice of ERANOS-2.0/ERALIB1 as the reference computational scheme. Further evidence was provided by a wide range of sensitivity studies, assessing the effects of changes in lattice geometry, material compositions, energy structure and various numerical options within the ECCO cell code.

To better qualify the data adjustments in ERALIB1, the effects of the individual adjustments on the GCFR-PROTEUS predictions was assessed using extended generalized perturbation theory (EGPT). Additionally, the GCFR-PROTEUS reference lattice was characterized by representativity factors with respect to three advanced gas-cooled fast-spectrum systems (ETDR, GFR and CAPRA-CADRA). This analysis has shown that the representativity is particularly high for systems fuelled with MOX (e.g. ETDR). On the other hand, lower representativity factor values were computed for the large Generation IV GFR. This indicates, as to be expected from the novel features such as the softer neutron spectrum, that new specific experimental investigations are indeed needed. A specific aspect brought out by GCFR-PROTEUS re-analysis is that the quality of minor actinide data remains low, predictions for spectral indices involving ^{237}Np being rather poor.

6.2.2 Development of the control assembly pattern and supplementary neutronics investigations

The development of the CA pattern for the reference GFR core was performed as an iterative process between neutronics and thermal-hydraulics investigations. First of all, 2D and 3D neutronics models of the GFR core were developed using the validated, reference ERANOS-2.0/ERALIB1 computational scheme. The starting point of the CA pattern development was the detailed analysis of the common pattern which had been developed for Superphénix and EFR. This served as a basis for neutronics investigations and optimization, in terms of the maximisation of the absorber fraction (for efficiency) and the minimization of the associated heterogeneity effects (within and between the CAs).

A key parameter considered was the axial distribution of the heat generation within the CA for different position of insertion. Iterative neutronics/thermal-hydraulics calculations were performed, using the ERANOS-2.0 and COPERNIC codes, to optimize the CA design. As principal goal, the cladding temperature had to be assessed since this to be kept below the limiting value dictated by the choice of cladding material (stainless steel of AIM1-type). The coolant mass flow rate and coolant volume fraction were carefully determined to match the corresponding limit of 630°C.

The optimized CA pattern arrived at consists of 54 absorber pins placed in a triangular lattice. Effectively, each absorber pin is a conventional stainless-steel tube filled with highly enriched ^{10}B boron carbide (B_4C) pellets. As a result of the investigations, the absorber pin diameter (20 mm) was chosen such as to minimize the pin-to-pin influence within the assembly.

During the optimization phase, a central part of the CA was designed without any absorber pins (static zone filled with stagnant helium), offering a significant reduction (in the range of 50 to 100°C) of the cladding temperature. Additionally, a reduction of heterogeneity effects was achieved through this feature (absence of absorber, and hence of self-shielding, in the central region of the control assembly).

Shadowing and anti-shadowing effects

The detailed static analysis of the CA worths, for different positions of insertion, revealed complex interactions which can occur between CAs in a large GFR. In the most severe case, the analysis showed that these interactions can amplify or reduce the CA worth by almost a factor 2, compared to the individual values calculated. Different possible ways to reduce these large effects (in terms of performance and safety) have been envisaged. However, in most cases, the possible ways, such as the cross-linking of CAs of different banks, were found not to be practical due to the operational constraints they would imply.

Heterogeneity effects

As part of the CA pattern characterization, the CA worth was computed with perturbation theory with improved accuracy, in order to better quantify the heterogeneity effect (i.e. the difference between homogeneous and heterogeneous treatments) which leads to a worth reduction in most cases. The estimated effect was -13% for the newly developed CA design, a value found to be significantly lower that the value of 20 to 30% for previously developed sodium-cooled systems. It has been observed that this improvement is mainly due to the optimal choice of the pin diameter and the corresponding reduction of shadowing effects. The proposed central, stagnant helium zone also contributes significantly to the improvement.

Reactivity control requirements

While optimizing the CA pattern, the reactivity control requirements were determined based on the reactivity margins considered for previous sodium-cooled reactors. A quantification of the reactivity margins is particularly important in the context of the determination of the implementation scheme matching operational constraints for the GFR. In more specific terms, the reactivity requirements were evaluated to account for physical changes, in particular the reactivity swing during the average fuel cycle and the hot-to-cold changes in operating conditions (mainly Doppler and core expansion effects).

Due to the absence of accurate design studies for the advanced GFR, particular care was taken to consider uncertainties coming not only from nuclear data and computational methods, but also from design assumptions. This has led to a relatively large total uncertainty on the reactivity requirements, a factor which is quite penalizing in terms of the number of CAs within the core.

Control assembly implementation scheme

To determine the CA implementation scheme, in terms of the number and positions of the assemblies within the GFR core, appropriate safety criteria were considered while matching the reactivity control requirements. The most penalizing case considered was core shutdown with a partial failure of the diverse safety shutdown system.

The analysis has shown that there are large reactivity margins (in the range of several thousands of pcm) for the first, conservatively designed implementation scheme. Consequently, the possibility has been indicated of reducing the number of CAs within the core, viz. to 15 in the two CSD banks and 4 in the DSD bank (19 CAs - "Variant II").

Revised "2007-Core" design

The neutronics investigations performed for the reference GFR core, in particular those related to the development of the CA pattern and implementation scheme, have directly contributed to the internationally agreed upon, proposal for the new "2007-Core" core design. The core geometry is significantly different, with the height-to-diameter ratio having been increased to 0.6, compared to 0.3 for the reference core. The parallel analysis of both core variants has shown, among other things, that the CA interactions are indeed reduced for the new design.

6.2.3 Development and application of coupled full-core models to control assembly driven transients

Full-core 3D neutron kinetics and 1D thermal-hydraulics GFR models

The development and validation of the coupled full-core 3D NK and 1D TH GFR core models ("2004-Core" and "2007-Core") were carried out in successive steps. First, the self-shielded macroscopic cross-sections and their derivatives (with respect to the fuel temperature T_f, coolant density ρ_c, and thermal radial (δ_r) and axial (δ_z) core expansions) were calculated with the cell code ECCO. For the purpose of detailed analysis, each CA was modelled individually, the standalone full-core neutronics model (PARCS) being developed separately to start with, in order to enable a systematic step-wise verification of the final coupled model.

In the second step, the full-core 1D TH model was set up with TRACE. Particular attention was paid to model each individual fuel SA in terms of a heat structure and a coolant channel. The aim was to have a sufficiently detailed core model for the study of local deformations of the 3D distributions of the calculated results (coolant and cladding temperatures), caused by localized reactivity insertions (CA withdrawals and ejections). In the third step, the NK and TH models were coupled together using external mapping schemes, containing the mappings of both the heat structures and the pipe components to the neutronic nodes.

The final step was the validation of the coupled full-core NK-TH models against reference ERANOS-VARIANT calculations for different core configurations, e.g. in terms of the k_{eff} values for different operating conditions. In particular, the CA worths and reactivity feedbacks were benchmarked, the discrepancies being found to be relatively low, viz. in the range of 5% ("2004-Core") to 8% ("2007-Core"). The accurate simulation of the CA worth, i.e. of the related shadowing and anti-shadowing effects, is particularly important in order to ensure reliable treatment of the CA driven, reactivity insertion accidents.

GFR core dynamic behavior under control assembly driven transients

The developed NK-TH GFR core models were subsequently used for the analysis of the GFR core response to a broad range of CA driven transients, i.e. withdrawals at operating or ejection speed. For the sake of obtaining a detailed understanding of the 3D core behavior and to identify the important parameters impacting the core safety under operational and accidental conditions, the following hypothetical CA driven transients were systematically analyzed, viz.

(1) “2004-Core” CA withdrawal cases at operational speed,
(2) ”2007-Core” CA withdrawal cases at operational speed,
(3) “2004-Core” CA ejection cases at higher speed,
(4) “2007-Core” CA ejection cases at higher speed.

For both GFR core designs, the transients were simulated assuming that the CAs are withdrawn at constant speed. The simulations were performed without the actuation of the scram, in order to study the core behavior under the influence of reactivity feedbacks alone. Due to uncertainties in the GFR design itself, special care was taken to assess the dependence of the core behavior and related spatial effects to various parameters, such as the CA implementation scheme, the CA withdrawal speed, the number of CAs being withdrawn/ejected and the core power level. From the various cases simulated, it has been shown that:

(1) The withdrawal at operational speed of one CA from the reference position does not significantly impact the core safety in terms of average outlet coolant, peak cladding and peak fuel temperatures. Consequently, the analysis has shown the adequacy of the developed CA pattern and related CA implementation scheme.
(2) The “2007-Core” design presents better safety features, compared to the reference core, with lower predicted values for the TH results (coolant, peak fuel and cladding temperatures). Moreover, the rates of temperature increase were found to be reduced for the new core, due to lower reactivity worths of the withdrawn CAs.
(3) The comparison of asymmetric and symmetric CA withdrawals indicates that spatial effects can be significantly reduced by, first, limiting the number of CAs simultaneously in movement and, second, by operating the CAs in a symmetric way. Additionally, the large spatial effects (up to +21% for the power shape deformations) were found to be directly correlated to the inserted reactivity. As such, they too are also significantly reduced in the new “2007-Core”, driven by lower interactions. This is a further advantageous feature of the second core design.
(4) A reduction of the number of CAs, as proposed in the “Variant II” implementation scheme (19 CAs in total), has been found to have relatively little influence on the GFR core behavior, i.e. there does not appear to be any associated safety problem.
(5) The dynamic analysis of a GFR core containing burnt fuel (BOEC fuel composition) has shown that predicted power peaking factors and associated temperatures are higher, compared to the fresh fuel situation. This has been shown to result from the reduced values of the safety-related parameters, especially the delayed neutron fraction and the fuel Doppler constant.

As a point of special interest, the detailed comparisons for simulations performed with a simplified, ring-wise TH model have shown the importance of a detailed core model to accurately predict the material temperatures associated with large spatial effects. Relatively large underpredictions of the cladding temperature (up to 100 K) were obtained using the simplified model. Nevertheless, solutions, such as the use of “engineering coefficients” to account for spatial effects, may be found for applying simplified models and/or methods in certain cases, e.g. for conducting a range of parametric studies.

6.3 Recommendations for future work

The present research has focused on the detailed characterization of the large Generation IV GFR core, from the viewpoint of the CA design and implementation scheme. This has been achieved via, first, a design phase based on static considerations and, second, safety-related analyses on the basis of NK-TH coupled, full-core transient calculations. Several aspects of the GFR control system have been explored in detail, but certain domains of investigation remain open. The suggestions for future work are given below.

Detailed analysis of the reactivity requirements and related uncertainties

The reactivity requirements for the GFR core were evaluated in order to dimension the CA implementation scheme in an appropriate manner. In this context, considerable conservatism had to be adopted while assessing the reactivity uncertainties, so that adequate safety margins could be ensured. This has been mainly due to the absence of accurate design studies for the GFR. In order to arrive at a better optimized, CA implementation scheme, it is essential that the reactivity requirements be assessed in greater detail, so that the associated uncertainties can be reduced to more realistic values.

Extension of the full-core thermal-hydraulics model to a system model

The NK-TH models developed were used to simulate CA driven transients on the basis of specified boundary conditions for the primary and secondary loops. As a consequence, it was not possible to accurately simulate transients initiated by TH effects, such as loss of flow and/or loss of coolant, etc.

For being able to use the developed NK-TH coupled models for a wider range of safety studies, an extension of the TH model from full-core to full-system is needed. This implies design work being completed also for system components such as the blowers and heat exchangers. The corresponding investigations are ongoing at the present time. Once the final specifications of the primary/secondary loops are available, a full GFR system model should be implemented with TRACE. This will then offer possibilities for a much wider range of transient analyses.

Implementation of a 2D mechanical fuel model

It is clear that, for a complete evaluation of the GFR core behavior under transient conditions, the fuel thermo-mechanical model plays a crucial role. Significant effort has already been made in the development of an advanced fuel model for the safety analysis of the GFR in a separate thesis, and the current research has made use of the 1D thermal model that has been made available in the framework of the FAST code system. To extend capabilities, in terms of a more in-depth analysis of the fuel behavior during the considered GFR transients, the developed NK-TH model would benefit from the implementation of a 2D thermo-mechanical fuel model. It would then become possible to predict not only the 2D temperature distributions, but also the stress-strain conditions within the fuel pellets, the SiC honeycomb matrix and cover plates.

Material properties and their burnup dependence

The dynamic analysis presented in this thesis has focused on the verification of the adequacy of the developed CA pattern, in particular under reactivity initiated accident conditions. It needs to be emphasized that the simulation results for the considered transients largely depend on the material properties assumed. Due to the innovative character of the SiC material used in the GFR, the database for material properties still needs to be improved in quality. It is still not known, for example, what the final choice of the form of the SiC will be, i.e. whether it will be bulk or fiber-reinforced. The material properties are quite different in the two cases (the current analysis has assumed the use of bulk SiC).

As part of the conducted sensitivity study, the impact of having burnt fuel in the core was investigated. This was done, however, solely from the point of view of assessing the effects of the deterioration in safety-related neutronics parameters. The thermal fuel properties were assumed to be those for fresh fuel. This significant simplification has been necessary due to the lack of available data as regards the burnup dependence of the material properties. Clearly, an appropriate extension of the experimental database is an important need in this context.

Appendices

Appendix A

A. Development of thermal-spectrum gas-cooled reactors

This appendix summarises the development history of thermal-spectrum, gas-cooled reactors. The historical overview presented is by no means exhaustive, but it serves to illustrate the experience acquired with gas-cooled systems before the Generation IV initiative was launched. It helps as well to understand the differences and similarities between previous gas-cooled reactors and the Generation IV GFR.

Immediately after the Second World War, several countries decided to start a civil nuclear program for energy production. They had to make their choice among different design possibilities. In brief, the different design options are characterised by a given, combined choice of a coolant, a moderator and a fuel. A very wide range of concepts resulted.

Gas-cooled reactors (GCRs) have had a long and varied history, which dates back to the very early days of nuclear energy development. From the very beginning, it was recognised that gas cooling has several benefits [72; 168; 169]. An important aspect is the reduction of the risk due to reactivity insertion following coolant voiding, since gas coolants have low macroscopic absorption cross-sections. Another fact that was immediately pointed out is the possibility to go to higher temperatures with gas (in particular, with helium), since, in contrast to water-cooled reactors, there is no possibility for change of phase. This means that the thermal efficiency for electricity production can be significantly increased with the power conversion systems working at high temperature.

A. 1 Magnox and AGRs in England

Due to technological constraints, most of the early development was centred on relatively low temperature systems using graphite moderator, metal-clad metallic fuel and carbon dioxide coolant. Commercial operation started in the mid-1950s with the Magnox stations (see Figure A.1), followed later by Advanced Gas-cooled Reactors (AGRs; see Figure A.1). These systems have been deployed solely in the United Kingdom. At the end of 1988 [168], a total of 56 electricity generating, gas-cooled reactors were in operation worldwide, i.e. 37 Magnox (and similar) systems and 15 AGRs. A list of the reactors is given in Table A.1.

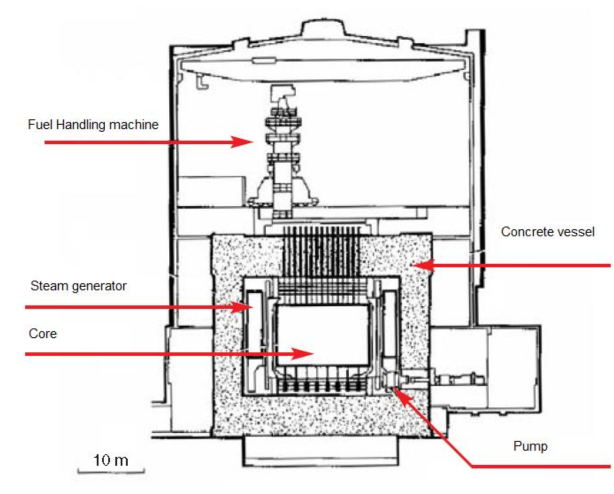

Figure A.1 Schematic of a Magnox reactor [72]

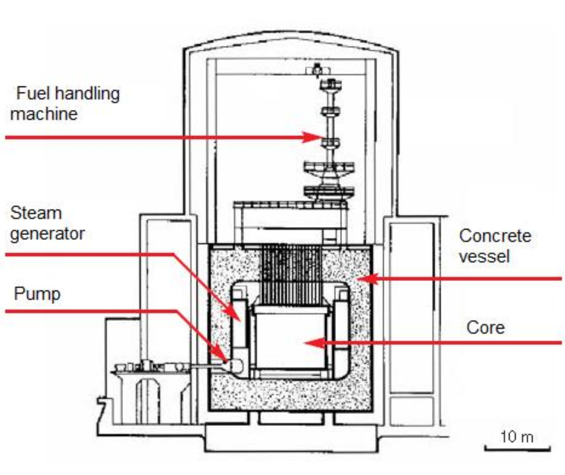

Figure A.2 Schematic of an AGR reactor [72]

Table A.1 List of gas-cooled reactors

Magnox and similar plants	Number of reactors	Total electrical output, MWe
United Kingdom		
Calder Hall	4	200
Chapel Cross	4	200
Berkely	2	276
Bradwel	2	300
Hunterston-A	2	320
Trawsfynydd	2	500
Hinkley Point-A	2	500
Dungeness-A	2	550
Sizewell-A	2	580
Oldbury	2	600
Wylfa	2	1180
France		
Marcoule	2	80
Chinon	3	750
St. Laurent	2	995
Bugey	1	540
Italy		
Latina	1	150

Japan		
Tokai	1	159
Spain		
Vandellós	1	480

AGR plants	Number of reactors	Total electrical output, MWe
United Kingdom		
Windscale	1	32
Hinkley Point-B	2	1250
Hunterston-B	2	1250
Dungeness-B	2	1250
Hartlepool	2	1250
Heysham-1	2	1250
Heysham-2	2	1320
Torness Point	2	1320
	15	8872

As indicated above, the first commercial GCRs were constructed in the United Kingdom in the 1950s, with commissioning of the first unit in 1962. An extensive program was undertaken to build Magnox reactors for electricity production. Magnox reactors operate with natural uranium metal fuel and utilise pressurised CO_2. The moderator is graphite, a cheap and available material, with fuel and coolant being located in coolant holes in the graphite lattice arrangement. Magnox alloy is used as fuel cladding. The term Magnox comes from the name of the magnesium alloy used to clad the metallic fuel elements. To control the reactivity, boron-steel control rods were used. The design was continuously refined, and very few units are identical. Early reactors have steel pressure vessels, while later units (Oldbury and Wylfa, for instance) are of reinforced concrete; some are cylindrical in design, but most are spherical. Working pressure varies from 0.69 to 1.935 MPa for the steel pressure vessels, and the two reinforced concrete designs operated at 2.48 and 2.7 MPa.

One of the main reasons to develop reactors operating with natural uranium was that the sole dependence was on uranium ore. Neither heavy water nor enrichment factories were available at that time.

The core size of a Magnox reactor is large due to the low power density, which is nominally 1 $MWth/m^3$. On the other hand, the low power density and the high heat capacity of the graphite result in relatively small changes in the graphite temperature, which is excellent for the reactor safety characteristics. Another aspect is the safe operation with graphite up to high temperatures. However, the internal temperature of Magnox fuel elements must remain below ~650°C to avoid fuel deformation. Correspondingly, the design value under steady-state operation is limited to about 500°C to ensure cladding integrity. As a direct consequence, the average gas temperature leaving the reactor was originally limited to about 400°C, giving a plant thermal efficiency of 31%. On-load refuelling was an economically essential part of the design, to maximise power station availability by eliminating refuelling downtime. This is particularly important for Magnox as the fuel had a low burn-up, requiring more frequent changes of fuel than most enriched uranium reactors.

As a direct consequence of the low power density and the low temperature allowed for the fuel (metallic), Magnox reactors have limited economic performance.

For improved economy, the United Kingdom rapidly developed the Advanced Gas-cooled Reactor, or AGR. As in the Magnox units, AGRs employ graphite moderator and carbon dioxide coolant. However, the fuel is low enriched uranium oxide contained in stainless steel cladding. The first AGR became operational in 1962 [72; 168; 170]. All commercial AGR power stations are configured with two reactors, each reactor with a power output in the range of 555 MWe to 625 MWe. The fuel is uranium dioxide pellets, enriched to 2.5-3.5%, in stainless steel tubes. The original design concept of the AGR was to use a beryllium based cladding. When this was proved unsuitable, the enrichment level of the fuel was raised to allow for the higher neutron capture losses in stainless steel cladding. This significantly increased the cost of the power produced by an AGR. The carbon dioxide coolant circulates through the core, reaching 640°C at a pressure of around 4.0 MPa, and then passes through steam generators located within the steel lined, reinforced concrete pressure vessel. Control rods penetrate the graphite moderator and a secondary shutdown system involves injecting nitrogen into the coolant. A tertiary shutdown system operates by injecting boron balls into the reactor.

Several advantages are observed for AGRs, compared to Magnox reactors. The use of enriched uranium allows a better neutron economy and permits one to overcome several neutronics constraints. Additionally, the AGR fuel can be operated at temperature higher than 2000°C. The limit is, in this case, coming from the cladding itself, which is increased to a design value of about 880°C. The average core power density is increased to 2 MWth/m^3, resulting in a net decrease in the physical size. The plant thermal efficiency is also increased (to about 40%), adding to the better economic performance.

The development of AGRs in the United Kingdom was not particularly easy due to engineering difficulties, especially coming from radiolytic corrosion problems caused by CO and the free radicals formed from carbon dioxide under irradiation. To overcome these technical problems, methane was included in the coolant, but the concentration control of this gas was complicated. Finally, 14 AGRs were built in the United Kingdom. Graphite-gas units have slowly been abandoned by France, Italy, Spain and Japan. Worldwide, GCRs today represent only 4% of the energy production, the decommissioning phase having started in 2002.

A. 2 Gas-graphite reactors in France

Almost parallel to the development of the Magnox reactors, France decided to start the development of reactors moderated with graphite, cooled with carbon dioxide under pressure and using natural uranium fuel elements, so-called Uranium-Naturel-Graphite-Gaz (UNGG) reactors [72]. These reactors, though developed independently, were globally quite similar to Magnox. Nine of these were built, with significant differences between the designs, since all were effectively new prototypes, having been built without awaiting feedback from experience with other installations. At the beginning, these reactors were operated to offer to France the capacity to produce high-grade plutonium. Finally in 1968, the construction of the last UNGG was not terminated for economic reasons, LWRs having already shown themselves to be more competitive.

As for Magnox reactors, the low average specific power of the UNGG imposed large core sizes. The design characteristics presented below are taken from the example of the St-Laurent 2 plant [72]. The core is located in a vessel containing the primary circuit and the heat exchanger. The pressure vessel is made of pre-stressed concrete, 33 m in diameter and with a height of 48 m. Leak-tightness of the vessel is assured by an inner steel “skin” of 25 mm thickness. The graphite core is cylindrical in shape, 10.2 m in height and 15.7 m in diameter, and made from a lattice of cylindrical elements held together with mortises.

The four CO_2-steam heat exchangers were mono-tube-shaped with cross-flow, the water entering in the lower part and the hot CO_2 in the upper part. The use of natural uranium did not allow high burnup of the fuel due to the low neutron economy. A typical value for the burnup was 6.5 GWd/t. As a consequence, online refuelling techniques with sophisticated fuel manipulators were developed, allowing the replacement of two to three fuel assemblies a day. The maximal operating temperature was fixed by the limiting fuel temperature (650°C at the inner face of the fuel element).

Representative design parameters for Magnox, AGR and UNGG reactors are compared in Table A.2.

Table A.2 Comparison of the design characteristics of AGR (“Hinkley Point B”), Magnox (“Wylfa”) and UNGG (Saint Laurent 2) reactors [72]

Parameter	Units	AGR	Magnox	UNGG
Mass U	t	114	395	430
Fuel		UO_2	U-metal	U-metal
Power density	MW/m^3	3	~1	~1
Enrichment	%	2.1 - 2.6	0.7	0.7
Cladding		stainless steel	Mg-Al alloy	Mg-Zr alloy
Coolant gas pressure	bar	41.9	27.6	29
Number of exchanger		12	4	4
Outlet temperature	°C	645	414	400
Maximal cladding temperature	°C	825	450	473
Graphite mass	t	1248	3735	2440
Electrical power	MWe	625	590	480
Efficiency	%	41.7	31.4	28.7
CO_2 flow rate	t/s	3.8	10.2	8.6
Burnup	GWd/t	18	4	6.5

GCRs have interesting inherent safety features. Two successive barriers, which ensure the confinement of fission products, are the cladding of the fuel element and the pre-stressed concrete pressure vessel. Particular attention was given to the control of the core cooling, which was ensured by independent systems. The operating temperature was very close to the technological limit and particular care was taken not to overpass it. Additionally, the cladding integrity was controlled by detecting any fission gas release in the coolant. Reactor operation was not allowed in the case of a damaged cladding to prevent oxidation of the metallic uranium by CO_2, which would then have contaminated the whole coolant circuit.

For these reactors, the reference design-base accident is the LOCA into the pre-stressed concrete vessel, typically resulting from a failure when operating the fuel manipulator or simply from a gas pipe break. Secondary safety cooling systems were installed to compensate for these events. The safety assessment studies confirmed the considerable degree of inherent safety because of the system design, low power density and gas coolant. As such, the reactors were not considered to require a secondary containment.

A. 3 HTR development

The goal of improving the thermal efficiency, combined with the desire for broader applications of nuclear energy such as providing industrial process heat, later motivated the development of high temperature gas-cooled reactors (HTGRs), or High Temperature Reactors [16] (HTRs) as they are more commonly called currently [168]. Important features were an increase in the core power density and the operating temperature, achieved through the use of a new fuel type, viz. ceramic fuel particles surrounded by coatings and dispersed in a graphite matrix.

Either prismatic type graphite moderator blocks (block type reactor) or spherical fuel elements (pebble-bed type reactor) are employed in HTRs. Helium is used as coolant, and flows though coolant holes (in the block design) or through the free space present in the core of the pebble-bed reactor. The use of helium coolant, which in contrast to CO_2 , is chemically inert, as also the refractory fuel employed, allow one to increase the outlet temperature up to 950°C (design value). A list of high temperature reactors is presented in Table A.3, along with the principal design characteristics.

The first HTR was the Dragon reactor at Winfrith in the United Kingdom [168], a 20 MWth experimental reactor built under the Dragon Project and funded by the OECD. The reactor was operated from 1965 to 1976 when the Dragon Project was terminated. The reactor was used as a fuel irradiation facility and also to gain some experience in helium utilisation. The same basic fuel type (coated particles) was used when the United States of America and Germany began developing commercial HTRs.

In Germany, emphasis was put on Pebble Bed Reactors (PBRs), the basic fuel element (pebble) being a graphite sphere of about 60 mm diameter, containing a large number of coated fuel particles. Each spherical fuel kernel is surrounded by three ceramic layers of different density, the so-called TRISO concept (see Figure A.3). The “Arbeitsgemeinschaft Versuchsreaktor” (AVR) was built to demonstrate the feasibility of PBRs. The AVR, a 15 MWe test reactor, first generated electricity in 1967 [168; 171]. In the present context of the Generation IV GFR, it is interesting to note that the AVR reactor achieved very high helium temperatures (average outlet temperature of more than 950°C). Additionally, Germany began construction of the Thorium High Temperature Reactor (THTR300) in 1972, with a power of 300 MWe. This prototype, which started operation in 1983, was shutdown in 1989 for economic reasons.

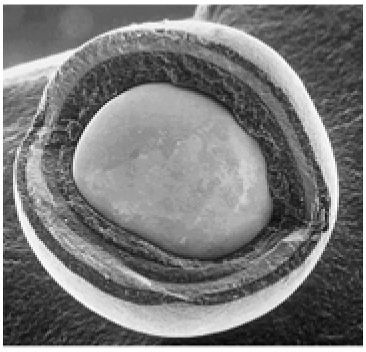

Figure A.3 Microscopic image of a TRISO particle [72]. Starting from the centre, the buffer layer, inner pyrolitic carbon layer, the light colored SiC sealing layer and the outer pyrolytic carbon layer are visible in the picture

In the USA, emphasis was on prismatic block fuel elements, with fuel “pellets” of graphite (containing coated particles) stacked within holes in the graphite moderator block. Another peculiarity of this design was the presence of separate helium coolant holes included in the moderator block. The 40 MWe Peach Bottom HTGR was the first HTR in the USA and was operated from 1967 to 1988. Basic feasibility was thus demonstrated with, in particular, a relatively high power density of 8.3 MWth/m^3. USA’s block-type prototype HTR, Fort St. Vrain (330 MWe), was operated between 1974 and 1989.

In Japan, JAERI has also started a research program to develop a high temperature reactor aiming at producing hydrogen. The core will combine the expertise obtained at the core level by the USA and on the coated particle fuel by Germany. A 30 MWth reactor, High Temperature Engineering Test Reactor (HTTR), was started in 1998, initially with helium at a temperature of 850°C. Test operation at a higher temperature (950°C) has already been performed [172].

Table A.3 presents the main design characteristics of various high temperature reactors, including the most recently built demonstrator installation, HTR10, in China.

Table A.3 High Temperature Reactors (HTRs) around the world and their principal design characteristics [72]

	Dragon	**Peach-Bottom**	**AVR**	**Fort St-Vrain**	**THTR300**	**HTTR**	**HTR10**
Place	Winfrith, UK	Penn-Sylvania, USA	Jülich, Germany	Colorado, USA	Schme-hausen, Germany	Oarai, Japan	Beijing, China
Start date	1964	1966	1966	1974	1983	1998	2001
Stop date	1975	1974	1988	1989	1989	-	-
MWth	20	115.5	46	842	750	30	10
MWe	-	40	15	330	300	-	-
He pressure (bars)	20	24.6	10	48	40	40	30
Inlet T (°C)	335	343	175	406	262	395	250-300
Outlet T (°C)	835	715	850	785	750	850-950	700-900
Power density (MW/m^3)	14	8.3	2.3	6.3	6	2.5	2
Fuel type	prismatic	prismatic	pebble	prismatic	pebble	prismatic	pebble
Fuel cycle	diverse	U/Th	^{235}U/Th	^{235}U/Th	^{235}U/Th	enr. U	enr. U

Various other HTR design activities have taken place worldwide. In parallel, considerable progress has been made, not only on heat exchangers, but also on gas turbines operating at high temperatures and the possibility of implementing the direct cycle in HTRs. All these elements, taken together, have allowed new concepts to be proposed, like the Gas Turbine - Modular High Temperature Reactor (GT-MHTR; see Figure A.4) developed by General Atomics or the Pebble Bed Modular Reactor (PBMR; see Figure A.5) developed by Eskom in South Africa [72].

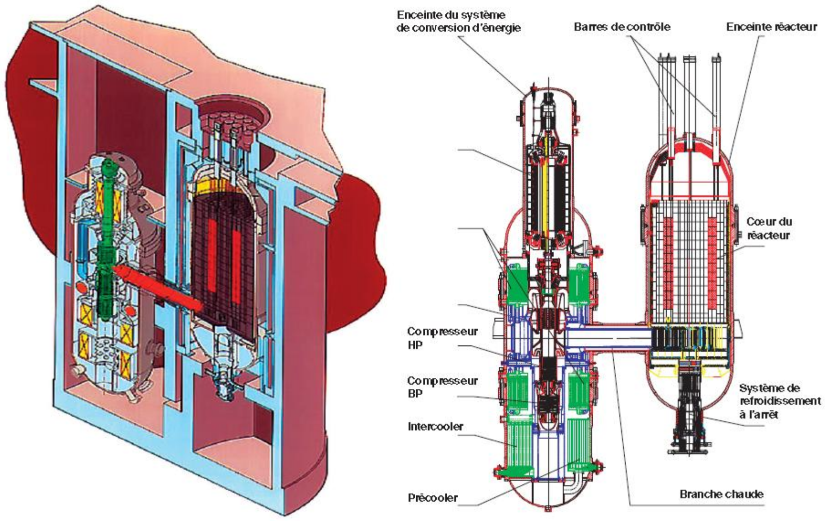

Figure A.4 The GT-MHTR project of General Atomics [72]

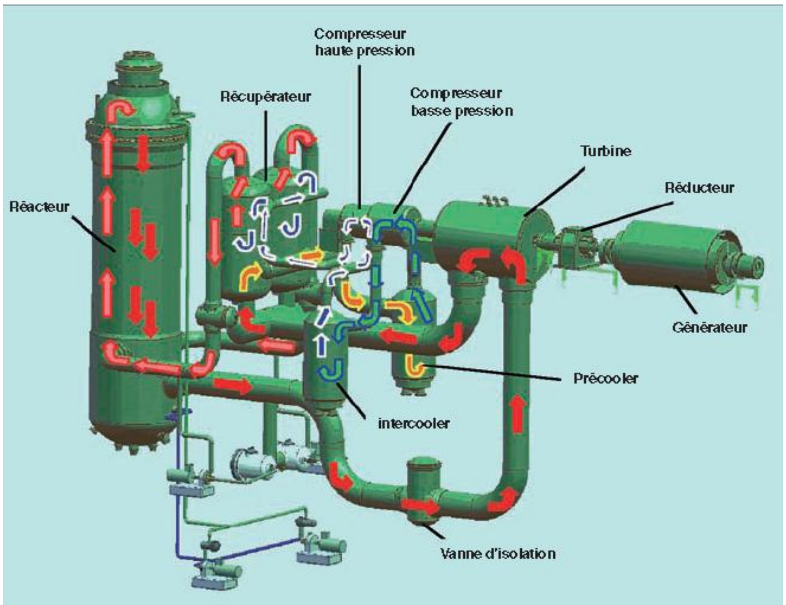

Figure A.5 The PBMR project of Eskom [72]

In summary, important milestones in the development of thermal-spectrum gas-cooled reactors have been achieved, with successful operation up to a very high temperature. The production and demonstration of robust high-quality fuel, and other key elements of HTR technology, have been successfully performed. Two distinct HTR concepts have been established, i.e. block (prismatic) and pebble bed, both based on the usage of ceramic coated-particle fuel.

Appendix B

B. Supplementary information and investigations related to GCFR-PROTEUS

B. 1 First phase of the program

This section describes each core configuration as investigated during the first experimental phase, i.e. that with only (U,Pu)O_2 fuel. A brief description, including the various available literature, is given, for each experiment, in terms of geometrical specifications and material compositions. The measured parameters and analytical approaches, which were used in the past, are also presented. The availability of correction factors, which convert the experimental values obtained in the test lattice into values to be compared within the framework of lattice calculations, is also discussed.

The database is described in detailed terms and can therefore be used for future analysis of interest.

Core 1: First lattice with UO_2 buffer

The program started with a central lattice filled with MOX rods and the buffer was made of natural-UO_2 rods. The main characteristics of the reference test lattice have already been given in Section 3.2.

The measured parameters were the neutron spectrum, as well as the reaction rate ratios C8/F9, F5/F9 and F8/F9, at the centre of the test lattice. These three reaction rate ratios were measured in all subsequent configurations as well and could therefore be used as a reference. Additional measurements were also performed in all subsequent cores depending on measurement technique improvements. The information necessary to construct a cell model, including pre-computed correction factors [118], as well as for setting up detailed 1D and 2D models of the whole reactor [173], is available. Homogenized material compositions were used, for regions surrounding the fast spectrum zone, to produce cross-sections for use in a diffusion code with a 10-group energy structure.

Core 2: Lattice with stainless steel rods

In this test lattice, one third of the fuel rods within the fast-zone were replaced by stainless steel (18/8-type) rods of the same dimensions, thus increasing the steel volume fraction from 11% to 26% [54; 174]. The central fast-zone is shown in Figure B.1.

The parameters measured, at the centre of the test lattice, were the neutron spectrum, as well as the reaction rate ratios C8/F9, F5/F9 and F8/F9 [117]. The information to construct a cell model, including pre-computed correction factors [118] as well for setting up detailed 1D and 2D models of the whole reactor, is available [118; 122; 173].

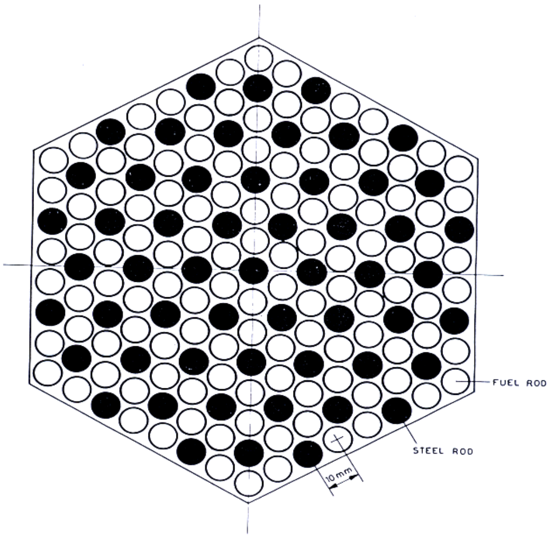

Figure B.1 View of the central part of the fast zone for GCFR-PROTEUS Core 2 (increased steel fraction)

Core 3: Reference lattice with U-metal buffer

The reactor configuration here was a modification of GCFR-PROTEUS Core 1, the UO_2 buffer being replaced by a U-metal buffer [122; 175; 176]. The use of this U-metal buffer significantly reduced the correction factors, viz. by about 2.5% on average. This implies that the neutron spectrum obtained in Core 3 is closer to that which one would obtain in a critical reactor made entirely of the $(U,Pu)O_2$ fuel. The fast test lattices of Cores 1 and 3 were identical.

The parameters measured, at the centre of the test lattice, were the neutron spectrum, as well as the reaction rate ratios C8/F9, F5/F9, F8/F9. The information to construct a cell model including pre-computed correction factors [120; 122], which are much closer to unity in this case, as well as detailed 1D and 2D models of the whole reactor [54; 173; 177], are available. As indicated earlier, all GCFR-PROTEUS configurations subsequent to Core 2, i.e., Cores 3 to 16, employed the U-metal buffer for the reason explained above.

Core 4: Power reactor features, including steam entry

In Core 4, several different power reactor features were investigated, effectively as different modifications of Core 3 [54; 174; 178; 179; 180; 181; 182; 183], with changes made in the central region of the test zone. These changes were:

(1) A central assembly of depleted UO_2 rods, replacing the $(U,Pu)O_2$ fuel rods in the central region, and being called Core 4.a. Specifically the UO_2 rods were of 140 cm length and arranged as a hexagonal assembly, 13 cm across sides. The UO_2-pellets ("cigars") used were of the same type as those in the axial blankets [173]. Experimental reaction rate profiles in the radial direction, i.e. for C8, F8 and F9, are available in the form of graphical representations. These profiles were measured in the central axial plane [50].

(2) A 8 mm thick hexagonal steel wall, representing the total thickness of adjoining sub-assembly walls, mounted around a central column of (U,Pu)O_2 fuel rods, 11.2 cm across sides, and being called Core 4.b. Available is the F8 reaction rate profile measured near the wall in the form of a graphical representation [54; 179].

(3) A 5.4 cm thick B_4C control rod, which replaced the central fuel rod, the B_4C density being somewhat uncertain [54; 179], and being called Core 4.c. Available in the form of graphical representations are profiles for C8, F8 and F9, measured in the vicinity of the control rod [54].

(4) Plastic inserts in each channel to investigate the effects of steam/water entry into the test lattice, and being called Core 4.d [180]. Thus, the presence of steam/water was simulated through the use of hydrogenous plastic [180; 181]. As a representative example, which is well documented, a central hexagonal volume, of sides 11.5 cm across and the whole nominal fuel length of 140 cm, was filled with expanded polystyrene beads, thus replacing the air, while in the remaining volume of the test lattice, 2 mm thick polypropylene disks were inserted between the fuel rods. Reactivity measurements are available, the resulting average hydrogen concentration corresponding, in this case, to steam at a density of 0.046 g.cm^{-3} [180; 181; 183]. For both configurations, i.e. with and without polystyrene, reaction rate ratios such as C8/F9, F8/F9 and F5/F9 were measured at the core centre [54; 181].

Core 5: Identical to Core 3

This configuration, and the experiments which were carried out, were the same as for Core 3, while the experimental techniques were improved. The data is not documented [54].

Core 6: "High-UO_2" lattice

Cores 6 to 8 were "null reactivity" test lattices in which the reference (U,Pu)O_2 lattice of Core 3 was modified to render k_∞, i.e. the ratio between total neutron productions and absorptions, close to unity [173; 184; 185; 186; 187]. This was done to obtain accurate experimental values of k_∞, thereby providing indirect information regarding the non-measurable reaction rate ratios, i.e. the ^{239}Pu capture-to fission ratio (α_9) in the "high-UO_2" lattice of Core 6, and the capture rates in structural materials (relative to F9) in the "high-steel" and "high-iron" lattices of Cores 7 and 8, respectively.

In Core 6, one third of the original fuel rods were replaced by depleted UO_2 rods. The close-to-unity fundamental mode k_∞ value in this lattice was measured by the null-reactivity technique. This, along with the experimental values of the measurable reaction rate ratios, i.e. C8/F9, F8/F9 and F5/F9, provided an assessment of α_9 but only to about 15% accuracy [54].

Core 7: "High-steel" lattice

This configuration is a modification of Core 3, the layout of the core being given in [54; 173; 174; 185; 186; 187; 188]. One third of the original fuel rods were replaced by stainless-steel 18/8 rods in order to examine the sensitivity of the close-to-unity k_∞ to steel absorptions. The experimental values of k_∞ and the measurable reaction rate ratios, i.e., C8/F9, F8/F9 and F5/F9, permitted the determination of an experimental value of the steel capture rate (relative to F9) to about 4 % accuracy [54].

The values reported are corrected experimental values and the original experimental values are not documented.

Core 8: 1st "High-iron" lattice

Similar to Core 7, except that a different steel was used [185; 187; 189; 190]. The experimental assessment of the iron capture rate (relative to F9) is reported to have been determined to an accuracy of about 6% [54].

Core 9: Core with an upper iron shield

In the framework of an international program aimed at benchmarking iron data, this configuration, a modification of Core 3, dealt with shielding measurements carried out primarily in a steel-37 cylindrical structure (120 cm in diameter and 60 cm thick) mounted above the reactor core (specifically, the test zone, buffer and D_2O-driver regions) [54; 182].

In this heterogeneous configuration, measurements were performed for absolute fission rates (e.g. F9 and F8) at different axial, as well as radial, positions in the reactor. Also carried out were activation measurements in dedicated threshold detectors, as well as spectrum measurements, at four radially-centered locations in the iron shield. A complete description of this core configuration, including experiments and calculations, is presented in [182].

Core 10: 2nd "High-iron" lattice

This configuration and the experiments performed were the same as for Core 8, but with improved experimental techniques.

The parameters measured, at the centre of the test lattice, were k_∞, C8/F9, F8/F9 and capture in Mn relative to ^{239}Pu fission [54]. The information to construct a cell model (including pre-computed correction factors), as well as for setting up a detailed 2D model of the whole reactor, is available [120; 173; 190]. The neutron spectrum at the centre of the core is also depicted in a graphical representation [191].

B. 2 Second phase with thorium

This section describes each of the core configurations investigated during the second experimental phase, i.e. that dedicated to studies with thorium as fertile material.

Core 11: (U,Pu)O_2 lattice

This configuration is the same as that for Core 5, and therefore also for Core 3 [192; 193]. However, a larger number of central reaction rate measurements were performed, primarily in relation to the later realization of the test lattices with Th. The additional reaction rates available, again expressed relative to F9, are C2, F2 and F3. Also measured were the Th(n, 2n) reaction rate, relative to C2, and F7/F9. All these were effectively infinite-dilution reaction rates, since there was no thorium (or ^{233}U) in the test lattice. It should be mentioned that F5/F9 is missing in this particular case.

Core 12: (U,Pu)O_2 Lattice with ThO_2

This core was a modification of Core 11, in which one third of the fuel rods were replaced in a geometrically regular way by ThO_2 rods (see Table 3.1 for a description of the ThO_2 rods) [192; 193; 194; 195]. Thereby, slightly different (U,Pu)O_2 rods of the same composition were used. These rods were made of 18 cigars in the centre and 3 depleted UO_2 cigars at the ends. The (U,Pu)O_2 active length was ~1.00 m, whereas the UO_2 active length was ~0.17 m. The ThO_2 rods consisted of three 0.33 m long cigars, bounded at both ends by the same length of depleted UO_2 as in the case of the (U,Pu)O_2 rods.

For this core, almost the same measurements were performed at the centre of the test lattice as for Core 11, i.e. the neutron spectrum as well as the reaction rate ratios C8/F9, F8/F9, C2/F9, F2/F9, and the Th(n,2n) reaction relative to C2 [192; 193].

Core 13: Lattice with a central ThO_2 blanket

Core 13 was a modification of Core 11. A ThO_2 blanket of 0.137 m diameter was built to replace the equivalent central region of the standard (U,Pu)O_2 lattice. This blanket consisted of 169 ThO_2 rods of the same type as used in Core 12 [192; 196; 197]. Central reaction rate ratios (relative to F9) and axially centered radial reaction rate profiles, viz. for F9, C2, F2, C8, F8 and F3 (with normalization to unity at the core centre and going across the blanket/core interface) were measured [196; 197; 198]. In addition, the Th(n,2n) reaction rate relative to the Th(n,γ) reaction rate was measured at the core centre [192].

Core 14: Lattice with an axial upper ThO_2 blanket

Core 14 was a modification of Core 12, in which the upper axial blanket was a ThO_2 lattice. The active length of the rods in the entire fast zone had to be slightly reduced [120; 199; 200; 201; 202]. More specifically, the fuel of the fast zone was composed of 15 (U,Pu)O_2 cigars, with three 168 mm long depleted UO_2 cigars below and one 330 mm long ThO_2 cigar above (see Table 3.1). The upper axial blanket was covered with a steel-shielding block 0.60 m thick.

The neutron spectrum, as well as experimental reaction rate ratios, viz. C2/F9, F8/F9, F3/F9, C8/F9, F2/F9 and Th(n,2n) relative to C2, were measured near the centre of the axial blanket [202; 203]. In addition, the Th(n,2n) reaction rate, relative to the Th(n,γ) reaction rate, was measured at the core centre [192]. Furthermore axial reaction rate profiles along the central axis were measured for F9, C2, F2, C8 and F8, across the upper blanket/core interface and with normalization to unity at the core centre [120; 198; 204; 205].

Core 15: Lattice with a central Th-metal blanket

Core 15 was a modification of Core 13, in which an inner radial blanket of Th-metal rods was used instead of a ThO_2 zone. More specifically, there were 37 Th-metal rods of 19 mm diameter arranged in a hexagonal pitch of 21 mm in the central region of the (U,Pu)O_2 test lattice [120; 206].

Axially centered, radial reaction rate profiles for F9, C2, F2, C8, F8 and F3 (with normalization to unity at the core centre and going across the blanket/core interface) were measured [120; 207]. In addition, the Th(n,2n) reaction rate relative to the Th(n,γ) reaction rate was measured at the core centre [192].

Core 16: Lattice with an axial upper Th-metal blanket

Core 16 was a modification of Core 14, in which the upper axial blanket was a Th-metal lattice (see Table 3.1), and again the active length of the rods in the test zone had to be slightly reduced [120; 208; 198; 209]. The axial blanket zone was made of 469 rods of 35.6 mm active length.

The neutron spectrum and the reaction rate ratios C2/F9, F8/F9, F3/F9, C8/F9, F2/F9, as well as C7/F9 and F7/F9 and Th(n,2n) relative to C2, are available at the centre of the axial Th-metal blanket [210]. Furthermore, axial reaction rate profiles along the central axis were measured for F9, C2, F2, C8 and F8, across the upper blanket/core interface and with normalization to unity at the core centre [192]. In addition, the Th(n,2n) reaction rate relative to the Th(n,γ) reaction rate was measured at the core centre.

B. 3 Preliminary neutronics analyses

A. Reference computational scheme (RCS) for ERANOS-2.0

The reference computational scheme (RCS) for ERANOS-2.0, for the reference fuel MOX cell, is reviewed in this section.

A large number of computational options, as well as the two nuclear data libraries JECCOLIB2 and ERALIB1 [97], were assessed in order to assess the Reference Computational Scheme (RCS), relative to the experimental values. The sensitivity of the following neutronics parameters to the computational options was analyzed:

(1) leakage,
(2) captures,
(3) fissions,
(4) productions,
(5) (n,2n) reactions,
(6) buckling value,
(7) C8/F9,
(8) F8/F9,
(9) F5/F9,
(10) C2/F9,
(11) F2/F9,
(12) F3/F9,
(13) (n,2n)2/C2,
(14) C7/F9,
(15) F7/F9.

The results of these calculations, which were performed in the fundamental mode spectrum, i.e. in conjunction with a critical buckling search, are presented below.

The established RCS consists of performing ECCO [87] calculations in the broad-group structure with the library consisting of cross-sections in 172-neutron groups (XMAS structure), in association with the P1 option, and which is particularly accurate for a variety of applications ranging from the analysis of fast-spectrum to thermal-spectrum systems. In association with this scheme, it is possible to vary the nuclear data library (i.e. to use either the JECCOLIB2 library or the adjusted ERALIB1 library, both of which are based upon the JEF-2.2 nuclear data evaluation), as well as the treatment of the self-shielding. For the latter, there are two main possibilities: (1) reference route, (2) design route. In the reference route, the elastic scattering and the self-shielding are calculated in the fine 1968-group structure with the sub-group method. However, in the design route, the self-shielding is only calculated in the broad-group energy structure ECCO [87]. Table B.1 presents calculation results obtained by combining each nuclear library with a specific self-shielding treatment (which gives the four cases indicated in Figure B.2).

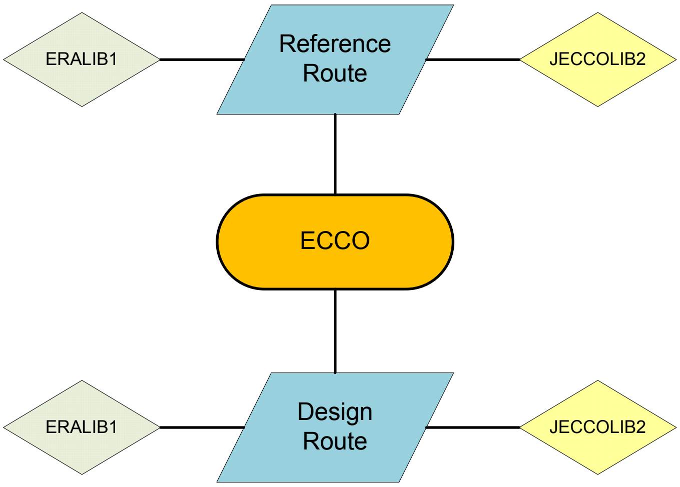

Figure B.2 Schematic representation of the main computational options in ECCO

Table B.1 Neutronics parameters calculated with the four computational schemes: (1) ERALIB1 and reference route, (2) ERALIB1 and design route, (3) JECCOLIB2 and reference route, (4) JECCOLIB2 and design route. The first column provides the values obtained with the first scheme, while the relative changes (%) are provided for the other three cases.

	ERALIB1, Ref.	**ERALIB1, Des.**	**JEC., Ref.**	**JEC., Des.**
Parameter	**Values**	**Rel. change, %**	**Rel. change, %**	**Rel. change, %**
Leakage	0.2144	0.37	-2.79	-2.41
Captures	0.3939	-0.20	1.17	0.96
Fissions	0.3944	0.00	0.34	0.34
(n,2n) reactions	0.0027	-0.09	-0.35	-0.44
B^2 (cm^{-2})	0.0013	0.49	-2.60	-2.10

In addition to the broad neutronics parameters presented in Table B.1, the differences in the neutron balance for the cell have also been investigated in greater detail. Using the RCS, the neutron spectrum of the MOX cell was calculated for both neutron libraries (ERALIB1 and JECCOLIB2), and the spectra are depicted in Figure B.3. Table B.2 details the reference case, i.e.

reference route in association with the ERALIB1 library, the cell flux being normalized to unit total productions. Table B.3 gives, for the other three cases, the relative changes of the macroscopic isotopic reactions, viz. captures (C), fissions (F) and productions (P).

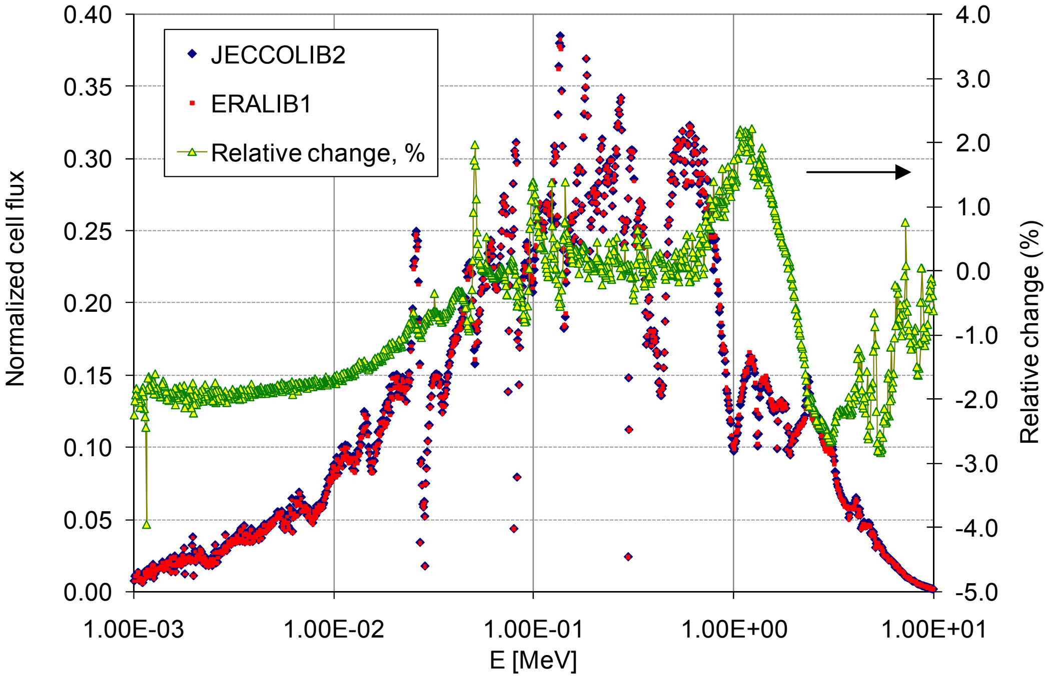

Figure B.3 Cell neutron flux in the fine energy structure for both libraries: ERALIB1 and JECCOLIB2

Table B.2 Detailed neutron balance of the cell with the reference route, in association with the ERALIB1 library, in terms of macroscopic isotopic reaction rates. For this case, values have been normalized to unit productions.

	REFERENCE ROUTE – ERALIB1 – XMAS					
Isotope	**Captures**	**%**	**Fissions**	**%**	**Productions**	**%**
O	2.84E-03	0.8	-	-	-	-
Al	6.51E-04	0.2	-	-	-	-
BdH	1.92E-06	0.0	-	-	-	-
^{235}U	2.11E-03	0.6	7.65E-03	2.2	1.90E-02	1.9
^{238}U	2.39E-01	70.1	5.81E-02	17	1.62E-01	16.2
^{239}Pu	6.17E-02	18.1	2.53E-01	74.0	7.48E-01	74.8
^{240}Pu	1.39E-02	4.1	1.37E-02	4.0	4.20E-02	4.2
^{241}Pu	1.57E-03	0.5	8.85E-03	2.6	2.64E-02	2.6
^{242}Pu	2.60E-04	0.1	2.13E-04	0.1	6.51E-04	0.1
^{241}Am	2.50E-03	0.7	4.82E-04	0.1	1.76E-03	0.2
^{54}Fe	1.72E-03	0.5	-	-	-	-
^{56}Fe	4.99E-03	1.5	-	-	-	-
^{57}Fe	4.83E-04	0.1	-	-	-	-
^{58}Fe	2.57E-05	0.0	-	-	-	-
^{50}Cr	2.91E-04	0.1	-	-	-	-
^{52}Cr	1.12E-03	0.3	-	-	-	-
^{53}Cr	6.27E-04	0.2	-	-	-	-
^{54}Cr	1.56E-05	0.0	-	-	-	-
^{58}Ni	3.11E-03	0.9	-	-	-	-
^{60}Ni	6.03E-04	0.2	-	-	-	-
^{61}Ni	7.36E-05	0.0	-	-	-	-
^{62}Ni	1.33E-04	0.0	-	-	-	-
^{64}Ni	1.43E-05	0.0	-	-	-	-
Mn	1.28E-03	0.4	-	-	-	-
Mo	1.74E-03	0.5	-	-	-	-
Si	3.30E-05	0.0	-	-	-	-
^{14}N	5.73E-05	0.0	-	-	-	-
^{15}N	1.79E-10	0.0	-	-	-	-
Total	3.41E-01	100.0	3.42E-01	100.0	1.00E+00	100.0

Table B.3 Changes (%), relative to the reference route with ERALIB1, of the normalized neutron balance components for the 3 remaining schemes, in terms of captures (ΔC), fissions (ΔF) and productions (ΔP)

	REFERENCE - JECCOLIB2			DESIGN – ERALIB1			DESIGN – JECCOLIB2		
Isotope	**ΔC, %**	**ΔF, %**	**ΔP, %**	**ΔC, %**	**ΔF, %**	**ΔP, %**	**ΔC, %**	**ΔF, %**	**ΔP, %**
O	65.56	-	-	-0.02	-	-	65.52	-	-
Al	1.08	-	-	-0.10	-	-	0.97	-	-
BdH	1.08	-	-	-0.05	-	-	1.02	-	-
^{235}U	-4.0	1.01	0.64	0.18	-0.06	-0.06	-3.95	0.94	0.58
^{238}U	0.41	2.50	1.92	-0.37	0.06	0.06	0.04	2.55	1.97
^{239}Pu	-2.14	-0.43	-0.65	0.19	-0.03	-0.04	-1.97	-0.47	-0.69
^{240}Pu	12.00	3.69	2.34	-0.12	0.40	0.39	11.84	4.11	2.75
^{241}Pu	21.70	2.46	2.43	0.11	-	-	21.77	2.45	2.42
^{242}Pu	13.82	5.75	5.76	0.46	0.62	0.60	14.27	6.41	6.40
^{241}Am	0.67	0.19	0.26	-0.08	0.38	0.36	0.59	0.59	0.64
^{54}Fe	1.39	-	-	-0.66	-	-	0.72	-	-
^{56}Fe	-1.46	-	-	0.31	-	-	-1.18	-	-
^{57}Fe	1.46	-	-	3.73	-	-	5.23	-	-
^{58}Fe	0.82	-	-	-0.51	-	-	0.25	-	-
^{50}Cr	1.53	-	-	-0.63	-	-	0.89	-	-
^{52}Cr	-2.69	-	-	2.35	-	-	-0.27	-	-
^{53}Cr	1.51	-	-	-0.22	-	-	1.27	-	-
^{54}Cr	0.65	-	-	-2.99	-	-	-2.34	-	-
^{58}Ni	16.39	-	-	-0.38	-	-	15.93	-	-
^{60}Ni	0.76	-	-	0.61	-	-	1.39	-	-
^{61}Ni	1.08	-	-	-2.05	-	-	-1.02	-	-
^{62}Ni	0.67	-	-	-0.69	-	-	-0.04	-	-
^{64}Ni	0.47	-	-	-0.36	-	-	0.09	-	-
Mn	1.23	-	-	3.50	-	-	4.79	-	-
Mo	0.97	-	-	-0.08	-	-	0.88	-	-
Si	0.86	-	-	-0.14	-	-	0.71	-	-
^{14}N	0.92	-	-	0.28	-	-	1.21	-	-
^{15}N	2.41	-	-	0.11	-	-	2.52	-	-

The calculations provided in this section have allowed one to assess the important calculational options in ECCO. In particular, it has been shown that:

(1) The computational route (reference or design) does not significantly impact the neutronics results, the differences being in the range of 0.3% (see Table B.1). The highest difference is obtained for the buckling value (0.5%).

(2) The neutron library (ERALIB1 or JECCOLIB2) has a higher impact on the neutronics parameters of interest in this study. In particular, the leakage is lower (by ~2%) when calculated with JECCOLIB2 compared to ERALIB1 (see Table B.1). The buckling value is correspondingly smaller (by ~2.5%).

(3) The neutron balance results provided in Tables B.2 and B.3 show again the low impact of the computational route. A good consistency is obtained for the main isotopes (U,Pu) while the differences are higher (n the range of 3%) for structural materials such as ^{57}Fe, ^{54}Cr, Mn.
(4) The effect of the nuclear data shows a significantly higher sensitivity to a broad range of isotopes (see Table B.3). The relative capture rate differences for the main isotopes are high with values up to 22% (^{241}Pu). Large differences are also obtained for oxygen (66%) and ^{58}Ni (16%) capture.
(5) The effects of the nuclear data adjustment on the neutron spectrum are depicted in Figure B.3. Particularly visible are the differences in the lower and higher energy regions.

B. Sensitivity calculations

As previously mentioned, the RCS was defined, based on preliminary calculations performed to assess the neutronics results sensitivity to the modeling and computational options. Specifically, the following options were tried out, and the results are presented below:

(1) Cell modeling: hexagonal vs. cylindrical model, to assess the geometrical effects.
(2) Aluminum nuclear density. In the GCFR-PROTEUS literature, certain inconsistencies have been found in the reported aluminum densities.
(3) Hydrogen nuclear density. Moisture content is difficult to measure accurately. Since hydrogen moderates neutrons strongly, the effect of the hydrogen nuclear density on the reaction rate ratios was assessed.
(4) ECCO code verification against BISTRO. The calculations for the fundamental mode spectrum are performed with the cell code ECCO. A verification was carried out using the SN code BISTRO.
(5) The sensitivity to the buckling value was evaluated for the fundamental mode calculation.

Cell modeling: hexagonal vs. cylindrical

A test performed was the comparison between the hexagonal fuel cell geometry and a simplified geometry with an equivalent cylindrical cell, i.e. implying only an adjustment to the size of the outermost air region with respect to the cell volume. The results showed that there are no differences in the reaction rate ratios calculated with the two models. This is mainly due to the fact that only the coolant zone is affected, in which the diffusion length is very large.

Sensitivity to Al and H nuclear densities

Sensitivity studies were performed by varying the material compositions, in particular the hydrogen density in the outermost cell region and the aluminium density within the fuel region. The reason for this study was that some of the material nuclear densities were not precisely known, and large uncertainties have been reported. Based on this observation, the influence of the density of these two materials was examined on the computed k_∞ and on the resulting C/E-values for the three important reaction-rate ratios (C8/F9, F8/F9 and F5/F9). The calculations were performed, by varying the material content beginning with the original material composition. In both cases, the sensitivity was assessed from two calculations based upon the design route and ERALIB1 cross-sections: (1) in the first calculations, the original density was preserved and (2) in the second calculation, the material was simply removed**.**

Results show (see Table B.4) that, for Al, there is almost no discrepancy between the two cases (i.e. with and without Al), with relative discrepancies of less than 0.2 % in the C/E-values, these discrepancies being much less than the 1σ experimental uncertainty (see Table 3.2). It should be mentioned that the principal reason for this sensitivity calculation was the fact that there was physically no aluminum in the fuel itself, the specified Al density in the model corresponding to the homogenizing scheme for the thin Al-cladding of the "cigars".

Table B.4 Comparison of reaction rate ratios (C/E) and k_∞ calculated with and without the original density of Al within the fuel

Ratio	With Al C/E	Without Al C/E	Rel. change, %
C8/F9	0.988	0.986	-0.17
F8/F9	1.036	1.038	0.19
F5/F9	0.99	0.989	-0.08
	Value	Value	Change, pcm
k_∞	1.4713	1.4731	183

For hydrogen, the measure of uncertainty on the nuclear density in the outer cell region was high, since it was related to the assessed moisture content of the air. Hydrogen affects the neutron spectrum, and therefore k_∞. The results of the sensitivity study are presented in Table B.5. Based upon the results, the difference between the calculations is seen to be higher than that due to the aluminum content, but still smaller than the 1σ experimental uncertainty in the case of the reaction rate ratios.

Table B.5 Comparison of reaction rate ratios (C/E) and k_∞ calculated with and without the original hydrogen density in the outermost cell region

Ratio	With H C/E	Without H C/E	Rel. change, %
C8/F9	0.988	0.987	-0.059
F8/F9	1.036	1.04	0.407
F5/F9	0.99	0.98	-1.003
	Value	Value	Change, pcm
k_∞	1.4713	1.48091	961

ECCO verification against BISTRO

In the case of the PROTEUS whole-reactor calculations (see Section B.4), the reaction rate ratios were computed using the RZ-geometry, transport-theory code BISTRO. It was thus of interest to check the consistency between reaction rates calculated directly from the cell code ECCO and from BISTRO (while simulating the same boundary conditions for the cell).

For this calculation, broad-group (33 groups) cross-sections for the homogenized cell were prepared with ECCO using the cylindrical cell model, which constitutes the first step of the verification. In a second step, an equivalent homogeneous (cylindrical) 1D model was set up to yield $k_{eff}=1$ by adjusting the radius, the critical value being r=62.15 cm (see Figure B.4).

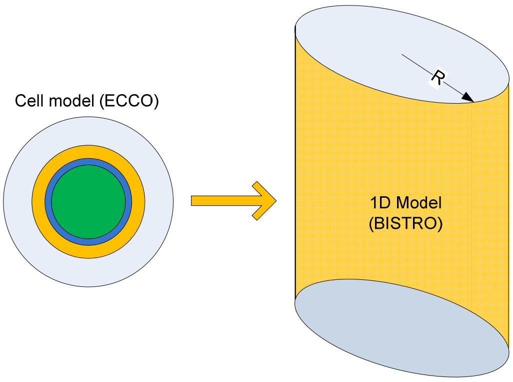

Figure B.4 Schematic of the 1D model, used in conjunction with BISTRO, to check the sensitivity of the reaction rate ratios to the methods (ECCO or BISTRO)

More specifically, this model was used with BISTRO, in conjunction with the macroscopic cross-sections obtained from ECCO. The numerical approximations used in BISTRO were P_1 for the anisotropy of scattering and S_8 for the angular discretization of the flux. Finally, the reaction rates were computed by calculating traverses across the model. The comparison with values obtained with ECCO is given in Table B.6 and no discrepancies are observed, confirming the non-sensitivity to the methods. One can thus analyze the GCFR-PROTEUS experiments using either ECCO or BISTRO calculations.

Table B.6 Relative changes (%) in reaction rate ratios as calculated with ECCO (E) and with BISTRO (B)

Ratios	Δ(B-E)/E, %
C8/F9	-0.08
F8/F9	0.19
F5/F9	-0.06

Fundamental mode and infinite-lattice cell calculations

Since the PROTEUS reactor was critical during the experiments, the calculations need to be performed for a cell in its fundamental mode. This is an approximation, since the fast zone is not critical without contributions from the surrounding thermal zones. Nevertheless, the cell of interest was located at the centre of the fast zone, where the spectrum discrepancy is small.

A calculation was performed to examine if the reactions rate ratios were sensitive to the reactivity level of the cell. For this purpose, calculations were done both for the infinite lattice (k_{eff}=1.36) and for the fundamental mode. The results are provided in Table B.7.

Table B.7 Relative changes (%) between infinite-lattice (I) and fundamental mode (F) cell calculations. Also provided in the last column is the relative difference (%) with respect to the 1σ experimental uncertainty.

Ratios	Δ(I-F)/F, %	$|\Delta\text{-}1\sigma_{exp}|$ /$1\sigma_{exp}$, %
C8/F9	9.5	449
F8/F9	-23.7	1758
F5/F9	4.0	173

The conclusion from these results is that the reaction rate ratios are significantly dependent on the criticality level of the cell, which was expected. As a direct consequence, calculations have to be performed in the fundamental mode spectrum, in order to take leakage effects adequately into account for comparison with the experimental data. This result is of importance for the Monte Carlo calculations, for which the cell model was adjusted to obtain k_{eff} close to 1.

Conclusions on sensitivity calculations

Based on the results obtained, one may make the following statements:

(1) The neutronics results of interest are not sensitive to the cell modeling (hexagonal vs. cylindrical).

(2) There is no significant sensitivity of the main reaction rate ratios to the Al-density in the fuel region, the relative differences being in the range of 0.2%.

(3) A higher sensitivity, viz. in the range of 1%, is observed to the hydrogen content in the outermost cell region.

(4) There is no significant effect of using the BISTRO code, instead of ECCO itself, for the fundamental-mode cell calculations, the maximal difference being 0.2% for the F8/F9 ratio.

(5) The reaction rate ratios depend on the criticality level. This clearly indicates that, for the MCNPX calculations, the cell height has to be carefully adjusted to have a critical cell.

C. Reference Computational Scheme (RCS) in MCNPX

The stochastic code MCNPX version 2.5e [101] has been used to study the nuclear data library sensitivity, as well as for benchmarking the ECCO calculations against Monte Carlo results, which can be considered as reference. Prior to the analysis (presented in Section 3.3), a MOX cell model was developed for use with MCNPX.

Supplementary verifications were performed to check the consistency of the analysis. The same strategy as for ECCO calculations was used, i.e. several computational options (mainly, the cell boundary conditions and the geometry modeling in this case) were tested and the results compared. Based on the sensitivity of the reaction rate ratios with respect to these options, a reference MCNPX computational scheme (RCS) was defined and then used to compute the reference values presented in Section 3.3. The preliminary tests as well as the final computational scheme are presented below.

The calculations were performed with different modern nuclear data libraries:

(1) JEF-2.2,
(2) JEFF-3.0,
(3) ENDF/B-VI.r8,
(4) JENDL-3.3.

Fuel cell modeling and boundary conditions

The first verification was a check on the cell's radial boundary conditions, with the axial height adjusted in each case to produce a k_{eff} of unity.

There are two different options, namely the "white" and "mirror" conditions in MCNPX. The "mirror" condition corresponds to the situation of a neutron reaching the cell boundary and then back into the cell with a randomly chosen angle. The "white" boundary condition considers a reflective direction (angle conservation). To illustrate the sensitivity of the reaction rate ratios with respect to these boundary conditions, a MCNPX test case was performed using the JEF-2.2 library. Table B.8 provides the results.

It is worth mentioning that the calculations have been performed in all cases with a fixed initial fission source. Furthermore, sufficient particle histories have been run to obtain reaction rates for which the 1σ is less than 0.2 %. The propagated uncertainty on the reaction rate ratios is therefore less than 0.4 %. For the following MCNPX results, one may assume that the 1σ uncertainty on the reaction rate ratios is 0.4 %, unless different values are specified.

Table B.8 Comparison of reaction rate ratios (C/E) calculated with "white" (W) and "mirror" (M) boundary conditions; MCNPX with the JEF-2.2 data library

Ratios	C/E, white	C/E, mirror	(M-W)/M, %
C8/F9	0.973	1.000	2.7
F8/F9	1.083	1.038	-4.3
F5/F9	0.971	0.986	1.5

It is seen that the “white” condition gives results, which are far away from the experimental values, i.e. the discrepancies are about 3 % (~$2\sigma_{exp}$) for C8 and F5 (relative to F9), and 8 % for F8, while better agreement is obtained with “mirror” boundary conditions.

The above calculations were repeated with two other libraries, namely JEFF-3.0 and ENDF/B-VI.r8, and the results are presented in Table B.9.

Table B.9 Changes (%) of the reaction rate ratios with “white” and “mirror” boundary conditions (relative to the JEF-2.2 results of Table B.8) when using the JEFF-3.0 and ENDF/B-VI.r8 libraries.

“white”	Rel. change with JEFF-3.0, %	Rel. change with ENDF/B-VI.r8, %
C8/F9	1.83	-5.49
F8/F9	1.53	3.43
F5/F9	2.00	-1.66
“mirror”	**Rel. change with JEFF-3.0, %**	**Rel. change with ENDF/B-VI.r8, %**
C8/F9	1.53	-4.73
F8/F9	1.73	2.77
F5/F9	1.79	-1.14

From the above, it is seen that the library effects are very similar when considering either “white” or “mirror” boundary conditions. In other words, the differences between the results obtained using the two different boundary conditions are approximately the same for each of the three libraries used.

Required accuracy on cell criticality

It was shown that the reaction rate ratios depend significantly on the cell criticality level. To establish this dependence, the three principal reaction rate ratios were calculated for two different reactivity levels, which were selected in an arbitrary manner; the first cell had k_{eff} =0.9999 and the second k_{eff} =1.0972. The reactivity level was varied by changing the cell height, and the results of the calculations are given in Table B.10.

Table B.10 Relative changes $\Delta R=(R_2-R_1)/R_1$ (%) in the 3 principal reaction rate ratios between two calculations: (1) k_{eff}=0.9999 (R_1) and (2) k_{eff}=1.0972 (R_2)

Reaction	ΔR, %
C8/F9	+3.3
F8/F9	-7.2
F5/F9	+1.7

Based on these results, and using a linear dependence for the most sensitive reaction rate ratio (F8/F9), it was decided that k_{eff} should be within ± 150 pcm of unity, in order to avoid any significant dependence on the reactivity level.

"Infinite-lattice" geometry

Due to the sensitivity observed with the boundary conditions, a test case without user-specified reflective radial boundary conditions for the cell was considered. For that purpose, a cylindrical geometry with the fuel rods arranged in a hexagonal lattice was created. This is called "infinite-lattice" geometry here. The radius of the cylinder was adjusted until the k_{eff} of the system was close to 1, and Table B.11 compares the C/E results for the reaction rate ratios with those for the two different cell calculations.

Table B.11 Comparison of reaction rate ratios (C/E) calculated using the "infinite-lattice" geometry (IL) with those from the "white" and "mirror" cell calculations; MCNPX with the JEF-2.2 library. The associated 1σ statistical error for IL is somewhat less than 0.6%.

Ratios	IL C/E	Mirror Rel. change, %	White Rel. change, %
C8/F9	1.023	-2.2	-4.8
F8/F9	1.020	1.8	6.2
F5/F9	0.996	-1.0	-2.6

It is seen that, within the statistical accuracies for the IL case, the reaction rate ratios are in good agreement with those obtained using "mirror" boundary conditions. This confirms the adequacy of the latter for serving as the reference cell model to be used.

Cell height adjustment

The procedure of adjusting the cell height (MCNPX) is for achieving the fundamental mode spectrum (k_{eff} =1) for the cell. It effectively corresponds to performing a "buckling search". As an illustration, the total cell height for k_{eff} ~ 1 is provided for the different libraries in Table B.12. The results are seen to be quite consistent.

Table B.12 Total height of the cell in order to have k_{eff} close to 1.

	JEF-2.2	JEFF-3.0	ENDF/B-VI.r8	JENDL-3.3
Cell height, cm	39.7	40.1	39.1	39.8

Instead of adjusting the cell height as presented above, it is also possible to consider a fixed cell height, e.g. H=39.7 cm, the critical JEF-2.2 value. In this situation, the k_{eff} of the cell is slightly different from one calculation to another, when considering different libraries. A comparison of the effects of using the JEF-2.2 critical-cell height on the principal reaction ratios for the three other libraries is shown in Table B.13. Discrepancies of up to 0.5 % are seen, mainly for F8/F9, but the differences remain less than the 1σ experimental uncertainty.

Table B.13 Relative changes (%) in the reaction rate ratios when calculated with the JEF-2.2 critical-cell height of H=39.7, for the nuclear data libraries JEFF-3.0, ENDF/B-VI.r8 and JENDL-3.3.

Ratios	JEFF-3.0 Rel. Change, %	ENDF/B-VI.r8 Rel. change, %	JENDL-3.3 Rel. change, %
C8/F9	0.12	-0.24	-0.15
F8/F9	-0.48	-0.51	0.23
F5/F9	0.06	0.20	-0.05

As a result of the various sensitivity studies carried out, the final MCNPX calculations have all been performed using the reference cell model with “mirror” boundary conditions and the library-dependent critical height.

B. 4 Independent check on correction factors

The correction of the reaction rate ratios measured in the GCFR-PROTEUS reference lattice, to “fundamental mode” values (see Section 3.2), has been carried using the correction factors given in the original literature. In order to provide an independent check on the magnitude of these corrections, a simplified 2D model of the whole reactor was set up and is described in this section. The configuration corresponds to GCFR-PROTEUS Core 11, as referred to in the original literature (see Section B.2).

A. The whole-reactor model

The 2D-RZ model of the quasi-cylindrical PROTEUS reactor is made of concentric regions filled with homogeneous materials for the zones surrounding the central fast zone (see Figure 3.2). The correspondence between the regions and the material names can be found in Table B.14, in which the various zone dimensions in terms of (RZ) coordinates are also given. Finally, Table B.15 provides the material nuclear densities of the different zones. These have been described as homogenized regions, except for the central MOX fast-spectrum test zone and the UO_2 axial blankets, for which detailed descriptions are provided.

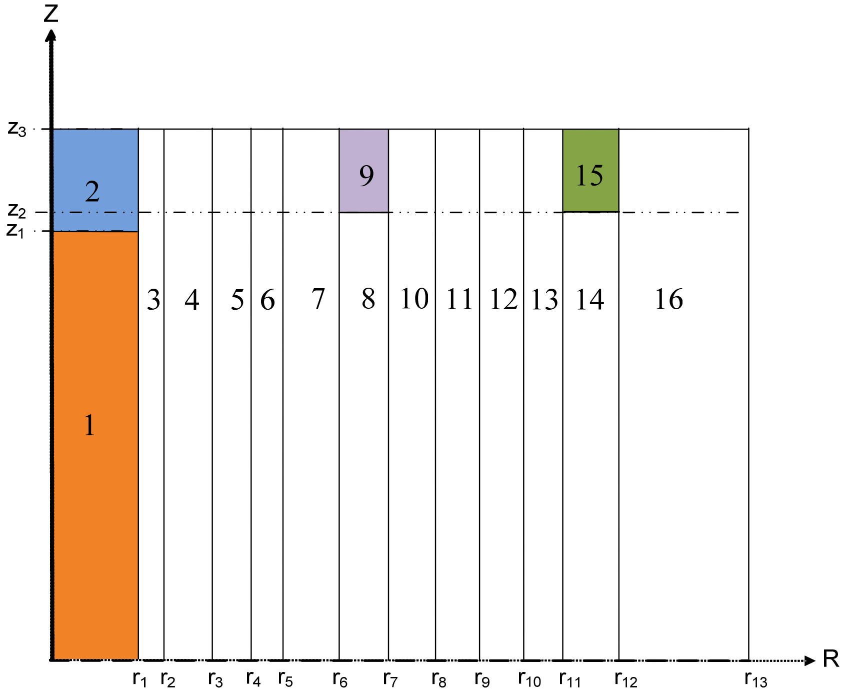

Figure B.4 A simplified RZ Model of the reference GCFR-PROTEUS reactor configuration. The model is symmetrical with respect to the radial and axial axes. All regions, labelled by a number on the picture, are presented in Table B.14. Note that the drawing is not to scale.

Table B.14 Dimensions and materials of the zones in Figure B.4

(r_i, z_i)	**R (cm)**	**Region**	**Material**
r_1	24.475	1	$(U,Pu)O_2$
r_2	26.343	2	UO_2 blanket
r_3	36.311	3	Steel + Air
r_4	38.300	4	U-met buffer
r_5	38.800	5	Air
r_6	40.018	6	Al
r_7	57.022	7	D_2O
r_8	61.300	8	D_2O driver
r_9	61.800	9	D_2O
r_{10}	62.828	10	D_2O
r_{11}	68.759	11	Al
r_{12}	78.800	12	Air
r_{13}	161.800	13	Low-density C
	z, cm	14	C-driver
z_1	44.450	15	C-reflector
z_2	46.050	16	C-reflector
z_3	69.100		

Table B.15 Material densities. The fast-spectrum regions are described in detail details (rod geometry), while homogeneous material densities are given for the other zones.

Material name	Inner-structure name	Inner-structure dimension (mm)	Isotopes	Concentration ($\cdot 10^{24}$ cm^{-3})
(U,Pu)O_2	MOX	3.350	^{235}U	8.26E-05
			^{238}U	1.95E-02
			^{239}Pu	2.74E-03
			^{240}Pu	6.05E-04
			^{241}Pu	7.31E-05
			^{242}Pu	1.33E-05
			^{241}Am	2.79E-05
			O	4.62E-02
			Al	3.91E-04
			H	2.13E-04
	Al	3.498	Al	3.50E-02
	Steel	4.100	Fe	3.94E-02
			Cr	1.05E-02
			Mo	7.26E-04
			Mn	1.49E-03
			Ni	6.05E-03
			Si	5.70E-04
	Air	5.250	O	1.02E-05
			Al	5.56E-04
			N	3.78E-04
UO_2 blanket	Fuel	3.350	^{235}U	9.85E-05
			^{238}U	2.33E-02
			O	4.67E-02
			Al	3.83E-04
	Inner Al	3.498	Al	3.50E-02
	Steel	4.100	Fe	3.94E-02
			Cr	1.05E-02
			Mn	1.49E-03
			Ni	6.05E-03
			Si	5.70E-04
			Mo	7.26E-04
	Outer Al	5.250	Al	5.56E-04
Steel + Air			Fe	4.53E-02
			C	4.23E-04
			N	1.77E-05
			O	4.75E-06
U-met buffer			^{235}U	2.20E-04
			^{238}U	3.03E-02

		Al	8.06E-03
Air		N	3.82E-05
		O	1.03E-05
Al		Al	5.84E-02
D_2O		O	3.28E-02
		Fe	1.08E-06
		Al	7.36E-04
		H	1.12E-03
		D	6.45E-02
D_2O driver		^{235}U	2.62E-05
		^{238}U	4.95E-04
		O	3.28E-02
		Fe	1.08E-06
		Al	1.15E-03
		H	1.08E-03
		D	6.24E-02
C low density		C	7.51E-02
C-driver		^{235}U	1.93E-05
		^{238}U	3.63E-04
		O	7.66E-04
		Al	3.03E-04
		N	3.55E-07
		C	7.79E-02
C-reflector		C	8.82E-02

B. Calculation of correction factors

The first step was running the transport-theory BISTRO module of ERANOS with the 2D RZ model of PROTEUS, using 33 broad-group cross-sections processed with ECCO. In particular, the cross-sections for the thermal-spectrum driver zones were derived using the 172 groups structure (XMAS), since the thermal energy range in this group structure is better described and neutron up-scattering is accounted for. Based on the whole-reactor calculations, the reaction rate ratios of interest were evaluated at the centre of the test zone.

The second step was carrying out fundamental-mode calculations for the reference MOX cell, using the same 33-group cross-sections as used for the test zone in the BISTRO model. Using the calculated reaction rate ratios for the critical cell, the various “new” correction factors could be deduced. Table B.16 gives the results obtained, alongside the originally reported values (which, as mentioned, are the ones actually used in the current GCFR-PROTEUS re-analysis). Figure B.5 provides a graphical comparison of the different values.

Table B.16 The newly computed correction factors for the different reaction rate ratios, along with the values actually used (from the original literature) and the 1σ experimental uncertainties

Relative reaction rates	1σ (%)	Used correction factor	New correction factor
C8/F9	1.2	0.994 ± 0.5 %	1.007
F8/F9	1.4	0.974 ± 0.5 %	0.962
F5/F9	1.5	1.004 ± 0.5 %	1.010
C2/F9	1.4	1.022 ± 0.5 %	1.036
F2/F9	2.1	0.979 ± 0.5 %	0.962
(n,2n)2/C2	2.6	0.973 ± 0.5 %	0.949
F3/F9	1.4	1.027 ± 0.5 %	1.009
C7/F9	2.5	1.020 ± 1.0 %	1.032
F7/F9	2.1	0.975 ± 1.0 %	0.963

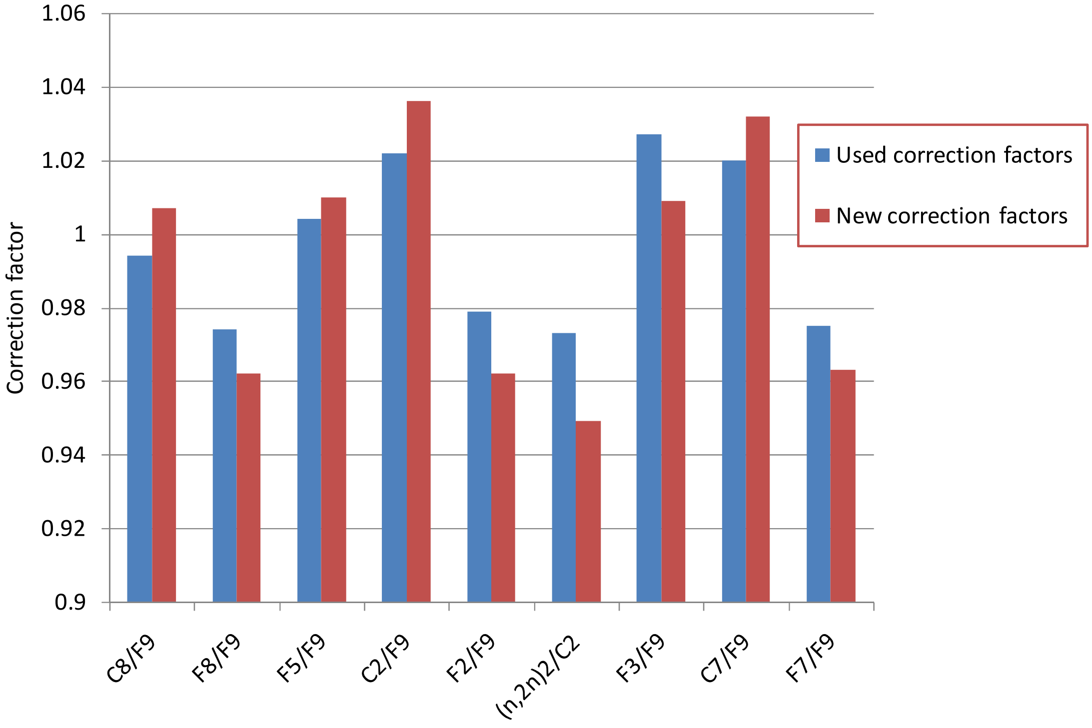

Figure B.5 Newly computed correction factors compared to the values actually used (from the original literature)

It is seen that the newly computed correction factors match the actually used (original) values mostly within three standard deviations. Bearing in mind that a value of three here corresponds, more or less, to the ratio of the 1σ experimental uncertainty to the standard deviation of the correction factor, the agreement can be considered satisfactory. Effectively, the differences between “corrected” reaction rate ratios remain within the experimental 1σ uncertainties, when using the two different sets of correction factors.

Appendix C

C. Supplementary studies for the CA pattern development

C. 1 Sensitivity studies for the ERANOS calculations

A. Nuclear data library

Table C.1 presents the eigenvalues and CA worths calculated by ERANOS using the two available nuclear data libraries: JECCOLIB2 and ERALIB1. It is seen that the eigenvalue is always lower with the JECOLIB2 library, but the trend is reversed for the CA worth, resulting from compensatory effects, with an average difference of only +48 pcm (compared to ERALIB1 values). As a conclusion, there is limited sensitivity (in the range of +0.3%) regarding the choice of the nuclear data library for the CA worth. Similar checks were performed using the JEFF-3.1, instead of the ERALIB1 data set, JEFF-3.1 being the latest nuclear data library available in ERANOS-2.1.The same order of magnitude was observed regarding the differences in eigenvalues [78].

Table C.1 Eigenvalue and CA worths calculated with the ERALIB1 and JECCOLIB2 (JEF-2.2) nuclear data libraries. Calculations were performed with the HEX-Z Model for "cold" conditions. The differences are expressed with respect to the ERALIB1 results.

	Core Reactivity, pcm		CA Worth, pcm		Differences	
Core Configuration	**ERALIB1**	**JECCOLIB2**	**ERALIB1**	**JECCOLIB2**	**Reactivity, pcm**	**Worth, pcm**
All CAs withdrawn	8647	8428	-	-	-219	-
All CSDs inserted	-6951	-7256	15598	15684	-305	86
1st bank inserted	6275	6019	2372	2409	-256	37
2nd bank inserted	2595	2354	6052	6074	-241	22

B. Operating conditions

CA worths

The impact of the operating conditions on the reactivity worths was assessed by means of two direct calculations:

(1) "Cold" conditions, i.e. temperature of 20°C for all materials,
(2) Operating conditions, i.e. "hot" conditions (see Table 4.2).

The results are summarized in Table C.2. From the first considered configuration, it is seen that a positive change of 2363 pcm in reactivity is obtained when going from "hot" to "cold" conditions, due to combined Doppler and thermal expansions effects. There is no large impact (in the range of ± 100 pcm) on the CA worth.

Table C.2 CA worth sensitivity to operating conditions. Calculations performed with the HEX-Z Model. The differences are expressed with respect to "hot" conditions.

	Core Reactivity, pcm		CA Worth, pcm		Differences, pcm	
Core Configuration	Hot	Cold	Hot	Cold	Reactivity	Worth
All CA withdrawn	6284	8647	-	-	2363	-
All CSDs inserted	-9178	-6951	15462	15598	2227	136
1st CSD bank inserted	3991	6275	2293	2372	2284	79
2nd CSD bank inserted	120	2595	6164	6052	2475	-112

Doppler reactivity

In the context of the determination of the reactivity needs for the GFR and for the transient studies, the Doppler reactivity effect ($\partial\rho = \rho_{operating\ conditions} - \rho_{isothermal,180°C}$) was computed, and a relatively large sensitivity (~20%) of this value to the CA positions was observed. Selected results are given in Table C.3. These results indicate that the flux distributions within the core (radially) are modified by the CA insertion, thus affecting the reaction rates, which in turn influence the reactivity. Considering that the Doppler effect is the main reactivity feedback in the GFR, the need for employing spatial kinetics in the context of CA-driven transients is thus clearly underlined (see Chapter 5).

Table C.3 Doppler reactivity effect for three core configurations: (1) CAs fully withdrawn (parking position), (2) CAs half inserted and (3) CAs fully inserted.

Configuration	Doppler Reactivity, pcm
CAs withdrawn	1657
CAs half-inserted	1533
CAs inserted	1307

C. Diffusion vs. transport theory

The impact of using either diffusion or transport theory, in association with the RZ BISTRO model, has been assessed. Table C.4 provides the results for the eigenvalues and the corresponding CA worths for the considered configurations.

In this case, large discrepancies are observed, e.g. the eigenvalue in the "all CAs withdrawn" configuration is lower by 1050 pcm for the diffusion theory result. It is also seen that the discrepancy is dependent on the CA positions, e.g. the difference is -2087 pcm in the "all CSDs inserted" configuration.

Table C.4 CA-worth sensitivity to the use of the transport or diffusion theory approximation in BISTRO, considered using the RZ model for operating conditions. The differences are expressed with respect to the transport theory results.

	Core Reactivity, pcm		CA Worth, pcm		Differences, pcm	
Core Configuration	Transp.	Diffusion	Transp.	Diffusion	Reactivity	Worth
All CAs withdrawn	6935	5885	-	-	-1050	-
All CSDs inserted	-11583	-13670	18518	19555	-2087	1037
1st CSD bank inserted	4287	3165	2648	2720	-1122	72
2nd CSD bank inserted	736	-503	6199	6388	-1239	189

D. Modeling: HEX-Z vs. RZ

The impact of the core modeling on the CA worth has also been assessed in terms of differences between transport theory results obtained using the RZ BISTRO/P1S16 model and the HEX-Z VARIANT model (nodal method “601”), both calculations being performed for operating ("hot") conditions. The comparative results are presented in Table C.5.

A large sensitivity is observed, both for the eigenvalue (+651 pcm) and the CA worth (~+20%) between the RZ with the HEX-Z results. Additional investigations were performed to see if the large discrepancy in reactivity was due to the CA modeling. It was found, for example, that the reactivity difference for a core without CAs is reduced to about +217 pcm, underlining the significant sensitivity to the presence of CAs. These results confirm a recent study [78].

Table C.5 CA-worth sensitivity to the use of the RZ and the HEX-Z models, both for operating conditions. The differences are expressed with respect to the results with the HEX-Z model.

	Core Reactivity, pcm		CA Worth, pcm		Difference, pcm	
Core Connfiguration	HEX-Z	RZ	HEX-Z	RZ	Reactivity	Worth
All CA withdrawn	6284	6935	-	-	651	-
All CSDs inserted	-9178	-11583	15462	18518	-2405	3056
1st CSD bank inserted	3991	4287	2293	2648	296	355
2nd CSD bank inserted	120	736	6164	6199	616	35

The two sets of results reported in Tables C.4 and C.5 provide clear indication that the calculational methodology is very important for CA-worth calculations. In the context of the transient calculations of hypothetical CA withdrawals, performed with the nodal diffusion code PARCS (see Chapter 5), benchmarking of the model has been performed in a systematic manner in order to assess the methods effect in an adequate manner (see Chapter 5, Section 5.2).

E. Computational options

A systematic verification of the computational options was carried out. In particular, the mesh size in the core geometry was investigated, and no significant discrepancies observed.

Rather large meshes (10 cm) have been considered as the reference mesh size for nodal calculations. In BISTRO, smaller meshes, in the range of 2-3 cm, have been used. The nodal transport calculation options in VARIANT were tested as well. It is recommended to use, for relative reactivity worth calculations the set “601” [127], which gives a good compromise between the CPU-time and the results accuracy for the calculation of CA worths (see Section 4.2.4).

The transport-options testing, in a limited range, is shown in Table C.6 for a core configuration with all CAs in the parking position. The flux development within the node was varied from order 5 to 6, the source development from order 0 to 2, and the flux development at the node interface from 0 to 5. From the results, it is observed that there is a rather limited sensitivity (a total of 45 pcm) for the core reactivity, relative to the reference set “601” (CPU-time of ~ 0.4 hr), while the CPU-time and the memory required gets very large.

Table C.6 Reactivity sensitivity to the nodal transport options in VARIANT, CAs in the parking position and core with operating conditions. The reactivity differences, relative to the reference options, are given for the two extreme cases, i.e. the maximal and minimal differences compared to the set “601”.

Case	Transp. options	Reactivity difference, pcm	CPU-time, hrs
Max	"502"	-25	~0.5
Min	"615"	20	~18

F. Verifications of the homogeneous cell treatment in ECCO

As mentioned earlier, the plate-type GFR sub-assembly is highly innovative, which is challenging for existing neutronic tools developed for traditional fuel pin designs. In the reference calculational scheme used in ERANOS-2.0, the fuel double heterogeneity, i.e. the pellet within the honeycomb structure and the fuel plate within the SA, is not taken into account at the level of the cell treatment. The cell calculation is performed for the homogeneous material mixture.

A limited verification of the homogeneous treatment has been performed at CEA-Cadarache, using the newly implemented plate-geometry option in ECCO included in ERANOS-2.1 [127]. For the purpose of the verification, only one heterogeneity level was addressed, i.e. the fuel plate within the SA, the ECCO modeling being carried out with homogenized fuel plates. Based on the results obtained, it was found that the plate geometry and the corresponding material temperature distribution, together induce a net negative core reactivity effect of 72 pcm. This indicates that the homogeneous treatment of the fuel plate, along with the adoption of the fuel temperature as the “homogeneous” temperature - which is the basis for the reference computational scheme (RCS) - yields reactivity values which are in good agreement with a more sophisticated treatment.

C. 2 Analysis of the heat generation for the ETDR startup core

The robustness of the procedure developed in ERANOS-2.0 to calculate the CA heat generation was tested by applying it to another core configuration, viz. the ETDR startup core

[67; 68], the ETDR being a He-cooled GFR prototype of 50 MWth with a power density of 100 MW.m^{-3}.

A RZ model of the startup core was considered, with a homogeneous description of the two envisaged CA "banks" (see Figure C.1):

1. A unique and central DSD assembly, shown in red in Figure C.1, containing 26.3%vol. boron at 90%-^{10}B.
2. CSD assemblies, of the EFR-type, design studies for which have not being performed to the present time.

All CAs were inserted at 33% in the situation studied. The average volumic heat generation calculated for the central DSD CA (see Table C.7) was P = 10.2 W.cm^{-3}, a value only about 4 % lower than the results presented in [68], for which the Monte Carlo code TRIPOLI4 was employed. This good agreement provides further confirmation of the currently used, HG assessment methodology for the GFR CAs.

Table C.7 Heat generation within the central DSD assembly of the ETDR startup core

Parameter	33% insertion
Integrated power, kW	33.0
Volume of absorber, cm^3	3.24E+03
Average volumic power density , W/cm^3	10.2
Gamma power density, W/cm^3	1.75
Gamma fraction, %	17.7

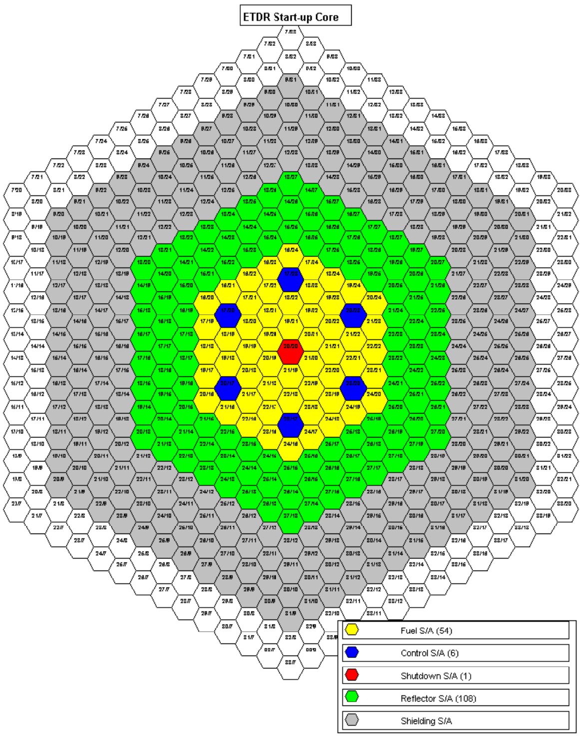

Figure C.1 Schematic of the ETDR startup core

C. 3 CA worth correction by perturbation theory

In ERANOS, the reactivity equivalence method requires the use of a specific procedure [147] to calculate the CA worth.

An iterative algorithm is used to compute equivalent cross-sections (by means of a fine 2D XY CA model surrounded by fuel) that gives the same CA worth as that obtained from a homogeneous CA description in the whole-core calculation. Finally, the algorithm produces the correction factors to be applied to the macroscopic cross-sections obtained with the homogeneous approach.

From a theoretical point of view, the method solves the Boltzmann equation, both with the homogeneous and the heterogeneous CA modeling. The forward flux Φ is the solution of the Boltzmann equation:

$$\left(A-\frac{F}{k}\right)\Phi = 0 \qquad \text{Eq. C.1}$$

where the operator *F* accounts for the production term and the operator *A* for all remaining terms, *k* is the multiplication factor.

We assume here that both operators *A* and *F* take into account the system with heterogeneous CA modeling. The corresponding operators, while representing the core with homogeneous CAs, are introduced as $\overline{A}$ and $\overline{F}$.

In this case, the Boltzmann equation for the adjoint flux $\overline{\Phi}*$ is:

$$\left(\overline{A}-\frac{\overline{F}}{\overline{k}}\right)\overline{\Phi}*=0 \qquad \text{Eq. C.2}$$

Perturbation theory permits one to express the reactivity discrepancy between both CA representations by means of a scalar product:

$$<\overline{\Phi}*,(\overline{A}-A)\Phi>+(\overline{\rho}-\rho)<\overline{\Phi}*,F\Phi>=0 \qquad \text{Eq. C.3}$$

The necessary and sufficient condition to have identical reactivity for both configurations is:

$$<\overline{\Phi}*,(\overline{A}-A)\Phi>=0 \qquad \text{Eq. C.4}$$

The operator $\overline{A}=\overline{A_0}$ is first computed by taking the cross-sections calculated in ECCO for the homogeneous design. In a next step, $\overline{\Phi_0^*}$ and $\overline{k_0}$ are computed by solving the Boltzmann equation. This is the first step of an iterative process. Then, $\overline{A_{i+1}}$ is determined by solving the equation: $<\overline{\Phi_i^*},(\overline{A_{i+1}}-A)\Phi>=0$. This is the first iteration, and the process is stopped when the desired accuracy is reached (~10 pcm).

To apply the algorithm, it is necessary to construct a 2D XY CA model, i.e. a heterogeneous model including the surrounding fuel. This is automatically done in ERANOS via the specification of the following four materials:

(1) Homogeneous fuel outside the CA,
(2) Wrapper,
(3) Absorber material,
(4) Coolant surrounding the absorber pins.

In the present work, the use of this procedure has allowed one, first, to accurately calculate the CA worth and, second, to have a measure of the heterogeneity effect in the CA design.

C. 4 Supplementary investigations with MCNPX

This section presents supplementary investigations performed with MCNPX, in order to assess the discrepancy in reactivity coming from uncertainties in computational methods (see Section 4.6). This has been done essentially via code-to-code comparisons of eigenvalues and CA worths.

In order to benchmark the ERANOS-2.0/ERALIB1 results, a full GFR MCNPX core model was developed for room temperature, thereby avoiding any possible discrepancies due to thermal expansion and self-shielding treatments. In the model, all CAs were considered as homogeneous media, so as to be consistent with the modeling used in ERANOS. The experience gained from the Monte Carlo simulations performed for the GCFR-PROTEUS verification studies (see Chapter 3) has been quite useful for the MCNP model development.

The multiplication factor of the GFR core was computed; first, for the CAs at the parking position, and, second, for different combinations of fully inserted CA banks. As shown by the results in Table C.8, which compares MCNPX with various ERANOS values, good agreement is obtained, there being a reactivity difference of -223 pcm between the ERANOS-2.0 calculation and MCNPX using the JEFF-2.2 based data library.

Table C.8 Comparison of the multiplication factors obtained for the reference GFR, at room temperature with CAs in the parking position. The ERANOS results (HEX-Z VARIANT and BISTRO) are expressed relative to the MCNPX values.

Method	Geometry	keff	Difference, pcm
MCNPX/JEF-2.2	HEX-Z	1.0973 +/- .0003	-
VARIANT/ERALIB1	HEX-Z	1.0947	-223
VARIANT/JECCOLIB2	HEX-Z	1.0920	-442
BISTRO/ERALIB1/Transport	RZ	1.1030	468
BISTRO/JECCOLIB2/Diffusion	RZ	1.0905	-575

Additionally, the CA worths are given in Table C.9, while the code-to-code comparison of radial flux traverses at mid core height is depicted in Figure C.2, for three different core configurations. Relatively good agreement is seen to be obtained for the CA worths, the differences being in the order of 5%. From Figure C.2, one also sees a very similar behavior in the radial flux distributions calculated with the two codes. On the basis of these code-to-code comparisons, no further investigations were performed, the ERANOS-2.0 calculations having been shown to be of a sufficient level of accuracy. Further comparisons are provided with the CA worth values obtained with the code PARCS, in the context of the transient analysis (see Chapter 5).

Table C.9 Code-to-code comparison of the CA worths

Core configuration	MCNPX CA worth, pcm	ERANOS CA worth, pcm	Difference, %
All CSDs inserted	14565	15598	-7.1
2nd CSD bank inserted	5733	6052	-5.6
2nd CSD bank + DSD bank inserted	11332	11818	-4.3
All CSDs + DSD inserted	20279	19171	5.5

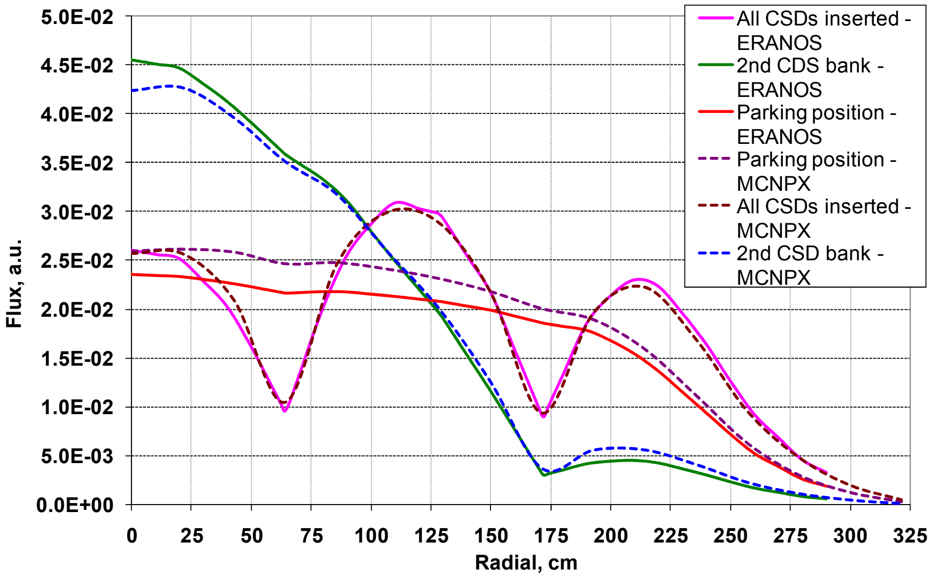

Figure C.2 Code-to-code comparison of radial flux traverses at mid-height for different core configurations: (1) all CSDs in parking position, (2) all CSDs inserted and (3) 2nd CSD bank inserted

Appendix D

D. “2007-Core” design and neutronics analysis

The aim of this appendix is to present the evolution of the GFR core design, the so-called “2007-Core”, along with the related neutronics investigations.

As indicated earlier, the neutronics analysis presented in Chapter 4 has represented a significant contribution towards developing and improving the GFR core design, the “2007-Core” having resulted partly due to this work. The main design features of this alternative core variant are presented in Section D.1, its neutronic characterization being described in Section D.2.

D. 1 GFR core description

The “2007-Core” design layout is shown in Figure D.1a, and for comparison the reference core layout is shown in Figure D.1b. Compared to the reference GFR core, the core geometry, in particular the height-to diameter (H/D) ratio, was significantly modified. The H/D ratio of the “2007-Core” is 0.62, instead of 0.35 for the reference core [211].

The core contains two zones of different Pu content: 15.7% in the inner zone and 19.6% in the outer zone, for a total of 246 fuel SAs implemented in 10 rings. The SA pitch was increased to 22.9 cm (+1.5 cm, compared to the reference core). The active fuel height was increased to 2.35 m and the diameter reduced to 3.77 m. The main design characteristics are summarized in Table D.1, along with, for comparison, the characteristics of the reference design.

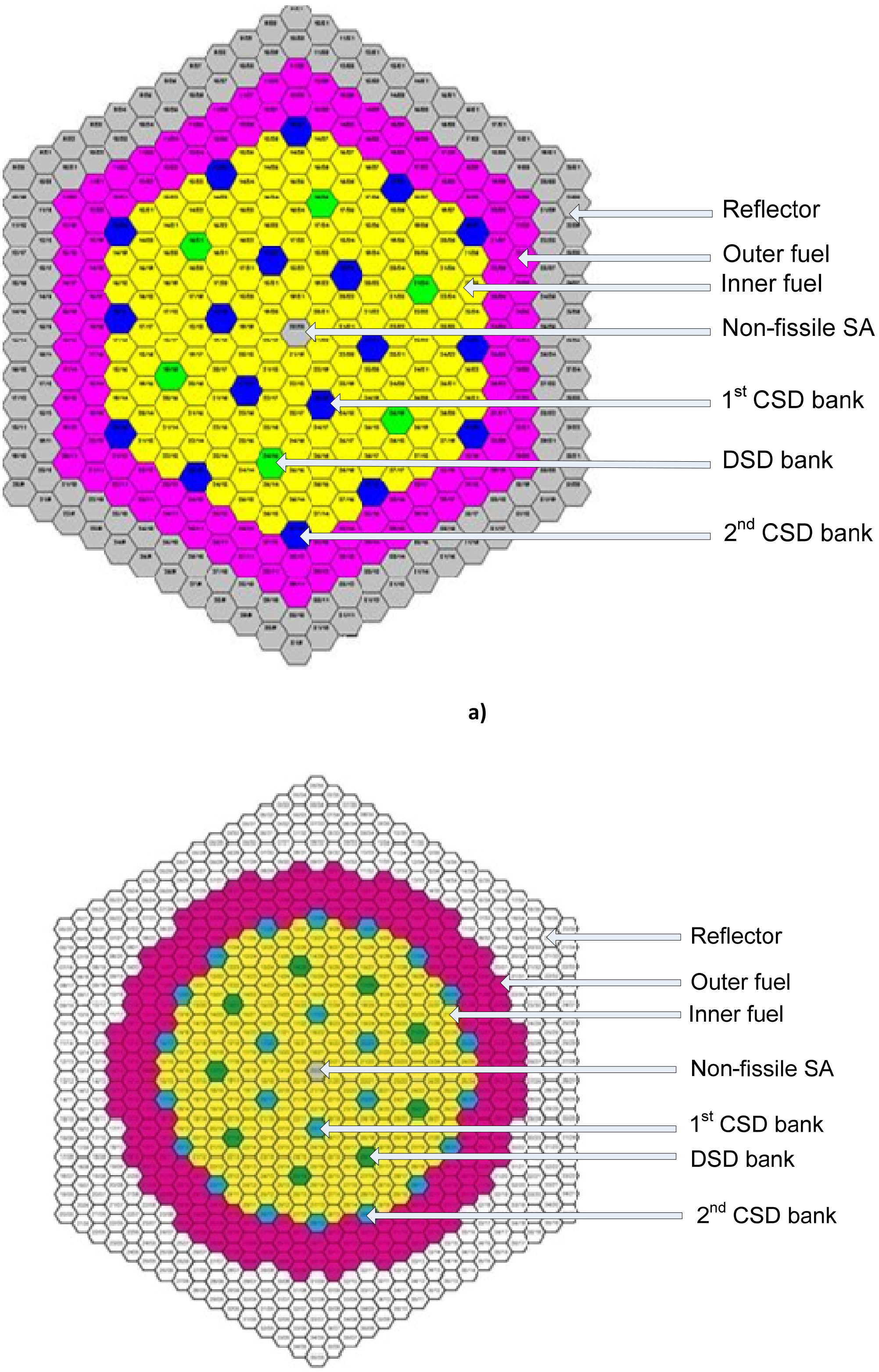

a)

b)

Figure D.1 a) "2007-Core" design layout; b) "2004-Core" design layout

Table D.1 Characteristics of the “2007-Core” design and, for comparison, the “2004-Core” design (already presented in Chapter 2, Table 2.4)

Parameter	“2007-Core” GFR design	“2004-Core” GFR design
Power, MW	2400	2400
Volumetric Power, MW/m^3	91.5	100.0
T inlet, °C	400	480
T outlet, °C	850	900
Fuel type	CERCER honeycomb	
Fuel assembly	Plates in hexagonal wrapper	
Total plate thickness, mm	8.4	7.0
Plate width, cm	12.4	12.0
Distance between fuel plates (channel width), mm	4.0	5.9
Fuel pellet height, mm	6.5	5.9
Lateral SiC wall thickness, mm	0.5	0.5
Number of control assemblies	24	33
Implementation scheme	3 banks	
Number of plates per assembly	27	
SA flat-to-flat distance, cm	22.9	21.4
Fissile height, cm	235.0	155.0
Reflector height (axial, both sides), cm	100.0	100.0
Height over diameter ratio	0.62	0.35
Max cladding/fuel T, °C	920 / 1318	1075 / 1210
Core pressure drop, MPa	0.14	0.06
Pu/U+Pu, %	~17.3	~15.2
Fuel management scheme, EFPDs	3 X 600 = 1800	3 X 831 = 2493
Burnup$_{mean/maximal}$, at%	6.6 / 10.1	10.1 / 14.7
Max dose (dpa in SiC)	111	163
Doppler constant (EOL), pcm	-1331	-1175
He void effect (EOL), pcm	259	253
Delayed neutron fraction (BOL), pcm	380	385

The homogenized volume fractions of the different materials in a fuel SA are reported in Table D.2.

Table D.2 Homogenized volume fractions of a fuel SA of the “2007-Core design and, for comparison, the “2004-Core” (already presented in Chapter 4, Table 4.1)

Homogeneous SA	Volume fraction “2007-Core”, %vol.	Volume fraction “2004-Core”, %vol.
(U, Pu)C	23.0	22.4
Coolant	36.0	40.0
He, gap in the plates	11.3	11.2
Structural and SiC matrix	28.7	26.4
Metalic liner (W-Re)	1.0	0.0

On the fuel SA side, specific adjustments were made, especially in terms of the material fractions and detailed composition of the fuel plates. One of the reasons is the permeability to fission products of the SiC/SiC-fiber composite, which is not excluded. Consequently, a protective layer against chemical interactions, the so-called liner, has been envisaged between the fuel pellets and the matrix. According to [164], the refractory metallic liner is placed within each fuel cell of the plate. The preference for the material choice is at the present time a 50 μm thick layer of W-Re. In total, the liner amounts to 1% of the SA volume fraction (see Table D.2).

Consecutive to the SA pitch increase, the CA pattern was slightly revised with an increase of the triangular pitch (25.7 mm instead of 24.5 mm) and the absorber diameter (22 mm instead of 20 mm). However, the basic CA design concept remains the same as that for the “2004-Core” (hexagonal CA, central static zone, multi-absorber-pin concept, metallic cladding, etc.). The homogenized volume fractions for the CAs are provided in Table D.3.

Table D.3 Homogenized volume fractions of the CAs; “2007-Core” design and, for comparison, “2004-Core” (already presented in Chapter 4, Table 4.8).

Material	Volume fraction “2007-Core”, %	Volume fraction “2004-Core”, %
SiC	15.1	15.9
AIM1	8.8	9.5
B_4C	30.3	34.6
Helium	45.8	40.0

The CA implementation scheme (so-called “Variant I”; see Figure D.1a) for the “2007-Core” design is based on the revised implementation (see Section 4.6.6) proposed for the reference GFR core design, which includes among other things a reduction in the CA number. It consists of a three-bank scheme, two CSDs (shown in dark blue) and 1 DSD (shown in light green) for a total CA-number of 18 CSDs and 6 DSDs. In more detailed terms, the first CSD bank contains 6 CSDs, and the second one 12. There are 6 DSDs in the intermediate safety bank. The active CA length (absorber part) is 2.35 m and reflects the increase of the fissile height.

D. 2 Neutronic characterization of the “2007-Core” design

The neutronics analysis of the “2007-Core” design was performed in a similar and consistent manner to the procedures used for the reference GFR core. Particular attention was given to assess the following:

1. Heat generation within the CAs,
2. CA interactions (shadowing and anti-shadowing effects),
3. CA worth and related heterogeneity effect,
4. CA safety cases (10 $, cold and hot shutdown, partial CA failure). These cases (see Chapter 4, Section 4.6) allow one to study the implementation scheme,
5. Reactivity parameters (reactivity swing during the fuel cycle, etc.) and reactivity effects: fuel Doppler, core thermal expansion, void, Np decay, etc,
6. Eigenvalue separation characteristics.

The goals of the analysis were:

1. To characterize the neutronics of the “2007-Core” design, in order to compare with the reference design,
2. To implement, within the core, the CA pattern developed for the reference core and to revise, if necessary, this pattern,
3. To verify, with this CA pattern, the reactivity requirements and the associated safety cases,
4. To assess the impact of the H/D-ratio increase on the neutronic harmonics propagations via the eigenvalue separation analysis,
5. To prepare the necessary neutronic parameters, i.e. the macroscopic cross-sections and related derivatives, in order to perform the core dynamic analysis under hypothetical CA-driven transient conditions (see Sections 5.4 and 5.5 in Chapter 5).

In the following subsections, selected results for the “2007-Core” are presented and compared with those for the reference core.

A. CA pattern verification and CA worth

Consecutive to the core design adjustments (in particular the H/D and the SA pitch), investigations were performed for the CA pattern, in particular to verify that the heat generation and the He mass flow rate needed are still well matched. For the reference GFR, the He mass flow rate required to cool the absorber pins was determined on the basis of the conservative approach of a 100% CA insertion. Accordingly, the heat generation results for the full insertion case in the “2007-Core” are provided in Table D.4.

Table D.4 Heat generation within the CAs for the 100%-insertion case; "2007-Core" design

Parameter	100%
Integrated power, kW	1240
Volume, cm^3	1.52E+05
Average power density, W/cm^3	8.1

Despite the height increase in the new core, the average heat generation is reduced (-7%), which in mainly caused by a lower ^{10}B fraction and a reduction in the power density (-9%). Within the follower, similar values were obtained in terms of average power density and gamma fraction, indicating a similar behavior between the two GFR cores for the CA.

These results show the adequacy of the main CA design developed for the reference GFR core. It shows, as well, that the mass flow rate can be reduced. This aspect of the analysis was not considered currently, the investigations expected to be similar to those performed for the reference core.

Having verified the adequacy of the revised CA pattern for the new GFR design (essentially in terms of heat generation), the CA worth and the heterogeneity factor were computed (see Table D.5), mainly in order to check the CA implementation scheme. The CA worth calculated for all CSD assemblies inserted is ρ = 15400 pcm, which corresponds to a heterogeneity effect of 12% (comparable to the value obtained of 13% for the reference core). The CA worth is relatively high compared to the reference GFR core, despite the reduction of the number of CAs from 33 to 24, due to the greater CA length (2.35 m compared to 1.55 m).

Table D.5 CA worths and heterogeneity effects; "2007-Core" design

Configuration	1st CSD	DSD	2nd CSD	Worth, pcm	Heterogeneity effect, %
1st CSD bank inserted	in	out	out	3047	-5.4
2nd CSD bank inserted	out	out	in	6244	-7.4
DSD bank inserted	out	in	out	4476	-13.6
Both CSDs inserted	in	out	in	15400	-12.4
Both CSDs and DSD inserted	in	in	in	19813	-12.9

B. Eigenvalue separation analysis (SVP)

One of the findings of the eigenvalue separation analysis (SVP) is the correlation between the importance of the harmonics and the core dimensions (see Section 4.4.4), especially in the radial direction. As mentioned earlier, an improved neutronic stability is expected for this core variant due to the reduction in the core radius. To confirm this, the CA bank interactions, amplification factors and interactions for individual CAs in the different banks were calculated and the values are reported in Table D.6, along with the reference-core values for comparison. Additionally, a new parameter – the normalized inverse-interaction, δ'_{rel} – is defined for comparison of the different cores:

$$\delta'_{rel} = \frac{\rho}{\delta} \qquad \text{Eq. D.1}$$

where ρ is the CA worth and δ is the CA interaction effect defined by Eq. 4.6 in Chapter 4.

This parameter, which is different in the two considered cores, gives the CA worth per unit of interaction or, in other words, allows one to normalize the interactions per unit of CA-worth.

Table D.6 Control assembly bank interactions (δ) and normalized inverse-interaction (δ'_{rel})

	"2007-Core" design		"2004-Core" design	
Bank interaction	**δ, %**	**δ'_{rel}, pcm/%**	**δ, %**	**δ'_{rel}, pcm/%**
Between 1st CSD and 2nd CSD	43	406	46	339
Between DSD and both CSD	33	681	31	618
Between DSD and 1st CSD	-26	260	-29	191
Between DSD and 2nd CSD	6	2043	8	1477

The values in Table D.6 show slightly lower CA bank interactions for the "2007-Core", i.e. in the range of a few percent in δ. More important for the comparison of the two GFR cores is the observed increase of the normalized parameter δ'_{rel}. As a consequence, the CA interactions per unit CA-worth are significantly lower in the second core design, which is favorable. This was expected, mainly due to the increase in the H/D ratio. As further confirmation, a SVP value of 6.4 was obtained for the "2007-Core", for the all-CA withdrawn configuration, i.e. significantly lower than the corresponding value of 8.2 for the reference GFR. As supplementary information to the SVP values, the radial power distributions of the fundamental and first-order eigenvalues are depicted in Figure D.2, for the two GFR cores ("2004-Core" and "2007-Core" designs).

A differential behavior is observed for the first-order eigenvalue, with a negative contribution in the inner core region for both designs. The interesting finding is the reduced contribution of the first-order eigenvalue, especially in the inner core region, for the "2007-Core" design. These results show that the new GFR core variant is less sensitive to neutronic perturbations induced by CA movements, which is of importance for core safety.

The adjustment of the core material composition (fuel plate, structural material, etc.) impacts the reactivity, which can be compensated by an adjustment of the Pu content. For this reason, the SVP was calculated as a function of the core average Pu-content (see Figure D.3). As seen from the figure, a linear relationship is observed between the two parameters. This shows that another way to reduce the interactions within the core, reflected by a reduction of the SVP value, is to reduce, if possible, the core average Pu-content.

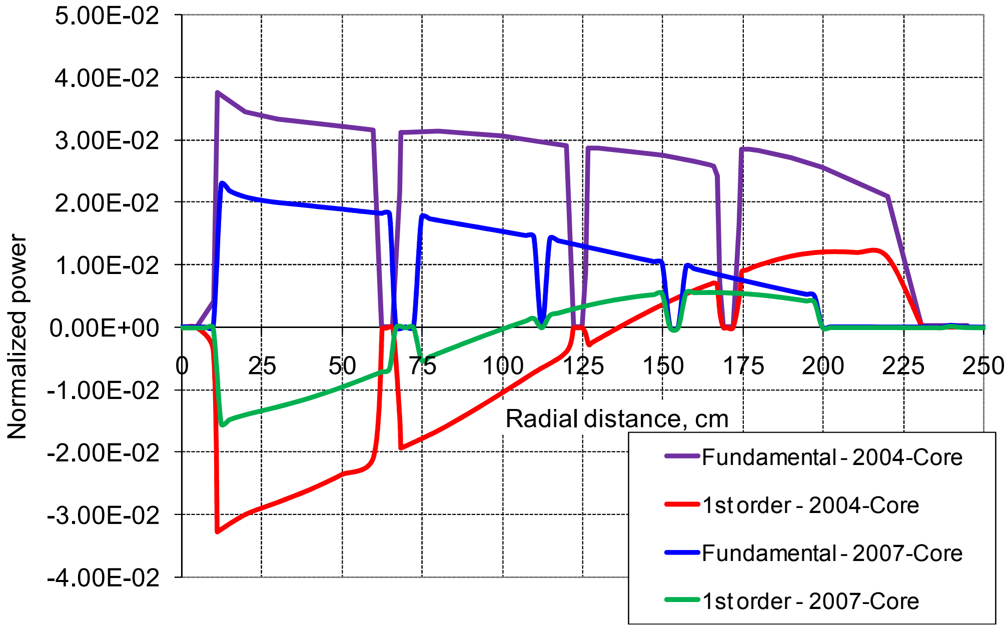

Figure D.2 Radial power distribution at mid-core height of the fundamental and first-order eigenvalue for the two GFR core designs, (1) "2004-Core" and (2) "2007-Core"

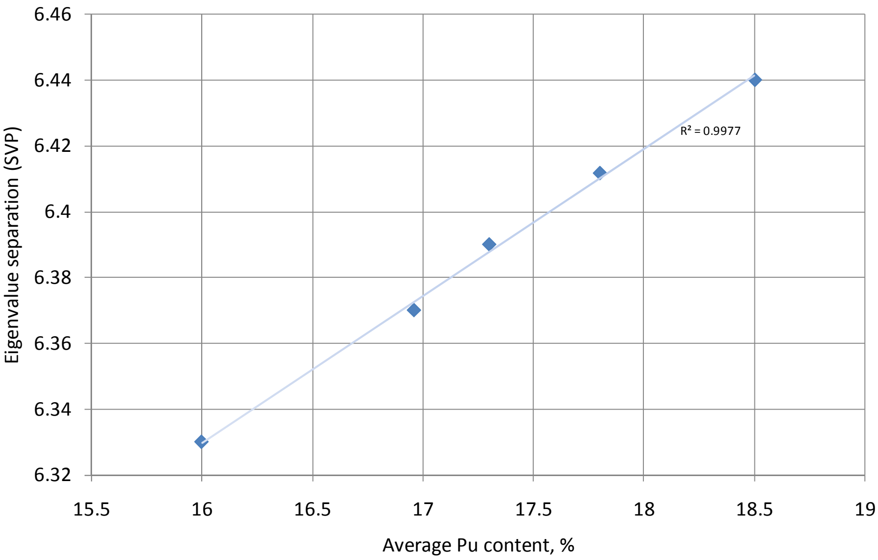

Figure D.3 Eigenvalue separation value (SVP) vs. average plutonium content of the core

C. Reactivity requirements and safety cases associated with CAs

The reactivity requirements have been analyzed in a similar manner as for the reference core (see Section 4.6 in Chapter 4), the total reactivity effects being found to amount to ρ = 3678 pcm (uncertainties not taken into account). This is a lower value (-398 pcm), compared to the reference core (see Table 4.19), due essentially to a reduced fuel cycle length and a lower reactivity loss per EFPD.

The four safety cases associated with CA insertion were re-analyzed (see Section 4.6.1 in Chapter 4), viz. (1) reactivity insertion of 10 $, (2) fuel handling error (CA replaced by fresh fuel SA of outer zone), (3) shutdown with partial failure of CAs at cold conditions and (4) shutdown with partial failure of CAs at hot conditions.

The neutronic uncertainties have been quantified using the same methodology as earlier (see Section 4.6.1). Large reactivity margins[13] (see Table D.7; "Variant I") are seen to be obtained in association with the initial implementation scheme proposed for the "2007-Core" design.

Table D.7 Reactivity margins (along with uncertainties) for the four safety cases related to CAs. Two CA implementation schemes are considered: (1) Variant I and (2) Variant II

	Variant I with 24 CAs		Variant II with 19 shorter CAs	
Safety cases	Reactivity margin, pcm	Uncertainties, pcm	Reactivity margin, pcm	Uncertainties, pcm
10 $	9300	3185	1824	1653
Fuel handling error	7236	2142	2148	1002
Shutdown with unavailability of half the CSDs and one DSD	5872	1930	174	1136
Shutdown with DSDs with unavalaibility of one DSD	1221	1219	189	699

The maximal reactivity margin calculated is 9300 pcm, for the 10 $ case. At the other extreme, the minimal reactivity margin is 1221 pcm, for the case corresponding to shutdown using only part of the DSDs. This remains a significant value, indicating further possible ways of optimization, e.g. by a reduction of the CA number.

For this reason, a second scheme (so-called "Variant II") was proposed [211], characterized by lower reactivity margins (see Table D.7). This scheme corresponds to a reduction of the CA number (by three CSDs and two DSDs) and a reduction of the CA length from 2.35 m to 1.6 m. The latter choice was also made in order to reduce the vessel volume above the core, required to fully withdraw the CAs into the parking position. More important, the CA-length reduction helps to reduce the reactivity worth per CA, and hence the impact on core parameters in the case of accidental withdrawal of a fully inserted CA (see Section 5.6.6 of Chapter 5). Additionally, the total CA worth is reduced ($\Delta\rho$ = ~ 9000 pcm), leading to reduced CA interactions.

---

[13] The reactivity margins provided in Table D.7 include consideration of the uncertainties. In this sense, the values provided clearly have potential for further optimization.

In more detailed terms, this second implementation scheme (“Variant II”) corresponds to six CSDs in the first CSD bank and nine in the second, the intermediate safety bank containing only four DSDs. To keep the azimuthal core symmetry, the central non-fissile SA within the core was replaced by a DSD. As shown by the results in Table D.7 (“Variant II”), the reactivity margins were significantly reduced, i.e. the maximal margin is 2148 pcm (fuel handling error) and the minimal is 174 pcm. This implementation scheme, optimized mainly on the basis of static considerations, was further assessed based upon the comparative study of CA-driven transients (see Section 5.6.1).

It is important to note that the present neutronic investigations of the “2007-Core” were conducted partly in parallel with the analysis of CA-driven transients (due to the iterative nature of the design process). For this practical reason, the reference CA implementation scheme retained for the transient analysis related to the “2007-Core” design has been “Variant I”. The transient analysis carried out with “Variant II” has simply served as a sensitivity case with respect to the number of CAs within the core (see Section 5.6).

D. 3 Findings related to the “2007-Core” design

The “2007-Core” design has been presented above with supplementary neutronic characterization, in terms of verification of the CA pattern verification and implementation scheme. Based on the eigenvalue separation analysis, this evolution of the GFR core features interesting neutronic characteristics, among them a reduction in CA shadowing and anti-shadowing effects.

The reactivity requirements and uncertainties analysis have shown the possibility to significantly revise the reference CA implementation proposed for the “2007-Core” design, i.e. via a CA reduction, mainly in the second CSD bank.

To summarize the sequence of developments:

(1) At the beginning of the design study for the reference GFR core (“2004-Core” design), a total of 33 CAs were envisaged, based upon considerations coming from previous commercial FRs.
(2) Detailed investigations showed that a reduction to 24 CAs was possible, based on reactivity requirements and safety analysis (implementation scheme “Variant 1”).
(3) In a next phase of investigations, the core geometry was refined, leading to the “2007-Core” design, and the neutronic performance of the GFR core was re-analyzed in a systematic manner.
(4) In the course of the analysis, large reactivity margins (associated with relatively large uncertainties coming essentially from the design viewpoint) were identified for the“2007-Core”. Subsequently, a revised CA implementation scheme (“Variant II”, consisting of 19 CAs) was proposed, which fully satisfies the reactivity requirements and related safety criteria specific to this core. For the “Variant II” CA implementation scheme, the additional reactivity margins (after large uncertainties) are close to zero, implying that a further reduction of CAs is not possible.

Appendix E

E. Fuel cycle analysis

The aim of this appendix is to present the fuel cycle calculations performed in the context of the safety-related dynamics studies for the reference "2004-Core" design, in association with a core composition corresponding to beginning of equilibrium cycle (BOEC). The calculations were performed as a preparatory step for studying the sensitivity of the GFR behavior to the presence of burnt fuel in the core. The transient analysis itself is presented in Subsection 5.6.3.

This appendix presents:

(1) The context of the fuel cycle calculations (see Section E.1),
(2) The computational methods (see Section E.2),
(3) A summary of the main results obtained (see Section E.3).

E. 1 Motivation and general context

Two of the main requirements of Generation IV reactors are:

(1) To reduce the amount of long-lived radioactive wastes,
(2) To increase the fuel sustainability in these reactors [34].

It is well known that the transuranic nuclides (TRU), i.e. plutonium and MAs, are the main contributors to the long-lived radiotoxicity of the spent fuel [21; 212]. From this observation, it is clear that, from the viewpoint of the reduction of long-lived wastes, future reactor systems need to provide an optimal management strategy for plutonium and the MAs.

In this context, a number of advanced fuel cycle concepts have been studied in the past, relative to the currently dominant LWR once-through cycle [213; 214]:

(1) Plutonium burning in LWRs and fast reactors,
(2) TRU burning,
(3) Double-strata strategy,
(4) Fast reactor strategy.

Within the frame of the present research, the most attractive solution is the one based on FRs (the last one mentioned above), where the fuel cycle can be closed with respect to all actinides on the basis of a single type of advanced nuclear system. Figure E.1 represents this concept for realizing the long- term goal for nuclear development, i.e. complete closure of the fuel cycle.

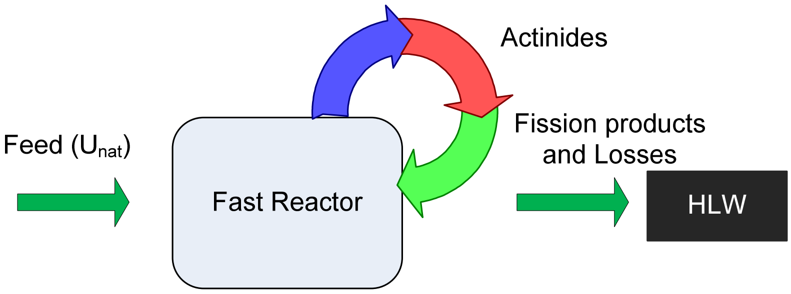

Figure E.1 Fast reactor operated in completely closed fuel cycle

This option is the one considered as the reference for the GFR fuel burnup analysis conducted currently. In practical terms, the reactor recycles all the actinides loaded within the core. This effectively implies that the GFR core should be capable:

(1) To breed new fuel from natural or depleted uranium,
(2) To recycle most of the actinides from its own spent fuel.

At the end of a given burnup cycle, the core is partially unloaded (as a function of the management scheme), and the amounts of discharged actinides and fission products are replaced by recycled actinides and “top-up” natural uranium (“feed”), the new fuel having been fabricated using the reprocessed TRUs after a certain cooling time. It should be noted that the operation in a completely closed fuel cycle will lead to an equilibrium fuel cycle resulting from the long-term operation of the reactor, with a constant fuel management scheme.

In most cases, the presence of MAs and FPs within the fuel deteriorates the safety-related core parameters (see Table E.1 below). This provides the main motivation for the supplementary core dynamics studies with burnt fuel in the reference GFR core. In more detailed term, the goals of the analysis are twofold:

(1) To assess the dependence of safety-related neutronic parameters, such as the delayed neutron fraction β_{eff} and the fuel Doppler reactivity effect, on fuel burnup. The analysis is presented in Section E.3.
(2) To assess the impact of this dependence (deterioration) on thermal-hydraulics results from the dynamic core analysis, e.g. the peak fuel and cladding temperatures, the power distribution deformation, the time to reach material temperature limits, etc. This analysis is presented in Subsection 5.6.3.

In order to perform the transient analysis, the fuel composition and the related neutronic parameters had to be evaluated. Specific 2D computational tools in ERANOS-2.0 were first developed and assessed (see Section E. 2). Second, the results of the fuel cycle investigations were obtained. These are presented in Section E. 3, along with a sensitivity study (mainly with respect to computational options).

Supplementary fuel cycle calculations associated with different management schemes have also been carried out using a new 3D tool (EQL3D), developed in the context of the FAST code system [85; 215], for which the core was simulated in 3D HEX-Z geometry (see Section 4.2.3

for a HEX-Z model description). Comparisons of results obtained with the 2D model are discussed, a good agreement being achieved between the two sets of calculations.

E. 2 Fuel cycle calculations

A. Burnup procedure

Fuel cycle calculations were performed with ERANOS-2.0, in association with the 2D RZ BISTRO model used for the heat-generation related calculations (see Section 4.3.1). A specific procedure was developed, the calculation scheme being illustrated in Figure E.2.

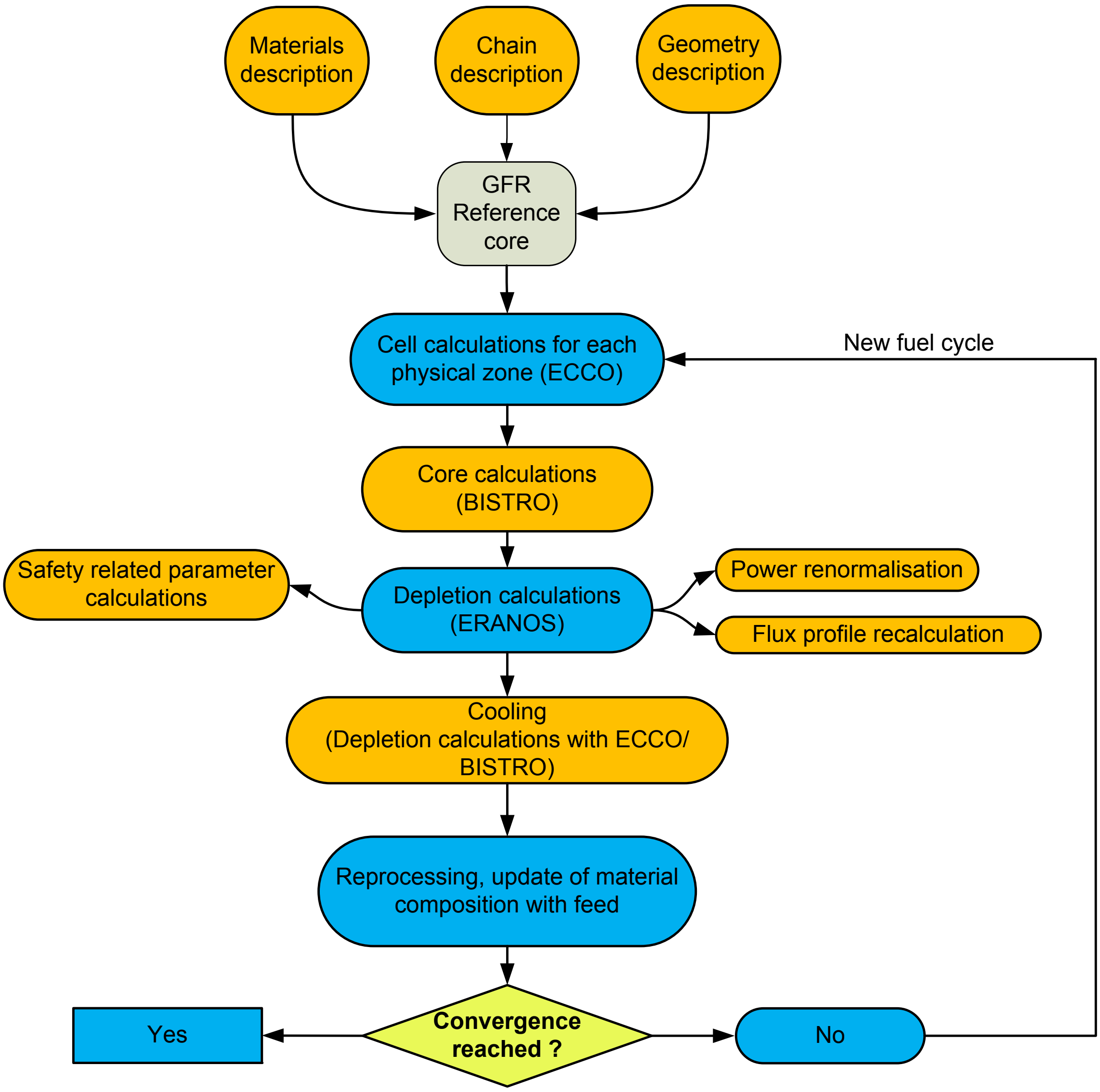

Figure E.2 Schematic of the calculational scheme for the burnup calculations

In a first step, following definition of the core to be analyzed, the self-shielded macroscopic cross-sections in 33 broad energy groups are prepared with ECCO. In a second step, the 2D core calculations with BISTRO are performed to obtain the space and energy dependent flux. In a third step, the depletion calculations are performed with ECCO/BISTRO, with the burnup cycle divided into suitable time-step intervals, to obtain the new material compositions. The depletion is done assuming a quasi-static approach: the microscopic cross-sections and the flux profile derived from core calculations are held constant during a depletion step [216]. Furthermore, during a depletion step, the flux is re-normalized to keep the core power constant, and the flux distribution is re-calculated by means of additional core calculations. The macroscopic cross-sections are updated using the material densities calculated during the previous depletion step. The re-calculation of the microscopic cross-sections, in order to take into account the change of slowing down and self-shielding, was not considered in the present calculational procedure.

B. Actinide chains and fission products

The fuel compositions were calculated using detailed chains including 29 actinides up to ^{248}Cm and 87 explicit fission products associated with the ERALIB1 nuclear data library [97].

C. Core management scheme

The reference GFR core management [78] is a three-batch scheme of 831 EFPDs for a total of 2493 EFPDs. Due to the limitation of the procedure used (2D), a fuel cycle was simulated in a single batch cycle, which is a common assumption for fuel depletion analysis [167; 213]. In this case, no reloading or shuffling schemes are simulated and each fuel SA is burnt at the same location within the core during the entire fuel cycle length. This simplification was verified against the earlier mentioned, 3D procedure EQL3D [215], and good agreement was obtained for the second batch of the cycle (see Section E.3).

D. Recycling options

In the procedure used, the fuel is unloaded and cooled for a given time at the end of a defined fuel cycle, allowing one to decrease the radiotoxicity and the fuel temperature. The actinide composition is explicitly simulated during the cooling time on the basis of cell/core calculations. After the cooling time, the recycling takes place and isotope-dependent reprocessing losses are applied. The reprocessing losses are typically 0.1% [213; 214]. In total, a time period of seven years was assumed for cooling and reprocessing, which corresponds approximately to a fuel cycle irradiation length (2493 EFPDs). Finally, the new fuel compositions are calculated with the specified feed used to replace the fission products and reprocessing losses.

E. Feed

The feed mainly depend on:

1. The fuel management strategy,
2. The availability of spent fuel for reprocessing,
3. The neutronic feasibility, i.e. not all feeds will be suitable to match the reactivity criteria and/or the safety-related parameters may have significantly deteriorated (e.g. if a high fuel fraction is composed of MAs),
4. The performance of the reprocessing methods (losses).

The evaluation of the fuel compositions at BOEC and at EOEC requires repeated fuel cycle calculations for arriving at a constant management scheme, corresponding to a constant core operation (full power) and a specific feed.

In the present research, the equilibrium fuel compositions were computed in the closed-cycle mode associated with two different recycling options (see Figure E.3):

1. *Reference option:* MAs included in the recycling (0.1% losses in reprocessing),
2. *Alternative option:* without recycling of MAs, i.e. only uranium and plutonium are recycled with associated losses of 0.1% in reprocessing.

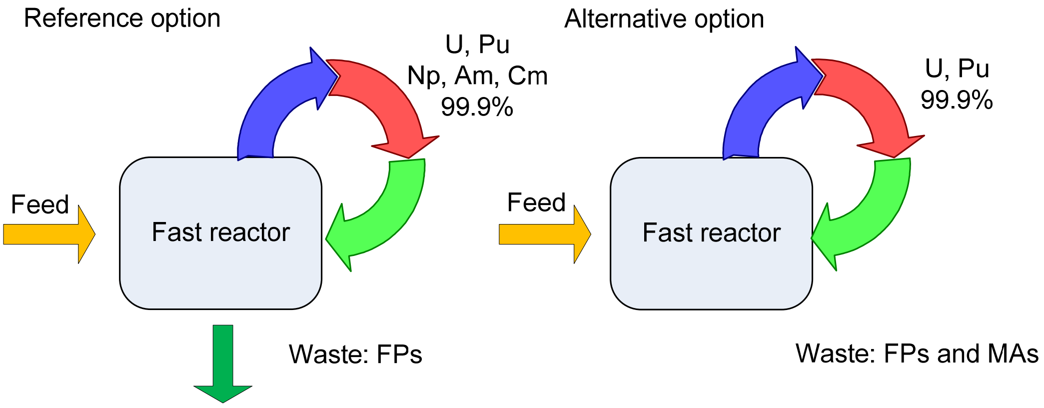

Figure E.3 The two considered recycling strategies: (1) all actinides are recycled ("Reference option") and (2) only uranium and plutonium are recycled ("Alternative option")

In both cases, the feed is composed of natural uranium together with plutonium of isotopic composition given by:

^{238}Pu / ^{239}Pu / ^{240}Pu / ^{241}Pu / ^{242}Pu = 2.7% / 56.0% / 25.9% / 7.4% / 7.3%

It is assumed in the procedure that the fraction (mass) of plutonium to be added in the core is determined in an iterative process, allowing a check on the initial reactivity. In this manner, the reactivity is made to remain constant at BOC (see Figure E.4 and Figure E.5 below).

E. 3 Results

The results of the fuel cycle analysis are presented for the “2004-Core” design, in conjunction with each of the two recycling strategies presented above.

A. Core reactivity evolutions

The reactivity evolution, with the two recycling options, is presented in Figure E.4 and in Figure E.5, for a total of 10 fuel cycles of 2493 EFPDs each. Table E.1 gives the main neutronics results for the first and equilibrium cycles in each case.

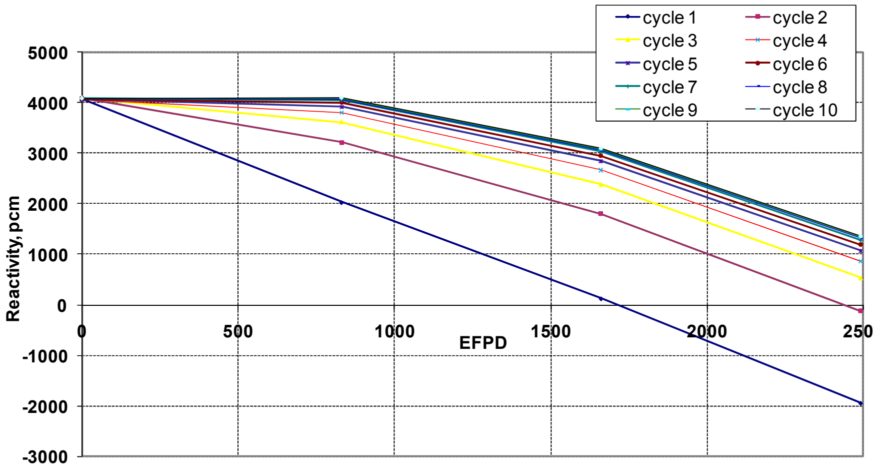

Figure E.4 Reactivity evolution for the first 10 fuel cycles operated in closed-cycle mode with recycling of all actinides

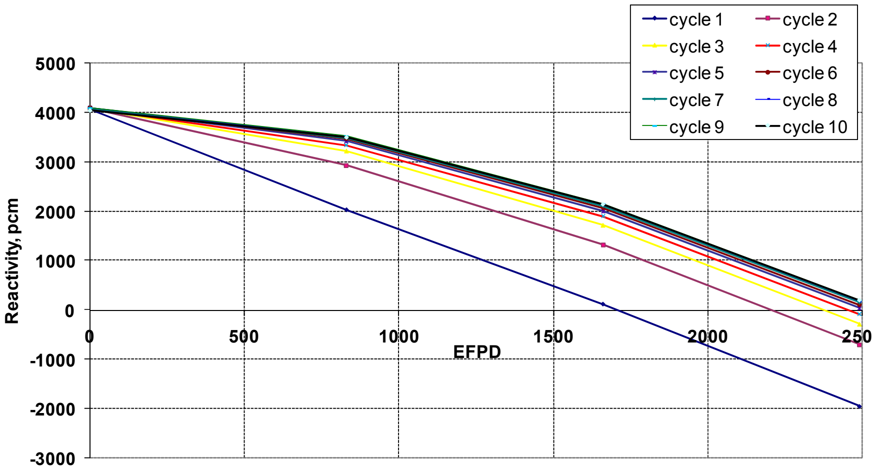

Figure E.5 Reactivity evolution for the first 10 fuel cycles operated in closed-cycle mode without recycling of MAs

From the curves, it is seen that the reactivity evolution of the GFR tends to equilibrium as postulated and that the recycling of the MAs induces a lower reactivity swing (~2700 pcm, compared to 3740 pcm without the MA recycling), as well as a higher breeding gain. To better visualize the convergence to equilibrium, which is attained after approximately ten cycles, the reactivity swing per fuel cycle is shown in Figure E.6.

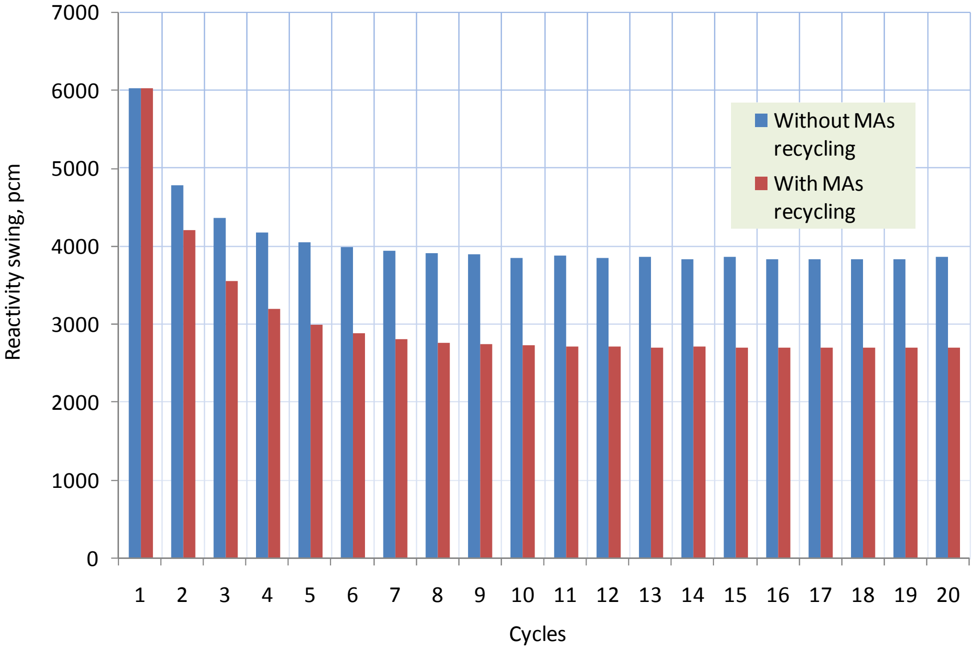

Figure E.6 Convergence of the reactivity swing

B. 1st fuel cycle and equilibrium cycle

To show the evolution of safety-related parameters, results for the first fuel cycle and the equilibrium fuel cycle are presented in Table E.1 in terms of:

(1) The core reactivity at BOC and EOC,
(2) The average reactivity swing during the cycle,
(3) The power peaking factor, which is the combined value of the axial and radial power peaking factors at BOC and EOC,
(4) The average (inner and outer zones) breeding gain at BOC and EOC,
(5) The void effect, calculated as: $\rho_{voided} - \rho_{reference}$ at BOC and EOC,
(6) The fuel Doppler reactivity constant, calculated as $\frac{\rho_{Tfuel,reference} - \rho_{Tfuel,180°C}}{\ln\left(T_{fuel,990°C}/T_{fuel,180°C}\right)}$ at BOC and EOC,
(7) The delayed neutron fraction β_{eff} at BOC and EOC,
(8) The average neutron life-time Λ at BOC and EOC.

Table E.1 Neutronics results for the first fuel cycle and equilibrium fuel cycle. Each of the two considered recycling options are shown: (1) with recycling of all actinides and (2) without recycling of MAs

Parameters	First cycle	Equilibrium cycle With recycling of all actinides	Equilibrium cycle Without recycling of MAs
Reactivity (BOC/EOC), pcm	4072 / -2174	4090 / 1419	4068 / 1194
Average reactivity swing, pcm/EFPD	2.5	1.1	1.5
Power peaking factor (BOC/EOC)	1.43 / 1.56	1.41 / 1.53	1.42 / 1.54
Breeding gain (BOC/EOC)	-1.49E-01 / -8.1E-02	5.74E-02 /-6.43E-02	4.54E-02 / -7.74E-02
Void effect (BOC/EOC), pcm	268 / 254	328 / 274	304 / 261
Fuel Doppler constant (BOC/EOC), pcm	-1580 / -1121	-907 / -932	-1445 / -1033
β_{eff} (BOC/EOC), pcm	379 / 348	332 / 331	346 / 341
Average neutron lifetime Λ (BOC/EOC), 10^{-6} s	1.73 / 1.53	1.46 / 1.35	1.61 / 1.42

The neutronic results obtained demonstrate that:

(1) In all cases, equilibrium is attained within a total of about 10 cycles, corresponding to approximately 70 years of operation at full power.

(2) The average reactivity swing during the cycle amounts to 2.5 pcm/EFPD for the first cycle, while a lower value is obtained at equilibrium, i.e. 1.1 pcm/EFPD and 1.5 pcm/EFPD with and without the recycling of MAs, respectively.

(3) The power peaking factor increases with burnup during a cycle. For the first cycle, the value is 1.43 at BOC and increases to 1.56 at EOC. Similar values are obtained for the equilibrium cycles.

(4) The breeding gain is negative throughout the cycle for the first cycle, while a slightly positive value is obtained during the first part of the equilibrium cycle. This shows that the core is being operated in the iso-breeder mode for the equilibrium cycle.

(5) The safety-related and kinetics parameters (void reactivity and fuel Doppler effects, delayed neutron fraction and prompt neutron generation time) are lower for EOC, compared to BOC conditions, and even lower at EOEC. Furthermore, the values of these parameters are lower when MAs are recycled. In more detailed terms, the magnitude of the fuel Doppler constant is reduced by ~23% relative to the BOC value for the first cycle (with MA recycling) and by ~9% (without MA recycling). Similarly, the delayed neutron fraction is reduced by ~12% and ~9%, with and without MAs recycling, respectively.

In the context of the analysis of the GFR core behavior during CA withdrawals and ejections (see Subsection 5.6.3), the interest has been focused on the MA-recycling option, due to the lower values of the safety-related and kinetics parameters. In this sense, the transient analysis performed (with the highest fraction of MAs) provides an “envelope case”. It was verified that the transient results at BOEC with the second recycling option (without MA recycling) are indeed contained between the values obtained for fresh fuel conditions and with the first recycling option, i.e. with the recycling of all actinides.

Finally, it is important to stress that the reported values have been calculated with a simplified 2D core model. As a direct consequence, the CAs have been homogenized in concentric rings by preserving the volume of absorber material which largely affects, for instance, the CA worth (e.g. see Appendix C.1). The delayed neutron fraction β_{eff} and fuel Doppler reactivity effects were checked against 3D reference values and no significant sensitivity was observed. It should of course be noted that, for the transient analysis, the CAs were represented explicitly (with the PARCS/TRACE modelling; see Subsection D of this appendix), thereby ensuing the correctness of the CA worths in this context.

The fuel and fission products compositions of the first cycle and the equilibrium fuel cycle are provided in Table E.2, both at BOC and EOC for the first cycle, and at BOEC and EOEC for the equilibrium cycle. The total mass of actinides is 58.8 tons, of which 9.6 tons are plutonium and MAs. At BOC, the MA fraction is 0.1% and increases with irradiation consecutive to the build-up of neptunium, americium and curium. At EOC, the plutonium content is increased to ~19% and the MA fraction to 0.6%. As a consequence, the neutron spectrum tends to shift to higher energy. At equilibrium conditions, the plutonium content is once again increased, the value being ~21%. Depending on the recycling option, the MAs fraction stabilizes around 0.6%, without recycling of the MAs. On the contrary, the value is significantly higher, viz. ~1.6%, if the MAs are recycled. To illustrate the increase of MAs in the fuel, their evolution is shown in Figure E.7 for the first 15 cycles, for each of the two recycling options.

Table E.2 Material compositions for (1) BOC, (2) EOC, (3) BOEC and (4) EOEC. Both the considered recycling options are presented: (1) recycling of all actinides and (2) without the recycling of MAs

Nuclides	**First cycle**		**Equilibrium cycle**			
			With recycling of all actinides		**Without recycling of MAs**	
	BOC	**EOC**	**BOEC**	**EOEC**	**BOEC**	**EOEC**
	Mass, %	**Mass, %**	**Mass, %**	**Mass, %**	**Mass, %**	**Mass, %**
U	83.70	80.85	78.79	76.87	80.55	78.25
Pu	16.18	18.53	19.64	21.61	19.37	21.17
Am	0.11	0.47	1.20	1.00	0.08	0.44
Np	0.00	0.06	0.11	0.14	0.00	0.07
Cm	0.00	0.09	0.26	0.38	0.00	0.07
MA fraction, %	0.11	0.62	1.57	1.52	0.08	0.57
	Mass, kg	Mass, kg	Mass, kg	Mass, kg	Mass, kg	Mass, kg
FPs	0.00	5580	0.00	5616	0.00	5613

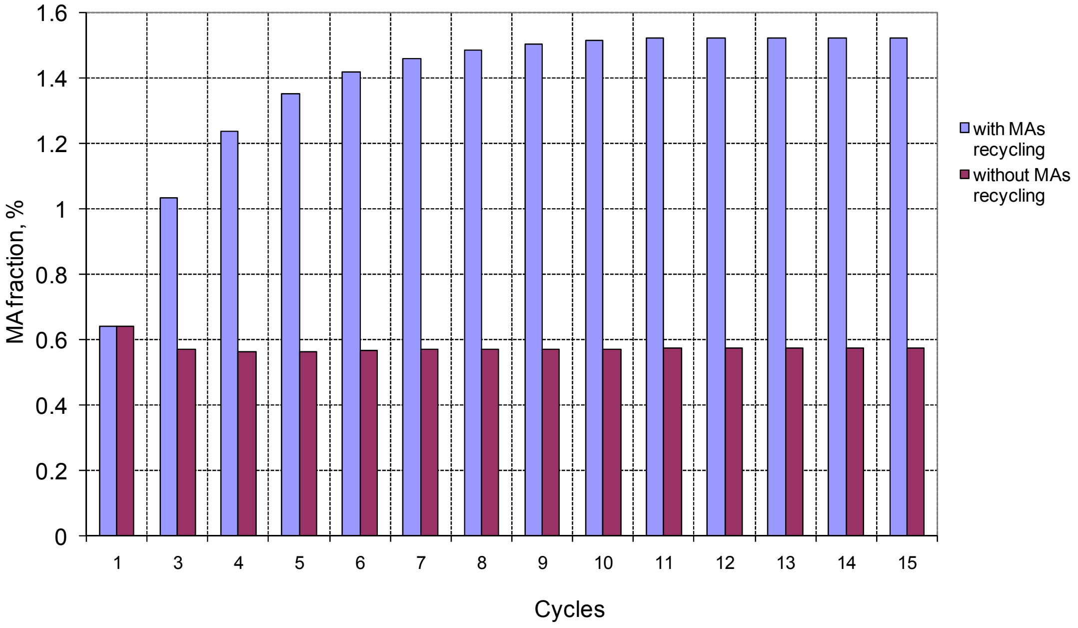

Figure E.7 Evolution of the MA fraction to BOEC values for the two recycling strategies: (1) with and (2) without recycling of MAs

C. Verification with 3D analysis methods

As mentioned above, the fuel cycle analysis has been performed using a 2D core description. In more detailed terms, the three-batch scheme was simulated using an equivalent one-batch approximation. For this reason, verification was performed using a 3D HEX-Z core description and nodal flux calculations (VARIANT), allowing one to study, in particular, different fuel reloading schemes [215], and to compare the results obtained with the two different methods. In the three-batch reloading scheme used with the 3D model, a fuel zone is subdivided into three concentric zones (ring-wise). At the end of a batch irradiation, one third of the fuel within each zone is moved towards the core centre.

Two important parameters were selected for comparisons:

(1) The reactivity evolution during the fuel cycle,
(2) The fuel Doppler reactivity effect[14].

Figure E.8 shows the core reactivity evolution, while the fuel Doppler reactivity effect is presented in Figure E.9. In both figures, results for the equilibrium fuel cycle (recycling of all actinides) are presented[15].

---

[14] Change of fuel temperature from 990°C to 180°C.

[15] The calculations were performed using the EQL3D procedure [215], while the values presented (especially in Table E.1) were obtained with the developed procedure.

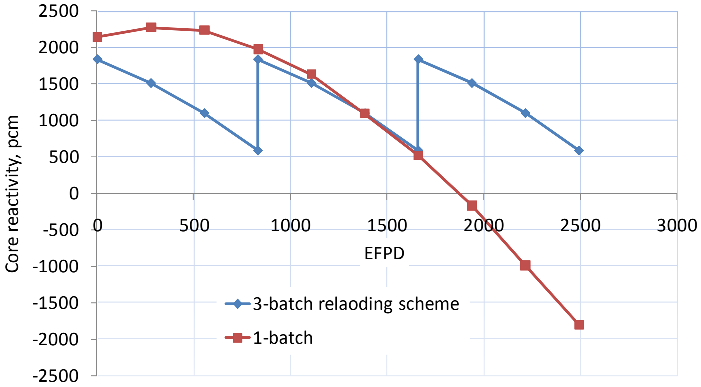

Figure E.8 Direct comparison of the core reactivity evolution calculated for the equilibrium fuel cycle (recycling of all actinides) for two different cases: (1) single batch, (2) three-batch reloading scheme

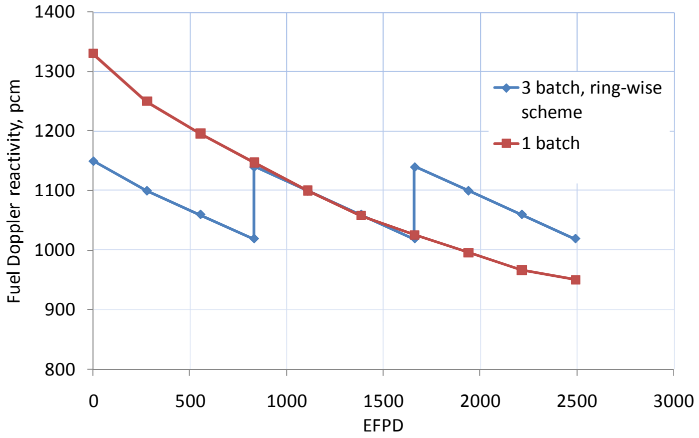

Figure E.9 Direct comparison of the Doppler reactivity effect calculated for the equilibrium fuel cycle (recycling of all actinides) for two different cases: (1) single batch, (2) three-batch reloading scheme

As seen from the reactivity curves above (see Figure E.8), there is a good agreement for the second fuel batch (so-called average fuel batch), which is precisely the batch considered for the transient analysis (see Subsection 5.2.6). In more detailed terms, the figure demonstrates that the one-batch model give satisfactory results in simulating the multi-batch cycle reactivity evolution, compared to a more sophisticated treatment. The advantage of the 2D treatment has to be seen mainly in the reduced computational time. A similar reactivity evolution for the average batch provides the indication that the amount of fission products within the fuel is comparable for the two model descriptions.

Similarly, there is a good agreement in the fuel Doppler reactivity effect for the second fuel batch (see Figure E.9). Thus, the 2D treatment is seen to yield satisfactory results as regards the important parameters verified, viz. core reactivity and fuel Doppler effect, due principally to the relatively small amount of fission products within the core.

D. Data provided to the PARCS/TRACE model

To study the transient behavior of the GFR core under equilibrium cycle conditions, a 3D core model was first constructed in ERANOS, taking into account the BOEC material compositions as presented in Table E.2 for the all-actinides recycling strategy ("envelope case"). This enabled one to provide to PARCS the self-shielded cross-sections and their derivatives with respect to state variables (fuel temperature, coolant density and thermal expansions). The derivatives were produced with the ECCO cell code, in the same manner as used for the fresh fuel composition (see Section 5.2.1).

E. Summary

The fuel cycle calculations for the reference "2004-Core" design have been presented in this appendix, along with a description of the computational tools developed and used for the purpose. Thus, the 2D fuel burnup procedure applied for obtaining the fuel compositions at BOEC has been presented, along with the main assumptions made thereby. Specific features have been discussed, such as the burnup chain, the fuel management scheme and recycling options, etc. In particular, two recycling options have been considered: (1) the recycling of all actinides and (2) the recycling of only the uranium and plutonium. The impact of these two options on the safety-related and kinetics parameters has been assessed.

Verification of the 2D fuel cycle analysis was performed on the basis of a 3D core geometry description. Good agreement was obtained between the models for the average fuel batch, as regards the evolution with burnup of the core reactivity and the fuel Doppler effect. Based on the BOEC material compositions obtained, an appropriate PARCS/TRACE model was developed in order to simulate CA withdrawal and ejections transients. The results of the transient analysis associated with a GFR core with fuel corresponding to fuel at BOEC are presented in Subsection 5.6.3.

References

1. World Nuclear association, http://www.world-nuclear.org, 2007.
2. Rapport annuel 2007, Forum nucléaire suisse - Nuklearforum Schweiz, 2008.
3. PRIS, Power Reactor Information System, http://www.iaea.org/programmes/a2/, 2008.
4. Forum Nucléaire suisse - Nuklearfroum Schweiz, Brunod Pellaud, 2007.
5. Forum Nucléaire suisse - Nuklearforum Schweiz, Rapport annuel 2008, 2009.
6. CEA ELECNUC, Les centrales nucléaires dans le monde, Nuclear power plants in the World, Edition 2006, 2006.
7. Journal, BBC News, http://news.bbc.co.uk/, April 2007.
8. Teollisuuden Voima Oyj (TVO), http://www.tvo.fi/www/page/etusivu_en/, 2007.
9. Forum nucléaire suisse - Nuklearforum Schweiz, Bulletin 1, January, 2008.
10. Communiqué de presse. Electricité de France (EDF), December 4, 2007.
11. Forum Nucléaire suisse - Nuklearforum Schweiz, Bulletin 2, February, 2008.
12. Conférence Générale, IAEA, 22 juillet 2008, Rapport d'ensemble sur la technologie nucléaire, 2008.
13. Forum Nucléaire suisse - Nuklearforum Schweiz, Feuille d'information, January, 2008.
14. Trade Tech Uranium Info, http://www.uranium.info/index.cfm?go=c.page&id=36, March, 2008.
15. N. Fujimoto et al., "Nuclear design", Nuclear Engineering and Design 233, 23-36, 2004.
16. V. Seker and U. Colak, "HTR-10 full core first criticality analysis with MCNP", Nuclear Engineering and Design 222, 263-270, 2003.
17. K. Kugeler and R. Schulten, "Hochtemperaturreaktortechnik", Springer-Verlag, 1986.
18. L. Massimo, "The Physics of High-Temperature Reactors", Oxfrord, Pergamon Press, 1976.
19. EFR Core data file, Novatome Technical Document, EFR C10551087D, 1993.
20. G. Melese and R. Katz, "Thermal and Flow Design of Helium Cooled Reactors", ANS, La Grange Park, 1976.

21. M. Cometto, P. Wydler, R. Chawla, "A Comparative Physics Study of Alternative Long-term Strategies for Closure of the Nuclear Fuel Cycle", Annals of Nuclear Energy 31, 413-429, 2004.
22. J.P. Crette, "Review of the Western European Breeder Programs", Energy Vol. 23, No 7-8, 581-591, 1998.
23. W. Marth and M. Koehler, "The German Fast Breeder Program (a historical review)", Energy Vol. 23, No 7/8, 593-608, 1976.
24. Nuclear Power Technology Development Section, IAEA, 2005.
25. J. Guidez and L. Martin, "Bilan de l'expérience de fonctionnement des rapides à sodium dans le monde et applications à la conception des futurs réacteurs", RGN Revue Générale Nucléaire, Mai-Juin 2007, 2007.
26. G. Flamenbaum et al., “Analysis of Specific Control Rod Experiments Involving Highly Distorted Flux Distributions”, Nuclear Science and Engineerig 106, 64-68, 1990.
27. Le Rigoleur, "Fast Reactor Development programme in France", CEA, AIEA-TECDOC 876.
28. Le démarrage de Superphénix et la filière des réacteurs à neutrons rapides, Revue Générale Nucléaire, Mai-juin, Vol. 3, 1987.
29. La centrale de Creys-Malville. Electricité de France, Direction de l'Equipement, Région D'équipement Alpes-Lyon, 1982.
30. J. Gourdon et al., "An Overview of Superphénix Commissioning Tests", Nuclear Science and Engineering 106, 1-10, 1999.
31. M. Vanier, P. Bergoenneau and J.C. Gauthier, "Superphénix Reactivity and Feedback Coefficients", Nuclear Science and Engineering 106, 30-36, 1990.
32. J.C. Cabrillat and M. Martini, "Power and Neutron Flux Distributions in the Core and Shielding", Nuclear Science and Engineering 106, 37-46, 1990.
33. J.C. Lefève, C.H. Mitchell and G. Hubert, "European fast reactor design", Nuclear Engineering and Design 162, 133-143, 1996.
34. A Technology Roadmap for Generation IV Nuclear Energy Systems: Technical Roadmap Report, December, 2002.
35. Gen IV International Forum, http://www.gen-4.org/.
36. U.S. Department of Energy, http://www.doe.gov/, Press Release July 13 2007, 2007.
37. http://www.iaea.org/INPRO, 2008.
38. IAEA, Methodology for the assessment of innovative nuclear reactors and fuel cycles, International Project on Innovative Nuclear Reactors and Fuel Cycles (INPRO), IAEA-TECDOC-1434, 2004.
39. http://www.genep.energy.gov/, 2007.
40. J.C. Garnier, "The Gas Fast Reactor Project", CEA, CAPRA-CADRA Seminar, 5-7 April, 2004.

41. K.V. Weaver and H.S. Khalil, "Gas Cooled Fast Reactor (GFR)", Amercian Nuclear Society, Winter Meeting, 2002.

42. J.C. Bosq, A. Conti, G. Rimpault, J.C. Garnier, "Methodology for a Large Gas-Cooled Fast Reactor Core Design and Associated Neutronic Uncertainties", PHYSOR-2004, Chaicago, April 25-29, 2004.

43. J.C. Garnier, C. Poette, B. Mathieu, A. Conti and J.P. Gaillard, "Preliminary design of an advanced Gas cooled Fast Reactor core, fuel forms and primary system concept", Proceedings of ICAPP'03, Cordoba, Spain, May 4-7, 2003.

44. Gas-cooled Fast Reactor Concept Review Studies, European Commission 5th Framework Programme, October, 2002.

45. R. Jacqmin, "Gas-cooled Reactor Core Physics R&D Activities in France", Gen-IV Reactor Physics Workshop, Chicago, April 30, 2004.

46. C. Bassi. “Core transient behavior of the Gas Cooled Fast Reactor”, Proceedings of International Congress on Advances in Nuclear Power Plants, ICAPP’03, Cordoba, Spain, May 4-7, 2003.

47. P. Dumaz et al., "Gas-cooled fast reactors - Status of CEA preliminary design studies", Nuclear Engineering and Design 237, 1618-1627, 2007.

48. R.H. Jones et al., “Recent advances in the development of SiC/SiC as a fusion structural material”, Fusion Engineering and Design, 41, 15–24, 1998.

49. J.Y. Doriath et al., "ERANOS 1: The Advanced European System of Codes for Reactor Physics Calculations", Joint Conference on Mathematical Methods and Supercomputing in Nuclear Appplications, Kalrsruhe, Germany, 1993.

50. R. Richmond, "The Swiss Programme in the Field of Fast Reactor Physics", EIR Internal Document, TM-PH-338, 1969.

51. M. Dalle Donne and C.A. Goetzmann, "Gas cooled fast breeder reactor design, development, and safety features", In Gas-cooled reactors: HTGR and GCFBR, ANS, Hindsale, USA, 1974.

52. Gas-Cooled Fast Breeder Reactor Demonstration Plant Nuclear Steam Supply System, Project Staff, Gulf General Atomic, Report GA-10064, May 15, 1970.

53. T.D. Newton, "Core Design Studies to Establish a Helium Cooled Pin Particulate Fuelled Core Design", CAPRA-CADRA Seminar, April 5-7, 2004.

54. R. Richmond, "Measurement of the Physics Properties of Gas-Cooled Fast Reactors in the Zero Energy Reactor PROTEUS and Analysis of the Results", EIR Internal Document, EIR Nr. 478, 1982.

55. F. Mellier, "The ENIGMA programme in MASURCA, status on experimental planning", GCFR Reactor Physics Meeting, CEA, Cadarache, March, 2006.

56. P. Fougeras, "Experimental Programs Laboratory, The PLace of EOLE, MINERVE and MASURCA facilities in the R&D activities of the CEA", CEA, Cadarache.

57. J. Tommasi,"GCFR physics experiments in MASURCA, Presentation EU-FP6, DEN/DER/SPRC/LEPh, January 6, 2004.

58. J. Tommasi, “The ENIGMA Program in MASURCA: Motivation and Presentation”, Technical Note, CEA-Cadarache, CEA/DEN/CAD/DER/SPRC/LEPH 04-207, February, 2005.

59. J. Tommasi, "Capacités de modélisation neutroniques des RCG-R avec ERANOS: état des lieux et besoins", Note Technique, CEA-Cadarache, CEA/DER/SPRC/LEPh 02-206, Avril, 2002.

60. J. Tommasi, "Configuration de MASURCA en soutien aux projets de RCG-R: étude de représentatitvité", Note Technique, CEA-Cadarache, CEA/DER/SPRC/LEPh 02-229, Mars 2003, 2003.

61. J. Tommasi, "Motivation et Proposition d’un programme experimental en support au RCG-G et au REDT dans MASURCA", Note Technique, CEA-Cadarache, CEA/DER/SPRC/LEPH 03-208, Juin, 2003.

62. G. Aliberti, G. Palmiotti and J. Tommasi, "Impact of Spectral Transition Zone in Reference ENIGMA Configuration", ANL-GenIV-053, Nuclear Engineering Division, Argonne National Laboratory, August 31, 2005.

63. J.C. Garnier et al., "Feasibility study of an advanced GFR, design trends and safety options status of France & US studies", Proceedings of International Conference GLOBAL 2003, Atoms for Prosperity: updating Eisenhower’s global vision for nuclear energy, New Orleans, Louisiana, 2003.

64. C. Mitchell et al., "Gas Cooled Fast Reactor Concept Review Studies (GCFR)", Proceedings of International Congress on Advances in Nuclear Power Plants, ICAPP ’03, Cordoba, Spain, May 4-7, Paper 3167, 2003.

65. F. Morin, "Preliminary Design of ETDR D10 Task 1.2", CEA/DEN/DER/SESI/LCSI/NT DO 15/05/2006, 2006.

66. C. Mitchell, "Final Technical Report, Gas Cooled Fast Reactor (GCFR)", EC 5th Framework Programme, ailable from http://www.cordis.lu/fp5-euratom/src/lib_finalreports.htm. 2002, NNC/C6395/TR/0012, Issue 1, October, 2002.

67. C. Poette, "ETDR Design Status at launch of the GCFR FP6 Project", ETDR Design, GCFR-DEL-001, Work Package 1.2, 2005.

68. J.C. Klein, "Detailed Physics Studies of the ETDR Start-up core", ETDR Design, GCFR-DEL-18, Work Package 1.2, 2006.

69. J.C. Bosq, “Proposal of general data and assumptions for the ETDR Start-up core detailed studies”, ETDR Integration, Design and Safety, GCFR-NCD-301, Work Package 1.2, 2005.

70. F. Morin, "Etudes préliminaires de la cuve du réacteur du REDT", Note Technique, CEA-Cadarache, DEN/CAD/DER/SESI/LCSI/NT DO 23, March, 2004.

71. D. Fovargue, "ETDR Control and Instrumentation, ETDR Design", GCFR-NCD-302, Work Package 1.2, 2006.

72. Les réacteurs nucléaires à caloporteur gaz, Commissariat d'énergie atomique (CEA), ISBN10 : 2-281-11317-5, Imprimerie Nationale, 2007.

73. T. Temitope, "U.S.: Summary of 2003 Gen IV Reactor Physics Workshops", Argonne National Laboratory, Chicago, Illinois, April 30, 2004.

74. P. Martin, N. Chauvin, J.C. Garnier, M. Masson, P. Brossard and P. Anzieu, "Gas Cooled Fast Reactor System: Major Objectives and Options for Reactor Fuel and Fuel Cycle", Proceedings of GLOBAL 2005, Paper No. IL002, Tsukuba, Japan, October 9-13, 2005.

75. N. Chauvin et al. "GFR fuel and core pre-conceptual design studies", GLOBAL 2007, Boise, Idaho, September 9-13, 2007.

76. J.P. Gaillard, G. Mignot, A. Conti, “Thermal-hydraulic design of a Gas Cooled Fast Reactor”, Proceedings of International Congress on Advances in Nuclear Power Plants, Proceedings of ICAPP’03, Cordoba, Spain, May 4-7, 2003.

77. E.A. Hoffman and T.A. Taiwo, “Physics Studies of Preliminary Gas-Cooled Fast Reactor Designs”, Proceedings of Global 2003, New Orleans, LA November 16-20, 2003.

78. J.C. Bosq et al., "Fine 3D neutronic characterization of a gas-cooled fast reactor based on plate-type sub-assemblies", ANS, Topical Meeting on Reactor Physics, PHYSOR-2006, Vancouver, 2006.A. Lüthi, "Les fichiers de dégagement d’énergie d’ERANOS", CEA-Cadarache, Note technique, SPRC/LEPh 97-231, 1997.

79. A. Torri and M. Driscoll, "Reactivity Insertion Mechanisms in the GCFR", GA-A12934, 1974.

80. G. Rimpault, J.C. Bosq, J.C. Garnier, "A feasibility study on a 600 MWth Gas-cooled Fast Reactor core", CEA, CAPRA-CADRA Seminar, April 5-7, 2004.

81. J.C. Garnier et al., "Status of GFR pre-conceptual design study", Proceedings of ICAPP 2007, Nice, France, May 13-18, 2007.

82. J. Rouault and T.Y.C. Wei, "The Gen-IV gas-cooled fast reactor, status of studies", Proceedings of Workshop on Advanced Reacors with Innovative Fuels, ARWIF, Oak Ridge, USA, 2005.

83. F. Carré et al., "Overview of the CEA program on high temperature gas-cooled nuclear energy systems: the gas “technology” path”, Proceedings of International Conference GLOBAL 2003, Atoms for Prosperity: updating Eisenhower’s global vision for nuclear energy, New Orleans, Louisiana, 2003.

84. D.F. da Cruz et al., "Neutronic benchmark on the 2400 MW gas-cooled fast reactor design", September 10-14 2006, PHYSOR'06, Vancouver, Canada, 2006.

85. K. Mikityuk et al., "FAST: An advanced code system for fast reactor transient analysis", Annals of Nuclear Energy, Vol. 32/15, 1613-1631, 2005.

86. K. Mikityuk and P. Fomitchenko, "FRED: Calculational Model of Fuel Rod Behavior Under Accident Conditions Coupled with RELAP5/MOD3". Proceedings of 8th International Conference on Nuclear Engineering, ICONE-8, Baltimore, MD USA, 2000.

87. G. Rimpault et al., "The ERANOS Data and Code System for Fast Reactor Neutronic Analyses", Proceedings of International Conference On the New Frontier of Nuclear Technology: Reactor Physics, Safety and High-Performance Computing, PHYSOR, Seul, Korea, 2002.

88. G. Palmiotti, J.M. Rieunier, C. Gho, M. Salvatores, "BISTRO Optimized Two Dimensional Sn Transport Code", Topical Meeting on Advances in Reactor Physics, Mathematics and Computation, Paris, France, April, 1987.

89. G. Palmiotti et al., "VARIANT: Variational Anisotropic Nodal Transport for Multidimensional Cartesian and Hexagonal Geometry Calculation", Technical Report, ANL-95/40, Argonne National Laboratory, 1995.

90. H.G. Joo et. al., "PARCS, A multi-Dimensional Two-Group Reactor Kinetics Code Based on the Nonlinear Analytic Nodal Method", PU/NE-98-26, 1998.

91. G. Rimpault., "Algorithmic Features of the ECCO Cell Code for Treating Heterogeneous Fast Reactor Subassemblies", International Topical Meeting on Reactor Physics and Computations, Portland, Oregon, May 1-5, 1995.

92. F. Odar et al., "TRACE V4.0 USER’S MANUAL", U.S. Nuclear Regulatory Commission, Office of Nuclear Regulatory Research, 2003.

93. K. Mikityuk et al., "LOOP2: Comprehensive Transient Code for Advanced Nuclear Reactors", Proceedings of PHYSOR, Seoul, Korea, October 7-10, 2002.

94. K. Mikityuk, " Modifications made in the TRAC-M/AAA code including introduction of the FRED fuel rod model", PSI Report TM-41-03-18, June 2003.

95. J.M. Ruggieri, "ERANOS 2.1: International Code System for GEN IV Fast Reactor Analysis", Proceedings of ICAPP'06, Reno, NV USA, June 4-8, 2006.

96. C.J. Dean, C.R. Eaton, P. Peerani, P. Ribon, G. Rimpault, “Production of Fine Group Data for the ECCO Code”, International Conference on the Physics of Reactors: Operation, Design and Computation", PHYSOR’90 International Conference, Marseille, France, Marseille, France, April 23-27, 1990.

97. E. Fort et al., "Improved performances of the fast reactor calculational system ERANOS-ERALIB1 due to improved a priori nuclear data and consideration of specific additional data", Annals of Nuclear Energy 30, 1879-1898, 2003.

98. A. Rineiski, "KIN3D: A space-time kinetics and perturbation theory module for TGV2", Note Technique, CEA-Cadarache, SPRC-LEPH, 97-203.

99. D. Honde et al., "ERANOS: Manuel des Méthodes, Les calculs de perturbations et les analyses de sensibilité", Note Technique, CEA-Cadarache, SPRC/LEPh 96-205, 1996.

100. G.I. Bell and S. Glasstone, "Nuclear Reactor Theory", ISBN 0-88275-790-3, 1970.

101. J.F. Briesmeister, "MCNP – A general Monte Carlo N-particle Transport Code, Version 4C", LA-13709-M, April 2000, 2000.

102. H.G. Hughes et al., "MCNPX for Neutron-Proton Transport, International Conference on Mathematics & Computation, Reactor Physics & Environmental. Analysis in Nuclear Applications", American Nuclear Society, Madrid, Spain, September 27-30, 1999.

103. S. Hendricks, "MCNPX26F Extensions", Los Alamos National Laboratory, LA-UR-08-1808.

104. MCNPX User's Manual, Version 2.4.0, LA-CP-02-408, Septemeber 2002, 2002.

105. M. B. Chadwick, P. G. Young, S. Chiba, S. C. Frankle, G. M. Hale, H. G. Hughes, A. J. Koning, R. C. Little, R. E. MacFarlane, R. E. Prael, and L. S. Waters, "Cross Section Evaluations to 150 MeV for Accelerator-Driven Systems and Implementation in MCNPX", Nuclear Science and Engineering 131, Number 3, 293, 1999.

106. C. Thévenoz and D. Haubensack, "Présentation de COPERNIC_4_00", Note Technique, CEA-Cadarache, CEA/DEN/CAD/DER/SESI/LESA/NT DO 26 26/09/06, 2006.

107. J.Y. Cho et al., "Hexagonal CMFD Formulation Employing the Triangular Polynomical Expansion Method", Mathematics and Computation International ANS Meeting, Salt Lake City, September, 2001.

108. R. Boer and H. Finnemann, "Fast Analytical Flux Reconstruction Method for Nodal Space-Time Nuclear Reactor Analysis", Annals of Nuclear Engineering 91, 123, 1985.

109. P. Brantley and E. Larsen, "The Simplified SP3 Approximation", Nuclear Science and Engineering 134, 1-21, 2000.

110. T.M. Sutton, "Wielandt Iteration as Applied to the Nodal Expansion Method", Nucl. Sci. Eng. 98, 169-173, 1988.

111. E. Bubelis, P. Coddington, K. Mikityuk, S. Pelloni, "Enhancement of the PARCS, TRAC/AAA and ERANOS codes for use within the FAST code system", Technical Note TM-41-05-21, Paul Scherrer Institut, 2005.

112. J.W. Spore et al., "TRAC-M/FORTRAN 90 (VERSION 3.0) THEORY MANUAL", LA-UR-00-910, July, 2000.

113. G. Girardin et al., "Comparative Analysis of the Reference GCFR-PROTEUS MOX Lattice with MCNPX-2.5e and ERANOS-2.0 in conjunction with Modern Nuclear Data Libraries", ANS, Topical Meeting on Reactor Physics, PHYSOR-2006, Vancouver, 2006.

114. G. Girardin, "Review of the GCFR-PROTEUS Experimental Programme", PSI Internal Report, TM 41-05-01, July 2005.

115. G. Girardin, P. Coddington, "A 2D Model of the GCFR-PROTEUS Reactor", PSI Internal Report, AN-41-06-07, October 2006.

116. G. Girardin, S. Pelloni, P. Coddington, “Analysis of ECCO/MCNPX Cell Calculation with modern nuclear data libraries for the Reference GCFR-PROTEUS MOX Lattice”, PSI Internal Report, TM 41-05-25, February 2006.

117. M. Jermann et al., "Comparison of Measured and Calculated Values of Neutron Spectra and Reaction Rate Ratios in Gas-Cooled Fast Reactor Benchmark lattices", EIR Report No. 298, 1976.

118. W. Heer and P. Wydler, "PROTEUS, Das schnell-thermishe SYSTEM PROTEUS; theoretische Ergebnisse", EIR International Document, TM-PH-404-4, 1972.

119. W. Heer and P. Wydler, “PROTEUS, Das schnell-thermishe SYSTEM PROTEUS; theoretische Ergebnisse”, EIR Internal Document, TM-PH-404, 1973.

120. R. Chawla et al., "Fast Reactor Experiments with Thorium at the PROTEUS Facility", EIR Report No. 444, 1981.

121. R. Richmond et al., "Measurements of Neutron Spectrum and Reaction Rates in a Gas-Cooled Fast Reactor Lattice", EIR Report No. 239, 1973.

122. W. Heer and R. Richmond, "Details of PROTEUS Core 3", EIR Internal Document, M-PH-152, 1976.

123. W. Heer and C. McCombie, "Specification and comparison of some models of the PROTEUS mixed critical system", TM-PH-597, 1976.

124. K. Gmür, "Techniques of Reaction Rate Measurement in the PROTEUS Reactor”, EIR Report No. 529, 1984.

125. W. Heer and C. McCombie, "Calculation of a Mixed Lattice Using the Code MURAL", EIR Internal Document, TM-PH-535, 1975.

126. J.T. Murgatroyd et al., "Optimisation of the CO2 cooled fast reactor for plutonium and minor actinide management", Proceedings of the ENS 2002, World Nuclear Expo, Lille, France, 2002.

127. J.C. Bosq and M. Vanier, "Caractérisation neutronique 3D d'un coeur de RNR-G à plaques", Note technique, CEA-Cadarache, SPRC/LEDC 2005-416 Ind. 0, Février, 2006.

128. G. Girardin, P. Coddington, F. Morin, G. Rimpault, "A Control Rod Design for the 2400 MWth Gas-cooled Fast Reactor", Report TM-41-06-19, Paul Scherrer Institut, 2 November, 2006.

129. G. Girardin, P. Coddington and G. Rimpault, "Control Rod Shadowing and Anti-shadowing Effects in a Large Gas-cooled Fast Reactor", Report TM-41-06-20, Paul Scherrer Institut, 12 October, 2006.

130. G. Girardin, P. Coddington, F. Morin, G. Rimpault, "Développement d’un dessin hétérogène de barre de commande pour le RNR-G de 2400 MWth", Note Technique, CEA-Cadarache, SPRC/LEDC/06-419, CEA-Cadarache, 17 novembre, 2006.

131. G. Girardin, P. Coddington, G. Rimpault, "Effets d’ombre et d’anti-ombre entre les barres de commande du RNR-G de 2400 MWth", CEA-Cadarache, Note Technique SPRC/LEDC/06-420, CEA-Cadarache, 17 novembre, 2006.

132. G. Girardin, G. Rimpault, P. Coddington and R. Chawla. "Control Rod Shadowing and Anti-Shadowing Effects in a Large Gas-cooled Fast Reactor", Proceedings of ICAPP'07, Paper 7329, Nice Acropolis, France, May 13-18, 2007.

133. G. Girardin, P. Coddington, F. Morin, G. Rimpault, R. Chawla. "Design of the control rod system for the 2400 MWth Generation IV Gas-cooled Fast Reactor", ICONE-10466, 15th International Conference on Nuclear Engineering, Nagoya, Japan, April 22-26, 2007.

134. G. Girardin et al. "Development and Characterization of the control assembly system for the large 2400 MWth generation IV gas-cooled fast reactor", Annals of Nuclear Energy 35, 2206–2218, 2008.

135. P. Petkevich, "Development and Application of an Advanced Fuel Model for the Safety Analysis of the Generation IV Gas-cooled Fast Reactor", Thèse EPFL N° 4180, 2008

136. S. Czernecki and J.M. Rieunier, "ERANOS: Manuel des méthodes, Les conditions de fonctionnement", Note Technique, CEA-Cadarache, SPRC/LEPh 99-213, 1999.

137. G. Rimpault, D. Calamand, P. Peerani, J.M. Rieunier and D. Honde, "Documentation of ERANOS 1.1, Energy Release and Displacement Damage Dose Calculations", Note Technique, CEA-Cadarache, DER/SPRC/LEPh/93-236, Cadarache, 1993.

138. A. Lüthi, "Development and validation of gamma-heating calculational methods for plutonium-burning fast reactors", Thèse EPFL N° 1854, 1999.

139. A. Lüthi, “Les fichiers de dégagement d’énergie d’ERANOS”, CEA-Cadarache, Note technique, SPRC/LEPh 97-231, 1997.

140. Y. Tachibana, H. Sawahata, T. Iyoku, T. Nakazawa, "Reactivity control system of the high temperature engineering test reactor", Nuclear Engineering and Design 233, 89-101, 2004.

141. T. Taryo et al., "Investigation on Control Rod Interaction in a Conceptual MTR-Type Reactor", IAEA-CN-100/90P, Research Reactor Utilization, Safety, Decommissioning, Fuel and Waste Management, International Conference, Santiago, Chile, November, 2003.

142. M. A. Ghafoor and P. J. Grant, "An experimental study of the interactions between control rods in a subcritical assembly", Brit. J. Appl. Phys., Vol. 15, 1964.

143. M. Itagaki et al., "Control-Rod Interference Effects Observed During Reactor Physics Experiments With Nuclear Ship MUTSU", J. Nucl. Sci. Technol. (Jpn.), Vol. 30, no. 5, 465-476, 1993.

144. T. Kitada and T. Takeda, "Evaluation of Eigenvalue Separation by the Monte Carlo Method", Journal of Nuclear Science and Technology, Vol. 39, No. 2, February, 129-137, 2002.

145. G. Aliberti, "Caractérisation neutronique des systèmes hybrides en regimes stationnaire et transitoire", Thèse de l'Université Louis Pasteur de Strasburg, Octobre, 2001.

146. G. Rimpault and J.C. Bosq, "Plans for GCFR physical investigation studies", GFR Reactor Physics Meeting, CEA-Cadarache, March, 7, 2006.

147. J. Tommasi, "Procédure d’équivalence en réactivité des barres de commande avec description automatisée de leur géométrie hétérogène", Note Technique, CEA-Cadarache, SPRC/LePh 06-203, 2006.

148. P. Smith and T. Newton, "Control Rod Heterogeneity Effects in the ETGCFR Core", AEA-Technology Report.

149. J.C. Gauthier et al., “Measurements and Predictions of Control Rod Worth”, Nuclear Science and Engineering 106, 18-29, 1990.

150. Novatome, EFR Core Variant 3 - Absorber efficicency in the single batch core, Technical Document EFR C1055155A, 1988.

151. J.C. Garnier, R. Sunderland, T. Newton. E. Kiefhaber, D. Verrier, "CAPRA Preliminary feasability studies - Oxide Reference Option: Neutronics and Design Studies", Technical Report DER/DIS/CAPRA/94-003.

152. Design of the Reactor Core for Nuclear Power Plants, IAEA Safety Standards, Safety Guide No. NS-G-1.12.

153. G. Girardin, K. Mikityuk, P. Coddington, R. Chawla, "A 3D Full-Core Coupled Thermal-hydraulics/Kinetics TRACE/PARCS Model of the 2400 MWth Generation IV Gas-cooled Fast Reactor", Proceedings of International Conference on the Physics of Reactors "Nuclear Power: A Sustainable Ressource", Interlaken, Switzerland, September 14-19, 2008.

154. G. Girardin, D. Blanchet, K. Mikityuk, G. Rimpault and R. Chawla, "Three-dimensional core behaviour analysis of the Gas-cooled Fast Reactor (GFR) during hypothetical control assembly withdrawal accidents", Vols. ICONE-17, 17th International Conference on Nuclear Engineering, Brussels, Belgium, July 12-16, 2009.

155. S. Pelloni, E. Bubelis, K. Mikityuk, P. Coddington, "Calculations of Reactivity-initiated Transients in Gas-cooled Fast Reactors Using the Code System FAST", Annals of Nuclear Energy, Volume 33, 499-509, 2006.

156. J.H. Kim, W.H. Li, "Heat Transfer in laminar flow along circular rods in infinite square arrays", Vol. 110:1, 1988.

157. M.S. El-Genk, B. Su, Z. Guo, "Experimental studies of forced, combined and natural convection of water in vertical nine-rod bundles with a square lattice", Issue 9, 2359-2374, International Journal of Heat and Mass Transfer, Vol. 36, 1993.

158. S.W. Churchill, R. Usagi, "A General Expression for the Correlatiojn of Rates of Transfer and Other Phenomena", American Institute of Chemical Engineers, Vol. 18, 1121-1128, 1972.

159. D.K. Edwards, V.E. Denny, A.F. Mills, "Transfer processes: an introduction to diffusion, convection, and radiation", edition 2, McGraw-Hill, Washington, Hemisphere Publishing Corporation, 1979.

160. F. Bentivoglio, "Validation of the CATHARE2 code against experimental data from Brayton-cycle plant", Nuclear Engineering and Design, Vol. 238, 3145-3159, 2008.

161. N. Tauveron et. al., "Steady-state and transient simulations of Gas Cooled Reactor with the computer code CATHARE", Proceedings of The 10th International Topical Meeting on Nuclear Reactor Thermal Hydraulics, NURETH-10, Seoul, Korea, October 5-9, 2003.

162. K. Mikityuk, "FAST: An advanced code system for fast reactor transient analysis", Annals of Nuclear Enrgy 32, 1613-1631, June, 2005.

163. A. Dall'Osso, "Reducing rod cusping effect in nodal expansion method calculations", Proceedings of the International Conference on the New Frontiers of Nuclear Technology: Reactor Physics, Safety and High-Performance Computing, PHYSOR 2002, Seoul, 2002.

164. J.Y. Malo, P. Anzieu, C. Mitchell, P. Coddington, N. Alpy, F. Bertrand, N. Chauvin, P. Dumaz, F. Morin, C. Poette, P. Richard, "Gas cooled fast reactor, preliminary viability report: main part", Note Technique, CEA-Cadarache, DR 5 05/12/07, 2007.

165. P. Petkevich, K. Mikityuk, P. Coddington, R. Chawla, "Development and benchmarking of a 2D transient thermal model for GFR plate-type fuel", Annals of Nuclear Energy 34, 707-718, 2007.

166. A. Epiney et al., “Comparative transient of the 2400 MWth GFR with TRACE and CATHARE codes”. International Conference on the Physics of Reactors "Nuclear Power: A Sustainable Ressource", Casino-Kursaal Conference Center, Interlaken, Switzerland, September 14-19, 2008.

167. J.C. Bosq, R. Soule, M. Vanier ,"Caractérisation neutronique de RCG chargés avec actinides mineurs", Note Technique, CEA-Cadarache, NT/SPRC/LEDC/04/414, 2004.

168. Gas Cooled Reactor Design and Safety, International Atomic Energy Agency (IAEA), ISBN 92-0-155090-1, Vienna, 1990.

169. S.K. Bhattacharyya, "An experimental study of the neutronics of the first gas cooled fast reactor bench-mark assembly, GCFR phase I assembly", Washington, 1976.

170. United Kingdom Atomc Energy Authority (UKAEA). History of Windscale's Advanced Gas-cooled Reactor.

171. Kernergie in Deutschland, http://www.kernenergie.de/r2/de/, 2007.

172. S. Fujikawa, "Achievement of Reactor-Outlet Coolant Temperature of 950.DEG.C in HTTR", J. Nucl. Science Technology, 41, 1245-1254, 2004.

173. U. Schmocker and S. Seth, "Das 2D-Modell der Nullreaktivitätsgitter 6, 7, 8 und 10 des PROTEUS-Reaktors", EIR Internal Document, TM-PH-713, 1978.

174. S. Seth and P. Wydler, "GCFR Benchmarks : Experiments and Analysis", 1975, Proceedings of Conference Nuclear Cross-Sections and Technology, Paper FA23, Washington, D.C., National Bureau of Standard, March, 1975.

175. W. Heer, "Einfluss von Aenderungen beim PROTEUS 3", EIR Internal Document, M-PH-121A, 1975.

176. M. Jermann, “PROTEUS Experimental Results (Core 3) – Neutronspektrumsmessungen im Zentrum von Core 3”, EIR Internal Document, TM-PH-554, 1975.

177. C. McCombie, "Intercomparison of transport and diffusion theory calculations for a large 2D reactor and shield model", EIR Internal Document, TM-PH-589, 1976.

178. S. Seth and R. Richmond, "Measurement and Calculation of Integral Cross-Section Ratios in a Central Breeder Zone in a GCFR Lattice", ANS Transactions, 21, 460, 1975.

179. R. Richmond and S. Seth, "Experiments with Simulated Power Reactor Features in the PROTEUS GCFR Lattice", ANS Transactions, 33, 1975.

180. C. McCombie et al., "Effect of Steam Entry into a GCFR Core", Proceedings of the International Meeting on Fast Reactor Safety and Related Physics, Chicago, Illinois, October 5-8, 1976.

181. W. Heer et al., “Simulation of Steam Entry in the PROTEUS GCFR Lattice”, ANS Transactions, 22, p. 700, 1975.

182. C. McCombie et al., "Assessment of Iron and Steel Cross-Section data for Shielding by Integral Experiment, Measurement and Analysis", ANS, Proceedings of Topical Meeting on Advances in Reactor Physics, Galtinburg, USA, 53, 1978.

183. C. McCombie, "Reactivity Calculations for the PROTEUS Steam Entry cores 4, 4a and 5", EIR Internal Document, TM-PH-615, 1976.

184. G. Brunson, "PROTEUS Experimental Results Reactivity Measurements in Core 6", EIR Internal Document, TM-PH-616, 1976.

185. S. Seth and U. Schmocker, "Determination of the Integral Capture Cross-Sections of Steel and Iron from the Neutron Balance in PROTEUS k-infinity ~ 1 GCFR Cores 6, 7 and 8", EIR Internal Document, TM-PH-683, 1977.

186. K. Gmür, "PROTEUS Experimental Results Cores 6, 7, 8", EIR Internal Document, TM-PH-624, 1976.

187. S. Seth, "Planning and Design of Null Reactivity Cores 6, 7 and 8 in Reactor PROTEUS", EIR Internal Document, TM-PH-618, 1976.

188. C. McCombie et al., "Benchmark Shielding Experiments for testing iron and steel data", Shielding Bechmark Programme, Proceedings of ANS Topical Meeting on Advances in Reactor Physics, Galtinburg, USA, 53, 1978.

189. G. Brunson, "Reactivity Measurements in PROTEUS, Cores 7 & 8", EIR Internal Document, TM-PH-617, 1976.

190. S. Seth, "The interpretation of Experiments on the PROTEUS Null-reactivity GCFR Lattices in Terms of Single-zone Parameters", EIR Internal Document, TM-PH-637, 1977.

191. S. Seth and U. Schmocker, "Analysis of PROTEUS Core 10 and Determination of the Iron Capture Cross-section", EIR Internal Document, TM-PH-694, 1977.

192. R. Chawla and K. Gmür, "Comparison of Th-232 (n, 2n)/(n, gamma) Ratio measurements in Various PROTEUS Cores", EIR Internal Document, TM-PH-812, 1979.

193. M. Jermann, "PROTEUS Experimental Results (Core 12) – Neutronenspektrums-messungen im Zentrum von Kern 12", EIR Internal Document, TM-PH-759, 1978.

194. U. Schmocker and P. Bourquin, "PROTEUS Experimental Results: Reaktivitätsmessungen in Core 12", EIR Internal Document, TM-PH-727, 1978.

195. K. Gmür, "PROTEUS Experimental Results Core 12", EIR Internal Document, TM-PH-725, 1978.

196. U. Schmocker, "Berechnung Radialer Reaktionsratenprofile im PROTEUS Core 13 und die Bestimmung einiger Reaktionsratenverhältisse im Zentrum der ThO2 Brutzone", EIR Internal Document, TM-PH-802, 1979.
197. K. Gmür, "PROTEUS Experimental Results Core 13", EIR Internal Document, TM-PH-741, 1978.
198. K. Gmür, "PROTEUS Experimental Results for Cores 14 and 16: F9-Cadmiumverhaeltnis in Th-Blankets", EIR Internal Document, TM-PH-845, 1979.
199. J.R. White and D.T. Ingersoll, "Analysis of the Thorium Axial Blanket Experiments in the PROTEUS Reactor", Report ORNL/TM-7471, 1980.
200. U. Schmocker, "Berechnung axialer Reaktionsratenprofile im PROTEUS Core 14", EIR Internal Document, TM-PH-797, 1979.
201. K. Gmür, "Programm für Reaktionsratenmessungen nach Folienaktivierungsmethode im ThO2-Blanket (Core 14)", EIR Internal Document, TM-PH-183, 1978.
202. M. Jermann, "Neutronenspektrumsmessungen im axialen Th-Blanket des PROTEUS-Reaktors (Core 14 und 16)", EIR Internal Document, TM-22-80-7, 1980.
203. M. Jermann, "Neutronenspektrumsmessungen im ThO2-Blanket des PROTEUS (Core 14)", EIR Internal Document, TM-PH-806, 1979.
204. H. Graf, "Experimental Results Core 14 – Np237 Spaltenverteilung", EIR Internal Document, TM-PH-776, 1979.
205. K. Gmür and R. Chawla, "Experimental Results Core 14 – Reaktionsratenmessungen", EIR Internal Document, TM-PH-754, 1979.
206. K. Gmür,"PROTEUS Experimental Results Core 15. Reaktionsratenmessungen", EIR Internal Document, TM-PH-800, 1979.
207. U. Schmocker, "Berechnung radialer Reaktionsratenprofile im PROTEUS Core 15 und die Bestimmung wichtiger Reaktionsratenverhaeltnisse im Zentrum der Thoriummetall-Brutzone", EIR Internal Document, TM-22-80-27, 1980.
208. U. Schmocker, "Berechnung axialer Reaktionsratenprofile im PROTEUS Core 16", EIR Internal Document, TM-PH-821, 1979.
209. K. Gmür and H. Graf, "Experimental Results Core 16, Reaktionsratenmessungen. 1979, EIR Internal Document, TM-PH-814.
210. M. Jermann and D.T. Ingersoll, “Neutron Spectrum Evaluation in the Thorium Axial Blankets of the PROTEUS Reactor”, Proceedings ANS Topical Conference on Advances in Reactor Physics and Shielding, Sun Valley, Idaho, 1980.
211. J.C. Bosq, F. Morin, G. Girardin, "Caractérisation neutronique 3D du coeur RNR-G 12/06 à plaques", Note Technique, CEA-Cadarache, SPEC/LEDC/DO 07-417, 2007.
212. M. Cometto, "Benchmarking of ADS calculational tools and their application to different waste transmutation scenarios", Thèse EPFL N° 2714, 2003.

213. OECD, Accelerator-driven Systems (ADS) and Fast Reactors (FR) in Advanced Nuclear Fuel Cycles, A comparative study, OECD, 2002.

214. Physics and Safety of Transmutation Systems, A Status Report of the Nuclear Energy Agency, OECD, 2006.

215. J. Krepel, S. Pelloni, K. Mikityuk and P. Coddington, "EQL3D: ERANOS based equilibrium fuel cycle procedure for fast reactors", Annals of Nuclear Energy 36, 550 - 561, 2009.

216. W.F.G. van Rooijen, “Improving fuel cycle design and safety characteristics of a Gas Cooled Fast Reactor”, PhD thesis, Technische Universiteit Delft, 2006.

Acknowledgments

The present doctoral research was carried out in the Laboratory for Reactor Physics and Systems Behaviour (LRS) of the Paul Scherrer Institut (PSI) and the École Polytechnique Fédérale de Lausanne (EPFL); more precisely, in the framework of the FAST project. The thesis work, conducted mainly at PSI, has formed part of an international collaboration between PSI/EPFL and the French Commissariat à l'Energie Atomique (CEA), and has been achieved with the support and valuable contributions of a large number of persons. I am particularly grateful to:

- Professor R. Chawla, the director of the thesis and head of the Laboratory for Reactor Physics and Systems Behavior at EPFL, for giving me the opportunity to carry out this research in LRS and for his advice and guidance throughout the doctoral work.
- Dr. P. Coddington, the former leader and instigator of the FAST project at PSI, for his kindness, advice and guidance on different aspects of the work.
- Dr. K. Mikityuk, leader of the Fast Reactors group, for his availability and the many productive discussions we have had during the last two years. His contributions have been decisive and of remarkable importance. His kindness, encouragement and support contributed to create an excellent atmosphere.
- Dr. S. Pelloni, the supervisor of the first part of this thesis, for useful and constructive discussions, especially concerning the ERANOS code.
- Professor G. Rimpault, for offering me the possibility to spend four months with him at CEA-Cadarache and for supervising my work, not only at CEA, but also at PSI. His knowledge and vision have contributed to give a broader perspective to this thesis work, for which I am sincerely grateful.
- Aaron Epiney, Paolo Vinai, Paul Blair, Davide Bertolotto and Sun Kaichao, with whom I shared an office, for contributing to create a "special" and pleasant working atmosphere, as also Petr Petkevich for providing support and for sharing with me pleasant outdoor activities, especially biking in the Alps. Thank you for the many good times.
- My colleagues and friends at CEA-Cadarache in the "230- and 212-buildings", Dr. L. Buiron, Y. Peneliau, M. Vanier, Dr. J.C. Bosq, D. Plisson-Rieunier, Dr. J. Tommasi, W. Khamakhem, F. Morin and Dr. P. Richard, for their kindness, contribution and availability, and for their interest in this work.
- All of my colleagues and friends at PSI: Grégory Perret, David Blanchet, Jiri Krepel, Aurélia Chenu, Matthias Horvath, Hanna Kroehnert, Martin Ritterath and many more, from whom I had a chance to learn many things and for fun times.
- P. Jacquemoud, R. Ringele and Dr. V. Markushin, for their availability and understanding, in solving all possible administrative and computer related problems.

I would like to express my deepest thanks to my family, for the constant and unconditional support and patience during the last five years. In this context, I would particularly like to express my gratitude to Vaida, for her comprehension.

Finally, I would like to thank Professor L. Rivkin, Professor R. Chawla, Dr. K. Mikityuk, Professor G. Rimpault and Professor J. Wallenius for accepting to form the jury.

CURRICULUM VITAE

Gaëtan GIRARDIN
Chemin des Pyramides 1
1007 Lausanne
gaetangirardin@gmail.com
Tel: +41(0)79’210’43’30
CH-Switzerland

Born: 16th January, 1980
in Biel/Bienne, Switzerland
Nationality: Swiss

Education

2004 – 2009	Ph.D. research “Development of the Control Assembly Pattern and Dynamic Analysis of the Generation IV Large Gas-cooled Fast Reactor (GFR)” Laboratory for Reactor Physics and Systems Behaviour (LRS) **Paul Scherrer Institut, 5232 Villigen-PSI / École Polytechnique Fédérale de Lausanne, 1015 Lausanne** *Prof. R. Chawla*
2006	Expert in radioprotection for B- and C-domains **Strahlenschutzschule – CH-5232 Villigen**
2004	Diploma-thesis “Caractérisation d’une nouvelle paire de barres de contrôle pour le réacteur CROCUS de l’EPFL” Laboratory for Reactor Physics and Systems Behaviour (LRS) **École Polytechnique Fédérale de Lausanne, 1015 Lausanne** *Prof. R. Chawla*
1995-1999	Preparatory scientific education at Gymnase français de Bienne (Maturité C), Biel/Bienne, Switzerland

Professional Experience

2008	Chef des installations nucléaires du LRS de l’EPFL Laboratory for Reactor Physics and Systems Behaviour (LRS) **École Polytechnique Fédérale de Lausanne, 1015 Lausanne** *Prof. R. Chawla*

2006	Scientific assistant Laboratory for Reactor Physics and Systems Behaviour (LRS) **École Polytechnique Fédérale de Lausanne, 1015 Lausanne**
2006	License “chef d’exploitation du réacteur CROCUS de l’EPFL” Laboratory for Reactor Physics and Systems Behaviour (LRS) **École Polytechnique Fédérale de Lausanne, 1015 Lausanne**

Internships

2006	Internship at CEA, Cadarache, 13108 St-Paul-Lez-Durance, France Laboratoire d’études et de développement des cœurs, 4 months *Prof. G. Rimpault*
2002	Internship at Verres Industriels SA, 2740 Moutier, Switzerland “Etude de la résistance mécanique du verre trempé KEM-REX® à la flexion”, 2 months *Dr. A. Jelli*

Publications

Journal paper

G. Girardin et al., “Development and Characterization of the control assembly system for the large 2400 MWth generation IV gas-cooled fast reactor”, Annals of Nuclear Energy, 35 (2008) 2206–2218, 2008.

Conference papers

G. Girardin, D. Blanchet, K. Mikityuk, G. Rimpault and R. Chawla, "Three-dimensional core behaviour analysis of the Gas-cooled Fast Reactor (GFR) during hypothetical control assembly withdrawal accidents" Vols. ICONE-17, 17th International Conference on Nuclear Engineering, Brussels, Belgium, July 12-16, 2009.

G. Girardin, P. Coddington, R. Chawla, “A 3D Full-Core Coupled Thermal-hydraulics/Kinetics TRACE/PARCS Model of the 2400 MWth Generation IV Gas-cooled Fast Reactor”, PHYSOR-2008, International Conference on the Physics of Reactors, Nuclear Power: A Sustainable Resource, Interlaken, Kursaal Conference Center, Interlaken, Switzerland, September 14-19, 2008.

G. Girardin, G. Rimpault, P. Coddington and R. Chawla, “Control Rod Shadowing and Anti-shadowing Effects in a Large Gas-cooled Fast Reactor”, Proceedings of ICAPP ’07, Paper 7329, Nice Acropolis, France, May 13-18, 2007.

G. Girardin, P. Coddington, F. Morin, G. Rimpault, R. Chawla, “Design of the control rod system for the 2400 MWth Generation IV Gas-cooled Fast Reactor”, ICONE-10466, 15th International Conference on Nuclear Engineering, Nagoya, Japan, April 22-26, 2007.

G. Girardin, S. Pelloni, P. Coddington, R. Chawla, "Comparative Analysis of the Reference GCFR-PROTEUS MOX Lattice with MCNPX-2.5e and ERANOS-2.0 in Conjunction with Modern Nuclear Data Libraries", PHYSOR-2006, ANS Topical Meeting on Reactor Physics, Vancouver, BC, Canada, 2006 September 10-14, 2006.

Presentations

G. Girardin, "Calculation of control assembly driven transients in the 2400 MWth Generation IV Gas-cooled Fast Reactor (GFR) using the coupled code system TRACE & PARCS – Selected Results", presented at the PSI/CEA bilateral meeting on ALLEGRO and GFR, CEA-Cadarache, October 7, 2008.

G. Girardin, F. Morin, G. Rimpault, P. Coddington, K. Mikityuk and R. Chawla, "Development and Characterization of the Control Assembly System in a large 2400 MWth Generation-IV Gas-cooled Fast Reactor", presented at the International Workshop on Gas-cooled Fast Reactor, Paris, February 5, 2008.

G. Girardin, "Calculation of control rod withdrawal transients in the 2400 MWth Generation-IV Gas-Cooled Fast Reactor using the code system TRACE & PARCS", presented at the PSI/CEA bilateral meeting on GFR Design and Safety, CEA-Cadarache, November 19, 2007.

G. Girardin, "The new core design: Core F. An assessment of the control rod interactions; Comparisons with the reference design Core 06/04", presented at the GCFR Reactor Physics Group Meeting, CEA-Cadarache, June 19, 2007.

G. Girardin, "Shadowing and Anti-shadowing Effects due to Control Rods in the 2400 MWth GFR", presented at the GCFR Core Physics Group Meeting, AMEC NNC, Booths Hall, Knutsford, UK, December 6-8, 2006.